DEVELOPMENT OF MODELS FOR MONITORING THE URBAN ENVIRONMENT USING RADAR REMOTE SENSING

CATHERINE TICEHURST

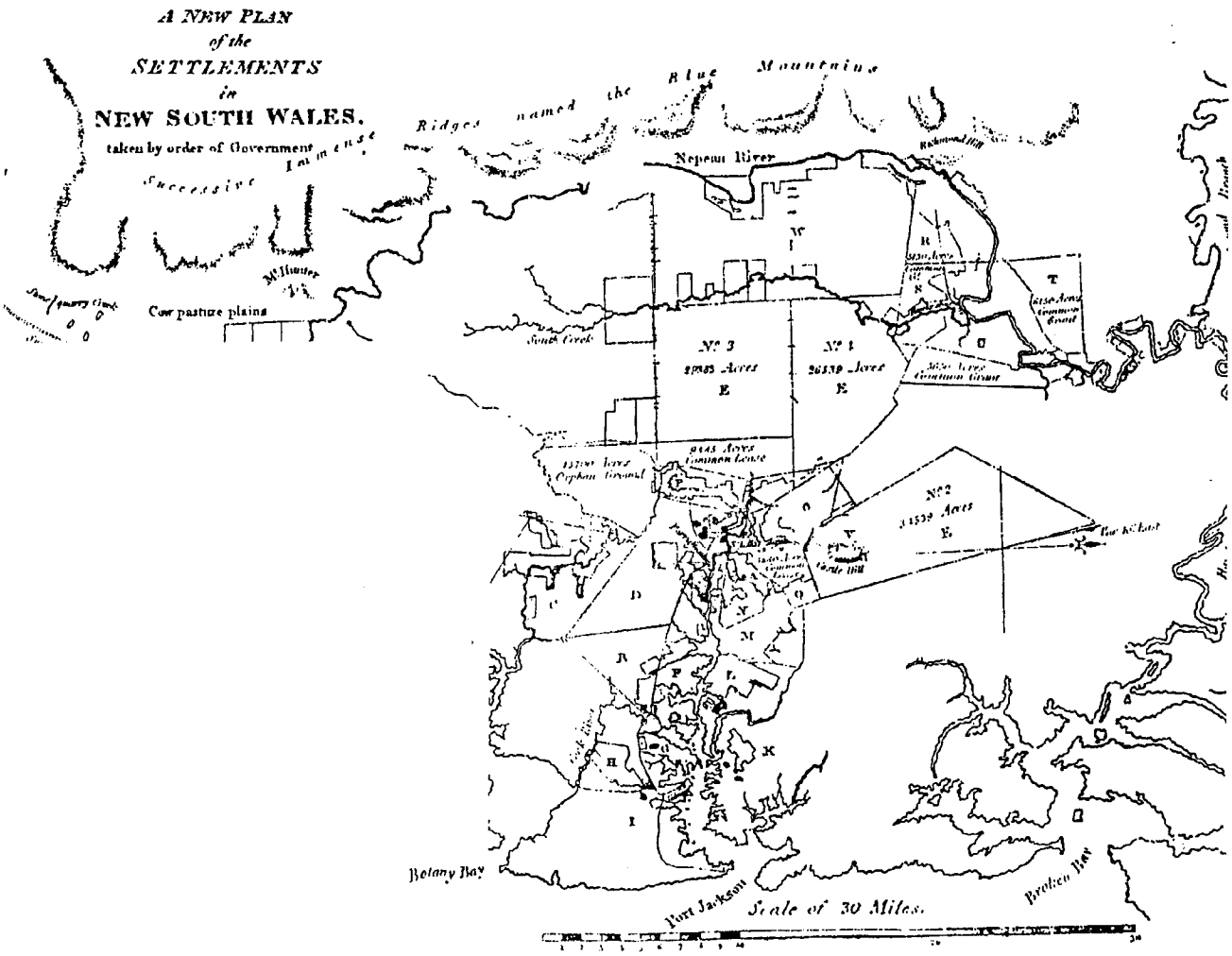

UNISURV S-54, 1998

Reports from

SCHOOL OF GEOMATIC ENGINEERING

THE UNIVERSITY OF NEW SOUTH WALES SYDNEY NSW 2052 AUSTRALIA

UNISURV REPORT S-54, 1998

DEVELOPMENT OF MODELS FOR MONITORING THE URBAN ENVIRONMENT USING RADAR REMOTE SENSING

CATHERINE TICEHURST

Received: November, 1997
Accepted: February, 1998

SCHOOL OF GEOMATIC ENGINEERING
UNIVERSITY OF NEW SOUTH WALES
SYDNEY NSW 2052
AUSTRALIA

National Library of Australia

Card No. and ISBN 0 7334 1679 9

ABSTRACT

The world's population is rapidly increasing, especially in urban regions to which many rural inhabitants are migrating. Such an effect results in the need for a more efficient method of monitoring cities, both in developing and developed countries. Present monitoring techniques are inefficient, and unable to effectively maintain up-to date information due to the population increase. Hence, the demand for settlement detection, urban classification and population estimation is apparent.

Radar remote sensing is showing great potential for assisting in such a matter. Its ability to discriminate between small buildings of sparse layout, and large, densely spaced, buildings is slowly being realised. This research addresses this issue through the development of a primarily theoretical model.

The urban environment is a complex mixture of built as well as natural elements. In order to simplify such a difficult situation, the backscatter expected from urban areas can be divided into simple scattering mechanisms. The most important ones chosen for this research are double bounce (from building walls and tree trunks), single bounce (from building roofs), and volume scattering (from tree canopies). The model has been designed to consider these scattering mechanisms, and their expected proportions, occurring in the urban environment.

One of the greatest difficulties created through using radar in the built environment, is due to the 'Cardinal Effect'. This occurs when there is strong double bounce scattering due to the intersection of the orthogonal building wall and ground surface being perpendicular to the look direction. An empirical investigation is conducted in the thesis to further understand this phenomenon.

In order to develop the model, many parameters, including those relating to the cardinal effect, need to be considered. Determination of such parameters is not a simple task, and requires some general assumptions to be made. The model

has been designed to determine the backscatter and polarisation information for two different urban classes (ie., residential and commercial). These classes are chosen because they generally represent the low and high density urban areas respectively.

The backscatter and polarisation information from a single building is developed and then expanded into a block of buildings, with consideration of radar shadowing effects. Trees are also included in the simulated residential areas.

In order to test the accuracy of the model for residential and commercial land use, test sites representing a large range of orientation and look angles, are chosen in the city of Sydney, Australia. AirSAR data for these test sites are compared to model simulations representing the same characteristics. The results show that L-band model output is quite comparable with the real data. The P-and C-band are less reliable, with the model C-band results showing little resemblance to the AirSAR information.

For the model to be further tested, a simple classification is performed over a large area of the Eastern suburbs of Sydney. L-band data is used due to the model simulations closely representing real data. Furthermore, the real P-, L- and C-band polarisation information were found to be quite similar, so a multi-wavelength classification using radar data was not seen to contribute significant information compared to a single band.

The classification is based on a comparison between the model and AirSAR total power, polarisation index and polarisation phase difference. The classification shows that the model has the ability to distinguish between low and high density urban areas. However, due to the difficulties in defining the characteristics of residential and commercial land uses, there is some overlap in the classification. Some tall, dense residential areas are classified as commercial. Similarly small scale commercial areas are classified to be

residential. Such a problem is related to the definition of land use rather than land cover.

The most important classification parameter observed through this exercise is the total power. The polarisation index proved of little use due to its incapability of distinguishing between residential and commercial classes for the real data. Classification using the total power and polarisation phase difference together gave a less accurate result than total power alone.

However, overall results show that the potential which radar has as a remote sensing tool for distinguishing between low and high density urban areas, and for classification (under the appropriate circumstances), is quite high. This is especially so when radar is combined with other information gathering systems, such as optical remotely sensed data. Such a combination could be very beneficial for the growing need for urban monitoring and population estimation.

ACKNOWLEDGMENTS

Completion of this PhD resulted from the knowledge and support of a number of people. I would like to thank my supervisor, Prof. Bruce Forster, for his strong guidance and complete support for the full duration of this project. I am also indebted to Dr. Yunhan Dong whose extensive knowledge in the fields of electromagnetics, radar analysis, and theoretical modelling have been invaluable to me.

I would like to thank my family and friends for supporting me during my highs and especially lows. Thanks goes to David for reviewing the thesis, and for his encouragement.

CONTENTS

6. THE MODEL PARAMETERS FOR THEORETICAL BACKSCATTER

7. A COMPARISON OF MODEL SIMULATION WITH REAL URBAN DATA

LIST OF TABLES

LIST OF FIGURES

GLOSSARY

Important and commonly used symbols, parameters and acronyms.

Symbols and Parameters

λ	wavelength of microwave signal
θ^*	look angle (also equivalent to incident angle for a horizontal surface)
ϕ^*	orientation angle - the angle between the perpendicular to a building surface, and the radar look direction
$\mathbf{k_0}$	wave number
σ^*_{ppq}	backscatter from surface *q* for *pp* polarisation
σ^{0*}_{ppq}	backscatter coefficient from surface *q* for *pp* polarisation
ε	dielectric constant
$\varepsilon_w, \varepsilon_r, \varepsilon_g$	the dielectric constant for the wall, roof and ground respectively
$\mathbf{R_{pw}, R_{pr}, R_{pg}}$	Fresnel reflection coefficients for the wall, roof and ground respectively, for *p* polarisation
$\mathbf{rms_w}$, $\mathbf{rms_r}$, $\mathbf{rms_g}$	route mean square surface roughness for the wall, roof and ground respectively
L	length of buildings
H	height of buildings
b	width of buildings
γ	slope of roof of buildings
$\mathbf{H_r}$	height of roof of buildings
x	distance between buildings along the rows
y	distance between buildings along the columns

cr	number of columns/rows of buildings in a block
N	number of buildings in a block
$\mathbf{A_b}$	area of building block
$\mathbf{N_t}$	number of trees in a block
$\mathbf{r_t}$	tree trunk radius
$\mathbf{H_t}$	height of tree trunk
R	radius of canopy spread
α	attenuation coefficient of the canopy
ρ	volume scattering coefficient of the canopy
S*	scattering matrix. When subscripted with *h* and/or *v* polarisation, it represents a component of the matrix
ℓ^*	Mueller matrix. When subscripted with *h* and/or *v* polarisation, it represents a component of the matrix
ϖ^*	the common term of the scattering matrix, independent of polarisation
χ	ellipticity angle of polarised wave
ψ	orientation angle of polarised wave
$\mathbf{L_p}$	dimension of the Metal Factor
$\mathbf{P_s}$	percentage of power able to penetrate a material
σ_{ma}	backscatter from $1m^2$ of building wall (without metal)
σ_{me}	backscatter from metal in $1m^2$ of building wall
TP	total power
PI	polarisation index
PPD	polarisation phase difference
HH	Horizontally transmitted and Horizontally received radar wave

VV	Vertically transmitted and Vertically received radar wave
HV	Horizontally transmitted and Vertically received radar wave
VH	Vertically transmitted and Horizontally received radar wave

* Subscripts may occur with these symbols to represent a different scattering object, ie., 'fw' - front wall, 'sw' - side wall, 'fr' - front roof, 'br' - back roof, 'cn' - canopy, 'tg' - trunk-ground, 'tr' - tree

Acronyms

CBD	Central Business District
SAR	Synthetic Aperture Radar
SLAR	Side Looking Airborne Radar
SIR-A	Shuttle Imaging Radar (flown in 1981)
SIR-B	Shuttle Imaging Radar (flown in 1984)
Seasat	an ocean monitoring radar satellite (launched in 1978)
ERS	European Remote Sensing Satellite
JERS	Japanese Earth Resources Satellite
RADARSAT	Canadian RADAR SATellite
AirSAR	Airborne Synthetic Aperture Radar (developed by NASA/JPL)
SPOT	Satellite Pour L'Observation De La Terre - French Earth Observation Satellite
MSS	Landsat MultiSpectral Scanner
TM	Landsat Thematic Mapper

1. An Introduction to Remote Sensing for Urban Monitoring

1.1 Introduction

Many people today are aware of the existence of environmental problems. Pressures placed on the land and resources due to human occupation and activities are rapidly growing (Barrett & Curtis, 1992).

Human activity is gradually reducing the life supporting capacity of this planet. This is partly due to the unequal consumption of world resources by a wealthy minority, and to the damage caused by technology and lifestyle. However, at the same time, the majority of the world's population is poor and struggling to improve living standards. Furthermore, increasing evidence reveals that many nations are degrading or even destroying natural resources in their attempt for advancement (Barrett & Curtis, 1992).

The world population has grown from about 200 million, around 2000 years ago, to about five billion today. Some estimate that this figure will increase to six billion by the end of the twentieth century. As the world population continues to grow, it is unknown as to when it will stabilise. Some authorities suggest this may not happen until numbers reach ten to 14 billion (Barrett & Curtis, 1992).

Fortunately an awareness of environmental problems and the need for conservation is increasing. There is a realisation that sustainable development is required, rather than exploitation and destruction of natural resources. It is here that remote sensing plays an important role. "Remote sensing is beginning to fulfil a long recognised need for both intensive and extensive monitoring of Earth, simultaneously in much more detail yet also with much greater uniformity than has ever been possible before" (Barrett & Curtis, 1992, p5).

1.2 Population Problems and the Need for Urban Analysis

Although urban areas occupy a relatively small portion of the Earth's surface, they are very significant in terms of the world's population, environmental impact (present and potential), and migration patterns (Henderson & Xia, 1997). Cities also represent centres of political, cultural, and economic activities (Xia, 1996). As a result, they are one of the most rapidly expanding and changing features of the landscape, resulting in a most complex and dynamic living environment (Henderson & Xia, 1997).

Over 70 percent of the population of developed countries live in urban areas (Henderson & Xia, 1997). Furthermore, over 1 million new urban inhabitants are added to the world each week (Kawamura *et al.,* 1996). It is predicted that the world population will increase from presently less than 6 billion up to 10 billion around the year 2100, most of this increase being in developing countries (Barrett & Curtis, 1992).

Over the past 20 to 30 years, many countries of the developing world have experienced rapid and uncontrolled growth as the rate of migration from rural populations increases (Forster & Ticehurst, 1994). More than 20 million people move from rural areas to the cities each year to find employment and escape rural poverty (Xia, 1996).

The pressures which an increasing population inflicts on the world's diminishing finite resources is of great concern to the world's scientific community (Henderson & Anuta, 1980). The rapidly increasing spread of urban settlements in many regions of the world has resulted in environmental problems demanding urgent attention (Kawamura *et al.,* 1996). Increased greenhouse gases due to growth of urban areas, industrialisation, the increasing role of vehicles as the economy improves, particularly in east Asia, are growing problems. Hence monitoring these environmental changes is a problem faced by various institutions today.

Governing authorities have the responsibility to detect and record changes occurring within urban centres. However, this is a difficult task because cities are constantly developing (Kressler & Steinnocher, 1996). Some cities in developing countries are growing too rapidly for governments to maintain up-to-date records of its growth and change in land use. This leads to problems in the prevention of urban sprawl and the over-development of fragile lands.

Whilst urban centres provide the greatest concentrations of living and working facilities, they also present a wide range of problems (Barrett & Curtis, 1992). The need for new urban infrastructure becomes more apparent as the urban population continues to grow (Kawamura *et al.,* 1996).

Information on the patterns of settlement growth is needed at local, regional, national, and global scales (Henderson & Herrig, 1996). Regular analysis of population estimation and migration patterns is necessary for assessing how the environment is withstanding the impact which human activities inflict upon it. Monitoring changes in urban land use is vital for "future economic development planning, natural resource allocation, and environmental ... management" (Henderson & Xia, 1997, p79).

There is presently a lot of interest being shown in the development of 'urban information systems' for the interrelation and practical utilisation of urban data from a wide range of information sources (Barrett & Curtis, 1992). Such information is vital for planners, economists, environmentalists, and resource managers (Xia, 1996).

Information about the present population distribution and human settlement growth is important for both census estimates and appropriate management of resources (Henderson & Herrig, 1996). Many city authorities do not monitor changes occurring between census surveys and are ignorant as to how their city is growing and how fast. Rates and directions of population change are uncertain. Even more importantly, city authorities do not know what is happening in their dynamic or new regions (Horton, 1974).

In developing nations, there is rapid population growth, poor data collection techniques, and a noticeable impact due to migration (Henderson & Herrig, 1996). There is an inadequate understanding of the existing urban system, resulting in a lack of sufficient, continually updated, spatial data, dramatically restricting the planning process (Kawamura *et al.,* 1996). However, developed nations are also seeking more efficient methods of acquiring population data. Thus one can conclude that the need for current information on population and human settlement is universal (Henderson & Herrig, 1996).

However, present methods of data acquisition, such as traditional field and aerial photography, and analysis, continue to be expensive, time-consuming, and extremely inefficient (Lindgren, 1974). Traditionally, data for urban social and economic studies, and sources of population data are obtained through national census and related statistics, collected by field surveys, interviews, and/or questionnaires. These are a time consuming and expensive method of data collection (Henderson & Xia, 1997). Developed countries only conduct a population census at five or ten year intervals. However, this is much less frequent for many developing nations, while others have never completed such a survey. Furthermore, insufficient resources often makes it impractical, if not impossible, to update census data in a timely manner. "This in no way matches the needs of the world's rapidly growing populations, changing societies, and economies" (Henderson & Xia, 1997, p79).

Therefore, the challenge is to gather the necessary information at acceptable costs and to develop suitable techniques for the extraction of required information within the time intervals required (Kressler & Steinnocher, 1996).

Remote sensing is one source of information about the earth's surface, and hence can be beneficial for urban monitoring. It provides a rapid method of data collection, and the final product can contain extensive information about an area. Satellite and airborne remote sensing systems are continually developing, with their technology improving and applications expanding.

1.3 Why use Remote Sensing for Urban Monitoring?

The effects of the increasing population concentrating in urban centres are being felt throughout the world. Hence, timely and detailed information is vital for planning in urban areas. Remote sensing can assist in this process (Forster, 1985). Remote sensing provides a method for the detection and distribution of activities and physical changes, which are then related to social and economic changes within the surrounds (Horton, 1974).

During its early stages of development, remote sensing could not be effectively used due to its low spatial resolution. However, an improvement in ground resolution has enhanced remote sensing in various fields. Land-cover classification information can be extracted and applied to land-use planning. Such applications include determining essential information such as building coverage ratio and bulk ratio (Deguchi *et al.,* 1995).

Remote sensing applications for settlement detection, population estimation, and urban analysis, have been investigated since the mid-1950's (Henderson & Xia, 1997). Social and economic characteristics of a residential district are related to "housing types, building densities, environmental characteristics, and the spatial relationships" it has with other land uses visible on remote sensing imagery (Henderson & Xia, 1997, p82).

Satellite sensors are very suitable for a number of different applications because of their low data recording costs, and their appropriate spatial, spectral, and temporal resolution. As the sensors are able to record large quantities of data, the techniques used for image analysis can be reliable and very efficient (Kressler & Steinnocher, 1996).

For urban studies, photo interpretation is usually used, however air photos are expensive to process, and require a lot of time for analysis. Satellites have a number of advantages, these include: regular repeat coverage; data recording from the same location at the same time of day; and maintaining constant scale and look-angle (Kressler & Steinnocher, 1996). If the remotely sensed data is

able to be utilised for analysis of the urban areas, the time period between data capture and final product will be minimal compared to currently used methods.

Since the launch of the first Landsat remote sensing satellite, in 1972, many attempts have been made to use remotely sensed data, both satellite and airborne, for monitoring and classifying urban areas (Forster, 1985).

During its early use, remote sensing's potential for urban monitoring was realised. Although research primarily involved photographic sensors, radar and thermal infrared system's potential for urban applications was apparent, producing encouraging results (Lindgren, 1974).

Although remote sensing is incapable of providing all the necessary information for determining social and economic attributes of an urban environment, it can provide a different perspective (Henderson & Xia, 1997). The potential usefulness of remote sensing for detecting changes, may help to improve the effectiveness of urban management and provide necessary information for developing plans for guiding the growth and development of the urban environment (Horton, 1974).

Remote sensing systems operating in the visible and near-infrared wavelengths have received a lot of attention and therefore provide the most advanced and widely used techniques (Henderson & Xia, 1997). However, such systems are of little benefit in areas of the world subject to a lot of cloud, rain and/or low light levels. In many cases these are precisely the developing countries of the equatorial zone, which most need urban data. It is these regions which would find radar imagery an attractive alternative. Radar's relatively coarse resolution creates some difficulties for population analysis, however in many cases it remains the only plausible sensor (Henderson & Anuta, 1980).

1.4 A Brief History of Radar Remote Sensing

Synthetic Aperture Radar was developed during the late 1950's - early 1960's (Richards *et al.,* 1994), particularly by the military. The development of this concept dramatically improved the resolution with respect to the ground range covered on a single image. It enabled satellites to produce images capable of detecting relevant detail.

The Seasat satellite was the first of the active microwave sensors to be launched, in 1978, beginning a new era of radar remote sensing (Richards *et al.,* 1994). Since then many radar imaging systems have been developed including SIR-A (1981), SIR-B (1984) (Richards *et al.,* 1994), ERS and JERS satellites launched in the 1980's and 1990's, along with the recently launched Radarsat (Raney *et al.,* 1991).

The development of multi-frequency, multi-polarisation, multi-incident angle digital airborne SAR systems during the 1980's, AirSAR being one such example, created many new possibilities. Since then, the design and successful testing of the SIR-C/X SAR satellite system in 1994 has resulted in many research projects and "will undoubtedly accelerate our theoretical understanding of the interacting mechanisms in the microwave region and lead to widespread, innovative applications in a large number of disciplines" (Xia, 1996, p2311).

For important terminology relating to radar, refer to Appendix A.

1.5 Radar Remote Sensing of the Urban Environment

A radar sensor's capability to characterise the physical nature of the land cover over a large region, is fundamental to many earth science investigations (Evans *et al.,* 1988). Radar remote sensing provides very different but potentially

complementary information to visible and near infrared (NIR) sensors (Forster *et al.,* 1996).

Microwave radiation, being a much longer wavelength than visible/infrared radiation, interacts with fundamentally different properties in the objects being observed, than do the optical wavelengths (Schumann, 1996). Optical systems are more concerned with the chemical properties of the targets, whilst SAR imagery provides information on the dielectric properties of materials (Nasr & Vidal-Madjar, 1991). Radar has the ability to penetrate the surface of an object on land which optical wavelengths are unable to do. However, the interaction with microwaves beneath the water surface is substantially limited compared to optical (Schumann, 1996).

Some of the differences and distinct advantages which radar has to offer over optical systems include:

i. its longer wavelength gives it the advantage of being able to penetrate cloud, and often rain;
ii. being an active system, it can operate any time of the day or night;
iii. Illumination can be in the optimum direction and incident angle to enhance desired features;
iv. radar systems provide additional information for identifying objects and mapping surface materials due to the backscatter intensity being predominantly determined by different properties of ground targets (such as moisture content and surface geometry);
v. the polarisation of the radar signal can be varied to investigate how different objects depolarise the signal, and;
vi. radar's long wavelength enables it to penetrate, to a certain extent, into vegetation, or the terrain surface, enabling the subsurface characteristics to be studied (Xia, 1996).

Apart from their independence from the sun as a source of illumination, one of microwaves greatest assets is its capability to penetrate clouds, and to some extent rain. Urban environments that are subject to a lot of rain and cloud cover,

require radar systems as their primary method of remotely sensed data collection. This is especially so in tropical countries that are developing rapidly and require relatively fast, efficient land information (Ulaby *et al.,* 1981). These also being the regions where least is known about present terrain conditions (Xia & Henderson, 1997).

Microwaves provide information about an object's physical structure and electro-magnetic properties. The depolarisation and spectral reflectivity of the radar backscatter from a surface provides information about the surface roughness, geometric structure, morphology, and dielectric constant of the surface, and sometimes the subsurface (Elachi, 1988). The two major characteristics of the object being its geometric and dielectric properties (Schumann, 1996).

Three types of urban-related projects have been identified for which radar's weather independence can assist: (a) when postponement of data collection owing to bad weather would be unacceptable; (b) analysis of general land-use patterns for large cities, and: (c) investigating large regions to determine the location and extent of small urban centres (Moore, 1968).

1.5.1 Urban Applications of Radar

With the launch of a range of spaceborne radar imaging systems, such as Seasat, Almaz-1, ERS-1 and ERS-2, JERS-1, and Radarsat, radar remote sensing has become an operational technology for mapping natural resources and monitoring the changing conditions of the built landscape (Xia, 1996).

Knowledge about settlement detection and changes, and the relationship between the radar system and environmental parameters is of potential interest to a large sector of the scientific community. This information can be beneficial for environmental monitoring and population assessments, especially where such data is overdue. Information such as population estimates and urban growth models, which may potentially be determined through radar analysis,

are important factors required by resource management users, especially in developing nations (Henderson, 1995).

Radar's unique properties provide a number of potential applications for urban monitoring. Early research using radar systems has concentrated on land use and the identification of small urban centres. K-band wavelength demonstrated its capability to detect linear transportation routes as well as general patterns of industrial, residential, and vacant-land cover (Lindgren, 1974). As a tool for identifying built-up areas, radar's capacity was apparent, especially in determining the relationship between area size and population. Such a relationship would enable rapid population estimates to be determined over large areas. This would particularly benefit many countries of the developing world (Lindgren, 1974).

The geometric relationship between radar and settlement patterns, the shapes and sizes of structures, and settlement morphology results in high contrasts between the built landscape and the natural terrain. The urban environment has an "abundance of unique dihedral and trihedral reflectors and patterns ideally susceptible to radar analysis" (Henderson & Xia, 1997, p82).

A few studies have noted differences in building material, and building density, were detectable on radar imagery. Further classifications such as defining building densities within central business districts, commercial and some industrial activity, and different levels of residential density may be possible (Henderson & Xia, 1997).

Bryan (1983) reported three areas where radar imagery could make valuable contributions to urban analysis: feature orientation and shape; spacing of large scatterers, and ; definition of the upper scattering surface of the city.

It has been suggested by Henderson and Xia (1997) that information about social and economic situations in the urban environment which may potentially be obtained from radar imagery include: the distribution of residential areas with respect to other urban cover types; the general age of the residential areas; the

location of recreation and open areas, commercial and industrial land use, and some institutions; the amount and position of vegetated areas; building density, and; major transportation routes.

1.5.2 Urban Bulk Density

Classification of the urban environment is an important aspect which may assist in monitoring city populations. The building coverage ratio and bulk ratio (ie., the amount of built space per ground space) are vital sources of information in land use planning as they provide the necessary restrictions for maintaining adequate environmental conditions within an area (Deguchi *et al.,* 1995).

While optical sensors can give an indication of the cover proportions in an urban area from a planimetric view, they cannot provide information about the vertical dimensions, unless more complex and time consuming stereoscopic image data is used. "To some extent all combinations of specular and diffuse backscatter will be a function of the height and bulk of buildings", hence there is potential for using radar backscatter to provide information about the vertical dimensions and size of the built environment (Forster & Ticehurst, 1994, p292).

1.6 Purpose of this Research

Little research has been undertaken into the application of radar remote sensing in the built environment. Most present research concentrate on the use of radar for analysis of natural elements, such as crop or forest monitoring. The urban investigations which have been performed are often based on settlement detection rather than a more detailed urban analysis, and generally use manual interpretation. Whilst this is a complex area of study, radar remote sensing's potential is great. Particularly with its ability to provide information about building densities and heights (a skill which visible/infrared systems are unable to achieve, unless stereoscopic images are acquired).

The aim of this research is to further investigate the complex interaction which microwave radiation has in urban areas, and to obtain an understanding of the scattering mechanisms occurring. Such a task will be achieved through the development of a model. Radar's potential ability to distinguish between densely spaced, tall buildings, and sparse, small buildings will be examined through the model by focusing on the simulation of commercial and residential land uses, respectively.

The model needs to be developed such that it can estimate both the intensity and polarisation information, for both residential and commercial land uses, for all possible radar look angles and look directions with respect to the buildings orientation. Due to the strong relationship which radar has with the orientation of urban areas, especially from double bounce effects, prediction of this phenomenon is necessary. Hence, the model must be tested over a range of building orientation angles with respect to the radar, to determine its robustness.

1.7 Summary and Overview of Thesis

The importance and complexity of the urban environment leads to a requirement for its constant monitoring and maintenance. As this chapter has shown, there is a definite role that remote sensing, especially radar remote sensing, can fulfil in relation to urban analysis. Microwave radiation's unique interaction with urban structures and objects is indicative of the potential use imaging radars have for applications such as settlement detection, population estimation, and urban planning.

Chapter 2 will expand on the applications that radar systems can have in relation to urban analysis, with reference to previous research. Common research areas of interest are settlement detection and radar's potential for population estimation, urban classification, and radar's unique properties and how they complement optical systems.

The remaining chapters are of a more theoretical nature, generating and testing a model for classification of the urban environment. An introduction to some important relationships that radar has with the built environment is presented in **Chapter 3**. This includes the formulae used to represent simple scattering mechanisms occurring between the microwave radiation and buildings, as well as the calculation of polarisation information.

Probably the most dominant relationship is between the radar look direction and building orientation, and for this reason a whole chapter is dedicated to this matter (**Chapter 4**). It begins with a brief discussion of previous research undertaken in this area, and details the outcome of a small investigation using real radar data.

Chapter 5 formulates the model, by integrating all the necessary building and radar parameters deemed necessary for predicting the radar backscatter. The model is expanded from a single building into a block of buildings, including consideration of radar shadow regions and vegetation found in residential areas. The polarisation information required for producing signatures is also given.

Definition of the relevant radar and building parameters are determined in **Chapter 6**, including an investigation into the sensitivity of these parameters. Consideration of metals found in both residential and commercial buildings is also discussed.

The model output is then compared with real data (**Chapter 7**). This is achieved through the selection of six urban test sites from real radar data, and a comparison of these with a model simulation representing equivalent characteristics.

A classification is performed in **Chapter 8** using the L-band model data. Two large urban test sites are chosen, covering a range of radar look angles and

building orientations. The results are analysed to test the model's ability to distinguish between real residential and commercial land uses. The resulting conclusions are discussed in the final chapter (**Chapter 9**).

2. PREVIOUS STUDIES ON APPLICATIONS OF RADAR REMOTE SENSING FOR URBAN MONITORING

2.1 Introduction

The applications of radar as a remote sensing tool have been expanding since it first became operational, during the 1970's. As introduced in Chapter 1, radar has many unique properties enabling it to provide different, and complementary, information to other data sources. Chapter 2 examines research that has been, and is currently being done with respect to the urban environment.

At present there is relatively little research being undertaken into monitoring of the urban environment using radar data. A literature search by Henderson and Xia (1997) indicates that urban settlement and population studies based on radar imagery have received less attention than other fields. Most work is orientated towards vegetation, agronomy, forestry, soils science, geology, hydrology, oceanography, and ice/snow studies, where radar remote sensing is emerging as an operational technology (Xia, 1996).

Optical remote sensing is often applied to urban land use mapping and detection of land cover changes. In comparison, the potential of imaging radar systems for urban land use mapping still remains to be investigated (Xia, 1996). As suggested by Xia (1996), possible reasons for this small number of radar urban applications are the variability of the urban landscape and the complexity of the interaction mechanisms between built features and radar signals. Also, until very recently, radar data was not readily available and had a relatively limited extent of land coverage.

The type of information which can be determined for an urban environment from remotely sensed data is related to such factors as: land use and land cover; the number of classification categories; the size, pattern and shape of

the building blocks; settlement history; economic factors; climate; and other aspects of the environment depending on output requirements (Xia & Henderson, 1997).

This chapter focuses on past and present research relating to urban mapping and monitoring. The most common applications of radar remote sensing in the urban environment concentrated upon in this chapter are: settlement detection and radar's potential for population estimation; classification, of such features as forests, open spaces, and urban areas, or individual classes within an urban district; and the unique properties of radar and how this information complements optically imaged data.

2.2 Settlement Detection and Population Estimation

Human settlements over a certain size can be detected using radar systems. If one could formulate a relationship between the strength of the backscatter from a particular settlement and the number and size of buildings, the potential for population estimation is possible.

In order to use remotely sensed data to determine population estimation and to investigate settlement patterns, it is first necessary to detect settlements. "Imaging radars are particularly suited to this purpose because settlements are generally accentuated on the imagery due to the presence, geometry, materials, types, and distribution of horizontal and vertical structures" (Henderson & Xia, 1997, p80).

Early work on settlement detection found that experienced photo interpreters could identify all cities having a population over 7000, 80 percent of settlements with a population over 800, and 40 percent of settlements having between 150 and 800 inhabitants (Lindgren, 1974).

Lo (1984) found SIR-A data to be a useful source of information for rural settlement distribution. It was found that the settlements reflect a strong

backscatter relative to the dark rural background, making individual settlements stand out, also indicating their size. Further work by Lo (1986) examined SIR-A's ability for detecting land use and estimating the density of settlements, showing promising results.

The effects of different look angles, polarisation, look directions, wavelength, and number of looks, on settlement analysis have been investigated. It was found that each of these factors affected the interpretability of urban land cover, within the radar image (Henderson & Xia, 1997).

Henderson & Anuta (1980) analysed multiple radar imagery of different scales and wavelengths, and over varying environments, to determine which factors resulted in good settlement detectability. X- and K-band RAR (Real Aperture Radar) were found to be of equal ability. However different settlements were visible on different images. It was generally found that imagery at a scale of 1:200,000 or larger was required for settlement detection. Sixty to seventy percent of the settlements having 200 to 300 inhabitants could be identified at this scale. Results improved with larger populations. Environmental factors also played an important role in settlement detection.

In a later study, three data takes of SIR-B imagery (L-band, HH) with different look angles were used for settlement detection analysis. Results indicated that steep look angles had the greatest errors, and hence were of minimal use. Accuracy improved as look angle increased from 20-23° up to around 41°, and then decreased for the 51° imagery. Look direction also played a role in the visibility of settlements (Henderson, 1995).

A further analysis of settlement detection with SAR imagery was undertaken using varying wavelength, polarisation, and look angle. The results demonstrated that larger look angles were better, agreeing with earlier studies. The research concluded that L-band imagery is better than X- or C-band for settlement detection. Cross-polarised imagery were more accurate than co-polarised, but the total power images proved to be just as beneficial, if not

better. However, the best data for settlement analysis were multispectral SAR composite images (Henderson & Herrig, 1996).

In general, Henderson and Xia (1997) found that most research indicates co-polarisation appears to be better for settlement detection but cross-polarised imagery is preferred when determining the extent of settlements.

Radar's potential for population estimation is still in its investigative stage. Even though only a small number of studies have attempted to actually estimate the population of a settlement using radar imagery, the results are promising. However, before it can improve, all radar and environmental parameters need to be defined and applied to algorithms developed to estimate population from radar data (Henderson & Xia, 1997).

An investigation into the relationship between settlement area and population using SIR-A imagery was performed by Harris (1985). Only settlements with a population greater than 1000 inhabitants were used due to difficulties in detection of smaller settlements. Harris found an r^2 value of 0.91 at a 99% level of significance when relating settlement area with population through linear regression. However, problems were encountered for larger settlements having a concentration of inhabitants in buildings greater than two storeys. Hence a population increase did not necessarily mean an expansion in settlement area, making this technique less robust.

Such a problem may be overcome by radar because one main advantage for population estimation is its backscatter strength has the potential to be indicative of the vertical dimensions in a built environment. According to Henderson and Xia (1997, p80), a settlement's built-up area should be "proportional to the population raised to some power". Radar imagery can directly measure the built-up area, and existing population data can be used for empirically determining the coefficient and exponent. Studies completed to date using radar for population estimation clearly show its potential for such applications (Henderson & Xia, 1997).

The use of radar for settlement detection and population estimation is dependent on many variables. Henderson and Xia (1997) have found that a number of researchers have reached some common conclusions:

i. settlement detectability varies with building type and construction material;
ii. surrounding land cover may create some confusion between settlements and other terrain features;
iii. the same land cover type may assist settlement visibility in one area and lead to confusion in another;
iv. it is easier to detect and define the limits of small to medium settlements rather than large ones;
v. wavelength, polarisation, look direction, and look angle all affect how a settlement appears in the imagery, and;
vi. the interpreter's experience and prior knowledge of the urban areas is important (Henderson & Xia, 1997).

2.3 Classification

"Land use mapping from radar data involves converting radar response patterns into information classes that are useful for the purposes of economic development planning, resource allocation, and environmental management" (Xia, 1996, p2311).

Early investigations into the use of airborne systems (K- and X-band) for classification demonstrated radar's ability to separate urban areas from other land covers such as agriculture, forest, water, and bare ground (Henderson & Xia, 1997). Since then, numerous level 1 classification work (eg., Anderson, 1972) with radar imagery, using various techniques, have been performed. Some of the different classes separated include: sugarcane, water, urban areas, and bush (Paudyal *et al.*, 1995); trees, short vegetation, urban and bare surface (Pierce *et al.,* 1994); urban, ocean and park (Hara *et al.,* 1994); and urban, open flat surfaces, short and tall vegetation (Dobson *et al.,* 1996).

Less research has concentrated on detailed urban classifications using radar imagery. However, the use of radar as a mapping tool of urban scenes does not need to be confined solely to the detection of a settlement. Radar data has the ability for very detailed mapping (Bryan, 1975). Studies have shown that seven or eight categories of urban land uses can be detected with some degree of reliability (Henderson & Xia, 1997).

Of the work that has been done, most has concentrated on image interpretation from visual analysis. As early as 1969 interest was shown in using radar as a classification tool. Lewis *et al.* (1969) performed a visual interpretation study of some K-band radar imagery. It was found that like-polarised imagery proved better for detection of linear features, such as railroads and power lines, when oriented parallel to the flight path, whereas cross-polarised images were better for detecting railroads and power lines oriented at an angle other than parallel to the flight path.

Classification of urban areas through visual interpretation of radar images, according to Martin-Kaye (1981), is related to four interpretative parameters: texture, context, shape, and brightness of tone. Brightness of tone, ie., the strength of signal return, is considered the least important for visual interpretation, although it is through changes in tone that features are characterised (Martin-Kaye, 1981). This may be true for visual identification, however for an automated approach the brightness is an important factor.

Early work by Bryan (1974) revealed that SLAR imagery was a relevant tool for urban classification. An analysis was conducted on visually interpreted radar imagery. It was reported that from the four images used (L-band and X-band, HH and HV) the accuracy of positive identification of the land-use categories in decreasing order were: residential; industrial; open and other; transportation and utilities; commercial and services; and institutional. Bryan (1974) suggests that radar imagery may be best for studying urban morphology and regional patterns.

Further work by Bryan (1975), also using L- and X-band HH and HV images, found that residential areas, linear transportation features, large water bodies and some industrial and commercial districts were easily and accurately identified, even by inexperienced interpreters. For overall interpretation, the L-band imagery was slightly better than X-band. When all four (X- and L-band, HH and HV polarised) images were used, at the 95% level of confidence, 100% of the land use sample areas could be identified, whereas 84% could be identified for a confidence level of 99%. When the images were interpreted separately, only 52% could be identified at the 99% level of confidence.

Henderson and Wharton (1980) have investigated Seasat SAR images in relation to land use classification and radar's ability to define the limits of urban growth, its direction and extent of change. The study involved both a visual interpretation and an automated approach to define the land cover type. For the automated technique, a density slice was performed and the grey values of these cover types were plotted to show the variation in tone. The plots demonstrated an obvious difference between digital value and urban class. In the urban scene, the denser the area the greater its grey value. The class order in decreasing grey value response was: specular reflectors - urban; high return - urban commercial and residential; low return - urban residential; fringe urban; and vegetation classes.

Further research was undertaken (Henderson, 1985) using dual-polarised (HH and VV polarisations) X-band SAR images. The images were again interpreted into different land-cover types and a detailed analysis was conducted to examine where misclassification occurred. The research showed that for X-band SAR co-polarised imagery, there were numerous misclassified land cover types. Institutional and commercial service activities were often mistaken for residential land cover, while schools, churches and small hospitals were also classified as residential land cover when located within residential areas.

The ability of different radar polarisations to separate urban land use classes were investigated by Henderson & Mogilski (1987), using X-band (HH and HV)

imagery. The land use classes included residential, commercial, industrial, institutional, transportation, and vegetation. Apart from the commercial class, there was found to be no significant difference between the HH and HV radar returns.

Haack (1984a) also used co- and cross-polarised imagery, X- and L-band, for urban land-cover identification. The images were examined to determine the intra-class variability, the number of channels necessary to distinguish between classes, and the best channels for classification using transformed divergence calculations. Again the classes included residential, commercial, industrial, transportation, and vegetated regions. The results showed that X-band like-polarised data were the most useful, L-band cross-polarised data were the least useful, and texture type variables did not contribute toward urban cover type delineation (Haack, 1984a). The X-band imagery was preferred for general interpretation over the L-band imagery because shorter wavelengths are more sensitive to surface roughness (Xia & Henderson, 1997).

The statistical nature of SAR data over an urban scene was addressed by Sieber (1985). Knowledge about the distribution of grey tones in the images assists in the discrimination process. As far as housing is concerned, Sieber (1985) reports that the SAR data makes it possible to differentiate between housing areas having low and high percentages of vegetation.

Henderson and Xia (1997), summarising from early studies, suggest that with K-band imagery, urban land cover types including industrial sites, shopping centres and commercial areas, and institutional areas could be distinguished, but found that vegetation created difficulties for residential identification. Most urban classes, with the exception of dense built-up areas, were more distinguishable using cross-polarised imagery.

A group of large buildings, unobstructed by vegetation, are generally identifiable on HH polarised imagery, but low density areas such as residential are less visible. According to Xia and Henderson (1997) detection of central business regions or small urban areas may be most easily recognised on HH

polarisation. However, HV polarisation would be preferable for investigating other urban cover types.

Different analysis methods, whether it be automated or manual interpretation, have led to mixed conclusions as to the preferred polarisation. Most research to date indicate a preference for cross-polarised imagery for mapping urban land cover types (Xia & Henderson, 1997). For example, both Bryan (1975) and Henderson (1985) found X-HV was best when only limited wavelength and polarisations were available. Henderson and Herrig (1996) also found cross-polarised imagery (for L-band) provided better separation between built-structures and vegetation. However, Haack (1984a) found like-polarised imagery was more valuable, while others such as Henderson and Mogilski (1987) found that cover type influenced the preferred polarisation.

Cross-polarised imagery is generally preferred because it is less susceptible to the corner reflections that lead to a strong specular return, occurring on like-polarised imagery. However, the cross-polarised return is usually a weaker signal return than the like-polarised and hence, is heavily influenced by noise (Xia, 1996).

Previous research has indicated that many classes can be distinguished in the urban area using radar remote sensing. Such classes include mining areas, ports, parks, new and old residential, transportation, commercial, fringe urban, vegetation, recreation and open space, golf courses, parking lots, and bridges (Henderson & Xia, 1997). Obviously this is dependent on the city and the radar characteristics.

The use of radar as a classification tool for the urban environment has promising potential. Results appear to indicate that visual interpretation enables more information to be extracted, however this technique is more labour intensive than an automated approach. Most research to date has only concentrated on single, as opposed to 'multi-parameter' information. As the proceeding chapters will show, more information can be extracted from polarimetry than is available to the visual interpreters.

2.4 Optical Remote Sensing and the Urban Environment

Optical remote sensing provides different information to radar data. As Section 2.5 will demonstrate, a combination of radar with visible/infrared data can be an advantage. A brief discussion will be presented here on some urban research using optical imagery.

Forster (1985) investigated the use of band-on-band ratios from visible/infrared imagery for distinguishing between different cover types such as trees, grass and urban. The ability of optical data to provide information about density and size prediction of housing units, is addressed in Forster *et al.* (1996). The building size refers to its planimetric area only.

Kawamura *et al.* (1996) researched the use of Landsat TM for providing a relatively inexpensive and fast method of updating urban information and assessing conditions in urban areas (termed the Urban Index). The Urban Index is related to vegetation and building coverage.

The ability of Landsat TM data for urban change detection is demonstrated by Kressler and Steinnocher (1996). Satellite images covering the same region from different dates were used. After the major cover types were determined, the built-up areas were then compared from the two dates, to successfully identify those areas where building activities had occurred.

2.5 Combining Optical with Radar Remote Sensing

Previous studies have combined radar and MSS data for investigation of different environments. Such areas include crop classification, forestry, and wetlands. These studies all indicated that there were advantages in using the combined data set over either independent set (Haack, 1984b).

Together optical and radar data provide complementary information. Visible/infrared data is related to the chemical composition of the materials

while microwave images reveal the physical and geometrical properties of such objects.

It is believed that SAR systems produce less detail and information compared to the optical sensors. As was evident from combined Seasat and Landsat TM analysis. However, together the data sets produced greater accuracy than either individual sensor, with the radar providing valuable texture and surface geometry information (Henderson & Xia, 1997).

Haack (1984b) investigated the benefits of Landsat MSS, SAR, and their combination, for assessing urban land-cover types, through examination of numerical data (rather than visual analysis). Training sites for eight urban land-cover types were located and statistics were obtained for all wavelengths. The results indicated that a selection of data from each of the major portions available from the electromagnetic spectrum would achieve the best classification results. This was evident since the best four-file combination included one of each of the radar, visible, reflective infrared, and thermal infrared files. Haack (1984b) concluded that the use of multisensor data sets, Landsat MSS and SAR, for urban land-cover classification provided superior results to either independent set.

Clarke (1980) used a supervised classification technique to determine the advantages of using SAR and Landsat MSS combined data for a study area in Los Angeles, USA. It was concluded that identification of commercial and services, industrial and transportation classes was significantly improved when SAR and Landsat MSS data were used together. For the 17 other defined classes, however, there was no great improvement in accuracy.

Land use classification of urban areas using Landsat MSS and Seasat SAR data separately and combined was also addressed by Toll (1985). The study area was divided into built-up and non built-up regions and then into two further subclasses. The MSS proved more accurate for the subclasses, while the SAR was best for discriminating between built-up and non built-up areas due to radar showing the morphological properties. It was concluded that a combination of

MSS and Seasat SAR data provided the most accurate results at all levels of classification.

Deguchi *et al.* (1995) have been investigating combining visible/near-infrared remotely sensed data (JERS-1 OPS VNIR) with SAR (ERS-1 and JERS-1) to provide land cover information and assist in land use planning. Backscattering coefficients of the test areas were compared with their calculated building bulk ratios. A reasonably strong correlation was found, suggesting its potential for land use planning. Deguchi *et al.* (1995) suggests the optical data be used to provide information about the planimetric density or "building coverage ratio" while radar data provides an estimation of the building "bulk" or vertical density.

Weydahl *et al.* (1995) investigated the advantages of combining ERS-1 SAR with optical data from SPOT and Landsat TM. Their study also showed that radar images may add complementary information when used together with optical images. Radar's contribution includes building direction, complexity of the object, and material of hard targets within a built-up area (Weydahl *et al.,* 1995).

The advantages of using radar and optical data in combination are apparent. Optical (visible and infrared) and radar remote sensing systems measure different aspects of urban morphology, and a "synergistic approach" using their complementary qualities appears to offer great potential for urban monitoring (Forster *et al.,* 1996).

2.6 Other Research

Apart from the radar applications for the urban environment discussed above, there are other less researched fields of study deserving of acknowledgement. Research in change detection, and radar interferometry are two such areas which will be briefly discussed as follows:

2.6.1 Change Detection

A new technique has been designed by Corr *et al.* (1996) for monitoring change detection from satellite SAR images. The method operates by measuring the degree of change between two images over the same area recorded at different dates. Unless the scene has changed, the speckle pattern in the image will not change. This technique was validated by testing building changes during construction and destruction.

2.6.2 Interferometry

SAR's potential for building height estimation was suggested many years ago by LaPrade and Leonardo (1969). The length of the shadows on a radar image has some relationship to the height of a feature. However, this would be impossible for buildings since they are usually smaller than the resolution size (Bryan, 1979), but as far as texture is concerned it may give an indication of building sizes in that area.

Research has progressed into the potential application of interferometric SAR for obtaining information about building heights. Carande's (1995) work involves analysing IFSAR (ie., InterFerometric SAR) images over cities. This interferometric SAR operates by measuring the elevation as well as the coherence and intensity of the radar return. Any changes in gradient in the IFSAR elevation correspond directly to "elevation edges" (Burkhart *et al.,* 1996). IFSAR can produce a model over an area which has an approximate accuracy of 1 metre resolution in the horizontal direction and better than 0.5 metres vertical accuracy. Although this method is presently less accurate than aerial photogrammetry, the time required to obtain an operational image is only minutes compared to several days (Carande, 1995).

Bickel *et al.* (1997) have also begun investigation into the use of interferometric SAR (IFSAR) for estimating building heights. There are many problems, such as layover and shadowing, which need addressing before interferometry can become an operational tool for building height estimation.

2.7 Summary

The potential which radar has in relation to the built environment has been made evident from previous and present research mentioned here. Radar remote sensing has the ability to not only detect settlements, but show some relationship to its size and density. Furthermore, the development of appropriate algorithms could enable population estimation of inhabited regions. There is a definite relationship between radar backscatter and land use, however the best polarisation and interpretation method appears to be dependent on individual land use characteristics, presently making classification difficult. This problem may be improved through the adoption of a combination of optical and radar remotely sensed data, as studies to date indicate.

The effect which building orientation has on radar return was not mentioned in this chapter. This factor has a major influence on backscatter strength. Due to its importance, Chapter 4 will be dedicated to addressing this matter.

A further understanding of radar's interaction in urban areas is still needed. The next chapter aims to introduce the important radar and urban parameters influencing radar return, and develop some mathematical relationships between the two.

3. General Theory and Concepts of Radar Remote Sensing in the Urban Environment

3.1 Introduction

There is a role for radar as a remote sensing tool in the urban environment, as discussed in the previous chapters. Radar has many unique characteristics which potentially provide valuable information to present methods of urban monitoring. This chapter examines the important properties of a radar system, its parameters, and how they relate to the urban environment (Section 3.2). Basic formulae used for modelling urban scattering mechanisms are introduced (Section 3.3) along with general polarisation techniques (Section 3.4) which will be used in later chapters for urban analysis.

3.2 The Characteristics of Radar Remote Sensing: Some Important Attributes

Electromagnetic waves interact with matter through different mechanisms which are dependent upon the composition and structure of the object. Different mechanisms change the characteristics of the wave (eg., polarisation, intensity, direction) such that the properties of the object can be uniquely identified. Physical (eg., slope, morphology, roughness, and inhomogeneities) and electrical (eg., dielectric constant) characteristics of the surface, and near subsurface, determine how the radar wave will interact with it (Elachi, 1988). Since radar systems are active, the transmitted wave has defined characteristics, hence the changes which this wave undergoes following scattering from a surface provide information about that surface.

Microwave remote sensing gives information about the morphological properties of the imaged area, in contrast to knowledge about the chemistry of

the surface provided by optical remotely sensed data. This is one reason why radar is showing promising results in the urban region. There are many varying factors affecting the intensity of radar returns from objects. The urban environment is a complex mixture of buildings (of varying shapes and sizes), vegetation (such as park land and trees), and other engineering structures. A building's size, shape, material, and spatial layout will influence the radar backscatter from an urban scene.

The main factors determining the characteristics of radar returns from urban features are the radar system parameters, properties of the surface, and environmental variables. Important radar system parameters include the wavelength, polarisation, look angle, look direction, and phase difference of the radar waves. Properties of surface features affecting radar signal returns include the complex dielectric constant, surface roughness and feature orientation. Orientation of features and terrain slope are important in relation to the look direction of the radar system, as they affect the intensity of the radar return. Feature orientation with respect to radar look direction is probably the most important factor with respect to radar's interaction in the urban environment. Important environmental variables include the shape of the land, land cover classes and spatial patterns (including building density), vegetation cover (especially shape, density, and pattern), settlement history, and local climate (Xia & Henderson, 1997).

The difference between the look angle and incidence angle (as defined in this research) must be noted. The look angle is the angle which the radar system transmits a wave with respect to the vertical. The incidence angle is the local angle, to the normal, which the radar contacts a surface feature, hence is dependent upon the orientation and shape of the object. Also, the look direction is the direction which the radar is 'looking', projected onto the horizontal plane.

The wavelength of the radiation with respect to the surface roughness will determine if the scattering will be specular or diffuse. (Figure 3.1 demonstrates specular and diffuse reflection). Specular scattering occurs when most of the

radar wave is reflected in a mirror like fashion. For a single flat surface most of the wave will reflect away from the sensor and backscatter will be very low. Energy dispersed in all directions is known as diffuse scattering. The amount of energy scattered in the different directions is dependent on the surface roughness with respect to the wavelength of the incident wave (Elachi, 1988). For a very rough surface, scattering will be uniform in all directions and hence, some of the radar wave will return to the sensor. The longer the wavelength, for a particular surface, the smoother the surface will appear. Rayleigh's criterion is one method of approximately determining the resulting scattering for a particular wavelength and surface roughness.

Figure 3.1. A simple representation of specular (left) and diffuse (right) scattering.

Rayleigh's Criterion is: $H \leq \frac{\lambda}{8\cos\theta}$ (Forster, 1994) (3.1)

where: H is the *rms* (root mean square) height of the surface, λ is the wavelength, and θ is the incidence angle (Forster, 1994). If H is less than the right hand side of the equation, the scattering will be predominantly specular. Here the incidence angle and look angle are the same due to the surface being horizontal.

Generally more surface features appear smoother at longer wavelengths than at shorter wavelengths. The wavelength of the radiation will also influence the depth of signal penetration into a vegetation canopy or terrain surface (Xia & Henderson, 1997).

As shown above, Rayleigh's Criterion is also a function of incident angle. The greater the incidence angle, the more specular the reflection. At large look angles on a radar image, most surfaces will appear quite smooth. At large incident angles most or all of the energy reaching a smooth surface will be reflected away from the radar system, while at small incident angles the specular reflection returns a lot of the energy to the receiving antenna. Rough surfaces produce reasonably strong intensity returns over a wide range of incidence angles (Xia & Henderson, 1997).

The look angle plays an important role in the urban environment. Its influence on range resolution affects settlement detectability. Small look angles produce a poor range resolution compared to larger angles. Higher resolution enables small settlements to be detected and small land cover classes to be mapped. However, larger look angles create more radar shadows concealing land cover (Xia & Henderson, 1997).

A radar system can transmit and receive a horizontally (H) and/or vertically (V) polarised wave. The backscatter from a particular surface will depend on the type of polarisation. For example, a horizontal metal wire will have a much higher HH than VV backscatter component. Surface scattering generally dominates the return for co-polarised imagery. Volume scatter is a major contributor to signal return of cross-polarised imagery (Xia & Henderson, 1997).

Another parameter influencing the strength of the signal return is the dielectric constant (ε). The dielectric constant describes a materials scattering and absorption characteristics. The dielectric constant is a complex number having both a real and imaginary component ($\varepsilon=\varepsilon_r+i\varepsilon_r$ where $i=\sqrt{-1}$, however for simplicity this will be expressed as $\varepsilon=\varepsilon_r+\varepsilon_i$ in the remainder of this thesis). The higher the amplitude of the dielectric constant, the stronger the scattering, resulting in a smaller depth of penetration into the surface.

The dielectric constant will affect the penetration depth, and therefore the origins of a returned radar signal. The dielectric constant of most naturally occurring objects is generally around 3 to 8, while water is approximately 80. Hence a small change in water content of an object will significantly effect its dielectric constant, and hence its scattering characteristics (Schumann, 1996).

Reinforced concrete, having a high proportion of metal, will reflect a large percentage of the wave, resulting in a minimal depth of penetration into the surface. A tile roof (terracotta or concrete), however, is considered to have a low real component of the dielectric constant (less than 10), so the depth of penetration into the surface will be greater. Once the wave penetrates the surface, the imaginary component and material composition determine whether the wave continues through the surface with little loss, or if the energy of the wave rapidly dissipates. If the medium below the surface is inhomogeneous, or a mixture of materials of different dielectric properties, then portions of the transmitted wave may be scattered, by the inhomogeneities, back to the surface again (Ulaby *et al.,* 1981).

Radar backscatter in an urban environment is very dependent on a building's size, shape, and density. Larger buildings give a stronger backscatter than small buildings of the same material. The shape will also affect the backscatter. The more building facets and corner structures facing the radar, the stronger the backscatter. A dense urban area results in a higher signal return compared to a sparse region. For example, a central business district consisting of many high rise structures will have a higher backscatter than a low density residential area.

One of the most important factors affecting the radar return, and the one which makes urban analysis of radar images the most difficult, is the orientation of the building with respect to the radar's look direction. A building's orientation is assumed parallel to the street direction. When a street is running perpendicular to the radar look direction, the return signal will be very strong. The reason for

this strong response is due to dihedral corner reflection from the vertical building walls and the horizontal surrounding surface, and facet reflection from the building roof facing towards the radar. The backscatter can be very high when the radar incidence angle is normal to the slope of the building roof, since it acts as a mirror reflector. At other times there is diffuse scattering, depending on the type of roof material, its orientation with respect to the incoming signal (Xia & Henderson, 1997), and the radar wavelength.

3.3 Theory of Different Types of Scattering Mechanisms Used in the Urban Environment

The dominant scattering mechanisms found in an urban environment are the corner reflector effect, facet reflections, and volume scattering. These will be discussed in more detail below. It is acknowledged that there are other scattering mechanisms in built up areas, some of which will be briefly introduced.

The formulae used here for the modelling of facet and corner reflections are based on the Physical Optics approximation to estimate the Chu-Stratton integral. For a facet this approach "provides an accurate means of predicting the near-specular values of cross section" (Kell & Ross, 1970, p27-28), and it is this near-specular scattering which is of concern in an urban context.

Furthermore, "physical optics has been successfully applied to predict the maximum radar cross section of a dihedral [corner reflector]" (Kell & Ross, 1970, p27-33). Formulae for the backscatter from double bounce corner reflections, as a function of polarisation and incidence and orientation angles, are given by Dong (1995a).

3.3.1 Dihedral Corner Reflection

Dihedral corner reflections are probably the most important and certainly the most notable effect occurring on a radar image of an urban scene. Corner reflection occurs due to double bounce of the radar wave from two perpendicular surfaces. For buildings, the angle between the vertical wall and the ground forms a corner reflector (Ulaby *et al.*, 1981). (Refer to Figure 3.2). As the AirSAR image in Figure 3.3 demonstrates, when the radar look direction is normal to the street direction, the response is very strong for all wavelengths (C-, L- and P-band).

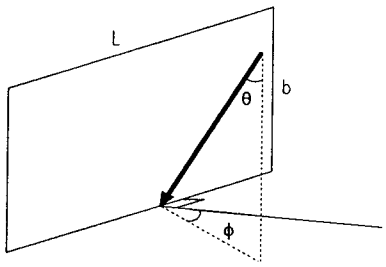

Figure 3.2. An illustration of double bounce corner reflection with respect to its parameters.

The formula for a dihedral corner reflector is:

$$\sigma_{ppcr} = \frac{16\pi}{\lambda^2} R_{pw}^2 R_{pg}^2 L^2 H^2 \sin^2\theta \cos^8\phi \, \mathrm{sinc}^2\left(k_o L \sin\theta \sin\phi\right) \quad \text{(Dong, 1995a)} \qquad (3.2)$$

where σ_{ppcr} is the backscatter, with *pp* representing either horizontal or vertical polarisation, λ is the wavelength, *L* and *H* are the length and height of the wall facing the radar look direction, θ is the look angle of the radar, and ϕ is the angle between the normal to the building and the radar look direction. (Refer to Figure 3.2 for an illustration of parameters). In future the angle ϕ will be referred to as the orientation angle.

k_0 is the wave number: $k_o = 2\pi/\lambda$ (3.3)

R_{pg} and R_{pw} are the Fresnel reflection coefficients for the ground and the wall respectively, where:

$$R_{hq} = \frac{\cos\theta - \sqrt{\varepsilon_q - \sin^2\theta}}{\cos\theta + \sqrt{\varepsilon_q - \sin^2\theta}} \quad \text{and} \quad R_{vq} = \frac{\varepsilon_q \cos\theta - \sqrt{\varepsilon_q - \sin^2\theta}}{\varepsilon_q \cos\theta + \sqrt{\varepsilon_q - \sin^2\theta}} \quad \text{(Dong, 1995a) (3.4)}$$

Figure 3.3. An extract from an AirSAR image over Sydney. It shows the total power for C-, L- and P-band, with the effect of radar return on building orientation being apparent. The radar look direction is from the top of the image to the bottom.

R_{hq} is the horizontal and R_{vq} is the vertical Fresnel reflection coefficient for surface *q*. If the ground or wall surface is rough, but satisfies the physical optics (Kirchoff) approximation (ie., in this case, the area of the wall must be much larger than the wavelength), the Fresnel reflection coefficient (R_{qr}) is then:

$$R_{qr} = R_q e^{-2k_o^2 h^2 \cos^2\theta} \quad \text{(Dong, 1995a)} \qquad (3.5)$$

where *h* is the RMS height of the surface.

The backscatter for the dihedral corner reflector is very strong when ϕ is small, but it rapidly diminishes and reaches a point where there is little change in backscatter with respect to ϕ. This will be demonstrated in more detail in the following chapters.

It should be noted that the formula for the backscatter from a dihedral corner reflector (Equation 3.2) is derived such that the projection of the reflection from the building wall determines the amount of ground area contributing to the backscatter. (Refer to Figure 3.4). This is unlike a traditional corner reflector where both the perpendicular sides have limited boundaries.

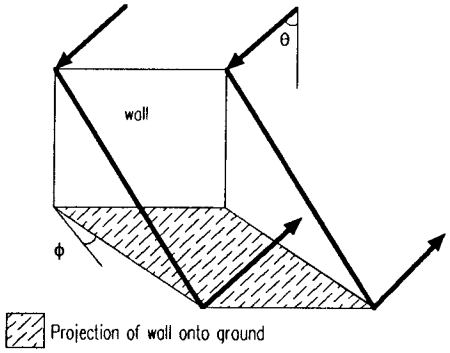

Figure 3.4. Diagram showing the projection area of the radar reflecting from the wall onto the ground, as used in Equation 3.2.

3.3.2 Facet Reflection

Facet reflections result in single bounce scattering. Single bounce reflections represent scattering from, for example, a building roof. This can be large when the radar is normal to the roof face.

The formula for single bounce is:

$$\sigma_{pps} = \frac{4\pi}{\lambda^2} R_{pr}^2 L^2 b^2 \cos^2\theta \left(\sin c\left(k_o L \sin\theta\cos\phi\right)\sin c\left(k_o b \sin\theta\sin\phi\right)\right)^2 \quad (3.6)$$

where σ_{pps} is the backscatter from a flat surface for *pp* polarisation (where *pp* represents *hh* or *vv* polarisation), *L* and *b* are the length and width of the facet, θ and ϕ are the incidence and orientation angles respectively, k_0 is the wave number, and R_{pr} is the Fresnel reflection coefficient. This formula is the same as that from Fung and Ulaby (1983) except that it also considers the Fresnel reflection coefficient. An illustration of this can be seen in Figure 3.5.

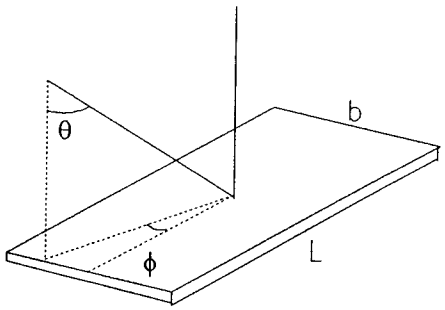

Figure 3.5. An illustration of the relevant parameters representing single bounce reflection occurring on a facet.

Clarification of the *sinc* function is required due to its inclusion in the formulae. The *sinc* function is *sinc(x)=sin(x)/x*. This causes oscillations when the backscatter is plotted with respect to, for example, the orientation angle. These oscillations become more frequent and have a smaller amplitude as the dimensions of the scattering surface(s) increase. As Figure 3.6 demonstrates, oscillations in the radar intensity occur when either θ or *L* changes causing the phase of the wave at the extremes of the object to be either in phase (as shown in Figure 3.6) or out of phase.

3.3.3 Volume Scattering from Vegetation

Volume scattering occurs in the urban environment due to vegetation, such as trees. When the corner or single bounce reflection is strong any volume scattering will be insignificant. As the orientation angle approaches 45° the backscatter from single and double bounce reflection from a building will be small and volume scattering from trees may then be noticeable. Scattering from vegetation is discussed in more detail in Chapter 5.

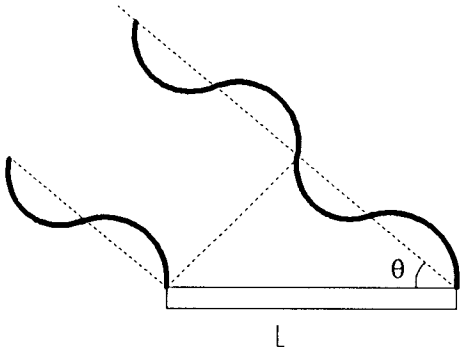

Figure 3.6. A simple representation of how the *sinc* function operates. The dark lines represent an oscillating electromagnetic wave at the extremes of an object. In this illustration, the interference of the wave from the extremes of the object is constructive, ie., in-phase.

3.3.4 Other Scattering Mechanisms

An urban environment can also provide trihedral corner reflections and scattering from wedges, due to the many building facets and their varied directions. However, the scattering from wedge-ground structures, such as the corner of a building wall, are "much weaker than the backscatter from dihedral

and trihedral corner reflector structures, and can be neglected" (Dong *et al.*, 1996, p6).

Trihedral corner reflections result in triple bounce. Two orthogonal walls and the ground form a trihedral corner reflector, hence this structure is very common in urban areas (Nasr & Vidal-Madjar, 1991). This effect can be very strong for perfectly conducting materials since the direction which the reflected wave exits the trihedral corner reflector will be parallel to the direction with which it first made contact. (Refer to Dong (1995a) for more information on trihedral corner reflections). One such application of this concept is the trihedral corner reflectors used for image calibration.

Trihedral corner reflector structures lead to odd bounce scattering since reflection occurs three times. However in the urban environment, the building materials and the ground dielectric constants are much lower than a perfect conductor. By the time the wave has undergone three reflections before returning to the receiver, its energy is much weaker than single bounce scattering (Dong *et al.*, 1997a).

3.4 Theory of Polarisation Signatures

Different polarisations provide different information about an imaged area. Polarisation information and analysis can be presented in a variety of ways. These may include: comparison of signal strength from HH, VV and HV polarisation images; polarisation signatures; and the polarisation index and polarisation phase difference. Comparison of images is a relatively common method of investigation. Polarisation signatures will be discussed in the remainder of this chapter. The polarisation index and polarisation phase difference will be introduced in Chapter 5.

A polarisation signature is a method of graphically presenting the radar scattering cross section as a function of polarisation. The synthesised

scattering cross section is plotted as a function of the ellipticity and orientation angles of the transmitted wave (Ulaby & Elachi, 1990), which will be explained later. To produce a polarisation signature requires a fully polarised data set, hence they cannot be produced from radar systems having only single polarisation. Airborne AirSAR data can be used to produce polarisation signatures, as the system measures quad polarised data. Quad polarised data is collected when the radar effectively transmits both a horizontally and vertically polarised wave and receives horizontal and vertical polarisation. This means HH, VV, HV, and VH polarisation combinations are measured enabling a complete scattering matrix to be determined.

Traditional imaging radars measure the reflectivity for each point in a scene for one polarisation only, whereas an imaging radar polarimeter can determine the dependence of reflectivity on polarisation. Unlike a single polarisation measurement, the radar polarisation signature of an object provides information about the physical scattering processes through identification and characterisation of the dominant scattering mechanisms. Hence it assists in providing some information about the geometric shape and dielectric constant of an object (Zebker *et al.,* 1987).

Polarisation signatures are useful because their shape is an indication of the major scattering components of the subject area. However, they are not unique to a particular object or environment (Ulaby & Elachi, 1990). Different environments can have the same polarisation response indicating similar types and proportions of scattering mechanisms.

A number of researchers have investigated polarisation signatures in relation to modelling and real data. Zebker *et al.* (1987) have examined theoretical polarisation responses from spheres, Bragg and double bounce models, and have noted the similarities that Bragg and double bounce models have with ocean and urban signatures of real data, respectively. The Bragg model represents scattering from a slightly rough surface, and hence can resemble the response from an ocean. An urban polarisation signature can be described

as containing double bounce as the dominant scatterer, along with an unpolarised component. Comparisons of Bragg and double bounce scattering with real ocean and urban data respectively are also shown in Van Zyl *et al.* (1987), revealing similar results.

3.4.1 The Polarised Wave

A polarised wave can be described as having a horizontal and vertical component each consisting of an amplitude, with a phase difference between them. It can also be described as having an ellipticity and orientation angle. The ellipticity angle χ is related to the flatness of the ellipse of the polarised vector wave. Mathematically the ellipticity is:

$$\tan\chi = \pm b/a \quad \text{(Ulaby \& Elachi, 1990)} \qquad (3.7)$$

where *a* and *b* are the semi-major and semi-minor axes of the ellipse respectively. The ellipticity can be positive or negative depending on the direction of rotation of the vector wave, and ranges from $-\pi/4 \leq \chi \leq \pi/4$. The polarisation is left-handed if $\chi>0$, and right-handed is $\chi<0$.

The orientation angle ψ describes the angle which the major axis of the ellipse forms in relation to the horizontal and vertical directions (Ulaby & Elachi, 1990). As Figure 3.7 shows, if $\psi=0°$ then the major axis is in the vertical direction, while if $\psi=\pm 90°$ then the major axis is horizontal.

When $\chi=0°$ the polarisation is linear. The orientation angle determines the direction of oscillation of the electric vector wave. Circular polarisation results if $\chi=\pm 45°$, with +45° representing left circular polarisation and -45° right circular (Ulaby & Elachi, 1990). Any other value of χ represents elliptical polarisation, hence the full range of polarisation states are covered (Kraus, 1984).

3.4.2 The Scattering Matrix and Stokes Vector

To enable the production of a polarisation signature, the Stokes vector and Scattering matrix need to be determined. The Stokes vector consists of four Stokes parameters, I_0, Q, U, and V, and can be represented by the vector:

$$F = \begin{bmatrix} I_o \\ Q \\ U \\ V \end{bmatrix} = \begin{bmatrix} I_o \\ I_o \cos 2\psi \cos 2\chi \\ I_o \sin 2\psi \cos 2\chi \\ I_o \sin 2\chi \end{bmatrix} \quad \text{(Ulaby \& Elachi, 1990)} \qquad (3.8)$$

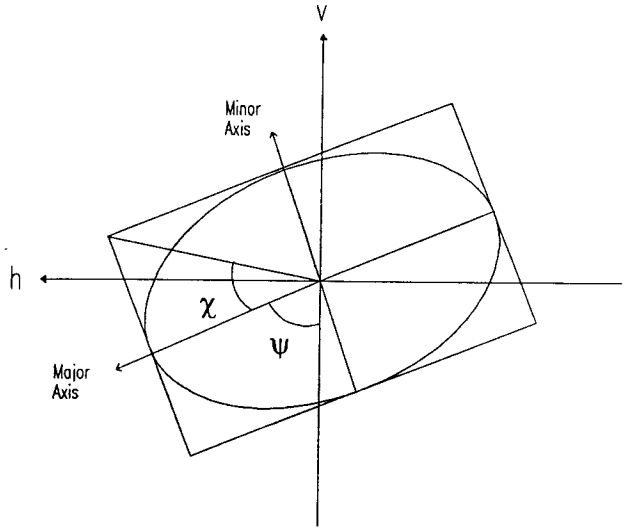

Figure 3.7. Graphical representation of a polarised wave including its ellipticity χ, and orientation angle ψ.

where I_0 is the intensity of the wave, Q is related to the flattening of the ellipse, and U and V describe the phase difference between the horizontal and vertical components of the wave. The Stokes parameters are all that are required to characterise the intensity and state of polarisation (Van de Hulst, 1957).

The Scattering matrix is defined as:

$$S = \begin{bmatrix} S_{vv} & S_{vh} \\ S_{hv} & S_{hh} \end{bmatrix}$$ (Ulaby & Elachi, 1990) (3.9)

where S_{pq} is a complex scattering amplitude containing both an amplitude and phase (Ruck *et al.*, 1970) for *pq* polarisation (*p* and *q* represents either *h* or *v* polarisation). Each element of S can be a function of frequency, the incidence and scattering angles, and the orientation of the scatterer (Ulaby & Elachi, 1990).

The Mueller matrix is a 4*4 matrix representing the scattering mechanisms. It is similar to the Scattering matrix, except the complex numbers in S are subdivided into their real and imaginary components.

The Mueller matrix is defined as $\ell = RWR^{-1}$ where:

$$W = \begin{bmatrix} S_{vv}^* S_{vv} & S_{vh}^* S_{vh} & S_{vh}^* S_{vv} & S_{vv}^* S_{vh} \\ S_{hv}^* S_{hv} & S_{hh}^* S_{hh} & S_{hh}^* S_{hv} & S_{hv}^* S_{hh} \\ S_{hv}^* S_{vv} & S_{hh}^* S_{vh} & S_{hh}^* S_{vv} & S_{hv}^* S_{vh} \\ S_{vv}^* S_{hv} & S_{vh}^* S_{hh} & S_{vh}^* S_{hv} & S_{vv}^* S_{hh} \end{bmatrix}$$ (Ulaby & Elachi, 1990) (3.10)

S_{pq}^* represents the complex conjugate of S_{pq}, and

$$R = \begin{bmatrix} 1 & 1 & 0 & 0 \\ 1 & -1 & 0 & 0 \\ 0 & 0 & 1 & 1 \\ 0 & 0 & -i & i \end{bmatrix}$$ (Ulaby & Elachi, 1990) (3.11)

The co-polarisation signature can be constructed by calculating the backscatter for all polarisation combinations of the transmitted wave, using:

$$\sigma(\psi_r, \chi_r, \psi_t, \chi_t) = 4\pi F^r . (Rt^{-1} W R^{-1}) F^t$$ (3.12)

where $\sigma(\psi_r,\chi_r,\psi_t,\chi_t)$ is the backscatter for a particular transmitting and receiving polarisation, F^t and F^r are the Stokes vectors for the transmitted and received wave, and Rt is the transpose of matrix R.

For cross-polarisation signatures, the only difference made to Equation 3.12 is that the Stokes vector for the receiving wave changes. As can be seen from Figure 3.8, to determine the cross-polarised response the receiving wave is rotated by ±90° and the direction of rotation of the vector is reversed, so χ changes sign. Hence $\psi_r=\psi_t$ and $\chi_r=\chi_t$ for co-polarisation giving $F^r=F^t$ as shown previously, but for cross-polarisation $\psi_r=\psi_t\pm90°$ and $\chi_r=-\chi_t$, so $F^r\neq F^t$. The following formula can be derived:

$$F^r=\begin{bmatrix}1\\ \cos\left(2\left(\psi+90^o\right)\right)\left(-\cos2\chi\right)\\ \sin\left(2\left(\psi+90^o\right)\right)\left(-\cos2\chi\right)\\ \sin\left(-2\chi\right)\end{bmatrix}I_o=\begin{bmatrix}1\\ -\cos2\psi\cos2\chi\\ -\sin2\psi\cos2\chi\\ -\sin2\chi\end{bmatrix}I_o=\begin{bmatrix}1\\ -1\\ -1\\ -1\end{bmatrix}F^t \qquad (3.13)$$

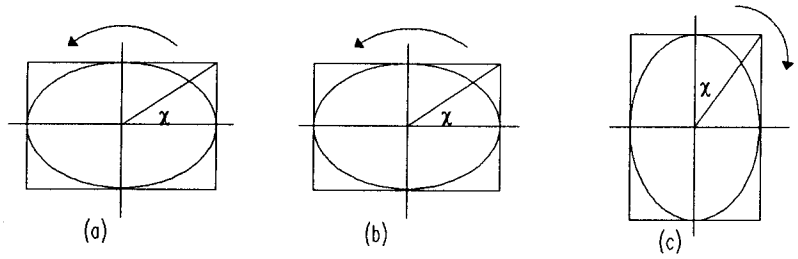

Figure 3.8. A graphic representation of the incident wave (a), and the receiving wave for co- (b) and cross-polarisation (c). The arrow represents the direction of rotation of the wave vector, and χ is the ellipticity (Dong, personal correspondence).

3.4.3 Examples of Polarisation Signatures

Two of the simplest, and yet important scattering elements in an urban environment are a flat surface and a dihedral corner reflector. Some examples

of polarisation signatures are next described, which represent two such features, made of a perfectly conducting material.

Figure 3.9 shows the co- and cross-polarisation responses from a perfectly conducting sphere. Its Scattering matrix is:

$$S = \frac{r}{2}\begin{bmatrix} 1 & 0 \\ 0 & 1 \end{bmatrix} \quad \text{(Ulaby \& Elachi, 1990)} \qquad (3.14)$$

where r is the radius of a sphere.

The co-polarised response shows that the maximum scattering cross section occurs for linear polarisation, and is independent of the orientation angle. This independence is due to the isotropic nature of a sphere's shape. For the cross-polarised response, the scattering cross section is greatest for circular and smallest for linear polarisations. The maxima occurs for circular polarisation because a circularly polarised incident wave is scattered such that it is still circularly polarised, but rotating in the opposite direction (Ulaby & Elachi, 1990). This signature is also identical to a large flat conducting surface (where the angle of incidence is normal to the surface), and a perfectly conducting trihedral corner reflector (with the incidence angle along boresight).

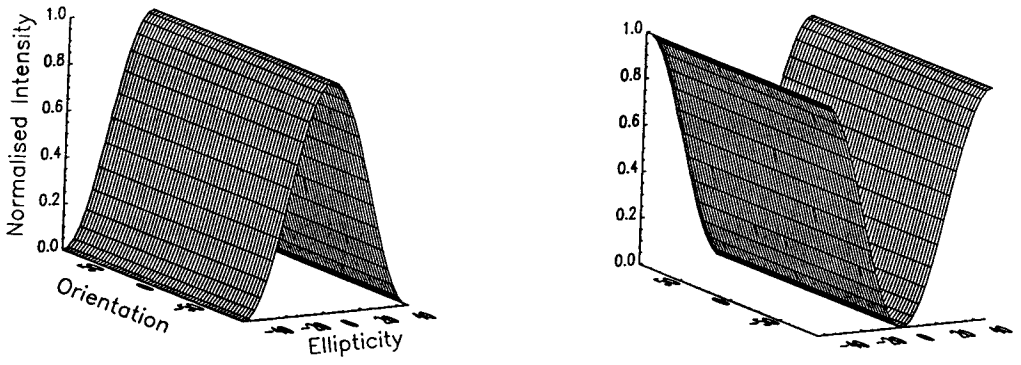

Figure 3.9. The co- (left) and cross-polarisation signatures (right) of a perfectly conducting sphere. This is the same response as from the normal to a large flat surface, and boresight of a trihedral corner reflector.

The reason why a conducting trihedral corner reflector has the same polarisation response to a sphere is because the waves are reflected three times before returning to the radar. Compared to a sphere, the extra two reflections introduce a 180° phase shift between S_{hh} and S_{vv}, leading to a total of 360° phase shift (Ulaby & Elachi, 1990). Hence there is no resulting phase difference between the horizontal and vertical components, which is identical to a conducting sphere.

The co- and cross-polarisation signatures for a perfectly conducting dihedral corner reflector are shown in Figure 3.10. It has a Scattering matrix:

$$S = \frac{k_o lb}{2\pi}\begin{bmatrix} -1 & 0 \\ 0 & 1 \end{bmatrix} \text{ (Ulaby \& Elachi, 1990)} \qquad (3.15)$$

where k_0 is the wave number, and l and b are the length and width of both of the perpendicular sides of the corner reflector.

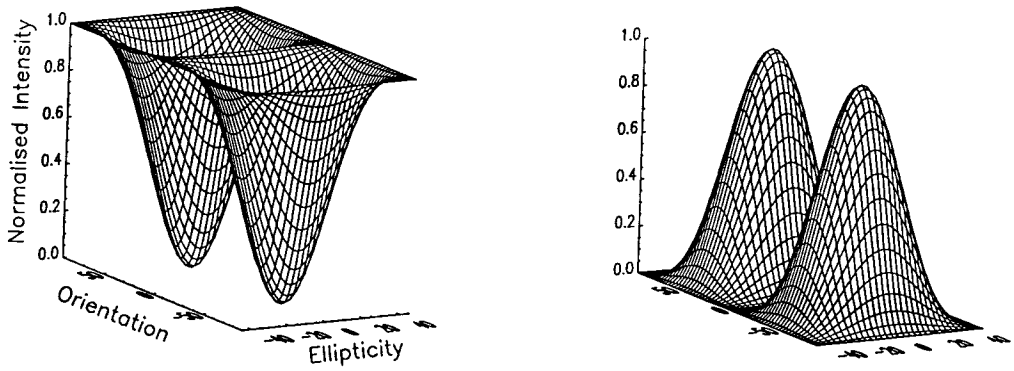

Figure 3.10. The co- (left) and cross-polarisation signatures (right) of a perfectly conducting dihedral corner reflector.

A dihedral corner reflector causes a different polarised response to a sphere. The co-polarised response has two minima occurring for linear polarisations offset by ±45° (ie., the orientation angle = ±45° and the ellipticity angle = 0°) from the horizontal and vertical polarisations. The cross-polarised response has the opposite affect with a maxima at these two locations. A dihedral corner reflector must undergo an extra reflection in comparison with a sphere. This

extra reflection introduces an additional 180° phase shift between S_{hh} and S_{vv} leading to these very different polarisation responses (Ulaby & Elachi, 1990).

3.4.4 Polarisation Decomposition

Many basic shapes are close approximations to real targets, hence their radar cross sections are similar. Complex bodies are also a mixture of many simple targets, hence studying the radar response from basic shapes is a valuable process (Kell & Ross, 1970). The Scattering, or Mueller, matrix as defined by Ulaby & Elachi (1990), is a matrix representing a scattering mechanism, or combination thereof, from an object or spatial feature. These enable physical information about the scattering of microwaves from surface and volume structures to be extracted. Determination of the individual scattering components is a difficult task, but a number of researchers have involved themselves in this process, known as Target Decomposition Theorems (Cloude & Pottier, 1996).

Recent work has been undertaken by Dong *et al.* (1997b) to determine the scattering components from polarisation information of real data, with particular emphasis on urban land use. Dong *et al.* (1997b) decomposed the Mueller matrix into four scattering components: odd bounce; double bounce; Bragg scattering; and cross scattering. A weighted least squares method was used to determine the best combination of these four components to give the reconstructed final polarisation signature. The results show that residential areas have a higher double bounce component than single bounce (about 60:30), which is quite different to commercial areas which have a greater percentage of double bounce than single bounce (around 85:15). The results were promising, with the accuracy being greater than 95% for linear polarisations and over 85% for other polarisations.

Other papers researching Target Decomposition Theorems include Van Zyl (1989), Freeman & Durden (1992), and Wang & Davis (1996). Van Zyl's (1989) method decomposes the total polarisation information into three scattering

mechanisms: odd reflections; even reflections; and diffuse scattering. When applied to an urban area, water is classified as odd bounce, urban areas having street directions near perpendicular to the radar look direction have an even number of reflections, and other urban areas with a street direction near 45° to the perpendicular are classified as consisting of a large diffuse component.

Wang and Davis (1996) used odd number of reflections, even number of reflections, and diffuse scattering with forestry applications. Freeman and Durden (1992) also used three scattering mechanisms: even-bounce; Bragg; and volume scattering. The results are used to distinguish between different vegetation types, geology, and urban regions.

Analysis of polarisation responses does appear to provide different and important information in relation to environmental investigation.

3.5 Summary

As has been presented in this chapter, radar observation of the urban environment is both complex and unique. The urban environment can be simplified into a combination of many simple scattering mechanisms. Through the use of simple formulae and radar polarimetry, a basic model can be used to represent a complex situation. This will be attempted in Chapter 5. The next chapter (Chapter 4), however, uses real data to examine how the corner reflector effect dramatically influences radar return in an urban environment.

4. AN INVESTIGATION INTO RADAR INTENSITY WITH RESPECT TO LOOK DIRECTION AND URBAN CLASS

4.1 Introduction

An urban area consisting of large, densely spaced buildings, will produce a greater radar return than smaller buildings of a more spacious layout. Both the brightness (ie., intensity) and textural information on a radar image, can reflect these different urban characteristics, which show some potential correlation with land use.

However, the appearance of urban targets is highly dependent on the geometric relationship between the radar look direction and feature orientation. The same type of land cover may appear very different on a radar image when it has a different orientation relative to the radar look direction (Xia & Henderson, 1997).

The angle between the vertical wall of a building and the ground forms a corner reflector. Other reflectors are found where walls (or walls and roofs) connect at right angles (Ulaby *et al.,* 1981). Corner reflections occur when microwaves interact with building walls and the ground through a double bounce effect. When the streets, and hence buildings, are aligned such that they are normal to the radar direction the backscattered response, represented by the grey tone of the image, can be very strong, if not totally saturated. A single band imaging radar system (ie., one wavelength) can cause such features to be enhanced or suppressed, or even disappear (when lines are parallel to the look direction of the radar) (Bryan, 1982). This phenomenon has a major influence on the analysis of radar return in a built environment and requires further examination to enable its effects to be taken into account. (Refer to Figure 3.3 of an AirSAR image illustrating the Cardinal effect).

This chapter begins with a brief introduction to previous work undertaken by various researchers analysing the corner reflector effect. A simple investigation, using a SIR-B image, then examines how the radar return varies with respect to building orientation, and urban land use.

4.2 Previous Urban Studies Examining Radar Response to Land Use and the Corner Reflector Effect

Radar's potential application in the urban environment was recognised early in its operational life. Nunnally (1969) used K-band HH and HV imagery and found radar was useful when variation in tone, texture, pattern and shape were examined. It was found that the centre of the city had finer texture and shapes, while on the outer edges of the city there was less rectangular pattern and a rougher texture. Responses were brighter in the city centre (containing the CBD), shopping centres, commercial, and industrial classes.

However, along with radar's potential use for analysis of the built environment, some of the difficulties have also been realised. One of the main problems being the corner reflector response, otherwise known as the cardinal effect. The term 'cardinal effect' originates from the fact that many of the towns in the United States have streets which run in a north-south and east-west direction, hence strong radar reflection occurs in these cardinal directions (Hardaway *et al.,* 1982).

Bryan's (1979) studies, of an empirical and quantitative nature, defined the angle at which the radar beam should strike building walls to obtain a significant brightening, and changes to image tone. (The angle between the projection of the radar look direction onto the horizontal plane and the normal to the building will be symbolised as "ϕ" in future). Areas where ϕ was less than 10° were bright on the radar image (for L-band, HH polarisation) and areas where ϕ was greater than 10° had a considerably lower image brightness. The

critical value for ϕ where the brightness changes was between approximately 10° to 15°, independent of land use. Different angles between the radar look direction and street pattern (hence building orientation) resulted in different grey tones within adjacent urban areas of Los Angeles. Large sections of the Los Angeles urban area had a large variation in grey tones. The darker regions being such features as gravel pits, airports, and flood control areas, and the very bright areas, industrial complexes. The mid-grey tones were generally well-defined, having geometric patterns with linear boundaries (Bryan, 1979).

Hardaway *et al.* (1982) also found the cardinal effect on a radar image to be evident. Through analysis of the relationship between radar image tone and street orientation, a reasonably strong correlation was found. The orientation of residential street patterns were found to have a noticeable effect on the radar image. After plotting the radar image tone with respect to the street orientation angle for a large number of urban areas, it was found that for ϕ of around 20° or less, the radar return is quite sensitive to changes in street orientation with an inverse relationship. There was a "moderately strong" relationship between grey value and ϕ (the street orientation with respect to the normal to the radar direction). The higher image tone values were associated with lower orientation values (ϕ).

Bryan (1982) later studied Seasat SAR data to identify which areas had high radar returns due to feature orientation relative to the radar antenna, and which were characteristic of the ground cover or land use. Images from two different look directions were co-registered and then subtracted from one another resulting in a "difference image" highlighting the direction sensitive features.

Bryan (1983) further demonstrated that by using a procedure called 'squint' processing at different Doppler frequencies, varying information or backscatter values were obtainable about feature orientation, shape and roughness.

The backscatter from a building is also dependent upon polarisation. Hussin (1994) studied HH, VV, HV, and VH polarised backscatter from a variety of urban corner reflectors, and found that co-polarised data gave a high response for simple buildings due to corner reflections, whereas cross-polarised responses did not. Architecturally more complex buildings showed a higher return than those of simple shape. Buildings either perpendicular or parallel to the radar look direction gave a high corner reflection on the HH image. However, this was not always the case for the VV polarisation.

"Thus, knowledge of this orientation, with respect to the azimuth angle (ie., look-direction) of the radar antenna, is of major importance" (Bryan, 1979, p1097).

While research into the dihedral corner effect in urban areas is continuing, further work is still required. Quantitative research is important for analysing this phenomenon.

A small-scale investigation is presented here involving a semi-empirical approach. It examines the grey tone of a radar image to try to determine the average responses for different urban areas. The relationship between building size, orientation angle with respect to radar direction, and backscatter intensity is also addressed.

4.3 Methodology for Urban Investigation

SIR-B data obtained over Sydney was used to provide the radar information. The area of Parramatta, in the Western suburbs, was chosen for this study because it contained a CBD (Central Business District), with tall buildings at a high density, and smaller scale commercial, industrial and residential areas. A colour aerial photograph (scale 1:25,000) of the Parramatta region was used along with orthophotographs for the areas outside the photographs field of view. Photographs, LEP's (Land Environmental Plans) and field inspection

enabled the area to be classified into residential, industrial, and commercial land uses. Institutional, transportation, and open spaces were not considered in this study.

One problem which may slightly affect the results was the time difference between the acquisition of the SIR-B image (1983), the photograph (1991), and the orthophotographs (1977) but there appear to be no major changes from 1977 to 1991.

Relevant test sites were chosen from the photograph. The areas used required regular street patterns to enable an orientation angle ϕ (of the street with respect to the radar direction) to be measured. This was to examine the corner reflector effect for different azimuths.

As many test sites as possible for the three classes were chosen and a variety of street orientation angles were selected. Unfortunately a considerable proportion of the area contained irregular street patterns restricting the number of areas which could be used for this study. Fifteen residential classes were chosen, having a variety of street orientation angles with respect to radar look direction ϕ. (Refer to Figure 4.1 for a pictorial definition of ϕ).

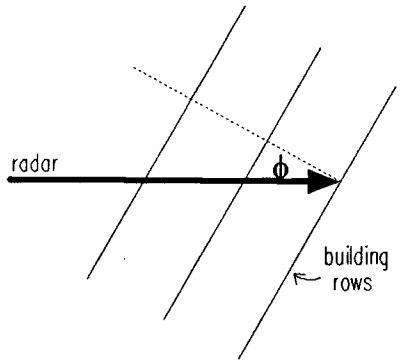

Figure 4.1. A diagram illustrating the geometrical definition of ϕ.

Unfortunately there were fewer commercial and industrial class test sites available, with residential being the most prominent class in the metropolitan area. Three commercial classes and eight industrial classes were chosen.

For every test site, the orientation angle was measured manually and an average grey tone value for the area on the SIR-B was calculated. This was done using the Farm Image software package (Balia & Evans, 1995) developed at the University of New South Wales. The average image tone (or count value) was determined by recording between 100 and 300 count values (ranging from 0 to 255) selected from the whole of each test site. The standard deviations were also taken because, from visual interpretation, there appeared to be brighter patches in the denser classes. Single standing houses and apartment blocks in the residential areas were also examined separately, as well as combined, to see if there were any differences in the average count values.

4.4 Results

A definite trend was visible for the residential results (refer to Figure 4.2). The response is highest at boresight (ϕ=0°). Then a rapid decrease in average radar response occurred as ϕ increased to around 20°, with a slight increase then stabilising for the larger values of ϕ. The average response values, or count values, are proportional to the radar backscatter (Dobson *et al.,* 1986).

The standard deviation for residential areas also show a definite trend. The highest standard deviation occurs when ϕ=0° (boresight), decreases to where ϕ is around 10-20°, then a slight increase as it evens out after 20°.

The results for commercial and industrial land use show a less regular trend, but due to limited data this is to be expected. However, the industrial areas again reveal a strong correlation between orientation angle and average radar

response. When ϕ=0° the response is greatest, and gradually decreases as ϕ increases. There was an insufficient number of commercial areas covering a variety of orientations for any trend to be evident.

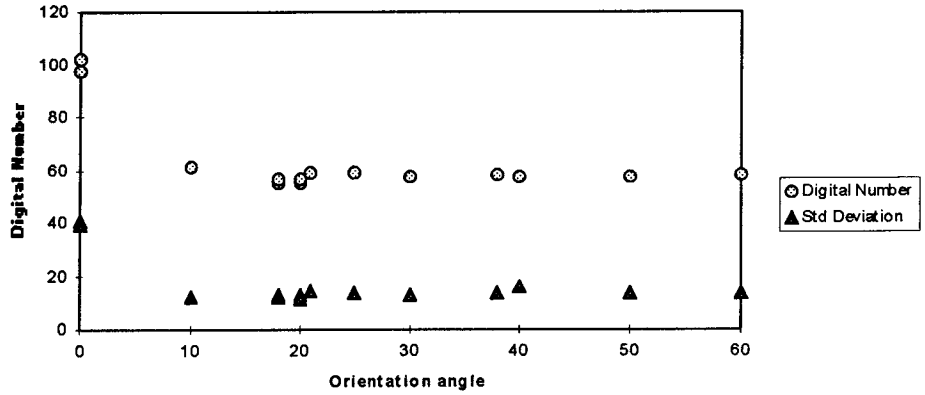

Figure 4.2. Graph showing the average digital number (which is directly related to the backscatter) with respect to the orientation angle for a number of real residential areas. The standard deviations are also plotted for their respective regions.

The standard deviations for commercial classes are higher than those of residential areas for their respective orientation angles. Similarly the industrial areas have a standard deviation higher than the commercial and residential regions for the same orientation angles.

As Figure 4.3 shows, the backscatter is dependent on land use, irrespective of orientation angle.

4.5 Discussion of Results

This study is only of small magnitude covering a minimal area (Parramatta and surrounding suburbs), with a limited amount of data for analysis. However, the results show there is a definite correlation between class (residential, commercial, and industrial) and average pixel value, including its corresponding standard deviation. Note that the assumptions made here about

average residential, commercial, and industrial class characteristics are only for the Sydney region examined. These characteristics will vary according to a city's income, culture, history and climate.

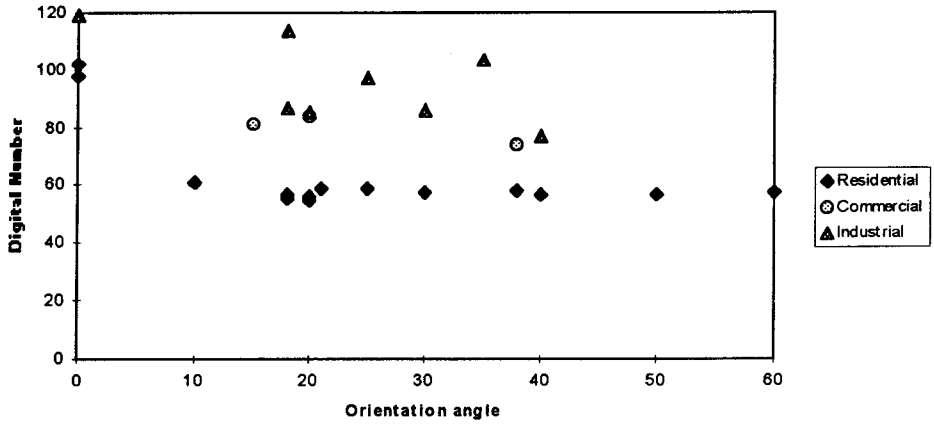

Figure 4.3. Graph showing the average digital number (which is directly related to the backscatter) with respect to the orientation angle for residential, commercial and industrial classes.

Although samples were small for industrial, and especially commercial land use, there are still trends evident. The industrial regions have a much higher average pixel value relative to both commercial and residential areas of similar orientation angle. Industrial areas are usually clad in metal, both for the walls and roof, giving a very high backscatter response. Metallic materials generally reflect more of the radar wave than other non-metals, due to its dielectric properties. Also industrial buildings are usually larger, in floor area and height, than residential and low development commercial. The radar response is directly related to building size.

Another reason for industrial areas having an average higher pixel value than commercial (including the CBD, which has much taller buildings) could be due to the different roof shape and materials. Industrial roofs are often sloping, where many CBD buildings have flat roofs. Industrial roofs tend to be metal, such as corrugated iron. Due to the relative roughness of corrugated iron with respect to L-band, a diffuse or Bragg scattering component may occur in the backscatter. A diffuse component will contribute to the radar return regardless

of its orientation. Bragg scattering is dependent on the distance between the corrugations of the roof relative to the radar wavelength.

Unfortunately industrial sites can lead to problems when trying to classify them from radar images. The layout of an area can vary greatly from site to site. Most buildings are oriented parallel to adjacent streets, but this is not always the case. The density of buildings on industrial sites also differs substantially. Some blocks can be crowded with buildings spatially ordered. Others contain a few buildings scattered randomly across the site with no regular orientation or spacing (eg., railway yards) which gives a much lower response as the radar has less objects to interact with. Hence the irregular responses in industrial areas.

The shape of industrial buildings can also vary. Some industrial regions have many round tanks giving a strong response regardless of orientation. Other buildings have a large main structure, with smaller rooms attached to the sides, contributing to multiple scattering effects.

The commercial regions shown here give an average pixel response between industrial and residential land use. This is expected since commercial areas generally contain buildings of different characteristics to both industrial and residential. Although one case shows an overlap between the commercial and industrial classes (refer to Figure 4.3).

Low density commercial areas, such as individual retail shops, are usually similar or slightly larger than average residential buildings. However, they are more dense and usually consist of corrugated iron roofs which reflect much more strongly than tiled roofs, which are most common in the residential areas examined here. The small scale commercial area has ϕ=38°, as seen in Figure 4.3. The other two commercial areas are part of the Parramatta CBD. This area contains many tall buildings. The height of some is over 15 storeys. Due to the building sizes (width and height) and density in the CBD, the average response here is higher than that of residential. Many of the buildings are made of glass

with some metal structure giving a higher reflection than brick clad residential buildings. The radar intensity for commercial land use is still not as high as industrial areas because metal has a higher dielectric constant than glass.

4.5.1 Comparison with Previous Research

Most of the previous research in the literature concentrates on residential classes rather than a variety of classes. The results presented here are in general agreement with other researchers findings. Hardaway *et al.* (1982) found a threshold value, ie., minimum backscatter, for ϕ to be around 20-22° for residential classes. Below this value of ϕ the radar response changed with street orientation, but above 22° a change of ϕ resulted in little change in image tone. Similarly Bryan's (1979) low point for the grey tone, occurring around ϕ equal to 10-15° off normal, is smaller than these results, but still in the general position.

As Figure 4.3 shows, the backscatter (which is directly related to the digital number) for residential land use is lower than commercial, which is generally less than industrial. A similar study by Dong *et al.* (1996) plotted one commercial and three residential classes of varying orientation angles. Those results showed that the commercial area, having an orientation angle less than 10°, has a higher backscatter for P-, L- and C-bands compared to a residential area of similar orientation angle. The two other residential areas had one orientation angle of about 40-45°, and the other a randomly distributed street orientation. The radar return from these two cases were below the residential area having an orientation angle less than 10° for all P-, L- and C-bands.

Hardaway *et al.* (1982) found that the standard deviation for the residential class was small for low angles of ϕ, indicating that tonal variations are reasonably constant (possibly due to saturation of the return signal), having a maximum when ϕ was in the mid-20's, and finally decreased to a low value as ϕ approached 45°. Hence, there is a discrepancy between Hardaway *et al.*'s

results and Figure 4.4 for the standard deviation for ϕ lower than 20°. This may be related to different methods of data acquisition, or different local characteristics of the data themselves.

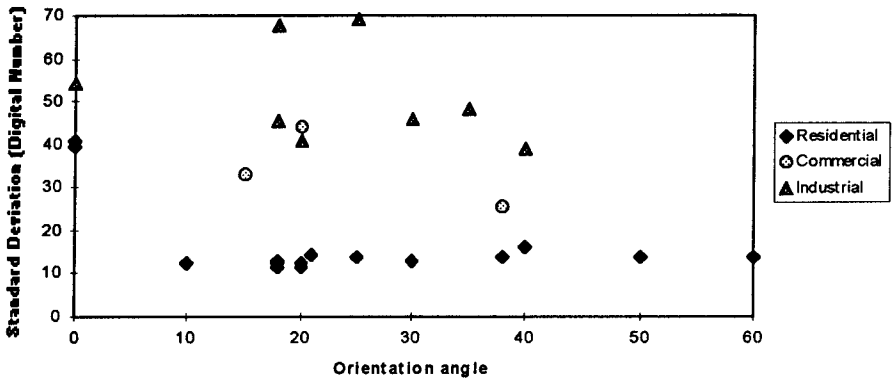

Figure 4.4. Graph showing the standard deviation (units are digital number) with respect to the orientation angle for residential, commercial and industrial classes.

4.5.2 Standard Deviation and its Relationship to Texture and Tone

The standard deviations from the three classes may be beneficial for distinguishing between residential, commercial, and industrial land uses. Residential areas have a lower standard deviation than commercial which are lower than industrial for their respective orientations. The reasons for this are related to such factors as the strength of the backscatter response and shadow regions. Shadow regions being the areas not exposed to the radar wave due to obstructions, such as buildings.

Texture and tone may play a role in identifying different urban classes. Martin-Kaye (1981) believes that the actual changes in tone over a feature was more important than the strength of signal return (ie., brightness). Bryan's (1983) studies concluded that the differences in texture on an image were determined to be a combination of street widths, the size of the housing lots, and the vegetation characteristics. Information about both texture and tone can be present in an image. A wide variety of discrete tonal features in a small area will result in texture being the dominant source of information, otherwise tonal

properties dominate. Texture in an image depends upon the size of the area under investigation, and the relative size and spatial distribution of the discrete tonal features (Baraldi & Parmiggiani, 1995). Land cover providing a homogeneous radar return, such as park land, will have a low variance or texture, while land cover having a high frequency of change, such as urban areas, will have a high variance or texture (Haack, 1984a).

The residential regions have a small range in pixel values because the maximum response does not vary far from its mean value. The buildings are smaller, meaning there is less shadow region (to give extremely low pixel values) so the tone is more homogeneous and the texture is finer than commercial or industrial regions. Commercial land use is in the middle of the range in average pixel response compared to residential and industrial land use. Although it has tall buildings causing shadow regions, its maximum returns are not as high as industrial, hence the standard deviation is not as high. Its tone is more constant than industrial land use. The texture of industrial regions can vary, depending on the site layout, but its high maximum pixel values alternating with the lack of shadow region response, result in this class having the highest standard deviation.

Texture may assist in distinguishing differences between urban classes. However the urban environment has such a variety of characteristics and classes other than residential, commercial, and industrial that texture and tone alone will not be sufficient for classification.

4.6 Summary

From the information presented in this chapter, one can conclude that the orientation angle is only critical when less than 30°. Above 30°, the backscatter is reasonably constant, and hence independent of orientation. Bryan (1979) suggests that prior knowledge about the orientation of features would assist in

setting flight tracks such that they are oriented to take advantage of this information.

Two approaches have been proposed for reducing the "cardinal effect" on radar imagery. These are to use cross-polarised, rather than co-polarised data, and to view the scene from several different look directions (Bryan, 1983). The problem with cross-polarised imagery, however, is that it is subject to significant noise due to the low signal. For satellite systems having a fixed azimuth, "an interpretation methodology, which considers the street patterns, is considered especially critical for proper and accurate interpretation of SAR imagery" (Bryan, 1979, p1097).

Accurate modelling of the cardinal effect is critical because street orientation can have a much greater influence on radar return than the dielectric constant and surface roughness of urban features (Xia, 1996). If the effect which the building orientation has on the radar response could be modelled, a good correlation between backscatter and building bulk (or volume) and density is possible (Dong *et al.,* 1997a). However, "if one can say that over a third of tone variation of the residential image is determined by street orientation alone, ... what factors determine the other 60 percent?" (Hardaway *et al.,* 1982, p403).

The proceeding chapters will attempt to model this dihedral corner effect, as well as determining the other important parameters influencing radar backscatter from an urban environment.

5. DEVELOPMENT OF A THEORETICAL URBAN SCATTERING MODEL

5.1 Introduction

Unlike most other environmental features analysed in remote sensing, urban areas are a combination of natural elements of the physical environment and built elements of the cultural landscape, constructed from a mixture of materials such as wood, sand, concrete, metal, glass and stone. Urban areas are complex due to such a variety of forms, sizes, shapes, and patterns (Xia & Henderson, 1997). The role of this chapter is to simplify such a problem, and determine the formulae necessary for estimating the backscatter in an urban environment from both natural and cultural elements.

5.1.1 Previous Research

Currently most research relies heavily on manual interpretation (Xia & Henderson, 1997). The disadvantage of manual interpretation is its very time consuming nature. Automated interpretation is the preferred approach, however, due to the inherent complexities of an urban scene and its radar return, only limited work has been undertaken.

Modelling of the urban environment is a very difficult problem. "Urban areas are a spatially complex mixture of both natural and built surfaces whose spectral and geometric properties are many and varied" (Forster *et al.,* 1996, p33). Furthermore, the urban environment contains a variety of length scales, ranging from much larger than a wavelength to much smaller than a wavelength. The largest scales are provided by the ground and buildings themselves, while the smallest by the roughness of the building surfaces (Taket *et al.,* 1991).

Taket *et al.* (1991) have designed a model based on ray tracing. The model is designed to simulate the effects of strong specular scatterers such as corner cubes, as well as the diffuse scatter from the rough surfaces of buildings. Scattering from the whole object is built up from the scattering properties of its individual components. The model output was tested on a simulation from a simple object, however, it was yet to be tested with real data.

Nasr & Vidal-Madjar (1991) use a modelling technique which embeds simulated man-made targets into a real background taken from SAR spaceborne scenes. The Geometrical Theory of Diffraction and the Uniform Theory of Diffraction were used for simulating the backscatter from a number of simple target shapes embedded in the real background. It was reported that the detectability of a target was dependent on: the morphology of the target; the attitude of the target with respect to the SAR illumination; and the polarisation. The results are promising in terms of target detectability of built structures in a SAR environment.

Tajbakhsh *et al.* (1995) also used the Geometrical Theory of Diffraction ray tracing as an approach to modelling the radar backscatter from objects. This method was applied to a simulated urban building to examine its results. Although time consuming, they were able to simulate a reasonably complex urban shape, in this case it was a semi-detached house with garages attached.

Dong *et al.* (1996) has also examined modelled target simulations in relation to the urban environment. The model uses the physical optics approximation for analysing dihedral corner reflection, trihedral corner reflection, and wedge-ground structures. The three targets simulate some of the scattering in the urban environment.

A different modelling approach to that mentioned above, uses the polarisation information to determine the dominant scattering components, such as Dong *et al.* (1997b) (described in Section 3.4.4). The model presented here attempts the opposite approach by determining the scattering components of the urban

class, and then forming the polarisation signature and polarisation information from these components. There are advantages and disadvantages of both methods. Decomposing polarisation information into its dominant components requires an initial assumption of the dominant scattering mechanisms before analysis can commence. However, the opposite modelling approach needs the general characteristics and parameters of the urban environment as input.

Most practical knowledge describing how ground objects reflect radar energy have been derived from empirical observations. However several theoretical models have been developed (Xia & Henderson, 1997), some of which were described previously. The approach of this model is primarily theoretical as it attempts to imitate the urban environment as a whole, for more than one land use.

5.1.2 General Characteristics of the Model

The aim of this model is to enable calculation of the backscatter, for HH and VV polarisation, and to produce a polarisation signature, both co- and cross-polarised, to assist in determining land use. The Polarisation Index (PI) and Polarisation Phase Difference (PPD) are calculated using these results to provide additional information and ease of analysis. The model will concentrate on L-band wavelength, but will also examine C- and P-band. The land uses to be examined in this study are residential and commercial, due to their relatively uniform characteristics. Furthermore these two classes generally represent low and high density land uses respectively. The model also allows for the determination of park land, which is an easy class to distinguish due to its low radar return.

This model has been designed to calculate the backscatter from a block of buildings. A block consists of homogeneous buildings of user defined characteristics. The major parameters affecting the backscatter from a building block are considered. The model's development began with the calculation of backscatter from a simple single building, and then was expanded to a block of

buildings. Finally, vegetation and spacing for the road was considered. Although radar images suffer from layout distortion and shadow effects, the assumption is made that the urban area is relatively flat so that these effects are considered to be minimal.

As previously mentioned, the land uses considered in this model are residential, commercial, and park land. The study is based in Sydney, Australia, and the land use parameters are chosen to represent average class characteristics in Sydney only. The main region of study is along the east coast of Sydney, from Kingsford in the south, to the Spit Bridge in the north, and west as far as Balmain. An approximate total area of 10km*10km ie., 100km^2. The reason for this limited area of study is because AirSAR data acquired in 1993 was available to provide test data, and this was the extent of its imaging.

Residential areas in the subject region consist of a mixture of single storey houses, and apartments of two to four levels. Most of the residential buildings are built with brick and have a reasonable glass content due to the windows. The roofs are primarily terracotta tiles. Tiles, being a dry material with a low dielectric constant, allow a large proportion of the radar to penetrate into the ceiling and interact with the components in this enclosure. (This effect will be discussed in detail in Chapter 6). The average planimetric size of the buildings, their surrounding (especially rear) open spaces, and vegetation content were estimated from aerial photographs. Chapter 6 addresses this issue.

The commercial areas considered concentrate on CBD's (Central Business Districts), consisting of tall buildings from around 5 up to more than 50 storeys in the city, with a large planimetric building density. The buildings generally have flat roofs and are predominantly clad in glass, metal and concrete. Structures of this size require some internal support usually provided by metal.

Park land in the subject area is generally flat land, with relatively short grass, and trees scattered throughout. These areas are easy to detect on an AirSAR

image because of their very low return from the short grass, which is a near-specular reflector for most wavelengths.

5.2 Determining Backscatter from a Single Building

A simple building was chosen for the model such that it represented the dominant shape of the real environment. As can be seen from Figure 5.1, the building consists of a simple rectangular base, with a double sided sloping roof of gable design. The building was chosen for its simplicity, and because it represents the main scattering mechanisms. All dimensions, and materials (ie., dielectric constant and roughness) of the building are user defined, such that the building's size and materials can be specified for each land use class. For example, a residential building will be small with a sloping roof, and a relatively low dielectric constant. A CBD building, however, is much larger with a flat roof, and higher dielectric constant. The input for the backscatter from a single building is: the wavelength (λ), look angle of the radar (θ); the orientation angle (ϕ); the dimensions of the building (*L, b* and *H*); the roof slope (γ); and the dielectric constant of the building roof (ε_r) and walls (ε_w), and the ground (ε_g).

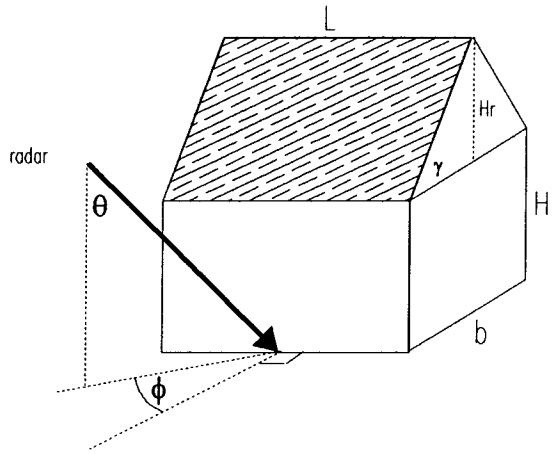

Figure 5.1. The shape and parameters of a single building used in the model, including the direction of the incident radar wave.

It can be seen from Figure 5.1 that there are four main scattering components: the front wall; the side wall; the front roof; and the back roof (when not shadowed). The total backscatter from the building is the total of these components, thus:

$$\sigma_{pptot} = \sigma_{ppfw} + \sigma_{ppsw} + \sigma_{ppfr} + \sigma_{ppbr} \tag{5.1}$$

where σ_{pptot} is the total backscatter for the building for polarisation *pp*, σ_{ppfw} is the backscatter from the front wall, σ_{ppsw} is the backscatter from the side wall, σ_{ppfr} is the backscatter from the front roof, and σ_{ppbr} is the backscatter from the back roof. In future, whenever *p* occurs as a subscript to a parameter, it is indicating that the polarisation can be either *h* or *v*.

The radar return from the **front wall** is a simple dihedral corner reflection. As given in Equation 3.2:

$$\sigma_{ppfw} = \frac{16\pi}{\lambda^2} R_{pw}^2 R_{pg}^2 L^2 H^2 \sin^2\theta \cos^8\phi \, \mathrm{sinc}^2\left(k_o L \sin\theta \sin\phi\right) \quad \text{(Dong, 1995a)} \tag{5.2}$$

where σ_{ppfw} is the backscatter for corner reflection off the front wall for *pp* polarisation, R_{pw} and R_{pg} are the Fresnel reflection coefficients for polarisation *p* for the wall and ground respectively, λ is the wavelength, and k_0 is the wave number.

The backscatter from the **side wall** is also a corner reflection, similar to the front wall, except that a few parameters have changed. The area has changed because the extra triangle at roof height is also treated as an extension of the wall. From Figure 5.2, the side wall of the model building, it can be seen that the total side wall area is:

$$Area = Hb + {}^{H_r b}/_{2} \tag{5.3}$$

where H_r is the vertical height of the roof.

The angle which the radar contacts the wall is not the orientation angle ϕ, instead it is: $\phi_{sw} = 90 - \phi$. The look angle remains the same. The backscatter from the side wall is therefore:

$$\sigma_{ppsw} = \frac{16\pi}{\lambda^2} R_{pw}^2 R_{pg}^2 b^2 \left(H + {}^{H_r}\!/_2\right)^2 \sin^2\theta \cos^8\phi_{sw} \operatorname{sinc}^2\left(k_o b \sin\theta \sin\phi_{sw}\right) \qquad (5.4)$$

The area of the side wall is not a rectangle, but a rectangle with a triangle above. The formula is designed for a rectangular wall, however this does not create problems. The phase of the wave at the extremes of the building are calculated only for the width of *b*, the phase component oscillations do not play a large role in determining the model's backscatter. As will be shown in the next chapter, the oscillations are smoothed before final output.

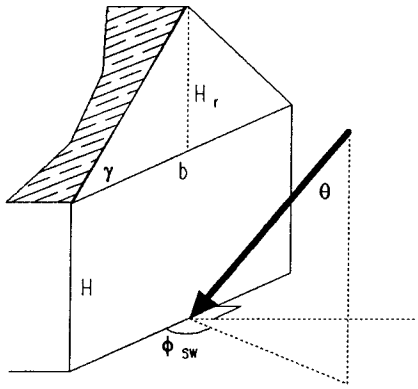

Figure 5.2. The side wall of the model building. The dark line represents the radar contact direction with respect to the wall.

The backscatter from the **front roof** is a single bounce reflection. The incident angle and the orientation angle with respect to the roof are not θ and ϕ as given in Equation 3.6 (from Section 3.3.2). It can be seen from Figure 5.3, that these angles are different to, but still functions of, θ and ϕ. Using spherical trigonometry:

$\cos a = \cos b \cos c + \sin b \sin c \cos A$ and

$\sin C \cot B = \cot b \sin a - \cos a \cos C$ (Harvey, 1994)

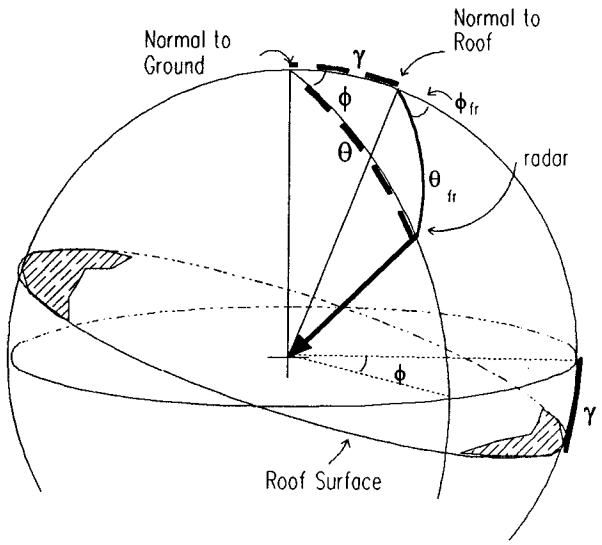

Figure 5.3. Diagrammatic representation of spherical trigonometry for calculation of the orientation ϕ_{fr} and incident angle θ_{fr} of the radar with respect to the front roof.

it can be shown that:

$$\theta_{fr} = \cos^{-1}\left(\cos\theta\cos\gamma + \sin\theta\sin\gamma\cos\phi\right) \tag{5.5}$$

$$\text{and } \tan\left(180 - \phi_{fr}\right) = \left(\frac{\sin\phi}{\sin\gamma / \tan\theta - \cos\gamma\cos\phi}\right)$$

$$\text{hence } \phi_{fr} = 180 - \tan^{-1}\left(\frac{\sin\phi}{\sin\gamma / \tan\theta - \cos\gamma\cos\phi}\right) \tag{5.6}$$

where θ_{fr} is the incidence angle for the facing roof, ϕ_{fr} is the orientation angle for the facing roof, and γ is the roof slope. The backscatter for the facing roof is therefore:

$$\sigma_{ppfr} = \frac{4\pi}{\lambda^2} R_{pr}^2 \left(\frac{Lb}{2\cos\gamma} \right)^2 \cos^2\theta_{fr} \left(\sin c^2(f) \sin c^2(g) \right) \tag{5.7}$$

where $f = \frac{k_o H_r}{\sin\gamma} \sin\theta_{fr} \cos\phi_{fr}$ and $g = k_o L \sin\theta_{fr} \sin\phi_{fr}$

The backscatter from the **back roof** is only considered when the look angle is not too large, otherwise the back part of the roof is shadowed. Backscatter for the back roof is calculated only when the look angle is less than the roof slope, ie., $\theta \leq \gamma$. Again the incidence angle and orientation angle are not equal to θ and ϕ. Refer to Figure 5.4 for a representation of the modified incidence and orientation angles for the back roof. Again using spherical trigonometry:

$$\cos\theta_{br} = \cos\gamma\cos\theta + \sin\gamma\sin\theta\cos(180 - \phi)$$

$$\text{hence } \theta_{br} = \cos^{-1}\left(\cos\gamma\cos\theta - \sin\gamma\sin\theta\cos\phi\right) \tag{5.8}$$

$$\text{and } \tan\phi_{br} = \left(\frac{\sin(180 - \phi)}{\sin\gamma / \tan\theta - \cos\gamma\cos(180 - \phi)} \right)$$

$$\text{so } \phi_{br} = \tan^{-1}\left(\frac{\sin\phi}{\sin\gamma / \tan\theta + \cos\gamma\cos\phi} \right) \tag{5.9}$$

Thus the backscatter from the back of the roof is now:

$$\sigma_{ppbr} = \frac{4\pi}{\lambda^2} R_{pr}^2 \left(\frac{Lb}{2\cos\gamma} \right)^2 \cos^2\theta_{br} \left(\sin c^2(d) \sin c^2(e) \right) \tag{5.10}$$

where $d = \frac{k_o H_r}{\sin\gamma} \sin\theta_{br} \cos\phi_{br}$ and $e = k_o L \sin\theta_{br} \sin\phi_{br}$

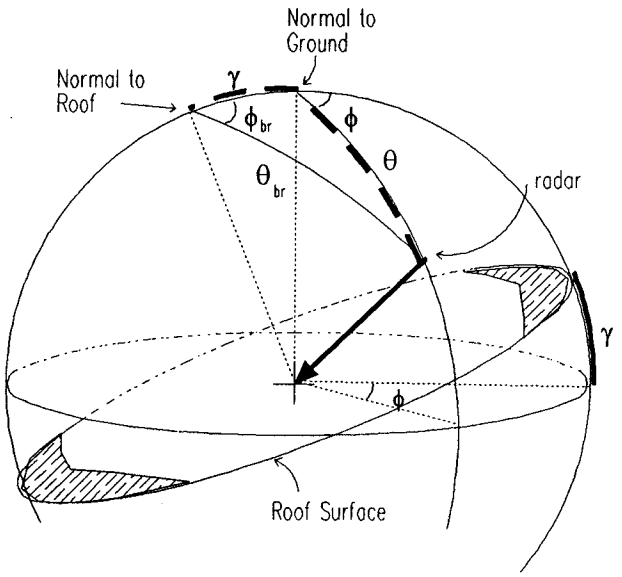

Figure 5.4. Diagrammatic representation of spherical trigonometry for calculation of the orientation ϕ_{br} and incident angle θ_{br} of the radar with respect to the back roof.

5.3 Expansion of the Model to Include a Block of Buildings

The radar return modelled on a single building needs to be expanded to form a block of buildings. This is achieved by extending the single building into a number of rows and columns. This is not as simple as multiplying a single building's results by the number of rows and columns because if they are sufficiently close, parts of the buildings will be in the radar shadow zone for particular radar angles. In addition, other multiple scattering effects may take

place, but it is assumed, due to the relatively low dielectric constants involved, that these effects will be insignificant.

In terms of the coverage of the radar's signal, there will be four types of building backscatter, depending on the interference from other buildings. (This methodology applies to both residential and commercial buildings). Referring to Figure 5.5, Building 1 will have no shadowing effects caused by the other buildings in the block, irrespective of how close they are together. Its backscatter is calculated using Equations 5.2, 5.4, 5.7, and 5.10 for a single building front wall, side wall, front roof and back roof respectively. Building 2 may have interference from Building 1 for its side wall double bounce reflection. Building 3 may have shadowing on its front wall caused by Building 1. Building 4 can have interference from Buildings 2 and 3, and in extreme circumstances from Building 1.

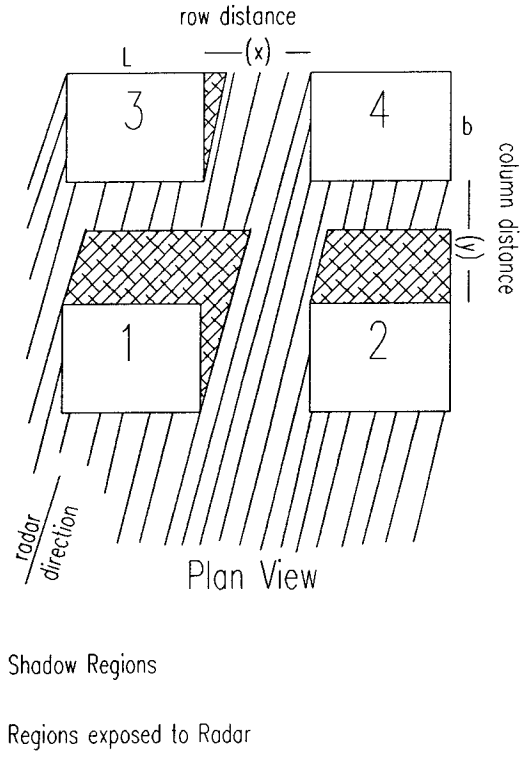

Figure 5.5. A plan view of the radar shadow regions caused by interference from adjacent buildings.

In a typical block such as this, the distance between the rows would be much smaller than between the columns. This is because Buildings 1 and 2 front one street and so are close beside each other, similarly Buildings 3 and 4 will front the opposite street. The area between Buildings 1 and 3 is their rear open space, as is the area between Buildings 2 and 4. An assumption is made that the distance between the building columns is generally small, but the distance between the rows can be large, especially for residential buildings. It also should be noted that the backscatter from the roofs, ie., σ_{ppfr} and σ_{ppbr}, will not be affected.

The next section examines in detail the amount of double bounce backscatter expected from the front wall and side walls subjected to the radar shadow areas. The calculations for corner reflection that follow are based on the fact that if there is no radar reaching the ground before the building wall, there can be no corner reflection. Even though the radar may contact the wall, the reflection will be lost through multiple bounce in the shadow region between the two buildings. The extent of radar exposure on the ground in front of the wall is used, with the look angle, to determine the height that the reflection will reach on the wall, based on simple trigonometry. (Refer to Figure 5.6).

5.3.1 Backscatter from Building Type 2

The backscatter from the **side wall** may vary depending on the spacing between Buildings 1 and 2. From Figure 5.7, if $x/\tan\phi \geq b$, (where x is the row distance) there will be full contribution from the wall. If not, then the width of the wall which will maintain full response will be: $b_f = x/\tan\phi$, and the height obviously is still H, the full height of the wall. The remainder will also contribute to corner reflection provided that $x/\sin\phi > H\tan\theta$. The width of this part is:

$b_s = b - x/\tan\phi$, and its height will be: $H_s = \left(x/\sin\phi - H\tan\theta\right)/\tan\theta$.

(Assuming ϕ is less than or equal to 45°).

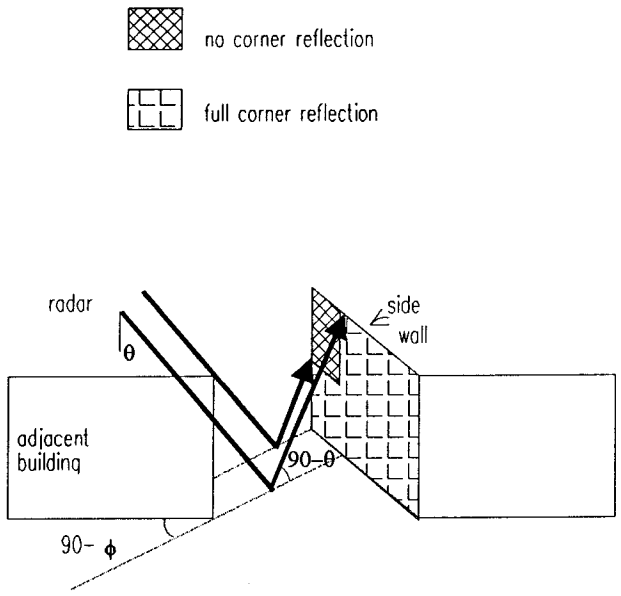

Figure 5.6. A 3-dimensional view of the radar shadow regions due to interference from adjacent buildings.

The total backscatter from the side wall will therefore become:

$$\sigma_{ppsw} = \frac{16\pi}{\lambda^2} R_{pw}^2 R_{pg}^2 \zeta \sin^2\theta \cos^8\phi_{sw} \tag{5.11}$$

where: if $x/\tan\phi < b$ and $x/\sin\phi < H\tan\theta$, then;

$$\zeta = b_f^2 \left(H + {}^{H_r}\!/_2\right)^2 \operatorname{sinc}^2\left(k_o b_f \sin\theta \sin\phi_{sw}\right) \tag{5.12}$$

or if $x/\tan\phi < b$ and $x/\sin\phi > H\tan\theta$, then;

$$\zeta = b_f^2 \left(H + {}^{H_r}\!/_2\right)^2 \operatorname{sinc}^2\left(k_o b_f \sin\theta \sin\phi_{sw}\right) + b_s^2 \left(H_s + {}^{H_r}\!/_2\right)^2 \operatorname{sinc}^2\left(k_o b_s \sin\theta \sin\phi_{sw}\right) \tag{5.13}$$

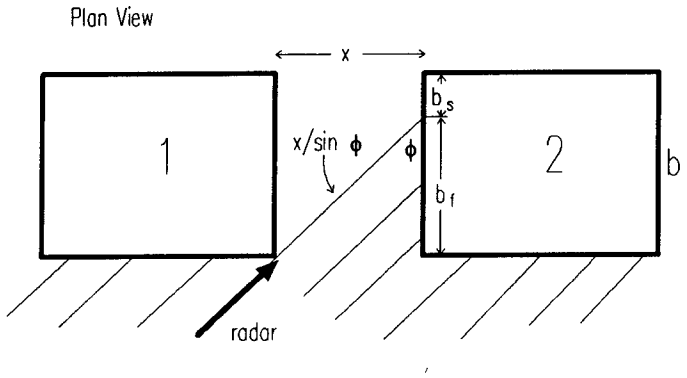

Figure 5.7. Plan view of Buildings 1 and 2, showing the shadow areas with respect to x and ϕ.

5.3.2 Backscatter from Building Type 3

The backscatter from the **front wall** of Building 3 may be affected from radar shadow due to Building 1. As Figure 5.8 shows, there will be full reflection if $y\tan\phi > L$, where y is the column distance. If this is not the case, then the length of the wall retaining full reflection is: $L_f = y\tan\phi$, and the height is H. The remainder of the wall will also contribute when $y/\cos\phi > H\tan\theta$. In this case the length of this part will be:

$L_s = L - y\tan\phi$, and the height is: $H_s = \left(y/\cos\phi - H\tan\theta\right)/\tan\theta$

The total backscatter from the front wall of Building 3 becomes:

$$\sigma_{ppfw} = \frac{16\pi}{\lambda^2} R_{pw}^2 R_{pg}^2 \zeta \sin^2\theta \cos^8\phi \qquad (5.14)$$

where: if $y\tan\phi < L$ and $y/\cos\phi < H\tan\theta$ then;

$$\zeta = L_f^2 H^2 \operatorname{sinc}^2\left(k_o L_f \sin\theta \sin\phi\right) \qquad (5.15)$$

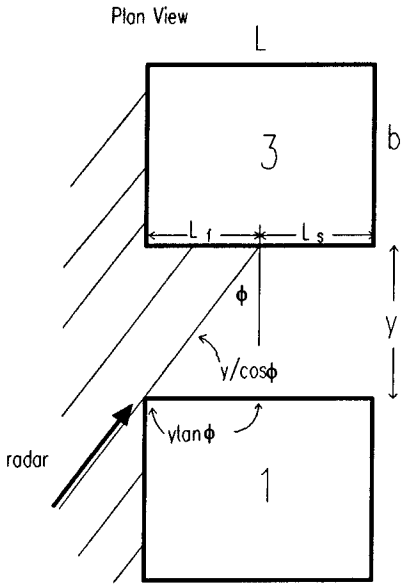

Figure 5.8. Plan view of the radar shadow regions forming on Building 3 due to Building 1, with respect to y and ϕ.

or if $y\tan\phi<L$ and $y/\cos\phi>H\tan\theta$ then;

$$\zeta = L_f^2 H^2 \operatorname{sinc}^2\left(k_o L_f \sin\theta\sin\phi\right) + L_s^2 H_s^2 \operatorname{sinc}^2\left(k_o L_s \sin\theta\sin\phi\right) \quad (5.16)$$

5.3.3 Backscatter from Building Type 4

The backscatter from Building 4 is the most complex since its dihedral corner reflections from both the front and side wall may be affected by radar shadow regions from adjacent buildings. (Figure 5.9 depicts the situation). If $x/\sin\phi>2H\tan\theta$ (indicating full bounce along at least part of the wall), then the amount of shadowing on both the front and the side walls are the same as the situations explained for Buildings 3 and 2 respectively. This should always be the case for residential buildings due to the large distance between rows, but not for typical commercial districts.

$x/\sin\phi < H\tan\theta$ is the most likely situation for a CBD. An assumption is made that $\phi < \tan^{-1}(x/y)$, indicating that $\phi \leq 45°$ if x and y are equal, which is most common in a CBD. Furthermore, once ϕ becomes greater than 45°, the side wall now becomes the new front wall. For calculation of the backscatter from the **side wall** the width b_n will have no reflection due to shadowing from Building 1. The section b_s will have some reflection starting from zero adjacent to b_n and gradually increasing up to the end of b_s.

The length of b_s is: $b_s = b + y - H\tan\theta\cos\phi$, assuming that $x/\tan\phi > b$ (which is true when $\phi \leq 45°$), and its height will vary from 0 up to $\left(\frac{b+y}{\cos\phi} - H\tan\theta\right) / \tan\theta$.

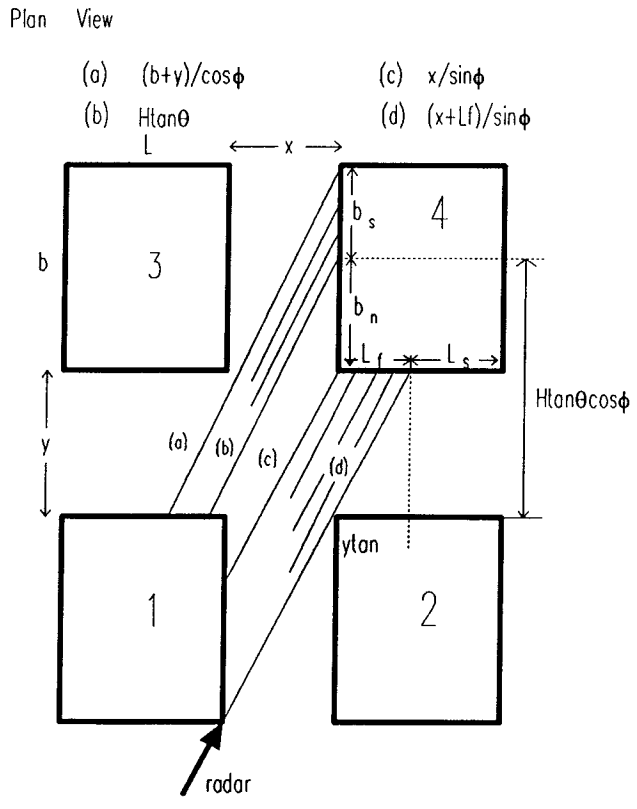

Figure 5.9. Plan view of the radar shadow effects on Building 4 caused by Buildings 1 and 2, with respect to θ, ϕ, *H*, *L* and *b*.

Therefore if this is averaged, from 0m up to the maximum final height, the height becomes:

$$H_s = \left(\frac{b+y}{\cos\phi} - H\tan\theta\right) \Big/ 2\tan\theta.$$

Finally, there is the situation when $2H\tan\theta > x\sin\phi > H\tan\theta$, however, considering commercial buildings are tall (hence $H\tan\theta$ becomes large) and dense, this case is most unlikely therefore will not be considered.

The total backscatter from the side wall of Building 4 affected by shadowing is:

$$\sigma_{ppsw} = \frac{16\pi}{\lambda^2} R_{pw}^2 R_{pg}^2 \zeta \sin^2\theta \cos^8\phi_{sw} \sin c^2\left(k_o b_s \sin\theta \sin\phi_{sw}\right) \quad (5.17)$$

If $x/\sin\phi < H\tan\theta$ (which is the only assumption made) then $\zeta = b_s^2 H_s^2$ (5.18)

Note that in the model, the commercial buildings are considered to have flat roofs so H_r is 0.

The backscatter from the **front wall** is also different. If $y/\cos\phi > 2H\tan\theta$, there would be full reflection from the front wall, however, as in the case for the side wall of commercial buildings, this is very unlikely due to the large H.

For a small orientation angle, the full height of the wall will be contributing to backscatter along L_f (refer to Figure 5.9). For a large orientation angle, Building 1 will cause radar interference on the front wall of Building 4. However, for large orientation angles the radar return from the front wall is small. Hence, the assumption will be made that for large orientation angles, the interference from Building 1 on the front wall of Building 4, will have a negligible effect on total backscatter. For this situation the backscatter from the front wall of Building 4 will be considered to be the same as that from Building 3.

The situation where $y/\cos\phi > H\tan\theta$, may sometimes exist. In this case there will be full return from the complete height of the wall along L_f, giving: $L_f = y\tan\phi$. The remainder of the wall L_s, is partially contributing to the backscatter.

Thus, $L_s = L - y\tan\phi$, and $H_s = \left(y/\cos\phi - H\tan\theta\right)/\tan\theta$.

$y/\cos\phi < H\tan\theta$ is most likely for a commercial region due to tall buildings. Referring to Figure 5.9, there will be no reflection from L_s. Backscatter from length L_f will depend on whether $x/\sin\phi > H\tan\theta$. If it is true then: $L_f = y\tan\phi$. The height ranges from $\left(\frac{x}{\sin\phi} - H\tan\theta\right)\Big/\tan\theta$ up to $\left(\frac{x+L_f}{\sin\phi} - H\tan\theta\right)\Big/\tan\theta$, so the average of these two is used, determining the height to be:

$$H_f = \left(\frac{2x+L_f}{\sin\phi} - 2H\tan\theta\right)\Big/2\tan\theta$$

The total backscatter from the front wall of Building 4 can be given by:

$$\sigma_{ppfw} = \frac{16\pi}{\lambda^2} R_{pw}^2 R_{pg}^2 \zeta \sin^2\theta\cos^8\phi \qquad (5.19)$$

where: if y/cosϕ<Htanθ then; $\zeta = H_f^2 L_f^2 \,\mathrm{sinc}^2\left(k_o L_f \sin\theta\sin\phi\right)$ (5.20)

and if y/cosϕ>Htanθ then;

$$\zeta = L_f^2 H^2 \,\mathrm{sinc}^2\left(k_o L_f \sin\theta\sin\phi\right) + L_s^2 H_s^2 \,\mathrm{sinc}^2\left(k_o L_s \sin\theta\sin\phi\right) \qquad (5.21)$$

It should be noted that when the orientation angle is small, there will be full reflection from the side wall, ie., $x/\sin\phi > 2H\tan\theta$. However, the amount of backscatter from the side wall will be negligible since the orientation angle in relation to the side wall ϕ_{sw} will be large.

5.3.4 Total Backscatter from a Building Block

Until now it has been assumed that $\theta+\gamma<90°$. From Figure 5.10 it can be seen that this is only one case. If $\theta+\gamma>90°$, then the building height casting the shadow increases. However this would not be common in real situations because typical roof slopes are around 30° (Dong, 1997a) and the maximum look angle being examined is not much larger than 60°. Thus it will not be considered further.

Any of the lengths, widths, or heights determined for shadowing in this chapter may calculate to be larger than the actual dimension of the building. If this is the case, then the dimension of the building becomes the value used.

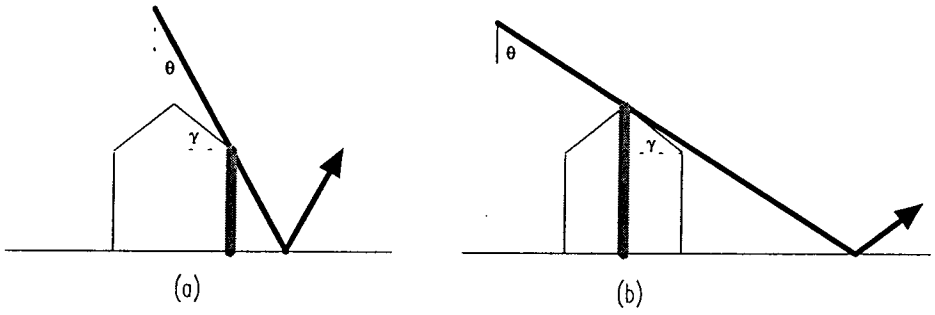

Figure 5.10. Diagram illustrating the two types of shadow projection heights (represented by the thick pale line) for a building with respect to the radar's position (represented by the thick dark line). Type (a) is for $\theta+\gamma<90°$ (as modelled in this research), and type (b) is for $\theta+\gamma>90°$, where the projection height increases.

The total return from a block of buildings is now the sum of all the backscatter from Buildings 1, 2, 3, and 4. For a larger block of buildings with *m* rows and *n* columns, the total backscatter for the block σ_{tot} will be:

$$\sigma_{tot} = \sigma_{b1} + (m-1)\sigma_{b2} + (n-1)\sigma_{b3} + (m-1)(n-1)\sigma_{b4} \qquad (5.22)$$

where σ_{bt} is the backscatter from one building of type *t*, with *t* representing 1,2,3 or 4.

5.4 Inclusion of Trees in the Model

Trees, whether in the garden or along the road, contribute to the total backscatter in residential areas, and so require consideration. The return from trees may not be significant for the total backscatter for small orientation angles, however as ϕ approaches 45° their role becomes more important. It must be noted that trees do exist, in limited numbers, in commercial areas. However, due to the high backscatter from the buildings, the contribution from trees will be minimal, and hence can be ignored.

Modelling the backscatter from vegetation is a difficult task. Some reasons for this are: the complex tree geometry; many elements of the trees are of comparable size to the wavelength; information is limited for determining the relative importance of tree constituents (such as leaves and branches) with respect to attenuation, and; the biophysical parameters defining tree foliage is minimal (Ulaby *et al.,* 1981). Hence, modelling the scattering from trees in an urban environment is complex. The variety and size of trees in residential areas is quite extensive, making accurate vegetation modelling impossible.

There are many vegetation models available in the literature, but most of these only consider dense tree coverage where the canopy can be treated as a continuous layer. The Michigan Microwave Canopy Scattering Model (MIMICS) models the trees as having a tree canopy with a crown layer, a trunk layer and a rough-surface ground. The crown layer is represented as a distribution of dielectric cylinders (representing needles and/or branches) and discs (representing leaves), and the trunks are treated as dielectric cylinders. The MIMICS model is based on a first-order solution of the radiative-transfer equation which is expressed in terms of a 4*4 Stokes-like transformation matrix (Ulaby *et al.,* 1990).

A simpler, continuous canopy model, was developed for L-band by Richards, *et al.* (1987). The forest stand is also modelled as layers with some vegetation components having different scattering mechanisms. Such components include volume scattering from the foliage, scattering from the ground (both with and without canopy), reflections from the branches, and backscattering involving the trunk.

A continuous layer is not satisfactory for modelling the urban environment, so a sparse canopy model is needed. Some of the more recent models consider scattered vegetation with a discontinuous canopy layer. In Sun *et al.*'s (1991) model, each tree is considered to be an individual scatterer in a background having a particular spatial pattern. This model uses the radiative transfer theory, Stokes matrices, and a gap probability approach to represent tree distribution. The MIMICS model has also been further developed for discontinuous tree canopies. The tree crowns are treated as random variables (McDonald & Ulaby, 1993). Other sparse canopy models include the "Santa Barbara Microwave Backscattering Model for Woodlands" (Wang *et al.*, 1993), which is an advancement of the model developed by Sun *et al.* (1991) and a "Three-Dimensional Forest Backscatter Model" described by Sun and Ranson (1995).

In this research the sparse forest backscatter model given by Kolawole (1991) has been chosen and adapted into an urban environment. In this model "an effort has been made to reduce [the complexity of parameter estimation] to a level that closely reflects [the] real situation without loss of credence" (Kolawole, 1991, p6). A further reason for choosing Kolawole's model is because the formulae are less computationally intense since there are no large matrix manipulations. The urban model being developed here, has a computationally demanding range of formulae from the building parameters alone before the vegetation response is even considered.

High accuracy of the radar return from the tree components in the urban model is difficult to obtain due to the heterogeneity of tree numbers, types, and sizes. Other vegetation models may be able to obtain more accurate results for a uniform forest, but they require detailed input parameters of the vegetation. Such parameters include the leaf thickness, leaf diameter, trunk moisture, branch length, branch diameter, and soil type (Ulaby *et al.,* 1990). These parameters are impossible to obtain in an urban region due to the diversity of vegetation species found. Furthermore, data is limited for relating the backscatter properties of tree canopies to their physical properties (such as leaf area index; tree type, size, age, height, and number-density of trees per unit area) (Ulaby *et al.,* 1981).

A further advantage of Kolewole's sparse canopy model (1991) is that, even though it has reasonably simple calculations, the radar return is still a function of such vital parameters as wavelength and polarisation.

In Kolawole's model there are four main types of scattering resulting from trees, these are: volume scattering from the canopy; scattering from the ground beneath the trees; double bounce scattering from the canopy to the ground and back to the sensor; and double bounce scattering from the tree trunk to the ground and back to the sensor (Kolawole, 1991). The two largest components are the trunk-ground double bounce, and the volume scattering in the canopy. For look angles greater than 30°, as used in this study, the surface scattering response has no affect on the total backscatter. Double bounce scattering in the canopy towards the ground under the tree is also minimal. These two scattering mechanisms were originally included in the model, but were found to produce no significant change to the total return when omitted.

Kolawole has made a number of assumptions for the **canopy scattering** to maintain simplicity. These assumptions are: the particles are identical in size, and are distributed uniformly; the shadowing effect of one particle by another is ignored due to the small concentration of particles within the volume; single scattering is the dominant contributor so multiple scattering is neglected; all

particles have a uniform radar cross section σ, and uniform attenuation cross section Q (Kolawole, 1991).

The total radar cross section ρ, per unit scattering volume, is defined as $\rho=N\sigma$ (m^{-1}) and the total power attenuation cross section α, per unit scattering volume, is: $\alpha=NQ$ (m^{-1}), where N is the number of scattering particles in the canopy per unit particle volume (m^{-3}). Q is the uniform attenuation cross section of the canopy (m^2) (Kolawole, 1991).

Further considerations of this scattering mechanism are discussed in Kolawole (1992). Here the canopy scattering coefficient is defined as;

$$\rho_{h,v} = \frac{24\pi t_c A}{\lambda^4}\left(\frac{\varepsilon-1}{\varepsilon+2}\right)^2 \quad \text{(Kolawole, 1992)} \tag{5.23}$$

where t_c is the effective thickness of the leaf, A is the area of the leaf, and ε is the leaf's dielectric constant. The attenuation coefficient is estimated as:

$$\alpha_{h,v} = \left(\frac{128A^3}{3t_c\lambda^4}\right)\left(\frac{1+m_g}{A_c}\right)\left(\frac{\varepsilon-1}{\varepsilon+2}\right)^2 \quad \text{(Kolawole, 1992)} \tag{5.24}$$

where m_g is the leaf gravimetric moisture content, and A_c is the canopy surface area.

As there is a limited amount of real data available on these vegetation parameters, and since high vegetation accuracy is not possible for the urban model, the values were taken from Table 1 given in Kolawole (1992). This table displays the mean leaf thickness t_c, mean leaf area A, and the mean gravimetric moisture content m_g measurements for white stringybark eucalypts. The measurements are subdivided into early, middle, and mature stages of the tree's life. In an urban environment the growth stages of vegetation varies, as do the species. Due to the complexity of vegetation in an urban environment,

and hence the difficulties of collecting field samples, the vegetation parameters in the model are estimated from the eucalypts at their middle growth stage. Such a decision is not unrealistic as eucalypts are found in many local urban areas of Sydney. This is explained in more detail in Chapter 6.

If a spherical canopy is considered such that the backscatter is independent of polarisation, then:

$$\sigma_{pqcn} = \frac{\pi\rho}{2\alpha_{pq}}\left(R^2 + \frac{\mathrm{Re}^{-4\alpha_{pq}R}}{2\alpha_{pq}} + \frac{1}{8\alpha_{pq}^2}\left(e^{-4\alpha_{pq}R} - 1\right)\right) \text{ (Kolawole, 1991)} \qquad (5.25)$$

where p and q are the polarisations (either h or v), ρ and α are the volume scattering coefficient and attenuation coefficient respectively (as just explained), and R is the radius of the canopy (considered to be a sphere). Hence an assumption is made that the spherical canopy is evenly distributed in all directions, ie., σ_{hhcn} is equal to σ_{vvcn}.

Due to reciprocity, σ_{hvcn} is the same as σ_{vhcn}, its magnitude in relation to the co-polarised results will be discussed in Section 5.5.6. For σ_{hvcn} to be determined the individual power transmittance for each polarisation is required, and although Hoekman (1990) has done some work in this area, the measurements were for X-band (Kolawole, 1992), which would be expected to be quite different to L- and P-bands. Determination of the transmittance requires local measurements, since values are dependent on the local environment, and tree type (Kolawole, 1992). However, measuring such information was beyond the scope of this research. Furthermore, this should not be such a problem because for longer wavelengths such as L and P bands, the foliage layer is not the dominant scatterer from vegetation (Dong *et al.,* 1995). Resolution of this matter is addressed in Section 5.5.6, and in future chapters when required.

The **trunk-ground scattering** model derived in Kolawole (1991) is based upon Richards *et al.* (1987). For the longer radar wavelengths, this is the dominant

scattering component from vegetation since the double bounce is strong. It can also play a significant role in the total backscatter from an urban area when the orientation angle is large, since the trunk-ground scattering is independent of the street orientation. The radar cross section for trunk-ground scattering is:

$$\sigma_{pqtg} = \begin{cases} 0 & p \neq q \\ R_{tp}^2 R_{gp}^2 \sigma_{cr} e^{-\alpha l_e} & p = q \end{cases} \quad \text{(Kolawole, 1991)} \tag{5.26}$$

where R_{tp} and R_{gp} are the Fresnel reflection coefficients for the tree trunk and ground respectively (for p polarisation), l_e is the mean wave path length, α is the attenuation factor of the wave through the canopy. σ_{cr} is the modified radar cross section of a dihedral corner reflector (Kolawole, 1991) and is calculated from:

$$\sigma_{cr}(\theta) = 8\pi r h_t^2 \sin^2\theta \lambda^{-1} \left|\sin(\pi a \sin\theta)\right|^2 \quad \text{(Kolawole, 1991)} \tag{5.27}$$

where r is the trunk radius, h_t is the trunk height, and $a = \left(0.5 r \lambda^{-1}\right)^{0.5}$, also;

$$l_e = 2R\sin(\theta/2) + h_t \sec\theta \quad \text{(Kolawole, 1991)} \tag{5.28}$$

where R is the radius of the canopy spread.

In order to find the total backscatter for a region sparse in trees in an urban area, the complete formula becomes:

$$\sigma_{tr}^{o} = \frac{N_t}{A_b}\left(\sigma_{ppcn} + \sigma_{pptg} e^{-2\alpha l_e}\right) \tag{5.29}$$

where N_t is the number of trees in the block and A_b is the area of the block.

5.5 Adapting Polarisation Signatures into the Model

A polarisation signature in an urban environment can be considered as having a combination of scattering mechanisms. In order to determine the final polarisation signature, the scattering matrix for each component needs to be determined.

As the previous sections have shown, the scattering components contributing to the final backscatter are:

double bounce from the front wall
double bounce from the side wall
single bounce from the front roof
single bounce from the back roof (when applicable)
double bounce from the trunk-ground
volume scattering from the canopy

All undefined parameters in the next section have already been defined in Section 5.2. A description of the Scattering matrix has been addressed in Chapter 3.

5.5.1 Scattering Matrix for the Front Wall

The front wall of the building contributes to double bounce scattering, resulting in the Scattering matrix:

$$S_{fw} = \begin{bmatrix} -R_{vw}R_{vg} & 0 \\ 0 & R_{hw}R_{hg} \end{bmatrix} \varpi_{fw} \tag{5.30}$$

where: $\varpi_{fw} = \sqrt{\sigma^{o}_{fw} / R^{2}_{pw}R^{2}_{pg}}$ (5.31)

and R_{pw} and R_{pg} are the Fresnel reflection coefficients described earlier. σ°_{fw} is the sum of the backscatter coefficients from the front wall of all the buildings. Note that σ°_{fw} is independent of polarisation once it is divided by $R_{pw}^2 R_{pg}^2$, hence ϖ_{fw} is also independent of polarisation. For example, if there were only two buildings, which are therefore of building types 1 and 2, then $\varpi_{fw} = (N\varpi_{fw1})^{0.5}$ since for the front wall $\varpi_{fw1}=\varpi_{fw2}$. N is the number of buildings and:

$\varpi_{fw1} = \left(\frac{16\pi}{\lambda^2} L^2 H^2 \sin^2\theta \cos^8\phi \, \mathrm{sinc}^2\left(k_o L \sin\theta \sin\phi\right)\right) \Big/ A_b$, where A_b is the total area of the block.

Note the assumption is made that the value for R_{pq} is positive. Even though this may not be the mathematical result, it is the theoretical definition.

5.5.2 Scattering Matrix for the Side Wall

The side wall of all the buildings in the block may contribute towards the radar return. Its Scattering matrix will be:

$$S_{sw} = \begin{bmatrix} -R_{vw}R_{vg} & 0 \\ 0 & R_{hw}R_{hg} \end{bmatrix} \varpi_{sw} \tag{5.32}$$

which is very similar to the front wall, and:

$$\varpi_{sw} = \sqrt{\sigma^o_{sw} \Big/ R_{pw}^2 R_{pg}^2} \tag{5.33}$$

If there were only two buildings (ie., types 1 and 2), the backscatter from each is not necessarily equal, and the simplification made for the front wall, ϖ_{fw}, cannot be used for ϖ_{sw}. For example, in the situation where $x/\tan\theta<b$ and $x/\sin\phi<H\tan\theta$ (refer to Building 2 in Section 5.3.1 for parameter definitions), then:

$$\sqrt{\sigma_{sw}^{o} / R_{pw}^{2} R_{pg}^{2}} = \varpi_{sw1} + \varpi_{sw2}$$

where:

$$\varpi_{sw1} = \frac{16\pi}{\lambda^2} b^2 \left(H + H_r/2\right)^2 \sin^2\theta \cos^8\phi_{sw} \, sinc^2\left(k_o b \sin\theta \sin\phi_{sw}\right) / A_b \text{ and:}$$

$$\varpi_{sw2} = \left(\frac{16\pi}{\lambda^2} \zeta \sin^2\theta \cos^8\phi_{sw}\right) / A_b \text{ where } \zeta = b_f^2 \left(H + H_r/2\right)^2 sinc^2\left(k_o b_f \sin\theta \sin\phi_{sw}\right)$$

(refer to Section 5.2 for the derivation of these equations, and definitions of terms).

These examples, showing the method for calculating ϖ for both the front wall and side wall of two buildings, can simply be adapted to many buildings by following the same methodology.

5.5.3 Scattering Matrix for the Front Roof

The backscatter from the front roof is a single bounce response. It has a Scattering matrix:

$$S_{fr} = \begin{bmatrix} R_{vr} & 0 \\ 0 & R_{hr} \end{bmatrix} \varpi_{fr} \tag{5.34}$$

where R_{vr} and R_{hr} are the vertical and horizontal Fresnel reflection coefficients for the roof, and:

$$\varpi_{fr} = \sqrt{\sigma_{fr}^{o} / R_{pr}^{2}} \tag{5.35}$$

where σ_{fr} is the total backscatter from the front roof of all the buildings in the block. Since the return from the roof does not suffer interference from surrounding buildings, then $\varpi_{fr} = (N\varpi_{fr1})^{0.5}$ where N is the number of buildings in the block and:

$$\varpi_{fr1} = \left(\frac{4\pi}{\lambda^2} \left(\frac{Lb}{2\cos\gamma} \right)^2 \cos^2\theta_{fr} \, \mathrm{sinc}^2(f) \mathrm{sinc}^2(g) \right) \Big/ A_b \tag{5.36}$$

where *f* and *g* are defined from Equation 5.7.

5.5.4 Scattering Matrix for the Back Roof

The backscatter from the back roof is also single bounce, although it only contributes when the look angle is smaller than the roof slope, ie., $\theta \leq \gamma$. The Scattering matrix is:

$$S_{br} = \begin{bmatrix} R_{vr} & 0 \\ 0 & R_{hr} \end{bmatrix} \varpi_{br} \tag{5.37}$$

$$\text{where: } \varpi_{br} = \sqrt{\sigma^o_{br} / R^2_{pr}} \tag{5.38}$$

and σ°_{br} is the total backscatter coefficient from the back roof of all the buildings in the block. As for the front roof, if there are *N* buildings then $\varpi_{br} = (N\varpi_{br1})^{0.5}$ where;

$$\varpi_{br1} = \left(\frac{4\pi}{\lambda^2} \left(\frac{Lb}{2\cos\gamma} \right)^2 \cos^2\theta_{br} \, \mathrm{sinc}^2(d) \mathrm{sinc}^2(e) \right) \Big/ A_b \tag{5.39}$$

where *d* and *e* are defined from Equation 5.10.

5.5.5 Scattering Matrix for the Tree Trunk

There will also be double bounce from tree trunks in residential areas. The Scattering matrix is:

$$S_{tg} = \begin{bmatrix} -R_{vt}R_{vg} & 0 \\ 0 & R_{ht}R_{hg} \end{bmatrix} \varpi_{tg} \tag{5.40}$$

$$\text{where } \varpi_{tg} = \sqrt{\sigma^{o}_{tg} / R^{2}_{pt} R^{2}_{pg}} \tag{5.41}$$

and R_{pt} is the Fresnel reflection coefficient for the tree trunk. From Section 5.4 it can be seen that:

$\varpi_{tg} = \sqrt{N_t \sigma_{cr} e^{-2\alpha l_e} / A_b}$, where N_t is the number of trees in the block.

5.5.6 Scattering Matrix for the Tree Canopy

Radar's interaction in the tree canopy will cause some volume scattering. Since the model used assumes that the vegetation is uniformly distributed and the leaves are randomly orientated, then the further assumption is made that the cross-polarised response is half the value of the co-polarised response. (This is discussed below). Therefore there are two scattering matrices:

$$S_{cnco} = \begin{bmatrix} 1 & 0 \\ 0 & 1 \end{bmatrix} \varpi_{cn} \text{ and } S_{cnx} = \begin{bmatrix} 0 & 1 \\ 1 & 0 \end{bmatrix} \varpi_{cn} / 2 \tag{5.42}$$

$$\text{where } \varpi_{cn} = \sqrt{N_t \sigma_{pqcn} / A_b} \tag{5.43}$$

σ_{pqcn} has been defined in Section 5.4 in the backscatter from the canopy.

The reason that the cross scattering was chosen to be half of the co-polarised matrix is because the leaves are not perfectly spherical. When scattering takes place from a large number of randomly oriented objects (eg., leaves), and when multiple scattering occurs, the probability of sizeable energy in the cross-polarised plane is high (Richards *et al.*, 1994). Freeman & Durden (1992) have modelled volume scattering from very thin cylinder-like scatterers, and through

some simplifications have found that $\langle |S_{hv}|^2 \rangle$ is a third of the co-polarisations, (ie., $\langle |S_{hh}|^2 \rangle$ and $\langle |S_{vv}|^2 \rangle$). Since the model used in this research is not assuming thin cylindrical scatterers, there will be more surface for scattering and S_{hv} will be closer to the co-polarisation response. Hence a value of half that of the co-polarisation for S_{hv} is deemed appropriate. As will be shown in Chapter 7, this value is not critical in the classification process since its effect on the total power, polarisation index, and polarisation phase difference is negligible, even when varied by many units.

5.5.7 Total Mueller Matrix

The Scattering matrix of each scattering component is converted into a Mueller matrix (as shown in Section 3.4.2) enabling the total Mueller matrix, ℓ_{tot}, to be used to calculate the final polarisation signature. ℓ_{tot} is the addition of all the Mueller matrices, giving:

$$\ell_{tot} = \ell_{fw} + \ell_{sw} + \ell_{fr} + \ell_{br} + \ell_{tg} + \ell_{cn} \tag{5.44}$$

where ℓ_{fw}, ℓ_{sw}, ℓ_{fr}, ℓ_{br}, ℓ_{tg}, and ℓ_{cn} are the Mueller matrices for the front wall, side wall, front roof, back roof, trunk-ground, and canopy respectively.

Note that the backscatter from the road has not been included in this model. This is because the road is a smooth, specular surface, so for look angles above 30° the response is too small to consider. This has been justified by originally including road backscatter in the model, and finding no change in total radar return when it was omitted. However, the increase in block area due to surrounding roads needs to be considered. This increase in ground area of a building block, without contribution to backscatter, will reduce the scattering coefficient.

5.6 Introduction of Polarisation Index and Polarisation Phase Difference

The polarisation index (PI) and polarisation phase difference (PPD) are used to provide additional information to assist in determining the landuse characteristics. The polarisation index (PI) and polarisation phase difference (PPD) can be defined in terms of the Fresnel reflection coefficients, giving:

$$PI \approx \left| R_{h1}(\pi/2-\theta)R_{h2}(\theta) / R_{v1}(\pi/2-\theta)R_{v2}(\theta) \right|^2 \quad \text{(Dong } et\ al.\text{, 1997b)} \qquad (5.45)$$

and:

$$PPD \approx Arg\left\{ - R_{h1}(\pi/2-\theta)R_{h2}(\theta) / R_{v1}(\pi/2-\theta)R_{v2}(\theta) \right\} \quad \text{(Dong } et\ al.\text{, 1997b)} \quad (5.46)$$

where R_{h1}, R_{h2}, R_{v1}, and R_{v2} are the horizontal and vertical reflection coefficients for surfaces 1 and 2. For a perfectly conducting material PI=1 and PPD=180° for a double bounce independent of incidence angle. For a trunk-ground structure, however, PI is about 4~6 and PPD is around 140~160° (Dong *et al.*, 1997b). The negative value given in the numerator of the PPD is dependent on the definitions of horizontal and vertical directions. This is explained in greater detail in Chapter 8.

Unless a target is non-symmetric in the azimuth plane, its backscattering properties should be identical for HH and VV polarisation at normal incidence. Hence, the PPD is expected to be close to 0° at and near normal incidence for most distributed targets (Ulaby *et al.*, 1987).

The benefits of using the polarisation index and phase difference as an additional source of information for urban analysis has only recently been recognised. Most research to date has concentrated upon vegetation applications.

Seifert *et al.* (1996) have examined the phase difference from a variety of bands and different seasons from Beech and Spruce for change monitoring.

The phase difference is dependent on the wavelength since the scattering mechanisms are different. The C-band phase difference responses are closer to 0° than for L-band, indicating more odd bounce.

Ulaby *et al.* (1987) analysed the polarisation phase difference of agricultural corn fields with respect to bare soil surfaces. The results showed that the bare soil gave a phase difference close to 0° while the scattering from the corn fields gave a phase difference ranging from 15 to 35°. The PPD from the corn canopies was attributed to a combination of bistatic reflection by the vertical stalks, and propagation delay between the horizontal and vertical polarised waves as they travelled through the canopy to the ground and back (Ulaby *et al.*, 1987).

In terms of urban applications, Dong *et al.* (1996) have undertaken some research on the polarisation index and polarisation phase difference. Four urban areas were examined, consisting of one commercial class having an orientation angle less than 10°, and three residential regions, having orientation angles of less than 10°, random distribution, and 40-45° respectively. It was found that the polarisation index varied with respect to wavelength for the commercial area, but remained similar for the residential areas. For the commercial and residential class having the smaller orientation angle, the phase difference was around 160° for both classes for all wavelengths. This value decreased for the other two classes.

5.7 Summary

An urban model must consider all the single bounce, double bounce, and volume scattering mechanisms present in an urban environment. Not only will the building components provide radar return, but the surrounding vegetation will also contribute. This chapter has presented all the computations necessary to determine the backscatter from a model block of buildings. In order to

visualise how all the formulae relate to each other, a flow chart is presented in Chapter 6 (after a few more necessary terms have been defined).

For these formulae to be used, the actual parameter values need to be estimated. Chapter 6 is devoted to solving this problem, and providing input vital for the model's function.

6. THE MODEL PARAMETERS FOR THEORETICAL BACKSCATTER

6.1 Introduction

Many authors (eg., Henderson & Anuta, 1980, Henderson, 1995 and Bryan, 1975) have found that the interpretability of an urban scene is dependent upon such factors as "terrain height, soil characteristics, types of land use, vegetation, density of houses, roof type, house construction material, and settlement type" (Xia & Henderson, 1997, p96). This introduces the complexities which need to be overcome to model an urban environment.

Backscatter in urban areas, however is most likely to be dominated by single bounce from roofs, double bounce from wall-ground structures, and "other metallic constituents such as water pipes, window frames, etc" (Dong *et al.*, 1997a, p1356). This helps to simplify the situation by addressing only the important components.

In order to form a simulation of an urban environment, many parameter estimations, including some of those mentioned above, need to be made. These estimates need to represent a typical urban area. However, a typical urban area does not exist in the real world. The street layout, building sizes and shapes, landscaping and other class characteristics vary between suburbs, cities, and countries. For a model simulation restricted to one city, average estimates can be made representing class parameters. This is because enough common characteristics exist enabling some approximations to be made for each land use.

This chapter presents all the parameters necessary to determine the theoretical backscatter and polarisation characteristics for the residential and commercial classes for the city of Sydney. It is divided into three main sections: the first

determines the class parameters for residential land use; section two defines the necessary characteristics of the commercial class, concentrating on the CBD's; the final section defines the necessary formulae and methods common to both classes used for determining some of the parameters.

Some of the methods used to determine the average characteristics of a class may appear to be a very simplified approach. However, the model was formulated to make a complex problem, ie., modelling the urban environment, as simple as possible. This was to prevent calculations becoming too computationally intense, and to maintain some flexibility in the model to enable it to be applied to different situations.

This study concentrates on L-band wavelength. L-band was chosen because it is the middle wavelength for AirSAR data, and generally represents the average response of the three wavelengths (C-, L- and P-band). As Chapter 7 will demonstrate, there is little change between the radar response from real data for different wavelengths. Although the magnitude of the backscatter varies between the C-, L- and P-band wavelengths, there appears to be little change in the shape of the polarisation signature between these bands for most of the situations. Furthermore the model parameters (presented here in this chapter) have a minimal change when determined for wavelengths other than L-band (as will be examined in Chapter 7).

In order to model the backscatter in an urban environment a number of parameters need to be considered. Some of these are very sensitive to the backscatter while others have negligible effects. The radar parameters which need addressing in the model are the wavelength, the look angle and look direction. The look angle is then related to the incident angle, ie., the angle at which the radar contacts the surface. The look direction is also related to the buildings orientation so is considered as a building parameter. The building parameters are: building walls and roof absolute orientation; building length, width, and height; spacing between buildings; roughness of building materials and ground; building and ground dielectric constant; roof slope (ie., defined as

"γ" in Chapter 5); the metal factor (introduced in Section 6.5.2); and for residential buildings, the number of trees and their dielectric constant.

It is worth noting that the polarisation is also a radar parameter. However, this is an output response from the model, and is therefore discussed in detail in Chapter 7.

This chapter begins with an investigation into the sensitivity of building and vegetation parameters, and their influence on the total backscatter from a building block. An estimation of relevant parameters are then determined for both residential and commercial land uses. A further discussion on parameters requiring extra attention is then addressed.

6.2 Sensitivity of Model Parameters

The model parameters were initially estimated to be placed in the model to calculate the total backscatter for the building block. A quasi-iterative approach was used. Many of these initial estimates also became the final parameters. (Their derivations are presented in the proceeding sections of this chapter). The parameters were varied one at a time to test which parameters had a large influence on the total backscatter from a block of buildings. A residential block was used as it also includes vegetation characteristics, unlike commercial blocks. An initial estimate of residential building parameters are:

Dielectric constant for the wall, roof, and ground respectively:	ε_w=3.4+0.1i, ε_r=3.4+0.1i, ε_g=8+2i
Building dimensions:	L=20m, b=10m, H=6.7m
Roughness of the wall, roof and ground respectively (*rms**):	rms_w=0.002m, rms_r=0.005, rms_g=0.015m
Spacing between the building's columns and rows:	x=3.5m, y=20m

Number of columns and rows	*cr*=9 (see Section 6.3.1.2)
Number of trees, trunk radius, trunk height, trunk dielectric constant, and canopy spread:	N_t=80, r_t=0.25m, H_t=7m, ε_t=15+5i, R=7.5m
Canopy parameters:	α=0.0023, ρ=0.023
The Metal Factor:	L_p=0.35 (see in Section 6.5.2.1)
Roof slope:	γ=30°

* root mean square

(All symbols not defined here have been defined in Chapter 5, or in the Glossary)

To determine which parameters are more sensitive to the final theoretical backscatter, and hence require more attention when estimating, each parameter has been varied by a small amount from its final estimated value (given above) to observe its effect on the total radar backscatter for a block of buildings. While this one parameter is varied, the others remain constant and are the values presented above. Some parameters are much more sensitive than others.

This section is not designed to cover every possible aspect relating to parameter sensitivity on the total backscatter for a block of buildings. Its aim is to give a general idea as to which parameter estimations are important. While one parameter is varied, the other parameters remain as the final estimated values, unless stated otherwise. L-band is the adopted wavelength for all variations given below.

Oscillations of the total backscatter from a building block occur due to the constructive and destructive interference from the wave at the extremes of the object (see Figure 7.1 for an example). The minimums can be quite extreme, but the backscatter is smoothed (ie., averaged) to reduce the magnitude of these oscillations since such a situation would not be expected to occur in the

real data. The reason for this is because there are always some diffuse and/or multiple bounce effects occurring in real data such that any minimums remain disguised. Another reason is, in order to reduce speckle, the pixel's are averaged, so the backscatter is the average over a number of pixel's.

As Table 6.1 shows, some parameters have a much greater influence on the total backscatter from a building block than others. It must be noted that a look angle of 45° was used for most tests because this is the median value on an AirSAR image (which will be used as a case study in Chapters 7 and 8). The orientation angle was deliberately kept small, unless the situation required a larger value to demonstrate a point, to highlight the sensitive parameters due to a strong return.

The height *(H)* of the building is a reasonably sensitive parameter to backscatter because an increase in height, and therefore the wall size, increases the backscatter from the front wall, without increasing the area of the block. Hence, the backscatter coefficient increases. An increase in the length of the front wall *(L)* has a similar but smaller effect.

A decrease in backscatter results when the side wall (*b*) is increased. This occurs due to the side wall contributing little radar return when the orientation angle ϕ is less than 45° (as assumed in this model). Therefore the area of the block increases, but the backscatter strength doesn't, reducing the scattering coefficient.

The spacing between the buildings (*x* and *y*) will influence the backscatter because an increase in the area of the block will reduce the backscatter coefficient unless the radar return also increases. The change is noticeable but not large. Distance between the rows (*y*) could vary with location in a real situation due to its dependence on the size of the rear open space. The spacing between the columns (*x*) would not be large since buildings are reasonably close to allow more buildings along a street frontage.

Table 6.1. Demonstration of the sensitivity of parameters on the total backscatter from a block of buildings. The 'parameters' are represented by their symbols (defined in Chapter 5, and earlier in this chapter). The 'change' indicates by how much the parameter was varied by (either + or -) to determine its influence in the total backscatter for a particular look (θ) and orientation (ϕ) angle. (Units are indicated where applicable). The final column represents the change in total backscatter from a building block, due to this change in parameter. The backscatter is recorded in dB's, and the (+) or (-) indicates whether it increased or decreased.

Parameter	Change	$\theta°$	$\phi°$	$\Delta\sigma_{tot}$ (dB's)
H	+1m	45	0	(+) 1.2
b	+2m	45	0	(-) 0.2
L	+2m	45	0	(+) 0.9
x	+2m	45	0	(-) 0.5
y	+2m	45	0	(-) 0.2
rms_w	+0.005m	45	0	(-) 0.3
ε_w (real)	+1	45	0	(+) 1.3
ε_w (imag)	+1	45	0	(+) 0.5
ε_w (real)	+1	45	10	(+) 0.5
ε_w (imag)	+1	45	10	(+) 0.2
γ	+5°	45	0	(+) 0.0
γ	+1°	30	0	(-) 8.0
γ	+1°	30	10	(-) 1.0
N_t	+20	45	0	(+) 0.0
H_t	+2m	45	0	(+) 0.0
R	1m	45	0	(+) 0.0
r_t	0.1m	45	0	(+) 0.0
N_t	+20	45	20	(+) 1.0
H_t	+2m	45	20	(+) 1.0
R	1m	45	20	(+) 1.0
r_t	0.1m	45	20	(+) 0.5

A change of only 1cm (*rms* of 0.005m) in the wall roughness, will change the backscatter by 0.3dB's. Even though this change is not large, the roughness may have an influence when difficulties arise in estimating their *rms*.

It is worth noting that although the surface roughness is a general term, the roughness spoken of here and in the remainder of this chapter refers to the distance between the surface's minimum and maximum roughness points. In the model, the roughness is accounted for through the *rms* of the surface. The *rms* is the deviation of the surface from the mean. The *rms* of a surface is therefore half the width of the roughness.

The dielectric constant appears to be a reasonably sensitive parameter. When the real component of the dielectric constant is varied by one unit, the change in backscatter is over 1dB. The imaginary component is less sensitive. However, this change will not be as important when the orientation angle is not normal to the buildings. This fact is demonstrated when the orientation is 10° and the sensitivity of the real and imaginary components reduces to 0.5 and 0.2dB's respectively.

The slope of the roof is an important parameter only when the look angle is close to the roof slope, and hence the radar direction is normal to the roof facet. There is no change in backscatter when the roof slope is varied, even by as much as 5°, for a look angle not equal to the roof slope. If the look angle is around 30° and the roof slope (30°) is varied by only 1°, the change in radar return is 8dB's, which is substantial. However, this is only when the orientation angle is 0°. Once this angle increases, the influence of roof slope on radar intensity dramatically reduces.

Table 6.1 also shows that the influence the tree parameters have on the total backscatter is dependent on orientation angle. The reason for this is due to strong double and single bounce effects from the building facets for small orientation angles. If the orientation is increased to 20°, then the sensitivity of

tree parameters on the radar return is significant. This effect is around 1dB when: the number of trees in a residential block increases by 20; the tree height is increased by 2m; or the radius of the canopy spread increases by 1m. There is an increase in backscatter of 0.5dB's when the trunk radius is increased by 0.1m.

6.3 Parameter Estimation

Since the parameters discussed above vary from building to building, and block to block, the average values are determined for the model, and their expected range is given where appropriate. Each parameter is examined to find an average estimate. Some very general assumptions are made as, due to the complexity of an urban environment, this was the only plausible solution without becoming too detailed. All the parameter estimates given in this section, apart from the dielectric constants, have been measured through personal observations of the area, and aerial photographs.

There is only limited information about the dielectric constant of building materials, soil and vegetation. Since the backscatter is not very sensitive to changes in the dielectric constant by one or two units, an approximate estimate of the values is acceptable for this purpose. Values for the dielectric constant measured for a variety of materials from different sources will be used to obtain a realistic value for the model. This information is presented in Appendix B.

6.3.1 Estimation of Residential Parameters

Estimation of residential parameters need to be determined to represent the theoretical backscatter from a typical residential area along the east coast of Sydney. Naturally, residential class characteristics will vary depending on location. For example, some of the high income suburbs will generally have more vegetation and larger single dwelling buildings. However, apart from the

outskirts of the city, where building density substantially reduces, these parameters are reasonably consistent for the whole city.

Figure 6.1 shows some photographs of typical residential buildings found along the east coast of Sydney. Note that many have surrounding parked cars, which will affect the backscatter, but have not been modelled in this research.

6.3.1.1 Building Dimensions

Residential areas in the subject region consist of houses and apartment blocks with scattered vegetation. Building dimensions are held constant since the building sizes appear reasonably homogeneous, and the average building size per block is not expected to vary greatly from one residential suburb to the next. From measurements of the aerial photograph, the average width of the buildings are around 10m (for both houses and apartments). The average length of a house is around 15m and for an apartment is 25m.

The orientation angle of the street with respect to the radar is calculated such that $\phi \leq 45°$. Hence, for some orientation angles, the longer side of the building is parallel to the street (where $\phi \leq 45°$) and providing the dominant corner reflection, for other angles it is the short side of the building. This can result in noticeable differences in radar return. For computational purposes, the buildings are modelled as square, so houses are 12.2*12.2m, and apartments are 15.8*15.8m. The average ratio of houses to apartments in a block appears to vary from about 30:70 up to 70:30 (from examination of the photographs and field observations). Using this to obtain an average building size per block gives a range from 0.7*(12.2)+0.3*(15.8)=13.2m up to 0.3*(12.2)+0.7(15.8)= 14.7m. The average building size becomes (13.2+14.7)/2=13.9m for both length *(L)* and width *(b)*.

The height of a single building is around 2.75m and an average apartment block with 3 storeys is 10.7m (Mann, 1989) . The building height will therefore

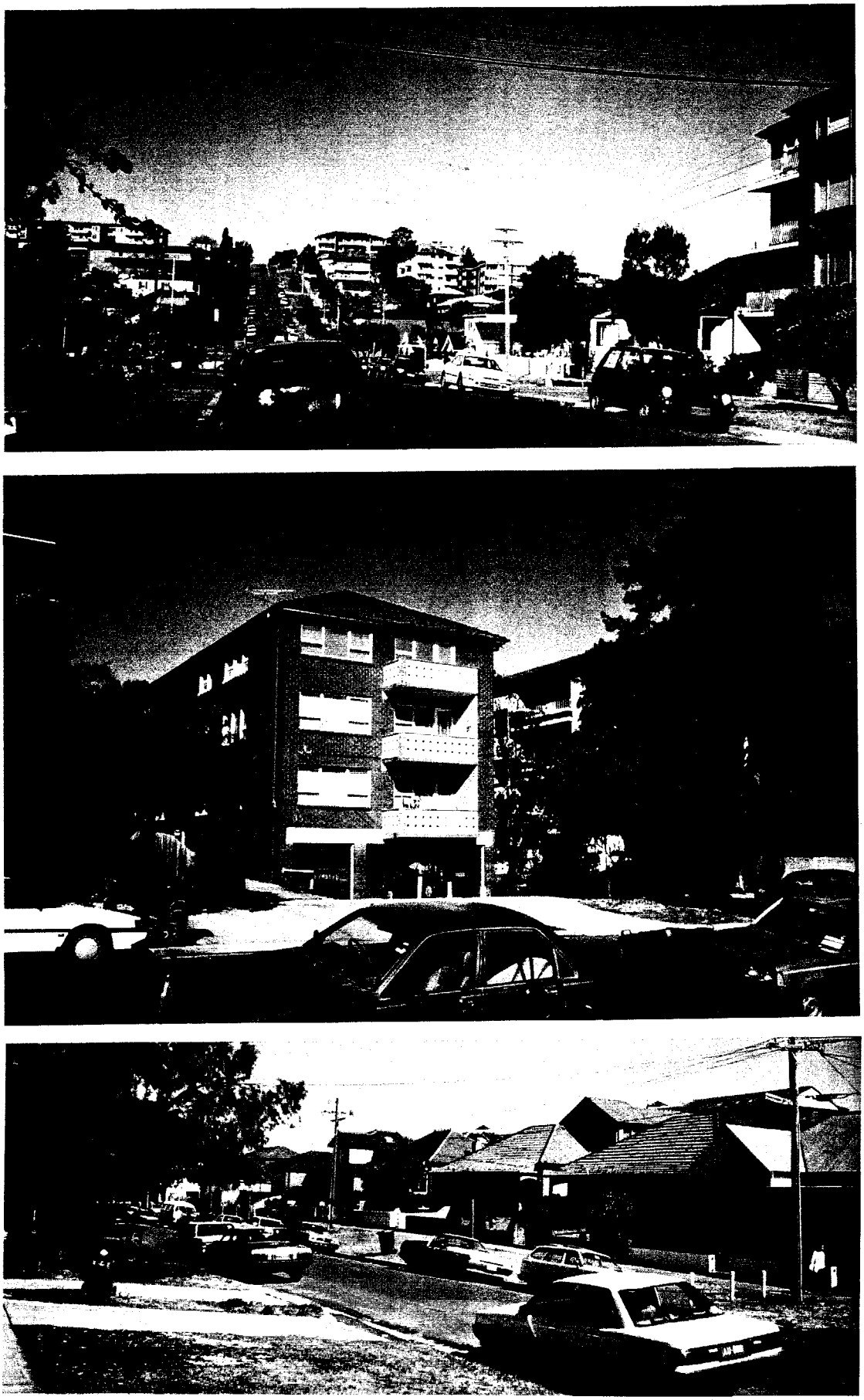

Figure 6.1 Photographs of some typical residential buildings found in the Eastern suburbs of Sydney.

range from 0.7*(2.75)+0.3*(10.7)=5.1m up to 0.3*(2.75)+0.7*(10.7)=8.3m. The average building height *(H)* is (5.1+8.3)/2=6.7m. However some blocks are purely houses and others consist only of apartment blocks.

6.3.1.2 Building Layout

The spacing between buildings is an important factor. The larger the distance between the buildings, the smaller the backscatter coefficient will be since the area of the block has increased while the radar return has not. The spacing between the buildings is often a function of income. Higher socio-economic areas are more spacious with larger individual blocks of land.

The average distance between two buildings facing the street (ie., parameter *x* in the model) appears to give an average range from 2m up to about 5m (to allow for driveways). The average distance between two buildings fronting opposite streets (ie., parameter *y*) varies from 14m up to 25m. Once again due to the irregularities in estimating whether the longer spacing is closest to facing the radar or not, the distance between the buildings will be averaged to give a square value. Hence, the spacing ranges from (14+2)/2=8m, up to (5+25)/2=15m, for both *x* and *y* since they will be considered even.

A single residential building block is usually oblong in shape enabling street frontage for all buildings and avoiding inefficient use of the land. However, an average extended block is frequently close to square in shape, often due to a small lane passing through the middle. These extended blocks are much easier to identify on the aerial photograph because the thin middle lane is disguised through vegetation and building shadow. In order to have a square shaped block (ie., two single blocks divided by a thin lane), approximately 12 columns by 4 rows of buildings form a square. This gives a street length around 225m (from measurements on the aerial photograph). If the model is going to consider an average building size of 13.9m*13.9m (determined in Section 6.3.1.1), and an average spacing of (8.5+15)/2=12m, the number of buildings in the street giving a block of length 225m is determined by $14cr+12(cr-1)=225$m

(where *cr* is the number of buildings in the column/row), giving *cr*=9 buildings. An illustration of a model block, along with an aerial representation of a real block are shown in Figures 6.2 and 6.3 respectively.

Allowance for the spacing between building blocks due to the roads need consideration. As is the case for the distance between buildings, the spacing between building blocks will expand the urban area without increasing the theoretical backscatter. To integrate this factor into the model, the area of the building block is increased by 10% (an estimate measured from the aerial photographs).

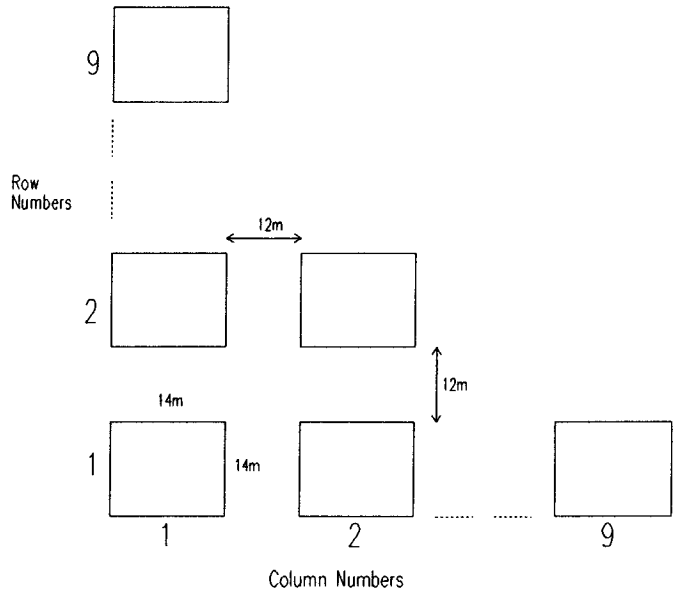

Figure 6.2. Diagrammatic representation of an average block of residential buildings, used in the model.

6.3.1.3 Roughness

The roughness of the building wall, roof, and the ground are sensitive factors for the backscatter. For a residential building the roughness of a **wall** is difficult to model since, for example, a brick is smooth but the wall is not due to cement

Figure 6.3. Aerial photograph of an urban block demonstrating their average size and shapes. There are approximately 12 columns and 4 rows of buildings forming an extended block.

connecting the bricks. Furthermore the appearance of a wall's roughness on a radar image is related to the wavelength. The roughness of a cement rendered wall can vary depending on aesthetic preferences. Windows form indentations in the wall, but the glass is very smooth. However, the indentations are not considered to be part of the wall roughness, instead this shape will lead to a comparatively small reflection due to the size of the total corner reflection of the building wall.

In the subject region most of the buildings are clad in brick rather than cement rendering. The indentation of the cement from the brick face, used to hold the bricks in place, was measured to range from about 0.5cm to 0.8cm. If glass forms about 30% of the wall and is smooth (a roughness of 0.0cm is assumed for this purpose), then the roughness of a residential building wall ranges from 0.3(0)+0.7(0.005)=0.0035m to 0.3(0)+0.7(0.008)=0.0056m giving an average *rms* of 0.002m (or an *rms* range of around 0.0015m to 0.0028m).

Most of the building **roofs** in the subject area are tiled. The tiles themselves are irregular in shape, and their placement on the roof causes a large roughness.

However, their surface is relatively smooth. Most of the tiles are of a standard size, with a thickness ranging from about 1cm in the middle to 2cm on the edges, which connect to adjacent tiles. This 2cm roughness is not continuous, it only occurs along the boundary of the tiles, so a 1cm value will be adopted as the roof roughness. The roof roughness is not a vital factor unless the look angle is the same as the roof slope, and the orientation angle is low.

The roughness of the **ground** surrounding the buildings will vary depending on whether there is grass (and if it is mown of not) or concrete. Through personal observation it appears that 70% of the area is grass, and 30% is concrete (which is realistic considering surrounding open spaces are often grass). The roughness of grass varies from around 3cm up to 6cm, however concrete is smooth (an estimate of 0.002m will be used), resulting in a ground roughness ranging from 0.7*3+0.3*0.2=2.1cm up to 0.7*6+0.3*0.2=4.3cm. Hence the average ground roughness is 3cm (or an *rms* of 1.5cm).

6.3.1.4 Dielectric Constant

A residential building's **wall** will be considered to consist of either brick or cement rendering, and glass. In the areas studied these were the dominant materials used for cladding. Brick is a reasonably dry material made of baked or dry clay so will have a similar dielectric constant to dry soil. The imaginary component is related to how quickly the energy is lost in the material. In brick, the penetration depth would be reasonably high, because ε_i is low. Therefore the dielectric constant of dry soil will be adopted to represent brick, ie., 3.4+0.1i (from Ulaby *et al.,* 1981). Note that any further references to dielectric constants are discussed in Appendix B.

Glass has a real component of the dielectric constant of ε_r=4-7 (Weast, 1986). (No imaginary components of the dielectric constant were available for glass). It is expected that the imaginary component is higher than dry soil, but no greater than moist soil (such as those recorded by Dong (1995b) of around 2.1i

to 3.5i). An imaginary component of 1 for glass seems appropriate. As mentioned earlier, its accuracy is not vital since a change of one unit in the imaginary component for a building wall leads to a change in backscatter of only 0.2 dB's. The dielectric constant range for a building wall, from which windows form about 30% of the building facade, is around 0.7*(3.4+0.1i)+0.3*(4+1i)=3.6+0.4i up to 0.7*(3.4+0.1i)+0.3*(7+1i)=4.5+0.4i. Hence the average dielectric constant is 4.0+0.4i. However, this is without any consideration of hidden metals.

Metals are also found in building walls, increasing the dielectric constant due to the high conductivity of metal. It is well known that metals are good radar scatterers (Ulaby *et al.,* 1981). In a residential building, metal can be found in a variety of places, both internal and external. Piping for water and gas, gutters, aluminium framing, and objects for connecting building materials, are made of metal. For a more detailed analysis of metal in residential buildings, refer to Appendix C.

Using this information, a very general estimation can be made as to the average amount of metal per square metre in a residential building. This is for the purpose of determining the dielectric constant of the wall with metal considered. For computational purposes, the wall is assumed two dimensional rather than three, hence an area, rather than cubic volume, is used.

For simplicity, it will be assumed that all the metal is situated behind the exterior building cladding. As given above, the average dielectric constant of the wall is 4.0+0.4i. For a square metre of residential building wall, a reasonable estimate of $0.1m^2$ is made to represent the amount of metal included in this portion of wall. This includes consideration that some of the building frames are wooden and others are steel.

Note that all calculations, and symbols presented for calculating the dielectric constant of a building material with metal in it, are explained in detail in Section 6.5.1.

Most of the radar penetration resulting in scattering from metals, not on the building exterior, is going to occur through the brick. The thickness of a brick is approximately 0.1m. The dielectric constant of a brick was estimated earlier as 3.4+0.1i. For a 0.23m wavelength (L-band) the power would be $P(x)=P(0)*0.86$. For the radar to reach the metal, and then reflect back through the exterior wall, the power of the remaining radar will be $P_s=0.86*0.86=0.75$, or 75% of its original strength. The metal is assumed to be equivalent to a metal plate of $0.1m^2$, so the backscatter from the metal square is: $0.75*\sigma_{me}$ where the intensity $\sigma_{me}=0.00072$.

The reflection coefficient from the $1m^2$ of wall, without metal, is calculated using $\varepsilon_w=4.0+0.4i$ (presented at the beginning of Section 6.3.1.4) and an *rms* 0.002m (determined in Section 6.3.1.3) giving $R_h^2=0.20$ and $R_v^2=0.04$. The backscatter from the wall (without metal) is $\sigma_{ma}=0.013$ for horizontal polarisation and 0.003 for vertical polarisation.

The total intensity from the square metre of wall, including metal, becomes $\sigma_{tot}=0.014$ and 0.003 for horizontal and vertical polarisation respectively, giving the reflection coefficients $R_{hn}^2=0.21$, and $R_{vn}^2=0.05$. A dielectric constant of 4.5+0.5i gives $R_{hw}^2=0.23$ and $R_{vw}^2=0.05$ which is close to R_{hn}^2 and R_{vn}^2. Hence, the adopted dielectric constant for the wall (ε_w), including metal, is 4.5+0.5i. Any inaccuracies encountered in determining the dielectric constant will have minimal effect on the final backscatter because, for double bounce, the ground also has a reasonably low dielectric constant resulting in extra loss of radar energy.

It is acknowledged that this is a simplified method of determining the dielectric constant of a wall. However, it would be impossible to obtain a more accurate value without taking dielectric measurements, which was beyond the scope of this research. Only an approximate dielectric constant is required since the model is taking a complex problem and trying to simplify it into approximate

parameters. The insensitivity of the total backscatter to the dielectric constant means its accuracy is not a vital parameter.

Tile **roofs** generally consist of terracotta, having a low dielectric constant such as dry soil, hence a roof dielectric constant (ε_r) of 3.4+0.1i is also adopted. The metals contained in the roof ceiling and surrounds are considered later in the Metal Factor (Section 6.5.2.1). Some buildings in the study region have iron roofs, but these are in the minority.

The only time an iron roof will directly influence the radar return is when the look angle is normal to the roof, or in some cases due to Bragg scattering (see Section 7.4.3). In the situation where the radar is normal to the roof face, this surface would be equivalent to a large metal facet perpendicular to the radar. If the roof has an area of about 50m^2 then the backscatter from the roof would become $=\frac{4\pi 50^2}{\lambda^2}$ (from Equation 5.7), this value would then be divided by the roof area to give the scattering coefficient. In situations not exactly normal, the backscatter from an iron roof will reduce dramatically. For the purpose of this study, due to their limited numbers, iron roofs are not considered.

The **ground** surrounding residential buildings is usually a mixture of concrete and grass. Concrete is dry and hence would show similar characteristics to dry soil, ie., 3.4+0.1i. Even though some concrete is reinforced, any scattering from the metal will lead to specular reflection away from the sensor. Grass contains more moisture than the concrete since most lawns are green and well kept, so it can be considered to be similar to soils under eucalypts, ie., ranging from 9.1+2.1i to 11+3.5i (discussed in Appendix B). The proportion of grass to concrete is 70:30 (assumed in Section 6.3.1.3), resulting in a ground dielectric constant (ε_g) ranging from 0.7*(9.1+2.1i)+0.3(3.4+0.1i)=7.4+1.5i to 0.7*(11+3.5i)+0.3*(3.4+0.1i)=8.7+2.5i.

6.3.1.5 Roof Slope

The roof slope can be a sensitive factor, however, due to the small variations in building design it is difficult to estimate to better than 5°. Dong *et al.* (1997a) define residential buildings in the city of Sydney to have roofs tilted about 25-35° from the horizontal. It would be illogical to use these values as an estimate for the range in roof slope for the model, due to its close relationship to look angle. For example, for a look angle of 25°, the roof slope would only be significant to the total backscatter if its slope was also 25°. Hence, the mid-value is adopted as the average roof slope giving 30°. This parameter is only critical for look angles with less than half a degree variation from 30°, and orientation angles close to 0°. Such a situation would occur infrequently in a real environment.

6.3.1.6 Vegetation Parameters

In an urban environment there is a large variety of vegetation, but the larger trees will give a higher radar return. In order to calculate the parameters for vegetation, average values for a middle age tree were chosen.

The vegetation parameters are estimated from Kolawole (1992) for a eucalypt at middle growth stage, as explained in Chapter 5. The gravimetric moisture was estimated to be around 0.497 (mg), enabling the attenuation coefficient α=0.0023 (Npm^{-1}) and volume scattering coefficient ρ=0.023 (m^{-1}) to be determined (Kolawole, 1992). This is for L-band wavelength only. For C-band, α=0.18 (Npm^{-1}) and ρ=2 (m^{-1}). No values were available for P-band (this matter is addressed in Section 7.5.1).

The number of trees in a block appear to vary from approximately half a tree up to one and a half trees per building. This is based on trees of substantial size in the aerial photographs, and does not consider small vegetation found in gardens. The remainder of the parameters will be held constant.

The average tree height obtained from Kolawole (1992) is 17.6m for white stringy bark. In Sydney a large proportion of trees are eucalypts, but they are not this tall. Through personal observation, the average height of a tree in a residential area is similar to the height of a three storey block of apartments, ie., 10.7m. The height of the trunk and primary branches falls between half and three quarters of the tree height. There are also many smaller trees, or shrub-like plants, in an urban area contributing a small amount to the total double bounce, hence a trunk height (h_t) of 7m is adopted.

Measurements taken from trees in the suburb of Kensington, Sydney, show an average trunk radius for the trees in the area to be around 0.25m. The canopy is difficult to estimate. However, since the backscatter is not very sensitive to this parameter, its magnitude is not critical. From the aerial photograph, the canopy measures an average diameter around 15m, giving a 7.5m radius. This measurement also includes smaller trees and shrub-like plants surrounding the larger trees, since individual outlines and heights are indistinguishable on the photograph. However, the canopy of smaller vegetation will contribute to the backscatter, hence its inclusion is justified.

The dielectric constant of the tree trunk also needs to be determined. The dielectric constant of the leaf and twigs for native eucalypts has been given as 9.4+4.4i from Dong (1995b). Different estimates for the dielectric constant of tree trunks have been given in the literature. The dielectric constant does vary between tree species, however, and urban areas do have a large variety. Some of the dielectric constants in the literature, estimated for tree trunks from different species, are: 4.0+2.0i for L-band (Richards *et al.,* 1987); 10.0+1.0i for L-band (Wang & Mo, 1990), 20.7+10i for P-band, 17.5+5.9i for L-band, and 14.4+4.7i for C-band (Chauhan *et al.,* 1991); 20.0+4.0i (P-band), 20.5+5.0i (L-band), 22.5+7.5i (C-band) (Sun *et al.*, 1991); and 30+10i for L-band (Wang *et al.,* 1993). Hence, using this information as a guide to estimating an appropriate dielectric constant for L-band, an average value of 15+5i will be used.

There is little information for determining an accurate estimate of the tree trunk dielectric constant for P- and C-band. The two examples of P-band given, are equal to (Sun *et al.,* 1991) or higher than (an increase in ε_r of only 2.5) (Chauhan *et al.,* 1991) the dielectric constant of L-band. For C-band, one example is higher than the equivalent L-band (Sun *et al.,* 1991), and the other is lower (Chauhan *et al.,* 1991). Hence, the dielectric constant for P- and C-band will also be adopted as 15+5i.

As the above literature shows (ie., Chauhan *et al.* (1991) and Sun *et al.* (1991)), the dielectric constant for the tree trunk is dependent, to a certain degree, on wavelength. By how much it varies is dependent on the tree type and also on how the dielectric constant was determined. If the dielectric constant for L-band is used in the model for P- and C-band, this may cause inaccuracies in the final backscatter. The extent of this affect is addressed in Chapter 7.

6.3.2 Estimation of Commercial Parameters

Commercial buildings considered here are primarily from CBD's. They are generally tall and densely spaced, with a high portion of metal forming their structures, and even some cladding. However, even shopping centres, though not as tall, are still dense and contain a high percentage of metal.

Figure 6.4 shows some photographs of commercial buildings.

6.3.2.1 Building Dimensions

Commercial buildings are taller, more densely spaced, and wider than residential buildings so will have different parameters from residential areas. According to observations of the aerial photograph, the average size of the commercial buildings range from about 25*25m up to about 45*45m. The buildings are of irregular shapes but the average appears to be square, or at

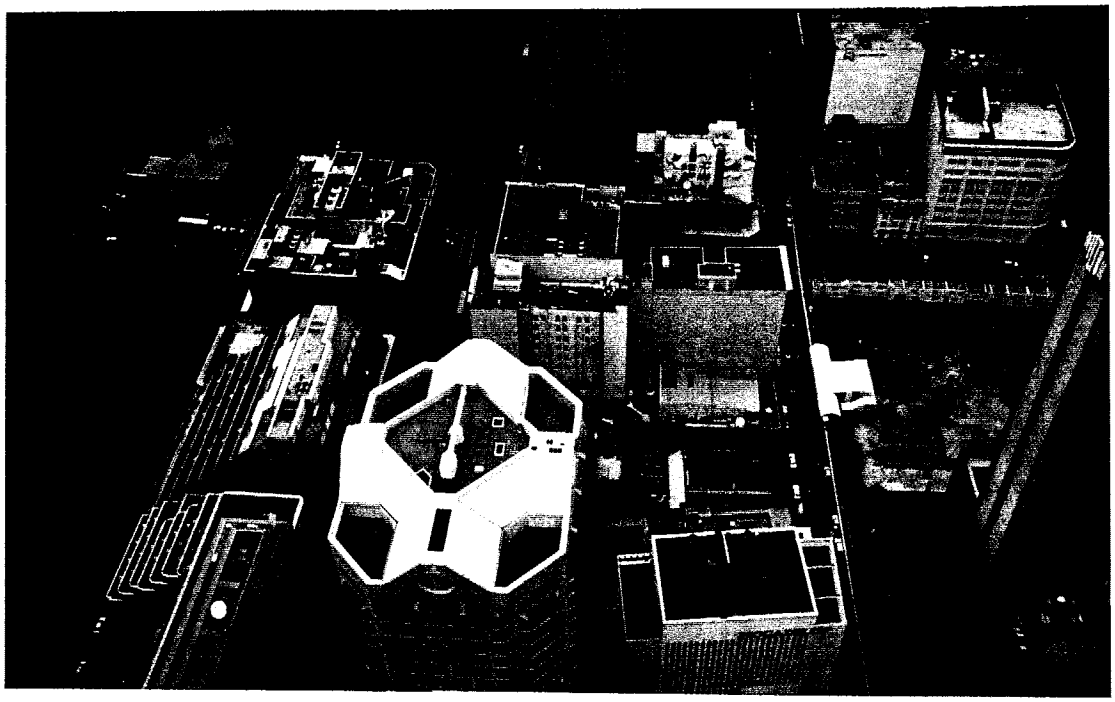

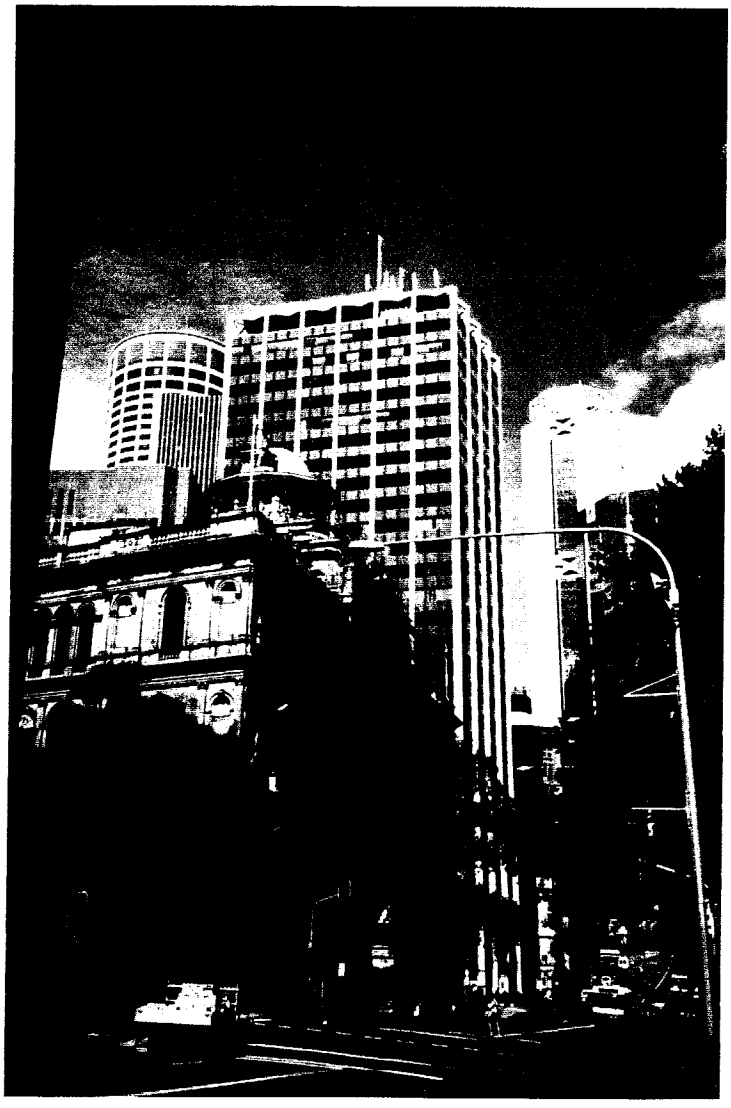

Figure 6.4. Photographs of commercial buildings found in the city of Sydney.

least rectangular. The average height of the buildings range from about 10 up to 50 storeys. Assuming there are 3.65m per storey (Mehta, 1978), the height ranges from 36 up to 182m. Some buildings in the city are taller, for example the MLC building has 68 storeys (Mehta, 1978) and the Governor Phillip Tower is over 60 storeys, but they stand above most of the CBD skyline and hence are an exception.

Since commercial buildings are close together, the actual height for the calculation of the wall-ground double bounce will not necessarily be the full height of the building due to shadowing effects. There is more likely to be double-bounce effects from tall building walls and adjacent smaller building roofs, reducing the effective building height used in the model.

For double bounce to occur, there must be some ground or building roof for the radar to interact with. For double bounce reflection with look angles between 30 and 60°, the projection of the maximum ground or roof area for reflection onto a tall building's wall will be much smaller than the full height of the building. The average building roof size is around 30m*30m. For a 30° angle this leaves a projection onto the tall building's wall up to (30/tan30°) 50m. If the double bounce is with the road (width of about 20m), for 30° look angle the maximum projection onto the building wall is 34m. This gives an average of 42m.

6.3.2.2 Building Layout

From observation of aerial photographs, the average commercial building block has about 3 rows and 3 columns. The minimum spacing between these tall buildings is generally about 10m which is enough to allow for pedestrian or light vehicle access. The maximum distance, which is the distance between the buildings on either side of the street, is about 20m. For the spacing between the buildings to be square, it can be assumed that the distance (ie., x and y) is (10+20)/2=15m.

6.3.2.3 Roughness

Commercial buildings have a higher proportion of glass to concrete (and brick for some smaller buildings) compared to residential buildings. The ratio of glass to concrete appears to be about 50:50 since some of the buildings are mostly clad in glass, others have walls which contain about half glass/half concrete, and some walls of large buildings have no windows due to aspect and interior design. If glass is again considered to be 0.0cm roughness and brick/concrete is from 0.5cm up to 1cm, the building wall roughness ranges from 0.5(0.0)+0.5(0.005)=0.0025m up to 0.5(0.0)+0.5(0.01)=0.005m, giving an average *rms* of 0.002m.

The roof will be smooth since they are mostly flat concrete no greater than an *rms* of 0.001m. They are generally flat rather than sloping. The ground, being predominantly of paving, concrete, and asphalt (from the road), will be flat although some of the paved surfaces are rough. A reasonable estimate for the ground is most likely about 0.002m (*rms*).

6.3.2.4 Dielectric Constant

A commercial block of buildings is a complex mixture of materials, including brick, concrete, glass, and especially metal (usually hidden). This makes the estimation of the dielectric constant a difficult task. The commercial areas considered in this study have a predominantly higher proportion of glass cladding, and a much smaller brick or concrete component than residential areas. Aluminium and stainless steel are also widely used as cladding in developed countries (Mehta, 1978).

As mentioned earlier, the **walls** can be considered to be 50% glass and 50% other (usually concrete) for the cladding, but for tall structures there is metal support in the walls which also needs to be considered. Metal, being a conducting material, has a high dielectric constant but its response depends on how much of the electromagnetic wave can reach it. A combination of just 50%

glass and 50% concrete would give a dielectric constant ranging from a minimum of about 0.5*(4+1i)+0.5*(3.4+0.1i)=3.7+0.5i up to 0.8(7+1i)+0.2(3.4+1i)=6.3+1i. (As mentioned earlier, the dielectric constant of soil is 3.4+1i and glass ranges from 4+1i up to 7+1i). If metal is taken into account, the dielectric constant will increase.

Metals can be found in commercial buildings as exterior cladding and to provide structural support. Reinforced concrete can contain up to 6% metal (Shaeffer, 1992) providing strength. However, many tall buildings with glass cladding most of the walls, have their windows tinted, usually with a metal coating. For a more detailed analysis of the metals found in a commercial building, refer to Appendix D.

To determine the dielectric constant of the wall, as with the residential buildings, the backscatter from a non-metal and then metal square plate will be examined to show the increase in intensity due to metal. Once again, the method and all formulae shown here have been derived and defined in Section 6.5.1. The non-metallic material is considered to be concrete and glass. As shown for residential areas (Section (6.3.1.4)), a dry material, such as concrete (having ε=3.4+0.1i), will cause the radar to lose about 14% of its transmitted power as it goes to a depth of 0.1m into the material and another 14% is lost on return giving 75% returning.

The glass component is also considered to be 50% of the building wall. Glass has a higher dielectric constant than concrete. From the residential section it was decided that glass ranged from 4+1i to 7+1i giving an average of 5.5+1i. The thickness of building glass ranges from 3mm up to 12mm (Lim *et al.,* 1979), giving an average of 7.5mm. From Equation 6.2, the power loss occurring from the radar penetrating the glass to reach the metal layer (assuming it is an interior layer) is 1-0.92=8%, so the two way power returning to the surface is 0.92*0.92=0.85 or 85%.

The approximate two way attenuation of radar energy through a commercial building wall will be considered to be the average power loss for concrete and glass. This gives 80%, so P_s=0.8. The average dielectric constant of concrete and glass is 4.5+0.5i, and its average roughness is 0.002m (*rms*). Hence, for 1m^2 of wall (without metal), the R_h^2=0.23 and R_v^2=0.05, and σ_{ma}=0.014 for horizontal and 0.003 for vertical polarisation respectively.

A metal plate of 0.2m^2 seems a plausible estimate for the metal found in a commercial building per square metre (metal occurring in a commercial building is discussed in Appendix D). This leads to σ_{me}=0.025. A square metre of building wall, including metal, gives σ_{tot}=0.040 and 0.029 for horizontal and vertical polarisation respectively. These values give R_{hn}^2=0.62 and R_{vn}^2=0.45. A dielectric constant of 44+4i with a roughness of *rms*=0.002m results in an R_{hw}^2=0.65 and R_{vw}^2=0.42, which are close to R_{hn}^2 and R_{vn}^2 so this dielectric constant will be used to represent a commercial building wall (ε_w) in the model.

The **roof** can be considered to consist of smooth concrete (of dielectric constant 3.4+0.1i and roughness *rms*=0.001m) and metal reinforcement. Single bounce specular reflection from the roof will contribute minimally to the total backscatter since the double bounce from the building wall is strong. As calculated previously in this section (following the methodology from Section 6.5.1), for a 1m^2 concrete area and at a depth of 0.1m, there is 75% left of the remaining power of the radar after interacting with the metal, ie., P_s=0.75. An estimate of 0.2m^2 of metal for every 1m^2 of concrete would give an R_{hn}^2=0.54 and R_{vn}^2=0.40. The roof dielectric constant (ε_r) of 30+3i has been adopted since the R_h^2 (=0.59) and R_v^2 (=0.35) are close to R_{hn}^2 and R_{vn}^2.

The **ground** is a mixture of concrete, asphalt, and brick paving. Due to the fact that CBD's often have underground rail lines or vehicle tunnels, there may be metals in the ground providing structural support. Even general paving is reinforced with metal rods. This may lead to a reasonably large dielectric constant.

Double bounce with the building walls comes from the ground ie., asphalt/concrete/paving and surrounding roofs. In future the dielectric constant of the asphalt, concrete and paving will be treated as that of concrete, which has a value of 3.4+0.1i. This is because all the materials have a low dielectric constant and concrete is the most common when considering the ground and roof. The surface has a roughness close to an *rms*=0.002m since a concrete slab on the roof will be smooth but ground paving will be rougher. From the formulae in Section 6.5.1, the loss of power of a radar wave through 10cm of concrete and back is 25%, so Ps=0.75.

Through observation of the aerial photograph, there appears to be a greater chance of corner reflection from the short roofs than the ground itself. An estimate of 40% double bounce backscatter from the ground-wall and 60% from the short building roof-wall seems realistic (as viewed from aerial photographs). The previously defined amount of metal in a building roof is $0.2m^2$. Since most of the ground is road or concrete, and the average amount of reinforcing used in concrete constructions is about 2% (MacGregor, 1988), an estimate of $0.02m^2$ of metal in a square metre of ground will be assumed. This leads to (0.6*0.2+0.4*0.02) $0.13m^2$ of metal resulting in R_{hn}^2=0.36, and R_{vn}^2=0.22. A dielectric constant of 12+1.5i results in R_h^2=0.43 and R_v^2=0.19 which is close to the required values, and hence adopted as the dielectric constant of the ground in a commercial area.

6.4 Consideration of Park Land

Parkland and large bodies of water can generally be distinguished from the other classes purely due to their low backscatter. Most parks are flat regions with a layer of grass giving a low backscatter for both HH and VV. (Although this is relative to whether the grass is mown or not and the wavelength of the radiation). There are, however, some areas having trees and other structures

increasing the radar return to levels comparable with low residential backscatter.

In Chapter 8, where an actual classification of an urban area is performed, parkland is classified based on its total power alone. This is because often the total power is all that is necessary, and the polarisation signature does not provide extra information since its properties often resemble those of a residential region (especially where there are trees). The difficulty in distinguishing between residential land use and tree covered areas is not within the scope of this research, however, suggestions for its resolution are discussed later.

The value of the total power was determined empirically. This low value does not include backscatter from trees and other structures in the parkland. The total power value is for the purpose of detecting flat, open parkland, or any other feature with a low backscatter such as water. One reason an empirical approach was used is because the absolute accuracy of L-band AirSAR data is ±1.2dB (Dubois *et al.*, 1995). This gives an intensity of ±1.3, which for low backscatter is a significant change in value.

6.5 Consideration of the Metals found in Buildings

Metals exist in all building structures to some extent. Estimations of the amount of metal expected in both residential and commercial buildings in the city of Sydney are examined in detail in Appendices C and D. This section will show the calculations necessary for determining an appropriate dielectric constant when considering its metal content. Then it will introduce the Metal Factor, which takes into consideration the metals that would be expected to contribute to single (or odd) bounce scattering.

6.5.1 Converting the Effect of Metal within a Building into an Equivalent Dielectric Constant

Compensation is made for metal in a building by determining an approximate equivalent dielectric constant which the material plus the metal would give. This is achieved by determining approximately by how much the metal would increase the backscatter compared to its response without it, and then converting this into a dielectric constant.

For metal to be accounted for in building materials, the approximate percentage of metal in the material is required, along with the loss of energy which the wave will encounter from travelling through the external building material to the metal, and back to the outside world. The backscatter is first determined for a square metre of the building surface without metal. This is done using Equation 3.6 where the incidence angle θ=45° and the orientation angle ϕ=0°. The reason 45° was chosen is because this is the middle of the range for incidence angles in the AirSAR image. ϕ is chosen as 0° since it makes the calculations possible to perform. As long as ϕ is kept the same for all these calculations, its value is of no great concern.

The size of the square is $1m^2$ so many of the terms in Equation 3.6 cancel out.

This gives $$\sigma_{ma} = \frac{2\pi}{\lambda^2} R_p^2 \sin c^2\left(k_o \sin\theta\right) \qquad (6.1)$$

where σ_{ma} is the backscatter from a square metre of building material without metal, and R_p is the reflection coefficient of the building material for either horizontal or vertical polarisation covering the metal. (R_p also considers the roughness of the material, ie., Equation 3.5).

The loss of radar energy through the material can be determined using the following formulae. The power of a wave as a function of *x* (the depth of penetration) can be written as:

$P(x) = P(0)e^{-2\alpha_a x}$ (Elachi, 1988) (6.2)

where P(0) is the initial power of the wave, x is the depth which the radar has to travel in the wall to reach the metal, and:

$$\alpha_a = {}^{\pi\varepsilon_i}\!/_{\lambda\sqrt{\varepsilon_r}} \text{ (Elachi, 1988)} \quad (6.3)$$

where ε_r and ε_i are the real and imaginary components of the dielectric constant of the material. $e^{-2\alpha_a x}$ will give the percentage of power not lost from the radar penetrating a depth of x, so squaring this value will give the percentage of power returning back to the surface, ie., $P_s = \left(e^{-2\alpha_a x}\right)^2$.

The backscatter from the metal in the square metre is now determined using:

$$\sigma_{me} = P_s \frac{2\pi A^2}{\lambda^2} \sin c^2\left(k_o L \sin\theta\right) \quad (6.4)$$

where A is the area of metal per square metre of building and the length of the metal square is $L=A^{1/2}$.

The total backscatter from the building material and the metal is determined for a $1m^2$ wall, giving: $\sigma_{tot} = \sigma_{ma} + \sigma_{me}$ (6.5)

This is then equated to a new dielectric constant. In order to determine the new dielectric constant, the square of the reflection coefficient is first determined from:

$$R_{pn}^2 = \sigma_{tot} \frac{\lambda^2}{2\pi \sin c^2\left(k_o \sin\theta\right)} \quad (6.6)$$

which is the basically the inverse of 6.1. This whole process is performed for horizontal and vertical polarisation, creating two values of R_{pn}^2. In order to convert this back to a dielectric constant, a trial and error method is used to

determine the dielectric constant (using Equations 3.4 and 3.5 for the reflection coefficients including the roughness) giving the closest reflection coefficient values to R_{pn}^2 for both horizontal and vertical polarisation.

This appears to be a rather crude method of accounting for metal in a building. Equation 6.1, for calculating the backscatter, does oscillate a little when parameters are varied. An estimation of the amount of metal per square metre in a building is also very approximate. However, a small change in the dielectric constant does not change the backscatter significantly. For high dielectric constant values where R_{pn}^2 approaches its maximum value of 1, changes in ε_r of 20 units have a very small effect on R_{pn}^2. Since the urban area has such a complex mixture of building materials, a precise estimation would be impossible. Due to the insensitivity of the dielectric constant this method is deemed appropriate.

6.5.2 The Metal Factor

The Metal Factor is a term developed purely for this research in order to model a complex situation. It is designed to account for the metal which is found in a building, leading to a strong single bounce. The place where this is viewed as most likely occurring is in a building's ceiling.

6.5.2.1 The Metal Factor for Residential Buildings

The model has not yet considered any backscatter from the metals that would be expected to be found in the ceiling of a residential building, and other metal combinations found in a building leading to odd bounce reflection. This includes the gas piping, hot and cold pipes for the water system, and gutters for water drainage. For a further discussion of metal found in a residential building contributing to odd bounce reflection, refer to Appendix C.

The hot and cold water pipes are often situated in the ceiling, along with the hot water heating system where appropriate. They are usually made of galvanised

iron or mild steel. These are all of cylindrical shape and although some of the water pipes run close to parallel with the roof edges, others are oriented at different angles in order to serve the required room. The hot water system is often a large cylinder standing around 1m tall with a 0.8m diameter, however due to its orientation with respect to the radar it will only contribute minimally to single bounce total backscatter.

Depending on materials used in the ceiling and the type of insulation, the radar wave may even penetrate the ceiling, entering the rooms below. The kitchen and laundry have a considerable metal content, such as the stove, sink, water pipes and white goods (eg., fridge, washing machine).

As it would be too difficult to take into account and then model all the metal to be expected in a roof, some simplifications must be made. Due to the complexities in modelling each piece of metal, the model uses the assumption that an equivalent square metal plate is facing the radar in the ceiling of the roof.

The expected total loss which the radar wave would suffer through penetrating the ceiling and then returning has been calculated below. Most of the wave will leave the building roof after interacting with the metal in the ceiling.

Using Equations 6.2 and 6.3 (from Section 6.5.1), if x is the thickness of a terracotta tile on a roof (about 2cm), and it has a dielectric constant of $\varepsilon=3.4+0.1i$, then for a wavelength of 0.23m (L-band), P(x)=P(0)*0.97. Therefore 97% of the initial wave would pass through the tile the first time. 97% of the remaining wave returning would penetrate back through the tile roof. Hence, about 0.97*0.97=94% of the original wave should penetrate the roof tiles twice returning to the antenna (provided that it is scattered in that direction).

The metal factor is included in the final backscatter by being added as a Mueller matrix to the total matrix L_{tot}. Since the metal factor is assuming single

bounce, and, being metal, its reflection coefficients are considered to be 1 for both R_{hr} and R_{vr}, the scattering matrix becomes:

$$S = \begin{bmatrix} 1 & 0 \\ 0 & 1 \end{bmatrix} \varpi_{mf} \tag{6.7}$$

where $\varpi_{mf} = l_{mf}\left(4\pi L_p^4 / \lambda^2\right)$ (6.8)

and L_p is the length of the square metal plate. ϖ_{mf} gives the backscatter from a plate (without reflection coefficients), where ϖ was introduced in Section 5.5. Since it is assumed that the plate is normal to the radar, the *sinc* function equals 1. l_{mf} considers the loss of power from the radar penetrating the roof (as a percentage), therefore is l_{mf}=0.94.

Determination of the metal factor is not a value which can be directly measured. The size of the metal plate required was determined by a semi-empirical approach, through examination of the polarisation signature shape. If the size of the metal plate required to give the correct polarisation signature was too large, then other building or vegetation parameters would need to be re-investigated. Using the average shape of a residential polarisation signature for a variety of look and orientation angles, the amount of single bounce lacking in the model's polarisation signature was determined. The size of the metal plate was chosen to be 0.35*0.35m for a residential building. This would lead to a backscatter intensity of $(\frac{4\pi 0.35^4}{\lambda^2})$ = 3.5. Therefore before any loss of the radar through the roof tile is considered, radar return from a 0.35m square metal plate would result in approximately 5.4dB's.

Since a residential ceiling consists of metal pipes, rather than plates, a comparison of the expected backscatter from pipes is required to test the validity of the metal factor. As can be seen from the graph in Figure 6.5, three different types of cylindrical backscatter were considered. These are described

in detail in Fung & Ulaby (1983), however for the benefit of analysis, a brief description is given as follows.

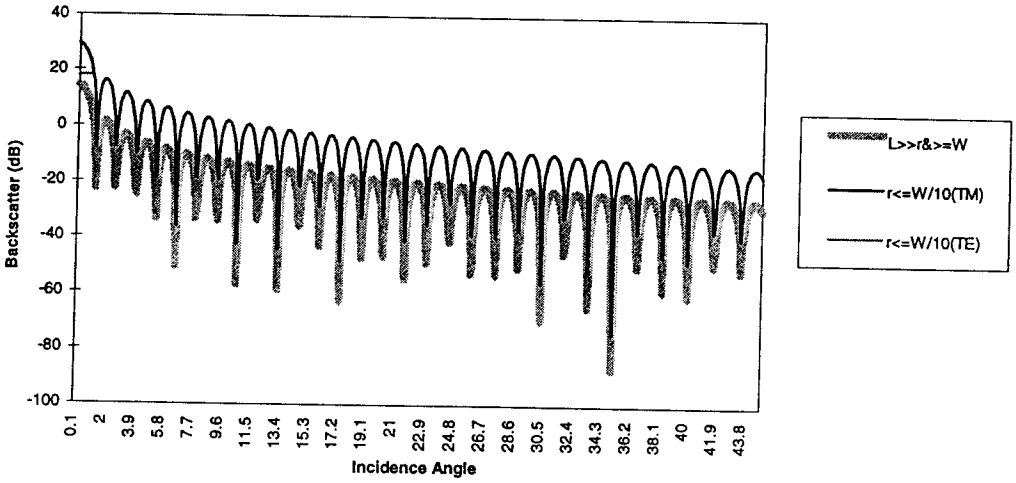

Figure 6.5. Backscatter from three different types of metal pipes, plotted with respect to the radar incidence angle for L-band. The thick line represents a short pipe (of length L=1.5m which is greater than or equal to the wavelength W) having a relatively large radius (r=0.4m). The other two lines represent a pipe of 5m length and a radius which is less than one tenth of the wavelength (r=0.02m), where the orientation with respect to the radar is of TM (the constant thin line), or TE type (the short line present only for a very small incidence angle).

The first of the three types of cylinders has the length of the cylinder much larger than the radius, and equal to or greater than the wavelength. Its formula is:

$$\sigma(\theta) = \frac{2\pi r L^2 \cos\theta_c}{\lambda} \sin c^2\left(k_o L \sin\theta_c\right) \quad \text{(Fung \& Ulaby, 1983)} \qquad (6.9)$$

where L is the length of the cylinder, r is its radius, k_o is the wave number, λ is the wavelength, and θ_c is the angle between the plane, perpendicular to the cylinder axis and the direction of scattering. This situation is for both transverse magnetic and transverse electric mode. The transverse magnetic mode (TM) is the situation when the electric-field vector of the incident radar wave lies

parallel to the cylinder axis. Transverse electric mode (TE) is when the electric-field vector is perpendicular to the cylinder axis (Fung & Ulaby, 1983).

If the radius of the cylinder is equal to or smaller than one-tenth of the wavelength, then the backscatter varies depending on whether the situation is the TM or TE mode. This gives:

$$\sigma(\theta) \approx \pi L^2 \frac{\left[\sin c\left(k_o L \sin\theta_c\right)\right]^2}{\left[\log_e \frac{2\pi r \cos\theta_c}{\lambda}\right]^2} \tag{6.10}$$

for the TM mode, and:

$$\sigma(\theta) \approx \left(9\pi/4\right) L^2 \left(2\pi r/\lambda\right)^4 \text{ (Fung \& Ulaby, 1983)} \tag{6.11}$$

for the TE mode. Note that the formula for the TE mode only enables calculation for the situation where the scattering is in the plane perpendicular to the axis of the cylinder (Fung & Ulaby, 1983), ie., when θ_c=0.

Figure 6.5 shows the backscatter for these three situations with respect to the varying θ_c. The thick line represents the backscatter from a cylinder of 1.5m length and 0.4m radius resembling a hot water system. As the graph shows, the hot water system gives a negligible backscatter for angles which the radar would contact it in an urban situation ie., 30 to 60°. The thin dark line represents the backscatter from a cylinder of 5m length and 0.02m radius representing a water pipe for the TM case. The TE case is shown for θ_c=0 (ie., the short line at the beginning of the graph). As the graph shows, a thin water pipe will give a strong return, above 10dB's, for the first 3° of θ_c for a TM situation. The backscatter for the TE case of a thin water pipe is just below 20dB's for θ_c=0°. A hot water system has a strong response when θ_c is 0°, but reduces to a negligible amount within a degree from this angle.

In order to justify L_p=0.35, a case study was undertaken on an average single storey semi-detached residential dwelling (ie., half of a single residential building) having a hot water system in the roof. The pipes were surveyed in the ceiling, and their size, length and approximate orientation with respect to the building walls were recorded. A plan is shown in Figure 6.6. The nine pipes were considered for their backscatter contribution. Looking at the TM and TE cases, there will be horizontal backscatter from pipes 1, 2, 3 and 4 (using the TM formula). Pipe 4 however has a large value for θ_c so will hardly contribute to backscatter. There will also be horizontal backscatter from pipes 5, 6, 7, 8 and 9 for the TE case. However, since the formula does not permit the calculation of backscatter for any angles other than θ_c=0°, these situations cannot be shown in this example.

Vertical backscatter can be calculated for pipes 1, 2, 3 and 4 using the TE formula, but only when θ_c=0°. This gives a high backscatter from pipes 1, 2, 3 and 4 when the orientation angle (ϕ) is 0, 10, 30 and 60° respectively. Again pipe 4 will give a minimal backscatter, and so will not be considered further. The vertical backscatter from pipes 5, 6, 7, 8 and 9 will be too small since θ_c is reasonably large.

The total backscatter expected from this series of pipes has been calculated using Equations 6.10 and 6.11. The pipe system is only for half a single dwelling, so the pipe system is tripled in consideration that some residential buildings are semi-detached (forming two pipe systems in the roof), and that apartment blocks are often equivalent to four single dwellings.

The total backscatter is shown in Figure 6.7. The TM and TE cases are plotted with respect to orientation angle (ϕ), with TM (being the continuous line) averaged using the smoothing function to eliminate large oscillations. (The smoothing function involved averaging each backscatter value with the three before and after it with respect to ϕ). The average TM value, calculated over the full 45° is also shown. The reason the average is calculated is because

pipe orientation is dependent on the building plan in relation to the bathroom, kitchen, and laundry. Hence it is random, and impossible to model in order to represent all residential buildings. As Figure 6.7 shows, the average is 7.7dB's. This is higher than the 5.5dB established for the metal factor. Consideration from the average TE response (if it could be determined for the full 45°) would most likely decrease the 7.7dB value to a certain extent.

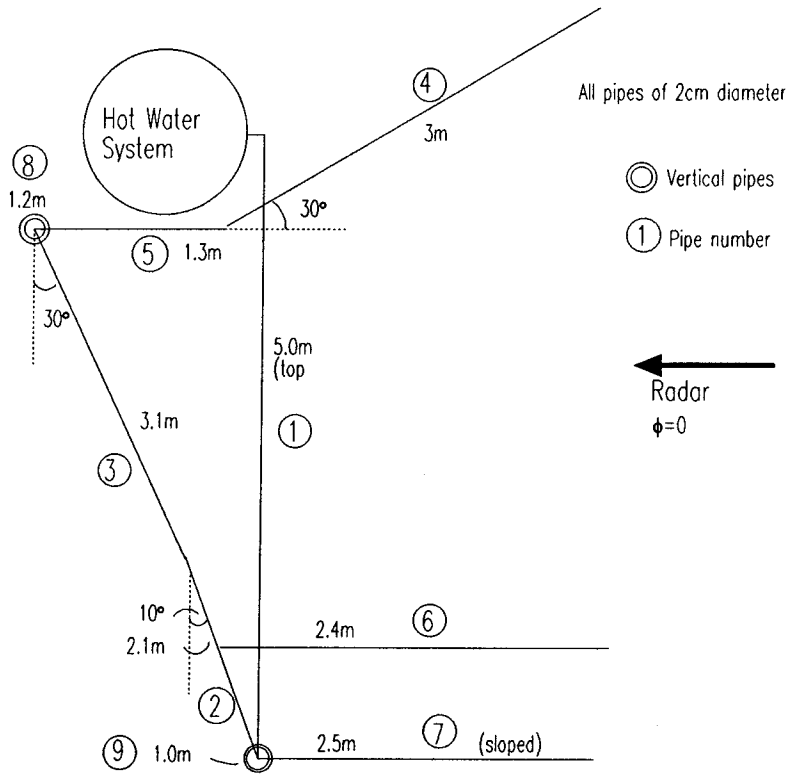

Figure 6.6. Plan view of the pipe layout from a hot water system in a real residential ceiling.

It is acknowledged that not all buildings will have a hot water system installed. There are, however, other metallic materials found in the residential building ceiling, and rooms. This case study was used since the modelling was possible. Providing the metal factor is of reasonable magnitude, its adoption is appropriate. As the above case shows, with metal water pipes, hot water

systems, and other metal used in the construction of a residential roof, a metal factor of 0.35m for each residential building is a reasonable estimate.

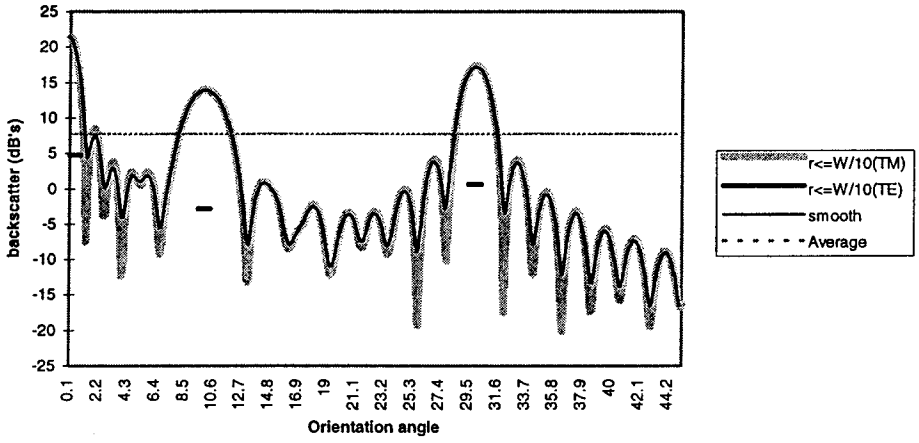

Figure 6.7. Backscatter with respect to orientation angle (ϕ), from metal pipes found in a real residential ceiling (used as a case study). The dark thin line represents the TM case after smoothing (note how it overlaps with most of the TM line before smoothing), the thick dark line segments represent the TE case (not a continuous line). The average backscatter for the TM case is also plotted as a thin dotted line.

6.5.2.2 The Metal Factor for Commercial Buildings

The city is comprised of buildings having a variety of shapes and designs. Some are irregular while others are a more traditional rectangular shape. Commercial buildings may also have building "accessories" attached to them, forming scatterers for the radar. These could be for aesthetic purposes or in older buildings it would include water pipes running in various directions. There is a lot of metal situated on the roof of commercial buildings, including air-conditioning systems. These are sometimes of spherical shape, forming an ideal single bounce scatterer for the radar sensor, independent of orientation or incidence angle. Even multiple (resulting in odd) bounce scattering, such as corner reflection, will still be strong if derived from metals. Metals are found around the windows providing framing or sun shade, which may also contribute to multiple bounce effects.

An L_p=1m for each building was decided upon. Even when the size of the air-conditioning system is considered alone, the L_p is a reasonable value. Commercial buildings are not only large, but window fittings, roof accessories, or any disjointed or uneven design features of buildings may lead to odd bounce scattering, making $1m^2$ per building a small but plausible amount. (Refer to Figure 6.4 for some photographs of commercial buildings).

Unfortunately there are no situations for commercial buildings where the orientation angle is approaching 45°. The metal factor for commercial land use may vary according to incidence angle, but without any real data as a guide, no modelling can be done here. AirSAR images of the same area in Sydney with a different look angle would have assisted with this problem, but the data was unavailable at the time this thesis was written.

6.6 Different Output Averaging Methods for Calculating the Total Backscatter from a Block of Buildings

Two different approaches were used for calculating the backscatter from a block of buildings. One method was designed to calculate the backscatter with respect to a varying look or orientation angle for either HH or VV polarisation (which will be called Method 1). The other was designed to give the backscatter and polarisation properties for only one look and orientation angle (Method 2). The reason two methods were used is because determination of polarisation information is computationally intense, so to program it such that it can be calculated for a varying θ or ϕ would be inefficient.

As Figure 6.5 demonstrates, any model using the *sinc* function will lead to an oscillating output with respect to θ and ϕ. This is why averaging was required, as explained in Section 3.3.2. As previously mentioned, Figure 6.7 shows the smoothed line which was determined by averaging the backscatter for a

particular ϕ, with the three backscatter values before and after it, with respect to a varying ϕ. This averaging technique is the process adopted in Method 1.

However, the averaging technique needs to be different for the two methods of calculating the backscatter from a building block. The reason for this is because if the results from Method 2 were to be averaged in the same way as those from Method 1, it would require calculating the total scattering matrix seven times, rather than once and averaging each element. This requires many more calculations for only a small change in backscatter (usually less than an intensity change of 0.01). Instead, the necessary elements of ϖ for each scattering mechanism (eg., front wall and roof) are averaged. The polarisation signatures (Method 2) are used primarily for visualisation, and Method 1 is used for calculation of the final backscatter.

The mathematical reason why there is a discrepancy between the averaged output from the two methods is now demonstrated. In Method 1 the averaging is:

$$\left(\varpi_{x1}^2 R_p^2 + \varpi_{x2}^2 R_p^2 + \ldots + \varpi_{x7}^2 R_p^2\right)/7 = R_p^2\left(\varpi_{x1}^2 + \varpi_{x2}^2 + \ldots + \varpi_{x7}^2\right)/7 \qquad (6.12)$$

(Averaging by the number 7, ie., with the three values before and after it, was chosen purely for the reason that it appeared to sufficiently smooth out the oscillations without losing important detail).

Whereas Method 2 averages using:

$$R_p^2\left(\varpi_{x1} + \varpi_{x2} + \ldots + \varpi_{x7}\right)^2/7 \qquad (6.13)$$

where R_p^2 is the reflection coefficient, and ϖ_{x1} is for the angle ϕ-3, ϖ_{x2} is for the angle ϕ-2, up to ϖ_{x7} which is for ϕ+3. Note that ϖ is defined in Section 5.5 for the front roof, front wall, etc, and is the common element (ie., independent of the reflection coefficients) from the total scattering matrix. The total scattering matrix is referring to the sum of all scattering mechanisms, from both the buildings and vegetation. The two different averaging methods will sometimes

result in a slightly different backscatter for a building block. However, this change is too small to be significant.

6.7 Summary

Determining the magnitude of all the building, ground and vegetation parameters is not an easy task. Figure 6.8 is a flow chart demonstrating how the formulae and different computation methods are used.

The urban environment consists of many complex shapes and different scale elements in relation to radar return. This chapter has introduced all the relevant parameters necessary for the model. Some large generalisations, and approximations were made, however this was the only realistic solution. Chapter 7 will now use these parameters, and test the model's performance against some real urban radar data.

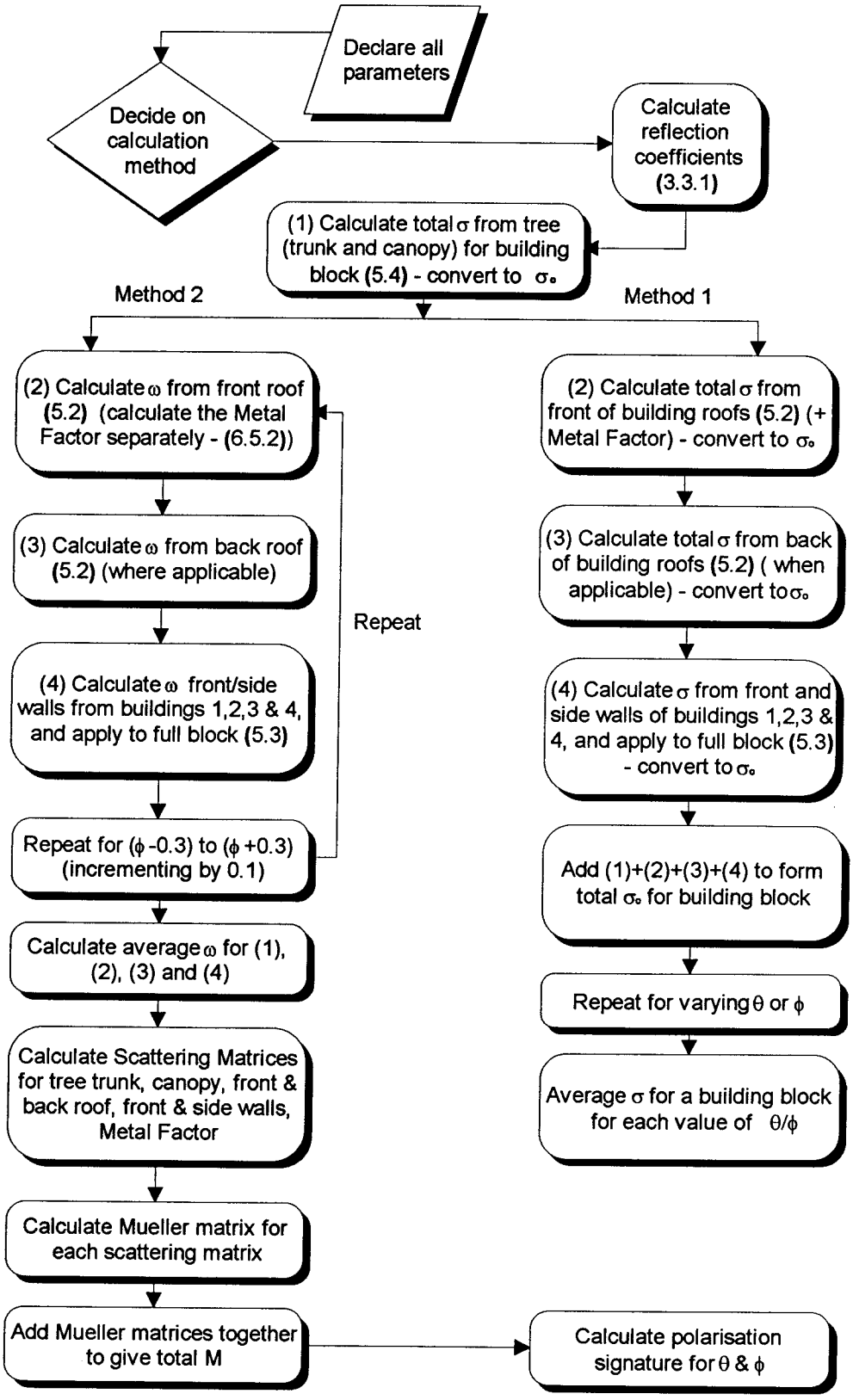

Figure 6.8. Flow chart demonstrating the two methods of calculating the total backscatter from a block of buildings. The numbers in bold brackets refer to the sections where the relevant formulae are discussed and defined.

7. A COMPARISON OF MODEL SIMULATION WITH REAL URBAN DATA

7.1 Introduction

Now that the model has been fully developed, it is necessary to test its accuracy by comparing the theoretical with real urban backscatter, both in magnitude and polarisation information. This is achieved in the latter part of this chapter through analysis of six case studies of urban areas by comparing AirSAR data to a model simulation representing the same urban characteristics. Such investigations are made for P-, L- and C-band, where the wavelengths are approximately 68cm, 24cm and 6cm respectively (as used for AirSAR).

To begin this chapter, a brief examination of the model output is given to show the major scattering components. This is necessary for understanding the polarisation signatures which will be presented later.

7.1.1 Model Output

In order to understand the model output in relation to the major scattering components, some simulations are provided. As Figures 7.1, 7.2, and 7.3 show, there are oscillations due to the radar wave at the extremes of the building resulting in either constructive or destructive interference. These oscillations are a function of most of the radar and building parameters, and therefore are smoothed to give a more realistic result.

Figure 7.1 is a graph demonstrating the backscatter with respect to a varying orientation angle ϕ for a residential area. The look angle (θ) is 60°. For small orientation angles, it can be seen that the front wall is the strongest scattering component. For larger angles, the backscatter is dominated by scattering from trees. This is expected since trees, being approximately round, are

independent of orientation angle. The contribution from the side wall is minimal, although it gradually increases to equal the response from the front wall when ϕ=45°. The backscatter from the front roof, where the roof slope is 30°, is also minimal for a look angle of 60°.

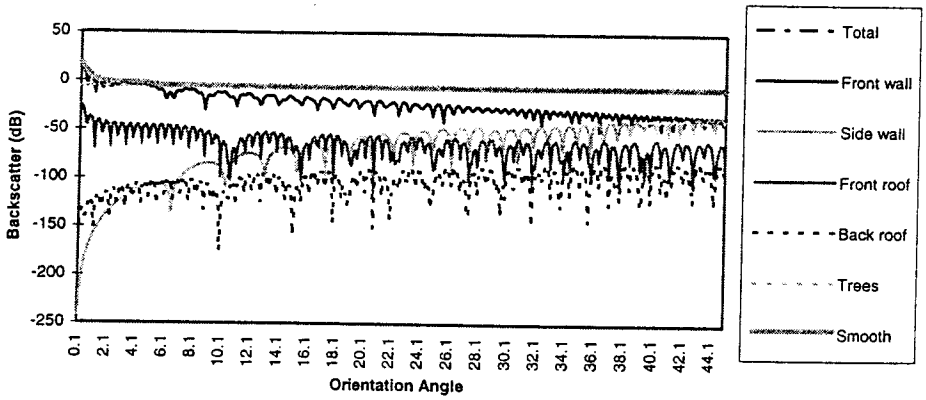

Figure 7.1. Backscatter from a residential block of buildings (for L-band, HH polarisation) with respect to orientation angle. Each scattering component is plotted (excluding the Metal Factor). The look angle is 60°. 'Smooth' represents the total backscatter after averaging, hence follows the 'total' backscatter but without the large oscillations. (Due to the thickness of the 'smooth' line, the 'total' backscatter is completely hidden beneath it in this example. The 'trees' line is also hidden beneath the 'smooth' line with the exception of the first five degrees of orientation angle).

It must be noted that the Metal Factor has not been plotted in Figure 7.1. This is because in the program used to calculate the model, the Metal Factor is an integral part of the calculations for the backscatter from the roof. However, plotting the Metal Factor as part of the backscatter from the roof would not demonstrate the scattering effects occurring on its surface, which is what this graph is designed to show. The graph is purely used to demonstrate the dominant scattering properties from the individual building components, and their relationship to each other.

Figure 7.2 demonstrates the backscatter from each scattering component of a residential building block as a function of the look angle, θ. The orientation angle was set to 0°. An important fact to note is how the backscatter from the front roof suddenly increases when the look angle is 30°. This factor has been

noted by Dong (1997a), who examined the shape of the polarisation signature over a residential area for a look angle near 60° and 30°. The polarisation signature indicated a strong single bounce component for a look angle around 30°. This was due to the strong backscatter from the roof since it has a slope close to 30°. As expected, the strong single bounce component was not apparent around 60°.

Apart from a look angle of 30°, the front wall is again the dominant scattering mechanism for small orientation angles, due to the strong wall-ground double bounce. Figure 7.2 also reveals how the double bounce is at its strongest when the look angle is close to 45°.

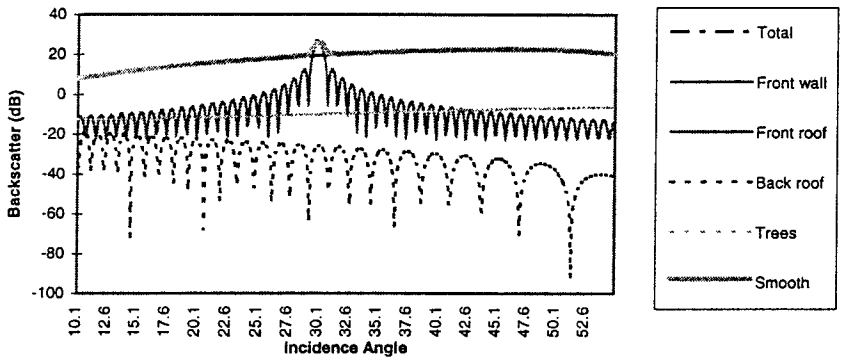

Figure 7.2. Backscatter from a block of residential buildings (for L-band, HH polarisation) with respect to look angle. The graph shows each scattering component from the block. The orientation angle is 0°. (Due to the thickness of the 'smooth' line, the 'total' backscatter is completely hidden beneath it in this example. The 'front wall' is also hidden beneath the 'smooth' line for all incidence angles except around 30°).

The backscatter from a residential region is different to that from a high density commercial area. Not only does the building shape and size change, but there is no vegetation (or very little in reality) in a commercial area, and building materials are different. A graph of the backscatter with respect to a varying orientation angle for a commercial area is shown in Figure 7.3. (The Metal Factor was also omitted here for the same reasons as given for Figure 7.1). A look angle of 48° was chosen as this is where most commercial areas are

situated on the AirSAR image used in examples to come. The main difference between a commercial and residential region is that the oscillations are much more frequent for larger buildings. As mentioned before, this is due to the *sinc* function.

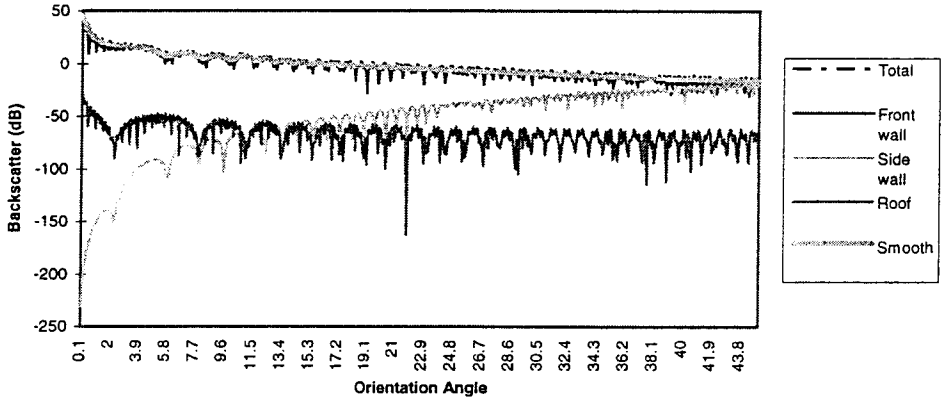

Figure 7.3. Backscatter from a commercial block of buildings (for L-band, HH polarisation) with respect to orientation angle. Each scattering component is plotted (excluding the Metal Factor). The look angle is 48°. (There is a strong overlap between the 'front wall' and 'total' lines, hence they are difficult to distinguish between. The 'smooth' line overlaps most of the 'total' line with the exception of the oscillations).

The information presented in this section has demonstrated the dominant scattering components for different situations. As the graphs show, the wall-ground double bounce is very much the stronger contributor to total backscatter for smaller orientation angles. The exception to this rule is when the roof is normal to the radar direction, and hence results in a strong single bounce. An understanding of the major scattering components assists in analysis of the polarisation signatures presented later in this chapter.

7.2 Model Parameters

All the parameters for residential and commercial buildings determined in Chapter 6 will be used as the model's building characteristics. The final

parameters for residential and commercial buildings are shown as follows (their extreme values, where appropriate, are in brackets).

Parameter	Residential	Commercial
Dielectric Constant:	ε_w=4.5+0.5i, ε_r=3.4+0.1i, ε_g=8+2I	ε_w=44+4i, ε_r=30+3i, ε_g=12+1.5i
Building Dimensions:	L=b=13.9m (13.2-14.7m), H=6.7m (5.1-8.3m)	L=b=35m (25-45m), H=42m (34-50m)
Roughness:	rms_w=0.002m (0.0015-0.0028m), rms_r=0.005, rms_g=0.015m (0.01-0.022m)	rms_w=0.002m (0.0012-0.0025m), rms_r=0.001, rms_g=0.002m
Spacing between buildings:	x=y=11m (8-15m)	x=y=15m
Number of columns/rows in block:	*cr*=9	*cr*=3
Number of trees:	N_t=81 (40-120)	Not Applicable
The Metal Factor:	L_p=0.35m (0.25-0.45)	L_p=1.0m (0.0-2.0)
Roof Slope:	γ=30°	γ=0°

No range has been discussed yet for the Metal Factor introduced in the previous chapter. Instead, an appropriate size is chosen, within reason, to give the maximum and minimum parameter values with a polarisation signature shape approximately resembling their class. However, the range in value of the Metal Factor chosen had to be of a realistic size. Due to the complexity of the urban environment this semi-empirical approach seems justified, especially since it can be accounted for (as demonstrated in Section 6.5.2). Although equations can attempt to give a theoretical answer, "empirical data often get to the heart of the matter better" (Hardaway *et al.*, 1982, p404).

For the residential class, a change in L_p of ± 0.1m is all that is required to account for the amount of single bounce required in a residential building for the parameter ranges. This range in L_p also is within exceptable limits of the amount of metal expected in a residential building, as discussed in Section 6.5.2.1.

For a commercial building, using the same technique as for residential, the metal contributing to single bounce will range from close to zero, up to more than $1m^2$. Hence, a range for L_p of ± 1.0m will be used when testing the extreme parameter values.

Section 7.3 demonstrates the minimum and maximum radar response values from a building block to be expected from the model. These are directly compared with real data.

7.3 General Analysis of the Model with respect to AirSAR Data

This section gives a general comparison of the theoretical backscatter with real data. To do this, some model backscatter values produced from the extreme model parameters, mentioned in Section 7.2, are plotted together with the equivalent AirSAR values. A number of examples are given, and each situation is explained as follows.

Figures 7.4 to 7.9 show the total model backscatter from an urban block, plotted against the orientation angle for these extreme parameter values. This is investigated for different urban situations for L-band wavelength. Some real data from AirSAR are also shown. Unfortunately, due to the orientation of the city, the data were unable to cover all orientation and look angles for residential and commercial land uses, however what was available is plotted in the graphs. There are four residential and two commercial graphs. The four residential graphs represent the radar responses from all combinations of HH and VV for a look angle of 60° and 30°. The commercial case is for one area

(θ=48°) for HH and VV. The one residential (Figure 7.4) and two commercial land use cases (Figures 7.8 and 7.9) show that the real data falls within the mid-range of the extreme values.

All the residential areas, except the region with a look angle of 60° for HH polarisation, fall close to the maxima of the extreme values. It appears that the model is giving results which are constantly lower than the real data. L-band AirSAR data is reported to have an absolute accuracy of ±1.2dB (Dubois *et al.*, 1995) which could be a partial reason for this discrepancy. The model appears to be less effective for larger orientation angles.

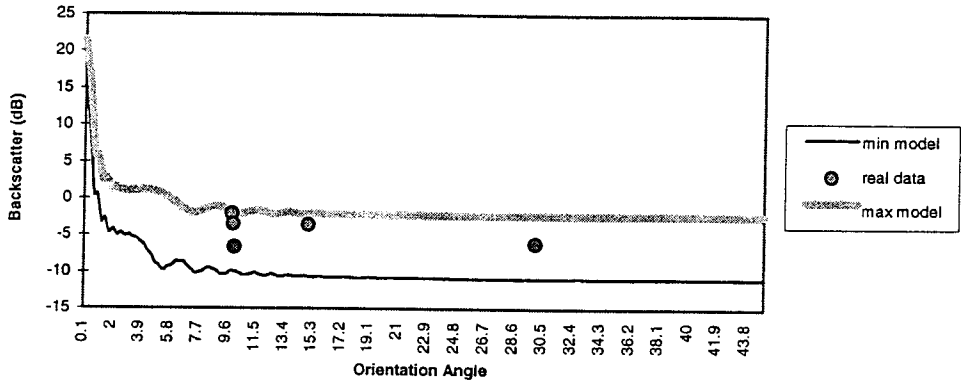

Figure 7.4. Comparison of total backscatter from extreme model values with real AirSAR data for a few selected orientation angles. This example is for a residential area having a look angle of 60° and HH polarisation.

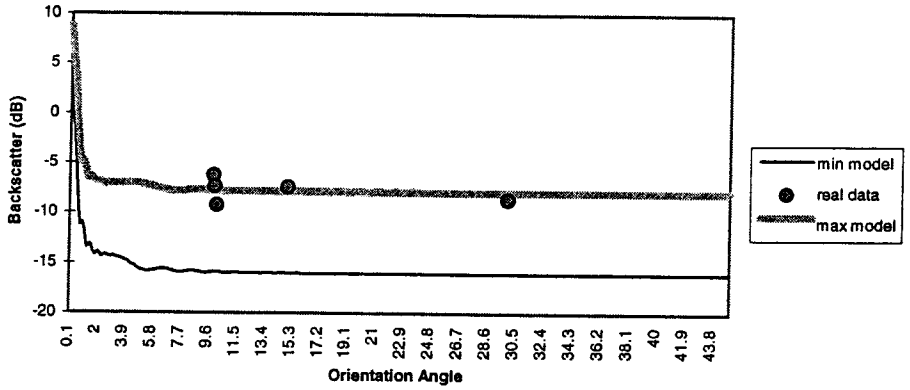

Figure 7.5. Comparison of total backscatter from extreme model values with real AirSAR data for a few selected orientation angles. This example is for a residential area having a look angle of 60° and VV polarisation.

For the commercial areas, examples of real data were limited for varying orientation angles having the same look angle. Figures 7.8 and 7.9 show that the AirSAR values were plotted for an orientation angle around 5°. The graph shows that the AirSAR values plot towards the lower of the extreme parameter values, indicating the model's response is a little too strong. However, this discrepancy is minimal.

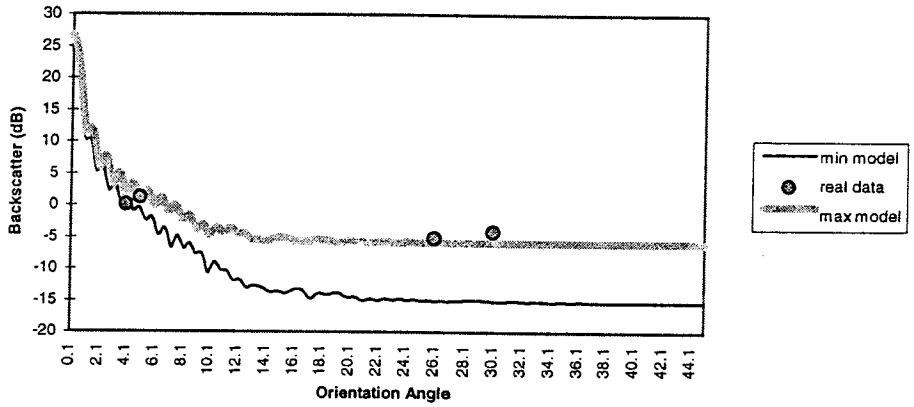

Figure 7.6. Comparison of total backscatter from extreme model values with real AirSAR data for a few selected orientation angles. This example is for a residential area having a look angle of 30° and HH polarisation.

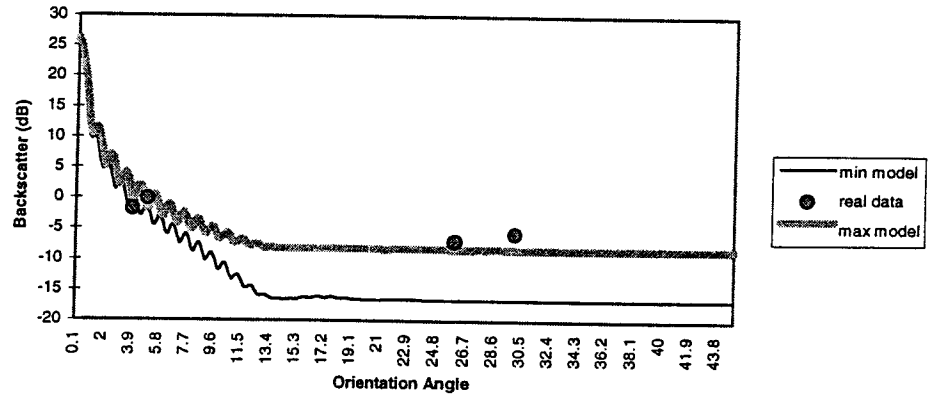

Figure 7.7. Comparison of total backscatter from extreme model values with real AirSAR data for a few selected orientation angles. This example is for a residential area having a look angle of 30° and VV polarisation.

As the graphs show, the commercial values from AirSAR plot reasonably well within the extreme model results. The residential values, with the exception of one case, generally plot towards the upper extreme of the model simulation. This means that the models average output is a little too low. However, as the next section will show, this difference is not substantial.

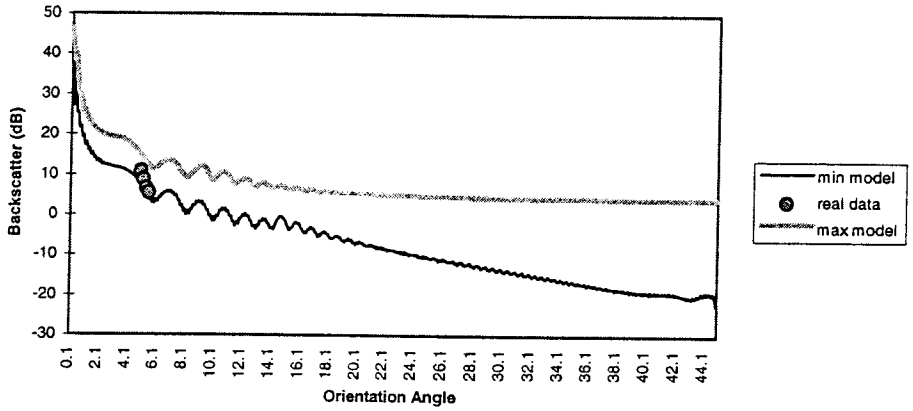

Figure 7.8. Comparison of total backscatter from extreme model values with real AirSAR data for a few selected orientation angles. This example is for a commercial area having a look angle of 48° and HH polarisation.

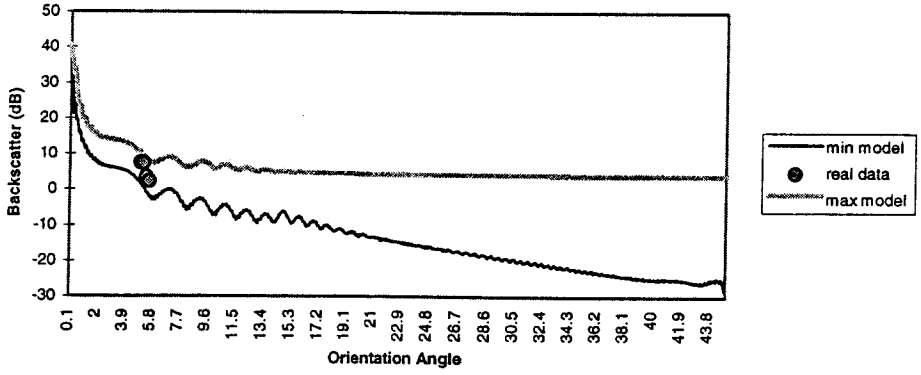

Figure 7.9. Comparison of total backscatter from extreme model values with real AirSAR data for a few selected orientation angles. This example is for a commercial area having a look angle of 48° and VV polarisation.

The results analysed in this section show that the relationship between the backscatter and orientation angle from the model is correct in terms of shape.

The only difference is that the magnitude of the model results are small for half of the examples presented here. However, the results are still reasonable.

To further test the accuracy of the model, some comparisons of the model and AirSAR data will be examined in detail. The remainder of the chapter consists of four main sections. The first three sections investigate and compare the results of the model simulation with AirSAR data for L-, P- and C-band respectively, and the final section concludes these results. For each wavelength, the magnitude and polarisation information are simulated from the model and compared with AirSAR data.

7.4 Detailed Comparison of the Model and AirSAR Data for Magnitude and Polarisation Information using L-band

This section examines the magnitude and polarisation characteristics (for L-band) obtained from the model, and compares it with the AirSAR results. Initially the magnitude of the theoretical and real data for HH and VV polarisation are discussed. The second section concentrates more on the polarisation information.

To test the accuracy of the model, six case studies were selected along the east coast of Sydney. Four residential and two commercial areas were chosen for their uniform characteristics over the block, and because they provided a variety of look and orientation angles. Each site's orientation angle and look angle were determined approximately using a ruler and protractor on an AirSAR image. Apart for θ and ϕ, all other parameters were held constant for each class type. The approximate location of these sites is shown in Appendix E.

Average residential parameter values, as shown in Section 7.2, were used for the model simulation as these will be eventually applied in the classification

process. Not only should the polarisation signatures be a correct shape, they should also be of comparable magnitude to the real data.

Of the four residential areas selected, two have a look angle close to 60°, and the other two are close to 30°. Their orientation angles ranged from close to 0° up to 45°. The results are presented as follows.

Site 1 is situated in the suburb of Kingsford. It has θ=61° and ϕ=8°. In future this site will be referred to as '61res8', where 'res' represents residential. The wavelength is placed in front (eg., c, l or p) when required. This convention will also be used for other sites.

Site 2 is in Kensington (60res30). Site 3 is located in the northern suburbs (30res5). Site 4 is situated near Site 3 (32res45), the main difference being that the orientation angle has changed considerably.

The commercial sites are more difficult to simulate with high accuracy since commercial areas have a wide range in minimum and maximum backscatter values over a small area. This gives a large standard deviation, hence polarisation signatures obtained from the AirSAR data will vary greatly in magnitude even for similar locations having the same look angle and orientation angle. Two sites were selected (Sites 5 and 6), one in the middle of the central commercial area of Sydney (48com5) and the other in the CBD of North Sydney (36com6). The two polarisation signatures were chosen because of the change in look angle. Unfortunately there are no commercial areas on the image having a large orientation angle.

7.4.1 Testing the HH and VV Responses of the Model (L-band)

Table 7.1 shows a comparison between the model and AirSAR results for HH and VV polarisation for all six sites. The results are reasonable, but the greatest difference is from the VV component of the model which is too low.

The four residential sites give good correlation between the AirSAR and model data for all the HH values, the smallest difference being 0.3dB and the largest difference is 1.8dB. The VV component gives less accurate results with the smallest and largest difference between the AirSAR and the model being 1.7dB and 2.2dB respectively. There appears to be a constant difference between the AirSAR and model of around 2dB for VV polarisation, with the model being too low. L-band AirSAR data has an absolute accuracy of ±1.2dB and a relative accuracy between the horizontal and vertical polarisation of ±0.5dB (Dubois *et al.*, 1995). Hence the model's results are comparable to the absolute accuracy, but the relative accuracy between the HH and VV polarisation's are larger than the expected accuracy of AirSAR.

Table 7.1. A comparison of the AirSAR HH and VV polarisation for L-band, with the model simulation output for six case studies. The results are expressed in intensity and (Decibels).

L-Band	AirSAR		Model	
Site No. (description)	HH int (dB)	VV int (dB)	HH int (dB)	VV int (dB)
Site 1 (61res8)	0.35 (-4.5)	0.15 (-8.2)	0.38 (-4.2)	0.09 (-10.4)
Site 2 (60res30)	0.25 (-6.0)	0.13 (-8.9)	0.28 (-5.5)	0.08 (-10.9)
Site 3 (30res5)	0.92 (-0.4)	0.64 (-1.9)	1.39 (1.4)	0.43 (-3.6)
Site 4 (32res45)	0.16 (-7.9)	0.13 (-8.9)	0.12 (-9.2)	0.08 (-10.9)
Site 5 (48com5)	13.2 (11.2)	5.8 (7.6)	12.7 (11.0)	3.3 (5.2)
Site 6 (36com6)	9.9 (9.9)	3.3 (5.2)	6.1 (7.9)	1.9 (2.8)

For Site 3, having the largest difference between the model and AirSAR data for VV polarisation, the ratio between the HH and VV (ie., HH-VV in dB's) for the AirSAR is 1.5dB's. For the model, the equivalent ratio is 5.0dB's. If the relative accuracy between the HH and VV polarisation for the AirSAR, as just mentioned, is ±0.5dB, then the difference between the model and AirSAR result is 3.5dB's which is outside this relative accuracy. The other three residential sites have similar or better results than this with the difference between the

AirSAR and model's HH-VV being 2.5dB, 2.5dB, and 0.7dB for Sites 1, 2 and 4 respectively.

For commercial sites the AirSAR data is different but still comparable to the model. The main difference is that the model's magnitude is generally a little too low for both HH and VV polarisation. Site 5 has a difference between the model and AirSAR data of only 0.2dB for HH polarisation. The largest difference between the AirSAR and model's VV component for Sites 5 or 6 is 2.4dB's. However the difference between the ratio of HH and VV from the AirSAR (3.6dB's) and the model (5.8dB's) for Site 5 is 2.2dB's. For Site 6 the equivalent values are 4.7dB for the AirSAR, and 5.1dB for the model, leading to a difference of only 0.4dB's. This reveals that the difference between the AirSAR and modelled data is not too large considering: (a) the AirSAR relative accuracy is ±0.5dB, and; (b) the estimation difficulties due to the high standard deviation of backscatter (influencing the total magnitude) from similar commercial areas.

7.4.2 Testing the Polarisation Information of the Model (L-band)

This section analyses the model output with respect to the AirSAR data for the polarisation characteristics. The polarisation information presented here are the polarisation signatures, the Total Power (TP), and the Polarisation Index (PI) and the Polarisation Phase Difference (PPD), which numerically describes each signature. The TP, PI and PPD were introduced in Section 5.6, and will be described mathematically in Chapter 8.

This study concentrates on the co-polarisation signatures, without giving any attention to cross-polarisation responses. The reason for this is the same stokes matrix is used to produce both the co- and cross-polarisation signature. Hence if the co-polarised response is similar for different wavelengths, so too will be the cross-polarisation.

Again the six sites will be examined to compare the AirSAR with the model values. The TP, PI, and PPD are taken from the Mueller matrix for a total block defined in Sections 6.3.1 and 6.3.2. For the AirSAR values, the TP, PI, and PPD are calculated from the average Mueller matrix over the whole defined block. Hence, the model and AirSAR TP, PI and PPD are comparable values.

Figures 7.10, 7.11, and 7.12 show the normalised **polarisation signatures** of the AirSAR data, the model, and the absolute difference between the two, for the six sites. As can be seen from the polarisation signatures of the residential areas (Sites 1, 2, 3 and 4), the pedestals for the model are about 10%, or 0.1, too low compared to the AirSAR data. The exception to this is Site 4 which has a similar pedestal height. These low pedestals mean that the RR (right circular transmitted and received) and LL (left circular transmitted and received) polarisations are too low. This can be equated to the double bounce scattering and cross scattering being too low (Dong *et al.,* 1997b).

Hence the model is slightly deficient in one, or both, of these scattering mechanisms. To increase the double bounce scattering (unless it is for a pure conductor where HH equals VV, see Figure 3.10), will increase the HH much greater than the VV. As shown in Table 7.1, the HH was of sufficient magnitude, and it was the VV which was lacking magnitude. So a double bounce addition to compensate VV would substantially alter the HH polarisation, which would not be appropriate.

As the difference signature shows, the largest discrepancy between the AirSAR and model for the residential sites occurs for Site 2 (l60res30), where the difference reaches close to 20%, or 0.2 of the normalised intensity. This is indicating the low VV component which was discussed in the previous section. It also shows that the AirSAR data has a stronger single bounce component than the model is adopting. A strong single bounce component will occur when there is reflection from smooth surfaces near normal incidence, or specular reflection from very rough surfaces where scattering is dominated by reflection from facets oriented perpendicular to the incident wave (Van Zyl *et al.,* 1987).

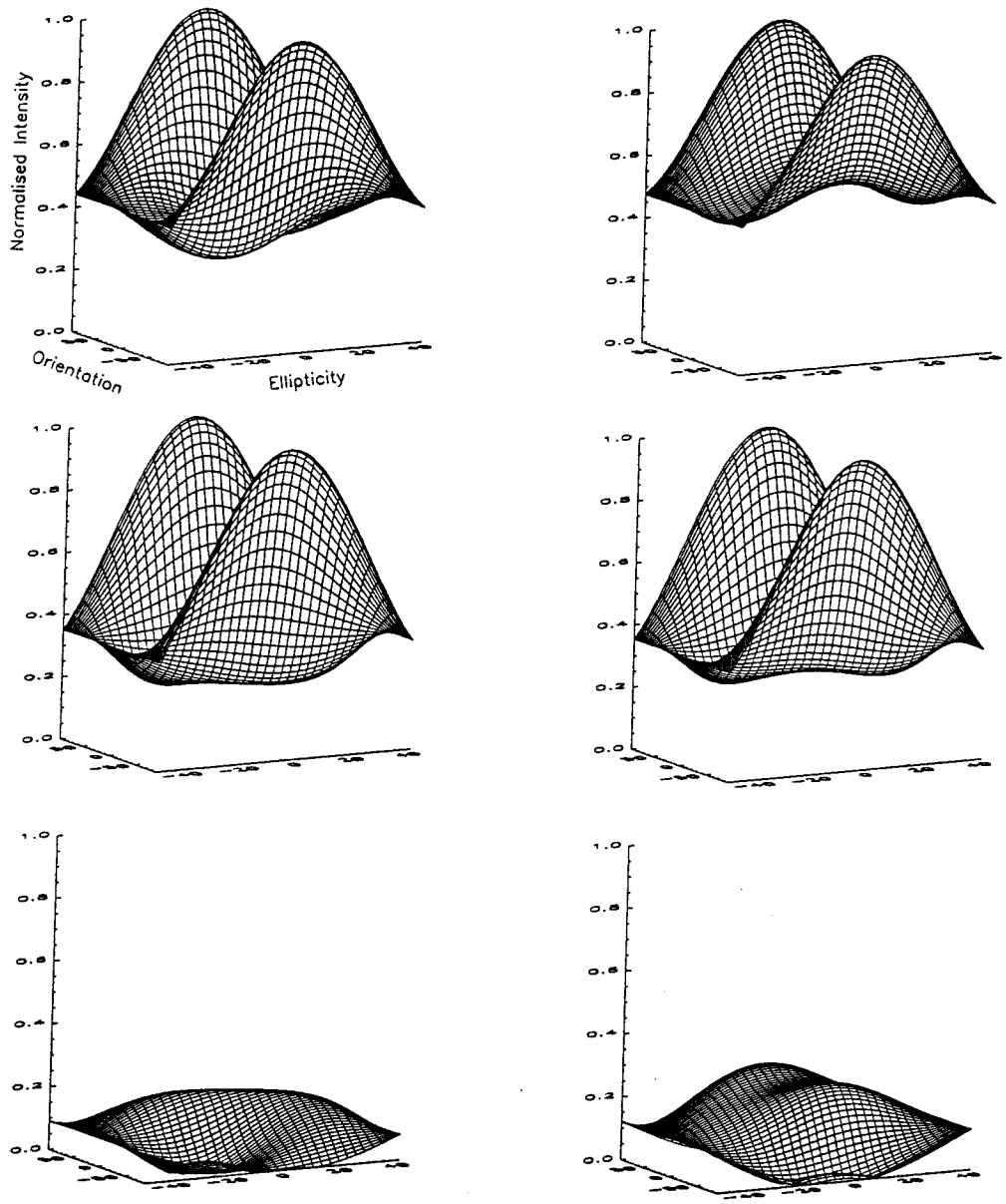

Figure 7.10 Comparison of normalised polarisation signatures from the model and AirSAR data. The top row is the AirSAR polarisation signatures, the middle row is the model polarisation signatures, and the bottom row is the difference between the AirSAR and model signatures. The left column is for Site1 (l61res8), and the right column is for Site2 (l60res30).

The other three residential sites have difference signatures much less then 0.2 of the normalised intensity. The differences between the polarisation signatures become more apparent when the TP, PI and PPD values are examined later.

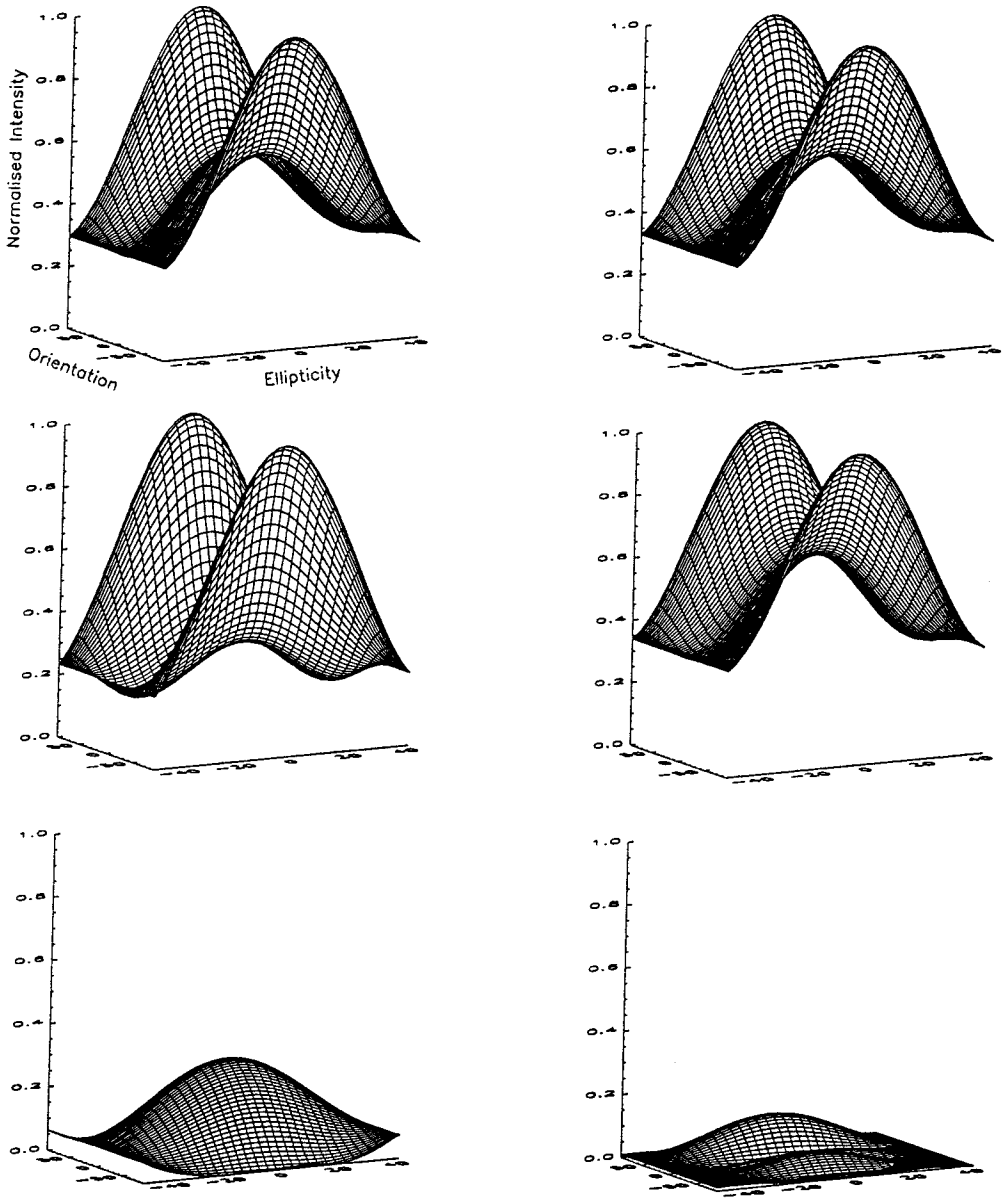

Figure 7.11 Comparison of normalised polarisation signatures from the model and AirSAR data. The top row is the AirSAR polarisation signatures, the middle row is the model polarisation signatures, and the bottom row is the difference between the AirSAR and model signatures. The left column is for Site3 (l30res5), and the right column is for Site4 (l32res45).

The commercial sites again show a reasonable accuracy between AirSAR and model polarisation signatures, with the maximum difference being less than 0.2 or 20% again. The notable differences are that the minima in the model are lower than those in the AirSAR data, especially for Site 6. This could be indicative of more odd bounce scattering in the AirSAR than the model is considering, or it could be related to a small diffuse component in the real data.

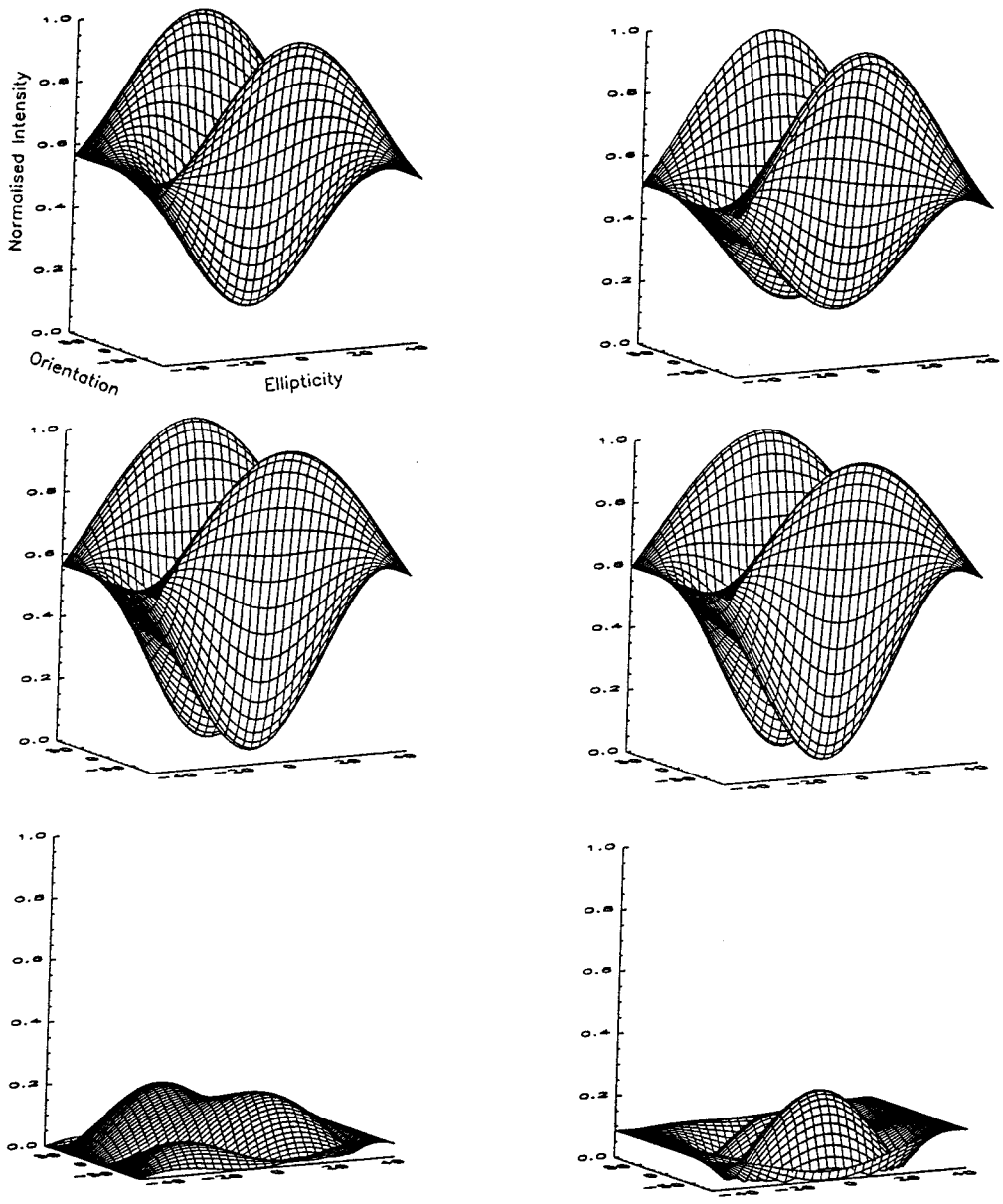

Figure 7.12 Comparison of normalised polarisation signatures from the model and AirSAR data. The top row is the AirSAR polarisation signatures, the middle row is the model polarisation signatures, and the bottom row is the difference between the AirSAR and model signatures. The left column is for Site5 (l48com5), and the right column is for Site6 (l36com6).

Site 5 shows that the maximum difference between the AirSAR and model occur because of the location of the minimum points of the signature. For the AirSAR the minimum points do not occur along the line where the ellipticity is zero (ie., linear polarisation), whereas the model does. For commercial polarisation signatures where the two minima occur where linear polarisation is at ±45° (ie., $\psi=\pm45°$ from Section 3.4.1), the phase difference between the

horizontal and vertical polarisation is close to 180°. For Site 5 the AirSAR polarisation signature, having its two minima off-centred, shows a mild resemblance to a quarter wave reflector having a phase difference of 90° (Hubbert *et al.,* 1992). However, a quarter wave reflector is a perfectly conducting trihedral corner reflector having side lengths of $3\lambda/8$ (Agrawal & Boerner, 1989). Hence the building dimensions are too large compared to the wavelength for this effect to have occurred.

Table 7.2 shows the **total power**, **polarisation index** and **polarisation phase difference** of the AirSAR and Model from the six sites. As the table reveals, the real and theoretical data are quite comparable.

From the residential cases shown in Table 7.2, the real and model data compare well. The total power between the AirSAR and the model are very similar with the largest difference being from Site 4 with an intensity difference of only 0.1. This demonstrates that although the magnitude values of the model, especially for VV, appeared to be generally too low (Table 7.1), the higher HH component increases the total power making it resemble the AirSAR data.

Table 7.2. A comparison of the AirSAR and the model Total Power (TP), Polarisation Index (PI) and Polarisation Phase Difference (PPD) for the six case studies for L-band. The units of the three factors are expressed in intensity, a ratio and degrees respectively. Note that the negative PPD of -177 is still an indication of strong double bounce.

L-Band	AirSAR			Model		
Site No. (description)	TP	PI	PPD°	TP	PI	PPD°
Site 1 (61res8)	0.13	2.1	97	0.13	4.4	96
Site 2 (60res30)	0.11	1.8	1.8	0.10	3.4	38
Site 3 (30res5)	0.47	1.3	1.7	0.46	3.2	5.6
Site 4 (32res45)	0.16	1.3	3.1	0.06	1.6	3.9
Site 5 (48com5)	4.9	2.3	154	4.0	3.7	177
Site 6 (36com6)	3.1	3.0	-177	2.0	3.1	178

The polarisation index for the residential sites of the model give quite good values with respect to the real data for most sites. Site 4 has the smallest difference between the real and theoretical data (of only 0.3). Site 1 has the largest difference (by about 2.3). This is due to the low VV component of the model since the PI is basically the ratio of HH to VV. The polarisation phase difference compares very well between the AirSAR and model value with two of the residential sites (Sites 1 and 4) having a difference of 1° or less. The exception is Site 2 (60res30), where the model's PPD is over 30° too high. This was unavoidable in the model due to the close relationship between Site 1 (61res8) and 2 (60res30). If the PPD for Site 2 was lower, this would reduce the PPD for Site 1. The delicate relationship meant a compromise had to be made. This phase difference is evident in the polarisation signature difference shown in Figure 7.10.

As mentioned earlier, the difference in the normalised polarisation signatures indicates that the AirSAR data has more single bounce than the model is allowing for. A single bounce component reduces the PPD closer to zero, hence the double bounce component, along with the PPD, is too high in the model relative to the real data. The difference between the AirSAR and model PPD's for Sites 1 and 2, being of similar look angles (approximately 60°), could be indicating that the model is not as sensitive to orientation angle as it should be for a particular scattering mechanism. What the scattering mechanism(s) is/are, is unknown. However, this sensitivity appears to be related to the look angle. Sites 3 and 4, having similar look angles (approximately 30°) but differing orientation angles (5° and 45°), show both the model and AirSAR response is less sensitive to orientation angle.

One possible reason for the discrepancy between the model and AirSAR PPD could be the double bounce from the vegetation being modelled a little too high. This is due to the trunk-ground double bounce being independent of the orientation angle. Therefore, as the double bounce from the front wall reduces

with an increase in orientation angle, the trunk-ground response becomes more prominent. Another reason could be that the model does not consider enough single bounce scattering. However, if there was an increase in single bounce scattering, which would have to be independent of orientation angle if it was for vegetation, then the PPD for Site 1 (61res8) would decrease, becoming too low.

The theoretical commercial results also show some resemblance to the real polarisation parameters, except that the TP from the model is a little too low (with a minimum difference of 0.9 for Site 5, and a maximum difference of 1.1 for Site 6). However, as the absolute accuracy of the AirSAR is ±1.2dB (as mentioned earlier) this may be contributing to some difference between the model and AirSAR data. The only large discrepancy here is a 23° difference between the AirSAR and model's PPD for Site 5. This could be suggesting that there is more single bounce in the AirSAR data than the model is acknowledging. Another contributing factor is because of the phase shift, as mentioned earlier when discussing the polarisation signatures. However, as previously noted, the CBD varies greatly for both magnitude and polarisation characteristics in a similar area.

7.4.3 Discussion of Results for L-Band

Although the results are not perfect, as the diagrams show the polarisation signatures from the model do show a strong resemblance in shape to the real data. The results demonstrate that the model has successfully considered the dominant scattering components found in a real urban situation. The magnitudes of the model and the AirSAR data are similar, although the VV component is generally a little too low relative to the HH component. A variety of possible reasons for the discrepancy between the theoretical and real data are discussed as follows.

The low VV in the model could be possibly due to lack of single bounce, or lack of double bounce from a highly conductive material. However, if the amount of

single bounce is increased, through the Metal Factor, the polarisation phase difference becomes too low to be comparable with real data. Double bounce from a purely conducting material does increase both the HH and VV by a constant amount. However, apart from the situation where a hot water cylinder is sitting on a metal "dish" to catch any overflow (which is dependent on the size of the "dish"), there is no reason why there should be double bounce from a metal object independent of orientation angle in a real urban situation. To include this factor would defeat the purpose of trying to model a complex situation into a relatively simple solution. Such a step would be "fine tuning" the model to give more accurate results which are not really justifiable or necessary for classification purposes in an urban environment.

One factor which has not been included in the model but may be responsible for some of the unacknowledged scattering, is the response from television and other antennas attached to building roofs. Antennas are usually long, very thin metallic cylinders situated vertically on the roof, making them independent of the orientation angle. However, double bounce from the antenna and roof would not be strong due to the high proportion of tile roofs (a low dielectric material) in the residential areas, unless there was some other reflecting facet contributing. Vehicles, both moving and parked in the street, will contribute to radar backscatter. Cars have a large proportion of metal in them facing a variety of directions. This could be responsible for some of the backscatter yet unaccounted for, however, such a phenomenon is not considered in the model due to its complexity.

A further reason for the relatively low VV component in the model may be related to the scattering from trees. As can be seen in Figure 7.13, a comparison of the polarisation from trees in the urban model and AirSAR are shown. The AirSAR polarisation signatures for the trees were taken from Centennial Park (a park in Sydney with a look angle of 58°). The area considered has scattered trees since this resembles the tree layout in residential regions. As can be seen, the VV component for the AirSAR data is relatively higher than that for the model.

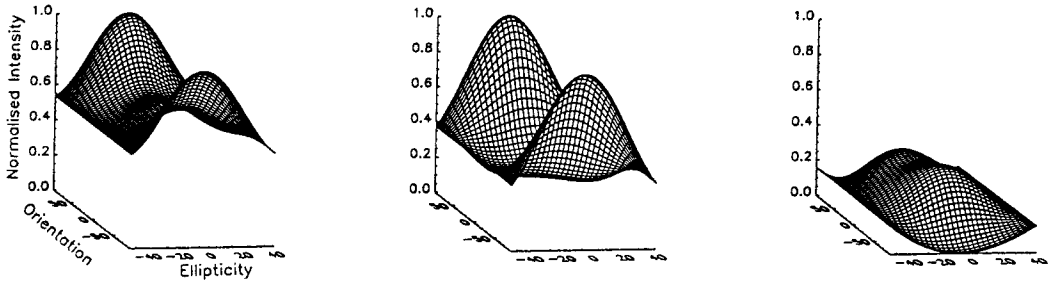

Figure 7.13. (Left) Normalised polarisation signature of scattered trees located in Centennial Park. (Middle) Normalised polarisation signature of model simulation of scattered trees in residential area. (Right) Difference between the AirSAR and model signatures.

It is the lack of single bounce in the model causing this difference between the theoretical and real data for the trees. The absolute difference between the model and AirSAR data is largest in the middle of the polarisation signature, ie., around VV polarisation. Modelling backscatter from vegetation where there a such an extensive variety is a difficult task. Furthermore, results indicate that the structure of trees can have a considerable effect on the radar return for forests (Imhoff, 1995). However, the low VV component is not considered to be a major factor, since the TP, and PPD are giving reasonable results.

As discussed in Chapter 5, the **cross scattering** factor needed further analysis here. S_{hv} was chosen to be half that of the co-polarisations. This is because the foliage was assumed to be randomly orientated and more round than cylindrical in shape. The S_{hv} is not a critical factor in determining the TP, PI and PPD for the model. If S_{hv} is changed from 1/2 to 1/8 of the co-polarisations, the PI and PPD remain unchanged for a building block, and the TP changes by less than 0.01. This change is negligible, hence the S_{hv} is not critical in the classification process.

The Brewster angle could also be responsible for the low VV component. When the incidence angle is close to 60°, a wall-ground structure (having a reasonably low dielectric constant) will result in a much weaker VV polarisation. However, this situation is an integral part of the formulae presented in this

research because it is representing this phenomenon occurring in the real environment.

Another possible reason for the low VV component could be due to **Bragg** scattering. If the extra distance travelled from the source to a surrounding peak, on the surface of an object or ground, is $\lambda/2$, the round-trip phase difference between the return signals from these peaks is 360°, so the signals add in phase; for any other distance not a multiple of $\lambda/2$, the interference is out of phase (Ulaby *et al.*, 1981). Therefore a random surface is divided into its spectral components; and the backscatter return is mainly due to Bragg resonance occurring from the spectral component [$n\lambda/2\sin\theta$] in relation to the incident wave (Elachi, 1988). With reference to Figure 7.14, if $L\sin\theta=n\lambda$ where n is an integer number, then the interference will be constructive. If $L\sin\theta=n\lambda/2$ then the interference will be destructive.

Metal roofs have been known to act as isotropic scatterers, and hence are independent of look direction (Haack, 1988). Weydahl *et al.* (1995) also found many metal roofs and walls, having a profiled, regular surface (such as corrugated iron), caused Bragg resonance.

For Bragg scattering to occur on a corrugated iron roof, not only does the incident angle need consideration, but the orientation angle is also an important factor. A change in orientation angle will directly affect the distance between the two iron peaks. As Figure 7.15 illustrates, the distance between the two peaks is $L=d/\sin\theta$ (where d is the distance between the corrugated iron peaks). The roof slope influences the incidence angle which the radar contacts the roof, this gives an angle of $(\theta-\alpha)$ instead of θ. Hence constructive interference will occur when $\frac{d}{\sin\theta}\sin(\theta-\alpha)=n\lambda$. Similarly destructive interference occurs for $n\lambda/2$.

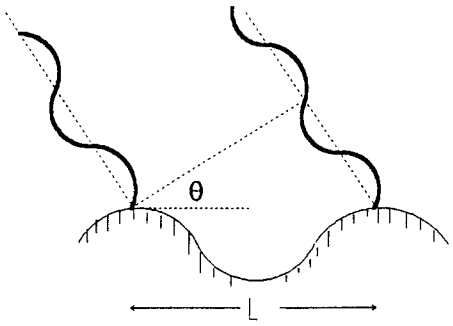

Figure 7.14. Example of Bragg scattering due to constructive interference of the incident wave.

An example of a polarisation signature representing Bragg scattering is shown in Van Zyl *et al.* (1987). Its shape rises to form a peak for VV polarisation, and therefore has a lower HH component. However, this shape is not the same as the difference polarisation signatures for the L-band results shown in this research. Hence, it can be concluded that the Bragg scattering may play a small role in the difference between the real and theoretical data, but it certainly is not the main reason for the discrepancies.

Bragg scattering was not included in the model. Dong *et al.* (1997b) showed through polarisation decomposition that Bragg scattering was negligible for both commercial and residential urban areas. The results reported that for residential land use, there was no Bragg scattering occurring from C-, L-, and P-bands for HH and VV polarisation. For commercial land uses, Bragg scattering was also minimal for L- and P-band. However for C-band Bragg scattering was evident, which will be addressed later.

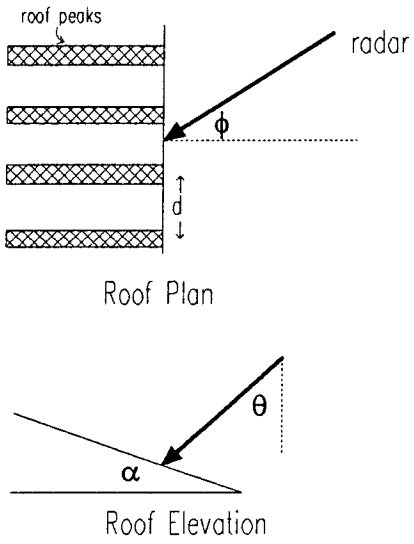

Figure 7.15. An illustration of Bragg scattering on a corrugated iron roof with respect to the radar incident wave.

The large variety of building characteristics in a real urban environment, leading to inaccuracies in parameter estimation, could be a further reason for differences between the real and theoretical data. Sieber (1985) found that statistical presentation of selected housing areas were different depending upon: (a) roof type present; (b) housing density, and; (c) the percentage of vegetation surrounding the houses.

The slope of the ground would also be a factor responsible for change in radar's scattering effects from simulated model conditions. The model has made the assumption that the building wall is perpendicular to the ground. This may be approximately correct for most situations, including the test sites used, but is certainly not true for all, especially for Sydney which has a considerable amount of undulating terrain in some areas.

The L-band results, although not perfect, are still very promising for application to an urban classification.

7.5 Detailed Comparison of the Model and AirSAR Data for Magnitude and Polarisation Information using P-band

Until now the model has concentrated on L-band since this is the middle wavelength available in AirSAR data. This section examines how well theoretical simulations resemble real data for P-band. The method of analysis is similar to the previous section for L-band. The same six case studies are used, and comparisons are made between the magnitude and polarisation signatures of the AirSAR and model simulations representing the same area.

The results presented here for P-band are similar to those for L-band both for AirSAR and model data, apart from a few magnitude differences. However, the P-band simulation will not be as accurate as the L-band results. This is because any parameters dependent on the wavelength have been calculated for L-band. The main parameters which have been calculated for L-band are the dielectric constant, and the canopy parameters. Though it is expected to make little difference between L- and P-band parameters, the overall discrepancies may lead to notable differences.

7.5.1 Testing the Dielectric Constant and Vegetation Parameters for P-Band

To test how a change of wavelength from L- to P-band will affect the **dielectric constant**, the residential building wall is used. The steps and formulae used here have been given in detail in Section 6.5.1, except that P-band is now the wavelength used. The dielectric constant for a building wall without metal has been given as 4+0.4i and the building roughness has an rms of 0.002m. This gives an R_h^2=0.20 and an R_v^2=0.04. From Equation 6.1, the backscatter from the wall without metal included is σ_{ma}=0.062 and 0.013 for horizontal and vertical polarisation respectively.

The amount of metal in a residential building wall has been estimated to be $0.1m^2$. If the dielectric constant for the wall (brick) is 3.4+0.1i (given in Chapter 6), and a brick is 0.1 metres wide, then P_s=0.88. This gives the backscatter from $0.1m^2$ of metal to be σ_{me}=0.009. The total backscatter from the wall, including metal is $\sigma_{tot}=\sigma_{ma}+\sigma_{me}$, giving σ_{tot}=0.707 for horizontal polarisation and 0.02 for vertical. The new reflection coefficients become R_{hn}^2=0.23 and R_{vn}^2=0.07. A dielectric constant of 4.8+0.5i for the wall gives R_{hw}^2=0.24 and R_{vw}^2=0.06.

Hence for P-band the calculated dielectric constant for a residential building wall is 4.8+0.5i. This is similar to ε_w calculated for L-band in Section 6.3.1.4, which was 4.5+0.5i. Since the dielectric constant is not determined to any high accuracy, it can be concluded that it remains reasonably constant for different wavelengths.

There were no values available for the volume scattering coefficient ρ or the attenuation coefficient α for the **tree canopies** at P-band. No measurements were able to be made to compensate for it. Instead, the values for L-band were used. If extrapolation was used, it appears that ρ and α would reduce in value below those for the L-band. This is because these parameters decrease as the wavelength increases from X- to L-band (Kolawole, 1992). However, a backscatter response from trees is only slightly lower for P-band than L-band. Dong *et al.* (1995) performed some simulations of the volume attenuation from a number of different forest stands for both L- and P-bands. The results indicate that the volume attenuation changes by much less than a decibel from L- to P-band over the same stands.

Although substitution of ρ and α, from L-band into P-band for vegetation backscatter, is obviously not as ideal as direct measurements, the scattering effects from the canopy at L-band are not too significant. Therefore this approach is satisfactory for testing the model. In order to justify such a decision, a number of polarisation signatures were obtained from the AirSAR

data over park areas containing scattered trees. The HH and VV responses are shown in Table 7.3. As the table reveals, the responses of the L- and P-band are only slightly different, if not the same, for all examples.

Table 7.3. Backscatter from HH and VV polarisation for L- and P-band from three vegetation sites located in Sydney park land.

AirSAR	L-band		P-band	
Site No. (description)	HH int	VV int	HH int	VV int
Site 1 (semi-scattered)	0.18	0.14	0.17	0.12
Site 2 (moderately dense)	0.19	0.12	0.18	0.12
Site 3 (scattered)	0.09	0.06	0.08	0.05

Two of the AirSAR polarisation signatures of the same area can be seen in Figure 7.16. As these signatures show, the shapes of the L- and P-band responses from real data are very similar. Hence, it can be concluded that the use of L-band parameters (α and ρ) is sufficient for modelling P-band vegetation.

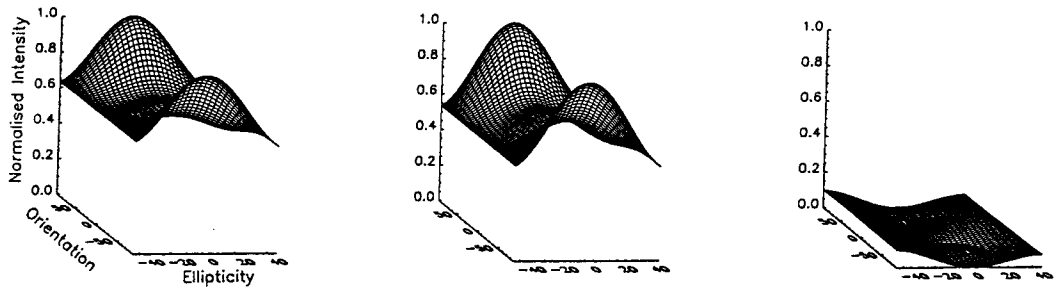

Figure 7.16. Comparison of AirSAR normalised polarisation signatures for P- (left) and L-band (middle) of scattered trees. Their absolute difference between the two is also shown (right).

7.5.2 Testing the HH and VV Responses of the Model (P-band)

The magnitude from HH and VV polarisations have been calculated for both the theoretical and real data for P-band. These results are shown in Table 7.4.

For the **residential** sites, the results are not quite as accurate as for L-band. The smallest difference between the AirSAR and model for HH polarisation is 0.2dB (for Site 2), however the largest difference is 3dB (for Sites 3 and 4). For VV polarisation, the minimum difference is 1.9dB (for Site 2) and the maximum difference is 3dB (for Site 1). Apart from Site 3, the VV component from the model simulation of residential sites is too low relative to the HH magnitude, similar to the L-band results.

Although the absolute differences appear to be large between the AirSAR and model, the given AirSAR accuracy for P-band of ±1.9dB (Dubois *et al.,* 1995) shows that the discrepancies are not great. There is a trend for the P-band model results to be a little too low, as was the case for the L-band results. The relative differences, ie., between the HH-VV, are larger here than for L-band. Site 3 has the largest difference, however for Site 4, the relative difference between the HH and VV for the AirSAR and model is 0dB. This indicates that the relationship between the HH and VV polarisation for the model is the same as that for the AirSAR.

Table 7.4. A comparison of the AirSAR HH and VV polarisation for P-band, with the model simulation output for six case studies. The results are expressed in intensity and (Decibels).

P-Band	AirSAR		Model	
Site No. (description)	HH int (dB)	VV int (dB)	HH int (dB)	VV int (dB)
Site 1 (61res8)	0.32 (-4.9)	0.16 (-7.9)	0.26 (-5.8)	0.08 (-10.9)
Site 2 (60res30)	0.16 (-8.0)	0.11 (-9.6)	0.15 (-8.2)	0.07 (-11.5)
Site 3 (30res5)	0.79 (-1.0)	0.65 (-1.9)	1.6 (2.0)	0.67 (-1.7)
Site 4 (32res45)	0.16 (-7.9)	0.13 (-8.9)	0.08 (-10.9)	0.07 (-11.5)
Site 5 (48com5)	4.9 (6.9)	2.5 (4.0)	12.4 (10.9)	3.2 (5.1)
Site 6 (36com6)	4.4 (6.4)	2.1 (3.2)	8.9 (9.5)	2.7 (4.3)

Site 3 (30res5) has the largest relative difference between the HH and VV polarisation for the AirSAR and model data. The HH and VV difference for the AirSAR is 0.9dB's, and for the model is 3.7dB's. This gives a difference of

2.8dB between the real and theoretical data. The relative accuracy between the polarisations of the P-band AirSAR data is ±1.3dB (Dubois *et al.,* 1995). Hence, the model's discrepancy is outside the expected accuracy of the real data, by 1.5dB. Mathematical reasons for the low VV response from the model, as explained for L-band in Section 7.4.3, could be due to either a deficit of single bounce, or potentially a lack of double bounce from a pure conductor.

The results for the two **commercial** areas show large discrepancies between the model's magnitude and the AirSAR data, with the model's HH polarisation being much higher. The largest difference occurs for Site 5 where the HH difference between the AirSAR and model is 4dB. The VV results are more comparable with the difference being 1.1dB for both Sites 5 and 6. It is expected that the magnitude of the backscatter changing from L- to P-band will decrease. This is because the longer wavelengths "see" the surfaces as smoother so the reflection will be more specular. Any reflection away from boresight is expected to reduce for longer wavelengths. The AirSAR data shows this phenomenon, but the model does not.

These high HH backscatter results from the model for commercial areas, indicate one case where the model is a little weak. Due to the use of the *sinc* function ie., $\mathrm{sinc}\left(k_o L \sin\theta \sin\phi\right)$, the model is sensitive to the length of the building L with respect to the wave number k_o (refer to Equations 3.2 and 3.6). As mentioned earlier, oscillations result in the total backscatter value with respect to a varying parameter, such as L, θ, or ϕ. This is due to phase effects of the radar wave along the extremes of the wall. As the length of the building increases, the backscatter from P-band eventually becomes lower than L-band as the phase effects subside. However, it has yet reached this stage in the model with the building dimensions. The reason that this effect in the model is evident for the commercial class, and not the residential class, is because the double bounce from the commercial building wall is the dominant scattering mechanism.

7.5.3 Testing the Polarisation Information of the Model (P-band)

The normalised **polarisation signatures** for the six sites are shown for P-band in Figures 7.17, 7.18 and 7.19. Their shapes are very similar to those of L-band over the same areas. As can be seen from the polarisation signature differences, the polarisation information is not as accurate as for the L-band results.

In a residential area the measured polarisation signatures of both L- and P-band are very similar because, for urban areas, all the odd and double bounce structures appear identical to both L- and P-band radar (Dong *et al.,* 1997b). It is worth noting how the backscatter decreases more for P-band than for L-band as the orientation angle increases. This is for both the real and theoretical data. As previously mentioned, the P-band will have a more specular scatter, so as the orientation angle increases (and the angle of incidence moves further from perpendicular to the building surfaces), the backscatter decreases more rapidly for P- than L-band.

In reference to Figures 7.17 and 7.18, one of the notable differences between the AirSAR and model output, for the residential areas, is that the pedestal height for the AirSAR data is higher than that of the model. As mentioned in the previous section, the reason for the high pedestal is a high double and/or cross scattering component. As Dong *et al.* (1997b) indicate, the double bounce is a little stronger for P- than for L-band. A further explanation of this low pedestal in the model will be examined in Section 7.5.4.

Site 1 has a model polarisation signature comparable to the real data, with the maximum difference less the 20%. However, Site 2 has a much larger discrepancy. Its maximum difference is closer to 30% of the normalised intensity, the main reason being the difference in pedestal height.

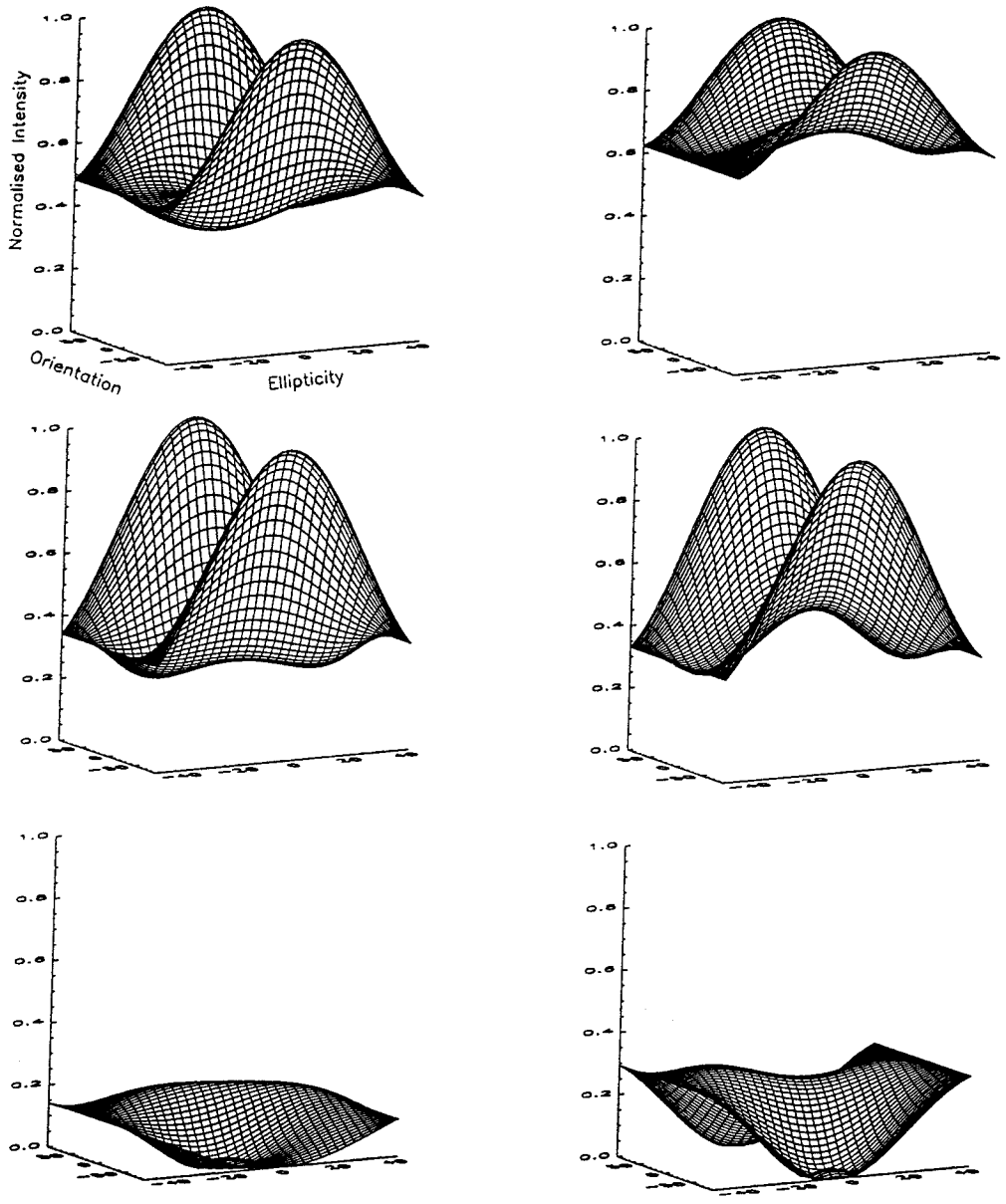

Figure 7.17. Comparison of normalised polarisation signatures from the model and AirSAR data. The top row is the AirSAR polarisation signatures, the middle row is the model polarisation signatures, and the bottom row is the difference between the AirSAR and model signatures. The left column is for Site1 (p61res8), and the right column is for Site2 (p60res30).

Site 3 in Figure 7.18 shows the model and AirSAR polarisation signatures are similar in shape. Again there is a discrepancy in pedestal height, however the main difference is due to the VV component of the model being a too low. Site 4 has the largest discrepancy between the model and AirSAR data, approaching 40% (or 0.4 of the normalised intensity). The main reason for this is once again due to the pedestal height. Site 4 has a large orientation angle of 45°, therefore it would be expected that more cross scattering would be

contributing to the total backscatter since specular return from building facets would be low. As the polarisation signature difference shows, the model does not account for enough of this factor.

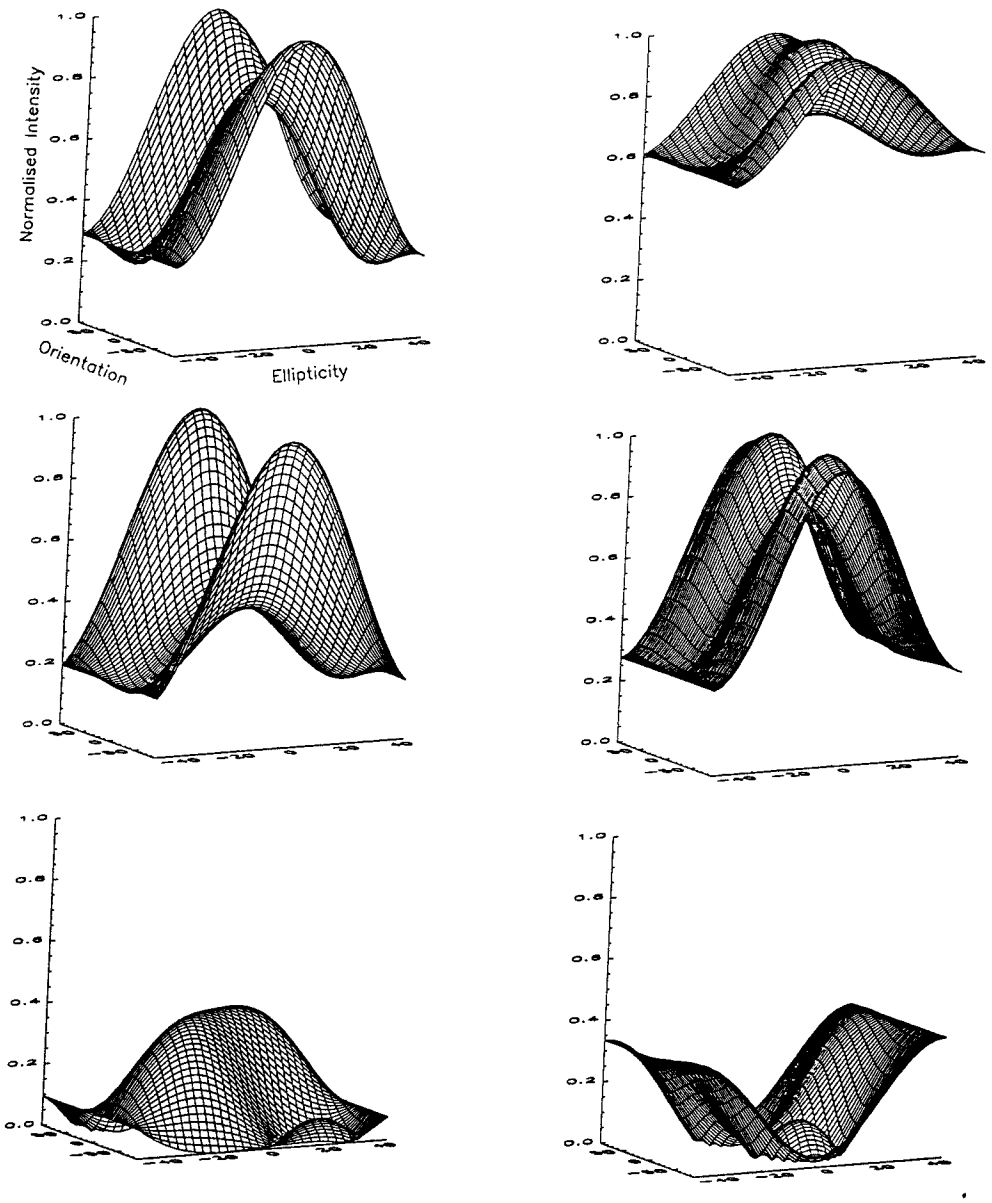

Figure 7.18. Comparison of normalised polarisation signatures from the model and AirSAR data. The top row is the AirSAR polarisation signatures, the middle row is the model polarisation signatures, and the bottom row is the difference between the AirSAR and model signatures. The left column is for Site3 (p30res5), and the right column is for Site4 (p32res45).

The polarisation signatures of the commercial areas are shown in Figure 7.19. As the difference signatures show, there are discrepancies between the AirSAR and model of up to 30%. As for the L-band results, the minimums from the model polarisation signatures are a little too low compared to the real data, one possible explanation for this is that the model does not consider enough single bounce scattering. The main reason for the differences however,

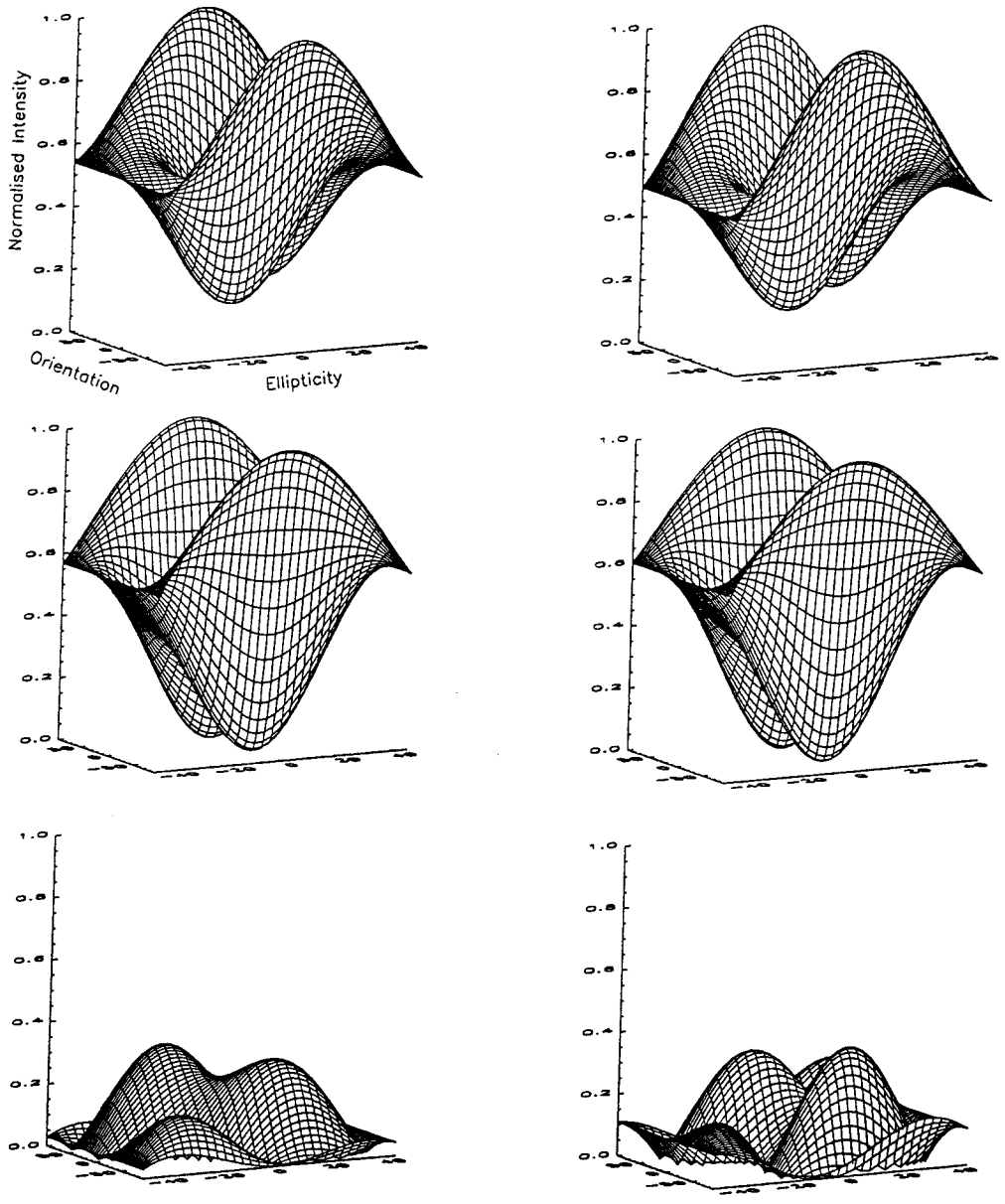

Figure 7.19. Comparison of normalised polarisation signatures from the model and AirSAR data. The top row is the AirSAR polarisation signatures, the middle row is the model polarisation signatures, and the bottom row is the difference between the AirSAR and model signatures. The left column is for Site5 (p48com5), and the right column is for Site6 (p36com6).

is due to the minima of the AirSAR data being off-centred from the line where the ellipticity is zero. Possible reasons for this phenomenon are unknown, however many complex structures are found in a commercial environment which may be responsible.

The **total power**, **polarisation index** and **polarisation phase difference** are shown in Table 7.5 for P-band. Although the model gives an HH backscatter up to 4dB too high for a commercial site, there still may be potential for its use in classifying the urban environment. This is because the total power is the important factor in the classification process. The model's total power may reduce due to the reasonable VV value. The TP, PI and PPD for P-band were determined in the same manner as for L-band.

Table 7.5. A comparison of the AirSAR and the model Total Power (TP), Polarisation Index (PI) and Polarisation Phase Difference (PPD) for the six case studies for P-band. The units of the three factors are expressed in intensity, a ratio and degrees respectively. Note that the negative PPD's around -30 is an indication of reasonably strong single bounce.

P-Band	AirSAR			Model		
Site No. (description)	TP	PI	PPD°	TP	PI	PPD°
Site 1 (61res8)	0.13	1.8	98	0.09	3.4	26
Site 2 (60res30)	0.08	1.3	-23	0.06	2.1	6.6
Site 3 (30res5)	0.39	1.2	-37	0.58	2.4	2.9
Site 4 (32res45)	0.10	1.2	-29	0.05	1.2	0.9
Site 5 (48com5)	1.9	2.1	129	3.9	3.9	178
Site 6 (36com6)	1.6	2.2	115	2.9	3.2	178

For the residential sites the total power output from the model are quite comparable to the real data, with a minimum difference of 0.02 (intensity) for Site 2, and a maximum of only 0.19 (intensity) for Site 3. The greatest difference for the PI is 1.6 which is reasonable. However it is the PPD where large discrepancies between the model and AirSAR show. Site 1 has a very large difference between the AirSAR and model PPD, with the model being 72°

too low. Apart from Site 1, the PPD for the AirSAR data is lower than the model results. These differences are between 30° and 40° too low.

The discrepancy between the PPD for the real and model data is suggesting that the model is not sufficiently sensitive to the orientation angle for one or more scattering mechanisms. For Site 1, the model PPD is too low indicating that there is either insufficient double bounce in the model or too much odd/single bounce occurring. The difference signature between the real and theoretical data does not show that such a large PPD difference exists since the signatures are reasonably similar.

For Sites 2, 3 and 4, the main differences between the model and AirSAR data is that the model has a low pedestal height, and the VV component is too low relative to HH polarisation. The generally high model PPD, with respect to the real data, must be a result of this discrepancy, and is evident in the polarisation signatures shown is Figures 7.17 and 7.18.

As mentioned earlier, the pedestal height is related to the double bounce and cross scattering (Dong *et al.,* 1997b). The more double bounce there is, the further the PPD moves from 0°. Hence, the AirSAR data may have more double bounce than the model is anticipating. This could be one explanation for the difference between the model and AirSAR PPD. The other reason could be due to a higher cross scattering occurring. The model was assuming that due to the long wavelength of P-band, there would be more specular, and less cross scattering than for the shorter wavelengths. P-band would be expected to have little interaction with the canopy. As the real data shows, cross scattering may be occurring from either the building or vegetation components.

Even though these discrepancies exist, the resulting difference between the total power of the AirSAR and model has a maximum of only 2.0 (intensity). The PI are also comparable with the largest difference being 1.8. The PPD is where the discrepancy lies. For the commercial sites the maximum difference between

the real and theoretical data is 63°, and as mentioned earlier the reason for this is the phase shift of the real data from 180°.

7.5.4 Discussion of Results for P-Band

In summary, the P-band theoretical results are less accurate those for L-band. The model is demonstrating that the general magnitudes, and polarisation shapes are comparable to the real data. However, it appears that the main reason the P-band is not performing as well as for the L-band is due to the higher pedestal height of the AirSAR data for residential areas, and the PPD phase shift away from 180° for the commercial areas. There are many possible reasons for these phenomenon occurring. Some of these reasons will be suggested in the following. The results basically conclude that the complexity of the urban environment is the main reason for these differences between the AirSAR and model results.

The cross-polarised returns are produced by: (a) quasi-specular reflection occurring due to the difference between the Fresnel reflection coefficients for a two dimensional, smoothly undulating, homogeneous surface; (b) multiple scattering from the surface roughness of the target; (c) multiple volume scattering due to inhomogeneities of the target surface, and; (d) non-isotropic characteristics of the targets (Ulaby & Elachi, 1983).

One would not expect much cross scattering from the ground since a reasonably large percentage of the ground is road, ie., asphalt. Even for wavelengths as small as C-band, the backscattering coefficient from asphalt for VV, HH, and HV polarisation are less than -15dB for incidence angles greater than 30° (Ulaby *et al.*, 1981).

Parkland has a relatively flat polarisation signature with a high pedestal. This is due to the reasonably high unpolarised return from the area (Evans *et al.*, 1988). The model has not considered the rear open spaces of buildings to be

extensive in size, but even so, their response may contribute a little to the pedestal height, even if the surrounding roads, and concrete do not. The rougher the surface, the higher the pedestal would become (Zebker & Van Zyl, 1991). However, for P-band, being a longer wavelength than L-band, the surfaces would appear smoother and the pedestal would not be expected to increase due to surface roughness. Hence, the pedestal height in the AirSAR may be due to some other reason.

The buildings modelled in this research have only been of simple shape. Hussin (1994) found that architecturally complex buildings had a reasonably high HV component for L-band. Hence, there is no reason why this may not also be the case for P-band.

Many built structures contain metal components whose high conductivity makes them good radar scatterers, furthermore corner reflector structures result from built components such as window frames, doorways, and chimney-roof junctions (Ulaby *et al.,* 1981). The height required for an object to behave as a corner reflector to the radar wavelength, and "to what degree building walls at certain orientations will cause multiple reflection remain unknown" (Xia & Henderson, 1997, p96). However, according to Ruck *et al.* (1970), multiple scattering is a major contributor to depolarisation for many objects.

Not only do buildings contribute to the total backscatter in an urban environment, but so do other structures. Metal structures (such as metal bridges, utility poles, and other such features) when oriented correctly with respect to the radar incident wave, contribute to strong radar returns (Xia & Henderson, 1997)

There are a lot of difficulties when considering all cross scattering possibilities in an urban model. For simulation of an entire urban scene (ie., the target and its environment), diffuse and deterministic reflections must be combined. However, to achieve this, a thorough knowledge of all the elements of the

scene is required, which is generally not so when the target under study is the only well-known object (Nasr & Vidal-Madjar, 1991).

Even though the modelled P-band does not perform as well as the L-band. The model's output still indicates a resemblance to the real data.

7.6 Detailed Comparison of the Model with AirSAR Data for Magnitude and Polarisation Information using C-Band

C-band wavelength appears to be less predictable than the longer wavelengths. The shorter wavelengths are more susceptible to diffuse scattering, and hence react in a less specular way and in a manner more difficult to forecast. This is because the shorter wavelengths "see" a building wall as being rougher than the longer wavelengths so the reflection is not as specular. The shorter wavelengths also interact with the tree foliage to a greater extent than for L- and P-band.

7.6.1 Testing the HH and VV Responses of the Model (C-band)

Table 7.6 shows the magnitude of the AirSAR and model results from the same six sites used for L- and P-band wavelengths. However, no explanation will be given about the magnitudes because, as the polarisation information will show, there are large discrepancies between the real and theoretical data.

7.6.2 Testing the Polarisation Information of the Model (C-band)

As can be seen from the **polarisation signatures** of the model and AirSAR data (Figures 7.20, 7,21 and 7.23), the model's results are very different to the real data for residential areas, especially for a look angle around 60°. The polarisation signatures from the real data are following similar trends to the results from longer wavelengths. The reason for this occurrence is unknown.

Table 7.6. A comparison of the AirSAR HH and VV polarisation for C-band, with the model simulation output for six case studies. The results are expressed in intensity and (Decibels).

C-Band	AirSAR		Model	
Site No. (description)	HH int (dB)	VV int (dB)	HH int (dB)	VV int (dB)
Site 1 (61res8)	1.12 (0.5)	0.40 (-3.9)	1.57 (1.9)	1.57 (1.9)
Site 2 (60res30)	0.53 (-2.7)	0.30 (-5.2)	1.57 (1.9)	1.57 (1.9)
Site 3 (30res5)	0.87 (-0.6)	0.82 (-0.9)	1.65 (2.2)	1.65 (2.2)
Site 4 (32res45)	0.82 (-0.9)	0.58 (-2.3)	1.57 (1.9)	1.57 (1.9)
Site 5 (48com5)	9.7 (9.9)	9.6 (9.8)	10.2 (10.1)	3.8 (5.8)
Site 6 (36com6)	7.4 (8.7)	6.6 (8.2)	7.8 (8.9)	3.5 (5.4)

For Sites 1 and 2, the AirSAR polarisation signatures are indicating a reasonably strong double bounce response from a dielectric material. The backscatter from a building wall is not expected to be as significant due to the roughness of the ground and building wall, reducing the backscatter strength for this shorter wavelength. Hence, one would assume that the scattering from C-band would be more diffuse than the longer wavelengths, and show a stronger response from the trees.

The model is showing that the backscatter response is due to the scattering from the vegetation. This was expected because it has been found that the "shorter wavelengths produce more volume scattering from vegetation canopy and conceal, partially hide, or obscure signals from cultural features" (Xia & Henderson, 1997, p94). For C-band, one would expect that most of the radar interaction will be at the canopy layer. The degree to which any penetration will occur is dependant upon the canopy density, but for C-band it is likely to concentrate on the upper layers (Schumann, 1996).

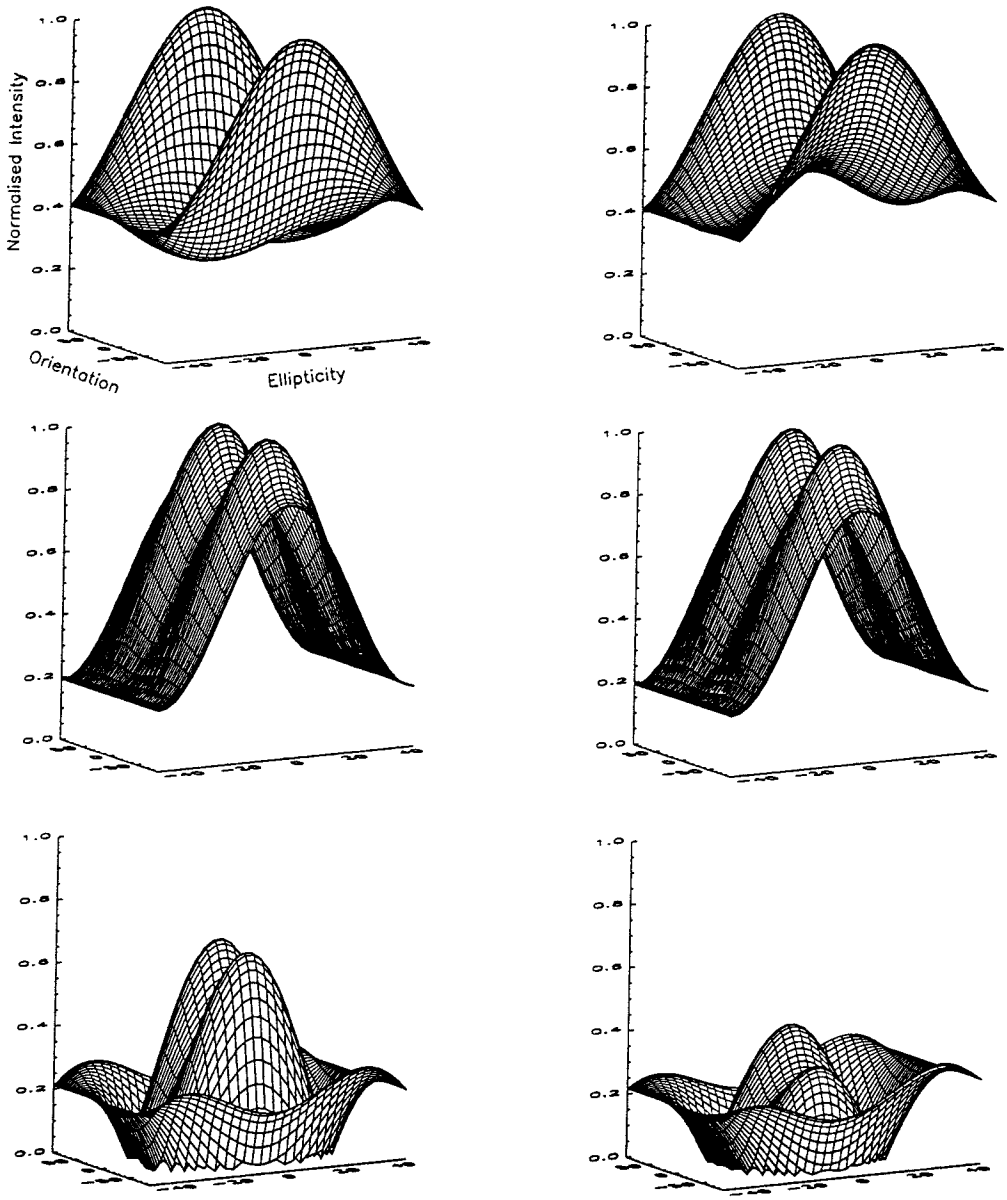

Figure 7.20. Comparison of normalised polarisation signatures from the model and AirSAR data. The top row is the AirSAR polarisation signatures, the middle row is the model polarisation signatures, and the bottom row is the difference between the AirSAR and model signatures. The left column is for Site1 (c61res8), and the right column is for Site2 (c60res30).

A low amount of canopy penetration will reduce the trunk-ground double bounce effect for the shorter wavelengths (Richards, 1990), so this cannot be contributing greatly to the double bounce scattering in the AirSAR data. It was found that for C-band, about 70% of backscatter from trees (Beech and Spruce in this case) is due to volume scattering, about 25% was due to surface scattering, while double bounce contributed to less than 5% (Seifert *et al.*, 1996).

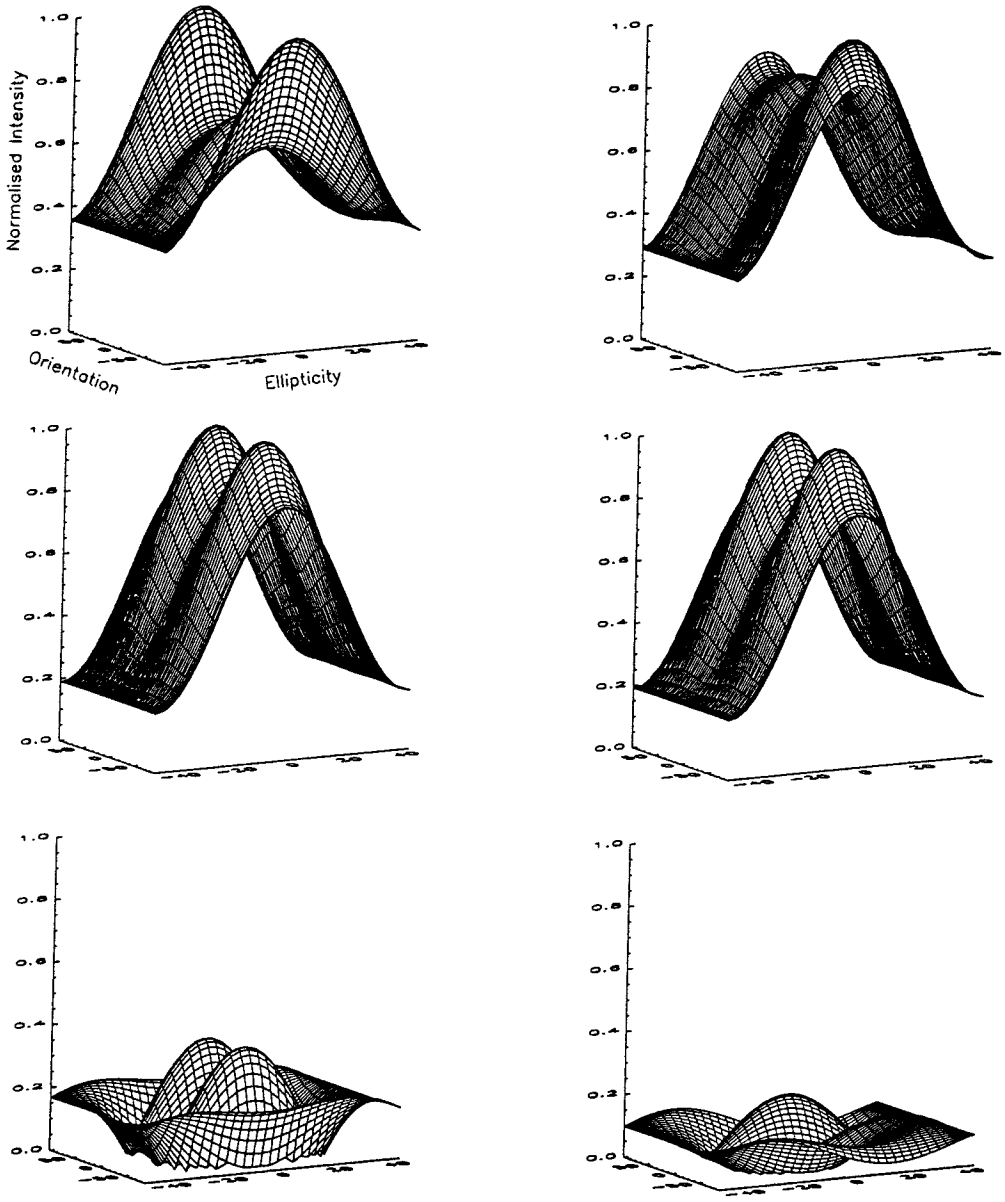

Figure 7.21. Comparison of normalised polarisation signatures from the model and AirSAR data. The top row is the AirSAR polarisation signatures, the middle row is the model polarisation signatures, and the bottom row is the difference between the AirSAR and model signatures. The left column is for Site3 (c30res5), and the right column is for Site4 (c32res45).

Site 3 for the AirSAR is giving a similar response to the longer wavelengths, whereas Site 4 is showing a much better comparison between the model and AirSAR. Site 4 has an orientation angle of 45° so most of the scattering would be expected to come from the vegetation, as both the AirSAR and model demonstrate. The AirSAR polarisation signature for Site 4 (c32res45) does give a response more similar to the model, with normalised differences being well less than 20%. A possible reason for this could be that the double bounce from

the residential building wall for real data becomes too small so canopy scattering may be more dominant in this situation.

As just mentioned, the polarisation signatures from the model for residential sites show a stronger resemblance to scattering from vegetation at C-band. As discussed by Dong *et al.* (1997b), for sparse tree cover, the odd bounce dominates for C-band. A polarisation signature was taken from Centennial Park for scattered timber at C-band (refer to Figure 7.22). This result also indicates that single/odd bounce is the dominant scatterer.

The magnitude of the AirSAR data from the trees is 0.10 (intensity) for HH, and 0.03 for VV, which is much lower than the total magnitude resulting from the residential areas at C-band. From this information it can be concluded that the trees are not responsible for the double bounce scattering which dominates the AirSAR polarisation signatures for C-band. Hence, the double bounce component must come from the residential buildings.

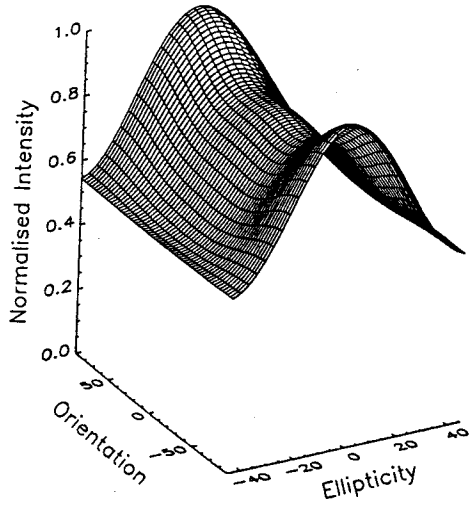

Figure 7.22. Normalised polarisation signature of scattered trees in Centennial Park. The data is taken from AirSAR at C-band.

The problem arises in that the model does not anticipate as much specular scattering from the building due to the shorter wavelength interacting with a

relatively rough surface, both from the ground and walls. However, a simple calculation of the Raleigh Criteria shows that if the building roughness is 0.002m, then for C-band wavelength (0.057m) at 45° incidence angle, H=0.01m (obtained from Equation 3.1). Since H is greater than the wall roughness, the building wall will appear reasonably smooth to C-band.

Vegetation scattering in the model is still quite different from that in the AirSAR data. The main reason for this is most likely because the HV component for cross scattering is not sufficiently accurate. In the model by Kolawole (1991), for scattering from trees, which has been adapted into the model, the canopy requires the power transmittance. Due to the impossibility of determining real measurements of this value, an assumption was made in this urban model that the co-polarisation was one half that of the cross-polarisation (as discussed in Chapter 6). This assumption worked well for the longer wavelengths since canopy scattering is not a dominant factor. However for C-band, this is obviously not so.

Even though the vegetation model for C-band is not entirely accurate, correction to this would still not result in the model giving an appropriate polarisation response compared to real data. This is because the dominant scattering in the residential model for C-band is from vegetation, whereas the real data gives a polarisation signature different in shape to that from scattered trees. This is indicating that the residential buildings are playing a more prominent role in the total backscatter than the model is calculating. The AirSAR data is presenting a stronger double bounce response than the model is allowing for.

Once again the polarisation signatures of the commercial sites demonstrate the unpredictability of shorter wavelengths in the urban environment. As the model's polarisation signatures for Site 5 and 6 show (Figure 7.23), the shapes are reasonably similar to those from the longer wavelengths. However, the real data is different. The AirSAR polarisation signatures for Site 5, in the city, have a very strong VV component, equivalent to HH polarisation. It is again showing

the strong double bounce, and potentially Bragg scattering. As Dong *et al.* (1997b) reported, backscattering from one commercial area was found to contain both double bounce and Bragg scattering as the main scattering components. Site 6, North Sydney, is giving a totally different and unexpected response from the AirSAR data. It is indicating a strong single bounce response. Reasons for this are unknown.

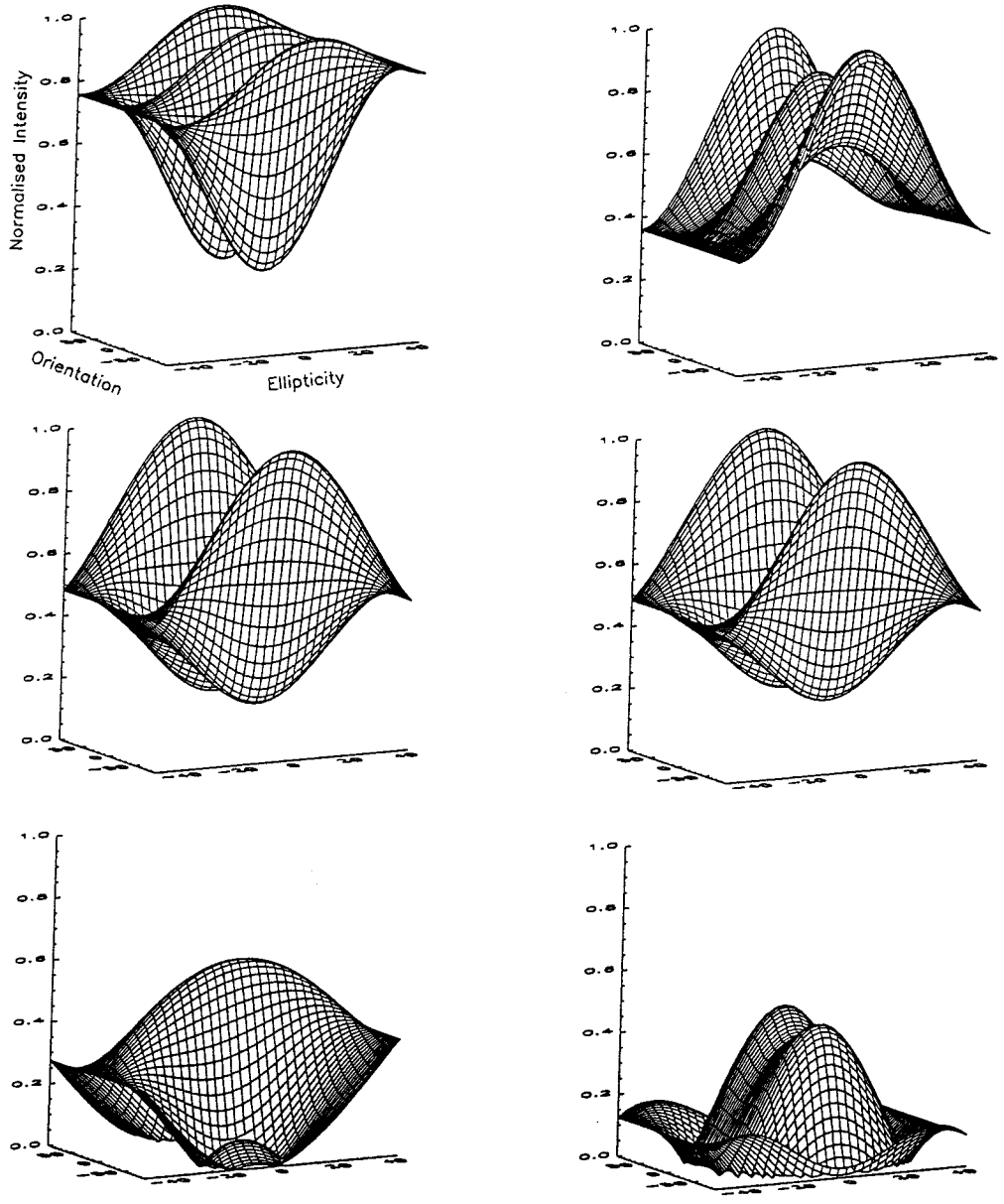

Figure 7.23. Comparison of normalised polarisation signatures from the model and AirSAR data. The top row is the AirSAR polarisation signatures, the middle row is the model polarisation signatures, and the bottom row is the difference between the AirSAR and model signatures. The left column is for Site5 (c48com5), and the right column is for Site6 (c36com6).

Table 7.7 shows the **total power**, **polarisation index**, and **polarisation phase difference** for the six test sites. The comparable results between the model and AirSAR data for the TP, PI and PPD are for Sites 4 and 5. Site 4 shows strong similarities between the AirSAR and model PI and PPD, with the total power having a difference of only 0.5 (intensity). For Site 5 the AirSAR data is showing a strong double bounce effect. This is also reflected in the model, although the VV component is not as strong.

Dong *et al.* (1997b) investigated P-, L- and C-band by analysing the main scattering components for a number of situations. They found that P- and L-band results performed well compared to the C-band. In this theoretical model, the C-band results were very different to L- and P-band. This shows that C-band is the least stable to model in an urban environment since it interacts differently with materials than longer wavelengths.

Table 7.7. A comparison of the AirSAR and the model Total Power (TP), Polarisation Index (PI) and Polarisation Phase Difference (PPD) for the six case studies for C-band. The units of the three factors are expressed in intensity, a ratio and degrees respectively. Note that the negative PPD of -4.5 is an indication of strong single bounce.

C-Band	AirSAR			Model		
Site No. (description)	TP	PI	PPD°	TP	PI	PPD°
Site 1 (61res8)	0.39	2.42	79.8	0.97	1.0	0.0
Site 2 (60res30)	0.25	1.94	16.2	0.97	1.0	0.0
Site 3 (30res5)	0.43	1.33	-4.5	1.0	1.0	0.0
Site 4 (32res45)	0.48	1.09	6.5	0.97	1.0	0.0
Site 5 (48com5)	5.14	1.00	174.4	3.5	2.7	176
Site 6 (36com6)	3.37	1.22	6.5	2.8	2.2	177

Due to the discrepancies between the model and AirSAR data, although some similarities do exist, C-band will not be included in this present model. A greater understanding of C-band is needed before this shorter wavelength can be modelled for an urban environment.

7.7 Using the Model for an Urban Classification

Considering the large number of parameters required when formulating the model for the two classes, as well as the ability of the model to account for orientation and look angles, the theoretical output performs well in relation to the real data for the longer wavelengths.

As this chapter has shown, the model is reasonably predictive for the L-band wavelength, and for residential regions it gives average results for P-band. However, it is quite unreliable for P-band in commercial areas, and for most of C-band. In order to use P- and C-band wavelengths in this model requires a greater understanding of how radar interacts in a complex urban environment (which is still a reasonably unexplored area) and then further development of the model. This further research is not within the scope of this present study.

Even though the original intention of this research project was to formulate a model which was able to perform for P-, L- and C-band wavelengths, the magnitude is the prominent distinguishing factor in the real data. That is, the polarisation signatures for the same urban area are very similar for the three wavelengths. This is demonstrated in Appendix F. Even though the six case studies did introduce some differences between the wavelengths, a more extensive investigation (refer to Appendix F) demonstrates that the general trend shows little difference between wavelengths. The greatest difference is between C-band and the longer wavelengths for commercial areas.

Dong *et al.* (1997b) mathematically defined the different scattering mechanisms present in residential and commercial land uses, for P-, L- and C-bands. The results demonstrate that there are differences between wavelengths, but these are not great, especially between L- and P-band. Hence, the use of three different wavelengths in the microwave region for providing polarisation information in the urban environment may prove to be only a little more useful than a single wavelength, in this case L-band.

The magnitude of the backscatter from an urban area is different for C-, L- and P-band. The response from C-band is higher than both L- and P-band for both residential and commercial classes. Similarly L-band is higher than P-band. Again this does not appear to provide additional information to help distinguish between land uses, in this case residential and commercial, than a single wavelength. Figures 7.24 and 7.25 demonstrate this point by plotting the HH and VV backscatter from AirSAR data for C-, L- and P-band for the six urban case studies presented in this chapter.

As Figures 7.24 and 7.25 show, there is little change in the relationship between the C-, L- and P-bands for the different residential and commercial sites, and polarisations. The one notable difference is the change in the order of backscatter magnitude from the three wavelengths for Site 5 (48com5). The HH graph shows that L-band is the strongest, then C- and P-band. This is in contrast to the VV component which has the C-band relatively high compared to L- and P-band.

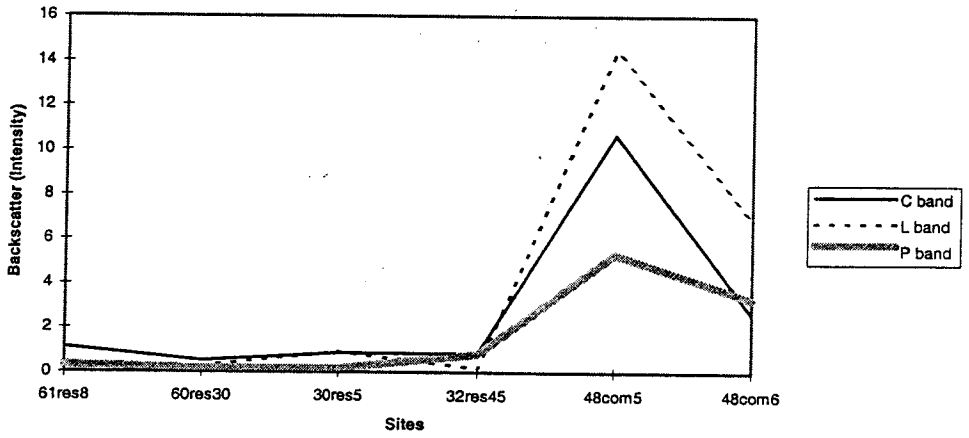

Figure 7.24. Comparison of backscatter for HH polarisation for P-, L-, and C-band for the six test sites introduced in the earlier part of this chapter

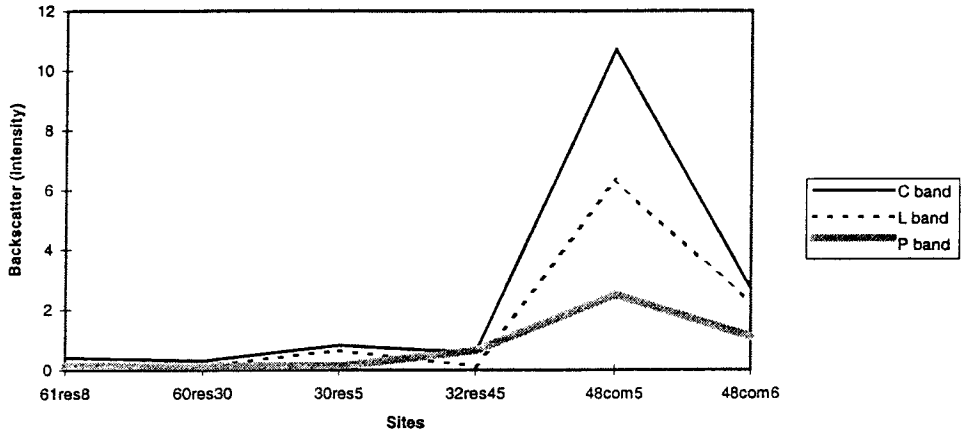

Figure 7.25. Comparison of backscatter for VV polarisation for P-, L-, and C-band for the six test sites introduced in the earlier part of this chapter

The relatively high VV component, compared to the HH polarisation, for C-band in commercial regions may be a useful factor in distinguishing between classes. As Section 7.6.1 showed, the intensity of the backscatter for C-band from a commercial area has an equal or higher VV component relative to the HH component. This is different for L- and P-bands which have HH as the stronger component.

Unfortunately this factor cannot be used at present as the model is not capable of modelling C-band accurately. However, this appears to be one of the only distinguishing factors making the use of multiple microwave wavelengths in the classification process more beneficial than a single band. Hence, the classification process will concentrate wholly on L-band.

The model simulations performed well for L-band with respect to the TP, PI, and PPD. These three factors will now be used to classify an urban environment. Chapter 8 will introduce the method and formulae used for the classification process, and then present the results of a classification determined over some Sydney sites using the L-band results calculated from the model.

8. USING THE MODEL TO CLASSIFY A REAL URBAN ENVIRONMENT

8.1 Urban Classification using Radar

When performing a classification on urban land, the problem arises as to the physical characteristics of each land use class. The radar images only the physical structures, irrespective of land use. Confusion often arises between land use and actual land cover. Anderson *et al.* (1972, p2) defines land use as "man's activities on land which are directly related to the land". Whereas land cover is a term which is defined as "the vegetation and artificial constructions covering the land surface."

Hence one of the fundamental classification problems is attempting to predict urban land use classes, which are a human concept, from remotely sensed data, when these sensors only measure the response from the interaction of electromagnetic radiation with the physical surfaces irrespective of land use (Forster & Ticehurst, 1994). Defined from remotely sensed images, spectral classes are not necessarily equivalent to the required information classes. "This is evident in the array of mixed urban classes that have been mapped to date" (Henderson & Xia, 1997, p83).

According to Bryan (1979) there is a noticeable lack of correlation between actual land use (low commercial and residential units) and radar image tone. Bryan (1974) believes it would be better to define land by land cover, rather than land use for urban radar imagery interpretations, due to mis-classification problems relating to the physical structures imaged. For example, small institutional areas were incorrectly identified as residential, similarly larger institutions (such as universities and major hospitals) were confused with commercial.

Haack (1984a) experienced difficulties in distinguishing between residential and combined commercial/services through a textural analysis. It was suggested that street orientation could have been the reason for this difficulty. A similar situation also occurred between a residential and industrial site. This raises the question of land use definitions. The radar will image only what it sees, and two buildings of different classes may have similar morphology making it appear the same to the radar.

Previous research indicates that areas where confusion among categories remains include: (a) single family residential and open spaces; (b) industrial and commercial, and: (c) commercial services and light industry mixed with medium density residential (Henderson & Xia, 1997). Henderson (1985) found that schools, churches and small hospitals located within residential land cover were indistinguishable. "As is the case with many other remote sensing systems, homogeneous spectral classes do not always correspond to desired homogeneous information classes" (Henderson & Xia, 1997, p81).

The potential of radar remote sensing in urban land use mapping remains underestimated through the forcing of radar image interpretation to fit an unsuitable classification. For example, Henderson (1982) was able to achieve around 84% average accuracy from land use mapping from Seasat SAR imagery, by defining a more detailed classification system.

Radar images are able to identify a variety of land use information, however, a further understanding is required so that radar can be used in an urban environment to its full potential.

This chapter presents the results from some classifications performed on the AirSAR data (L-band) over Sydney, using the model to define class characteristics. The land uses distinguished by the model are residential, commercial and park land. In order to use the model to provide a basis for class distinction, the Total Power, Polarisation Index, and Polarisation Phase Difference are used as the classification parameters. The methodology used is

to compare these parameters from an urban area on the AirSAR image with the model database to determine which class each pixel most likely belongs to.

8.2 Using the Stokes Matrix for Calculating the TP, PI, and PPD

To enable the PI (Polarisation Index), PPD (Polarisation Phase Difference), and TP (Total Power) to be calculated, the Stokes matrix needs to be extracted from the AirSAR image. Apart from the initial headers in the data, the image is stored as a binary file with 10 bytes per pixel (for more information, refer to Dubois & Norikane, 1987). Only M_{11} from the Stokes matrix is needed to calculate the total power. The formula required is:

$$M_{11} = \left(byte(2)/254 + 1.5\right) \cdot 2^{byte(1)} \cdot gen\_fac \quad \text{(JPL, 1995)} \qquad (8.1)$$

where *gen_fac* is the general scale factor found in the image data header.

The horizontal and vertical scattering components, s_{hh} and s_{vv}, are also needed for calculating the PPD. They are determined from M_{11}, M_{12}, M_{22}, M_{33}, M_{34}, and M_{44}, of the Mueller matrix. In terms of the AirSAR data in byte format, the matrix elements are:

$$M_{12} = byte(3) \cdot \frac{M_{11}}{127}$$

$$M_{33} = byte(8) \cdot \frac{M_{11}}{127}$$

$$M_{34} = byte(9) \cdot \frac{M_{11}}{127}$$

$$M_{44} = byte(10) \cdot \frac{M_{11}}{127}$$

$$M_{22} = M_{11} - M_{33} - M_{44} \quad \text{(JPL, 1995)}$$

The **total power** is an average of the horizontal, vertical and cross-polarisations. It is equal to M_{11} of the Mueller matrix which is:

$$M_{11} = \frac{1}{4}\left(S_{hh} \cdot S_{hh}^{*} + S_{vv} \cdot S_{vv}^{*} + 2S_{hv}S_{hv}^{*}\right) \text{ (JPL, 1995)} \tag{8.2}$$

The **polarisation index** has been defined in Chapter 5 in relation to the Fresnel reflection coefficients. This means it can also be represented by S_{hh} and S_{vv}. The only difference between S_{hh} and S_{vv} is the Fresnel reflection coefficient. The remaining terms (such as the incidence angle and wavelength) are stored in ϖ (as explained in Section 5.5). The PI can be defined as:

$$PI = \left|\frac{S_{hh}}{S_{vv}}\right|^2 = \frac{S_{hh}^2}{S_{vv}^2} = \frac{S_{hh} \cdot S_{hh}^{*}}{S_{vv} \cdot S_{vv}^{*}} \tag{8.3}$$

where:

$S_{hh} \cdot S_{hh}^{*} = M_{11} + M_{22} + 2M_{12}$ and $S_{vv} \cdot S_{vv}^{*} = M_{11} + M_{22} - 2M_{12}$,

From the Mueller matrix:

$$M_{12} = \frac{1}{4}\left(S_{hh} \cdot S_{hh}^{*} - S_{vv} \cdot S_{vv}^{*}\right) \tag{8.4}$$

$$M_{22} = \frac{1}{4}\left(S_{hh} \cdot S_{hh}^{*} + S_{vv} \cdot S_{vv}^{*} - 2S_{hv} \cdot S_{hv}^{*}\right) \tag{8.5}$$

The **polarisation phase difference** can be defined as:

$$PPD = \arg\left\{\frac{S_{hh}}{S_{vv}}\right\} \tag{8.6}$$

In Chapter 5 the PPD was defined as having a negative numerator for double bounce, which is related to the definitions of the vertical and horizontal directions by the user. In the AirSAR data format, the S_{hh} is positive. The ratio of S_{hh} and S_{vv} can be expressed as:

$$\frac{S_{hh}}{S_{vv}} = \frac{\Re(S_{hh}) + i\Im(S_{hh})}{\Re(S_{vv}) + i\Im(S_{vv})} = \frac{\left(\Re(S_{hh}) + i\Im(S_{hh})\right)\left(\Re(S_{vv}) - i\Im(S_{vv})\right)}{\Re^2(S_{vv}) + \Im^2(S_{vv})} \tag{8.7}$$

where $\Re(S_{pp})$ and $\Im(S_{pp})$ represent the real and imaginary components of S_{pp}. Equation 8.7 can be separated into its real and imaginary components *(a+ib)*, resulting in:

$$a = \frac{\Re(S_{hh})\Re(S_{vv}) + \Im(S_{hh})\Im(S_{vv})}{\Re^2(S_{vv}) + \Im^2(S_{vv})} \text{ and } b = \frac{\Im(S_{hh})\Re(S_{vv}) - \Im(S_{vv})\Re(S_{hh})}{\Re^2(S_{vv}) + \Im^2(S_{vv})} \quad (8.8)$$

The PPD now becomes:

$$PPD = \arg\{a + ib\} = \tan^{-1}\left\{\frac{b}{a}\right\} \quad (8.9)$$

and is defined to be between -180°<PPD<180°, so the directions of *a* and *b* need consideration. The denominator of *a* and *b* are the same so they cancel out leaving:

$a = \Re(S_{hh})\Re(S_{vv}) + \Im(S_{hh})\Im(S_{vv})$ and $b = \Im(S_{hh})\Re(S_{vv}) - \Im(S_{vv})\Re(S_{hh})$.

Since $\Re(S_{hh} \cdot S_{vv}^*) = a$ and $\Im(S_{hh} \cdot S_{vv}^*) = b$, these values can be extracted from the Mueller matrix giving:

$$\Re(S_{hh} \cdot S_{vv}^*) = M_{33} - M_{44} \text{ and } \Im(S_{hh})\Re(S_{vv}) = -2M_{34} \quad (8.10)$$

where:

$$M_{33} = \frac{1}{2} S_{hv} \cdot S_{hv}^* + \frac{1}{2}\Re(S_{hh} \cdot S_{vv}^*) \quad (8.11)$$

$$M_{34} = -\frac{1}{2}\Im(S_{hh} \cdot S_{vv}^*) \quad (8.12)$$

$$M_{44} = \frac{1}{2} S_{hv} \cdot S_{hv}^* - \frac{1}{2}\Re(S_{hh} \cdot S_{vv}^*) \text{ (JPL, 1995)} \quad (8.13)$$

The definitions of the Mueller matrix given above are for the AirSAR data. The model has a few slight changes to the standard, previously defined, Mueller matrix due to the definitions of the directions of the horizontal and vertical parameters used in the model. The changes are: $M_{12model}$=-$M_{12airSAR}$; $M_{23model}$=-

$M_{23airSAR}$; and $M_{34model}$=-$M_{34airSAR}$. Apart from these three exceptions, the calculations of the PI and PPD are exactly the same.

8.3 Establishing a Basis for Comparison between AirSAR and the Model

In order for the model database to be used for classifying AirSAR data, both information sources require comparable parameters. This is achieved by averaging the pixels on the AirSAR image to equate it to a block of buildings, and by establishing a range in values for the model parameters.

8.3.1 Averaging the Pixels on the AirSAR Image

In order to obtain the total power, PI and PPD for the AirSAR image, a number of neighbouring pixels are averaged. This is because the model defines the backscatter and polarisation properties in relation to a block of buildings. A single pixel would give an unrealistic class characteristic since an urban area has a combination of high backscatter (from double and single bounce) and low backscatter areas (from, for example, open flat spaces surrounding the buildings). Speckle on a radar image is also a problem. The TP, PI and PPD can vary by a large amount between surrounding pixels so averaging is performed on a number of adjacent pixels producing a more average class characteristic.

Two sizes of pixel averaging squares are examined to compare and decide which gives the best results. The pixel squares are 9*9 and 15*15 pixels in size. This means, for a 9*9 pixel averaging square, a pixel on an AirSAR image is averaged with 80 of its surrounding pixels. That is, a square is formed from the middle pixel such that it is a distance of 4 pixels to the left, right, up and down.

8.3.2 Estimating a Range for the Model Parameters

The classification method uses a parallelepiped approach (Forster, 1996). Although the parallelepiped approach is a primitive classification technique, it is deemed appropriate for this demonstration. Especially because no statistical weighting is going to be applied to the classes, and only the pixels within class criteria need to be classified. Ideally one would want to use a segmentation process for defining building block boundaries, and then perform a classification on this individual block. However, such a technique is still in the research stage (eg., Dong *et al.,* 1997c).

The model defines the average class TP, PI and PPD for a commercial and residential block, for their respective orientation and look angles. However the standard deviation of these parameters is determined empirically. The reason why this step was necessary is because the range in TP, PI and PPD could not be determined from the model. Even though the beginning of Chapter 7 examines the models range in magnitude, this could not be expanded into a range for the polarisation information because the extreme parameters of the model may not give extreme polarisation characteristics. Hence, a number of urban areas representing average commercial and residential blocks were needed from the AirSAR data.

Four test sites were chosen to enable an appropriate range of total backscatter over a building block to be estimated. The test sites consisted of two residential (one having an look angle around 55° and one near 60°) and two commercial areas (around 48° and 55°). They were chosen for their uniformity of class, especially in relation to the orientation angle.

Once again a 9*9 and 15*15 pixel averaging square were processed over the four test sites. The range in TP, PI and PPD were initially examined visually to obtain information about their spread of values for both commercial and residential classes.

The two commercial areas (one spanning a 33*42 pixel area and the other, 33*21) had quite a large range in total power, PI and especially the PPD for the 9*9 pixel averaging square. The PPD covered close to the full range of possible values for the 9*9 pixel average. This is a large variation to be comparing with the model since these characteristics may overlap with residential areas.

For the two residential areas (which are 54*57 and 68*62 pixels in size respectively), the PPD was the most unreliable parameter because it covered the full range of possible values. These ranges in phase differences are too large for distinguishing between classes.

A larger averaging square, such as 15*15, will cause a slightly different classification. This range helps to reduce the chances of overlap in the PPD range between commercial and residential class parameters. However the problem with averaging a large number of pixels is that there is more potential for overlap into other adjacent classes. For an AirSAR pixel size of around 7m (being 4-look imagery), a 15*15 pixel square is close to 105m in side dimensions. This may lead to parkland going undetected when surrounded by residential areas giving a higher backscatter.

In order to compensate for the large range in PPD values, the standard deviation was used. This reduces the range, and omits any extreme PPD values, yet still includes the most common values. One standard deviation from the mean results is 68% of the PPD values falling within the range, according to Gaussian statistics (Harvey, 1991).

Even though the four sites were not of the same look angle, their TP, PI and PPD values revealed enough similarity to be compared. However, as the range in values and magnitudes show, there is a strong possibility that there will be some overlap between residential and commercial classes.

The results are tabulated in Table 8.1. The standard deviation of the values for the polarisation phase difference has also been calculated for use in the classification.

The PPD has a defined possible range from 0 through to +180° then from -179 to -1°. Therefore a phase difference in the range from +170 to +180°, or -179 to -170°, is indicating strong double bounce effects. A phase difference around 0 to 10°, or from -10 to -1°, would be indicative of a strong single bounce response.

Table 8.1. Range in values of the TP, PI and PPD (also presented as the standard deviation, SD), from the AirSAR data for the four test sites and two pixel averaging squares.

L-band - Range of Values							
Commercial θ=55°							
Pixels	TP min	max	PI min	max	PPD min	max	SD
9*9	0.15	3.9	0.5	3.5	2.8	-9.7	25
15*15	0.7	2.6	0.8	2.8	148	-147	10
Commercial θ=48°							
9*9	0.44	22.7	0.9	8.9	122	-142	19
15*15	1.0	11.3	1.0	6.7	136	-160	16
Residential 1 - θ=60°							
9*9	0.04	0.3	0.84	4.1	0.8	-0.6	51
15*15	0.05	0.24	1.1	3.1	0.9	-134	43
Residential 2 - θ=55°							
9*9	0.08	0.54	0.7	3.0	0.1	-0.1	60
15*15	0.10	0.57	1.0	2.5	0.3	-0.1	41

The main distinguishing factor from Table 8.1 is the total power. It is this parameter which shows minimum overlap between residential and commercial classes. The polarisation index appears to contain no useful information for distinguishing between residential and commercial urban classes. The PI range

for commercial areas is greater than the range for the residential areas. However this information is not useful for the classification process since a classification is performed on a single averaged pixel at a time, and the overlap between the residential and commercial class PI is extensive. The PPD appears to be generally lower for the residential class than commercial. The larger residential area, however, does have a higher maximum value.

For a threshold value to be set for park land, an empirical approach was adopted. Parks are not considered a modelling problem because, as will be addressed later, optical data can easily distinguish between vegetation and non-vegetation. Two large park lands were used to determine an appropriate total power representing the maximum radar return expected. The average response between the two large sites was adopted, they were 0.06 (intensity) for a 9*9 pixel averaging square, and 0.05 for a 15*15 square.

8.4 Classification Requirements

The classification process involves comparing the AirSAR pixel (averaged with either a 9*9 or 15*15 square) with the model for an equivalent look and orientation angle. These angles on the AirSAR image must be predetermined. The look angle in known from the pixel location in the scene. The orientation angle is presently entered manually. A technique for digitally determining the orientation angle during the classification process is needed. Currently such a method does not exist. However "the buildings' orientation is envisaged to be determined by finding the streets' orientation using edge enhanced optical/NIR and radar images" (Dong *et al.*, 1997a, p1361). Work is currently progressing in order to fulfil this need (Dong *et al.*, 1997c). The model data is stored in an additional file which is accessed during classification. The model data contains the TP, PI and PPD values for all the possible combinations of look and orientation angles for residential and commercial classes.

For the AirSAR and model parameters to be realistically compared, the model needs to allow for the large range in TP, PI, and PPD in the AirSAR data. Since the parallelepiped technique is used, a single range in model values for residential and commercial land uses are required. As mentioned earlier, the determination of the range in values was found empirically since this issue is not a modelling problem (described in Section 8.3). The model ranges were determined from Table 8.1. The largest parameter range from the commercial and residential land uses were adopted as the TP, PI and PPD values for the classification. These values are shown in Table 8.2.

The range in values given in Table 8.2 form the extremes of the parallelepiped used for the classification process. Obviously there is going to be overlap between the PI and PPD for residential and commercial land use. To avoid this problem, the total power is used as the initial, and hence prominent, classification parameter. Then the PI and PPD are used to determine how well the pixel's polarisation characteristics match the class it has been assigned to.

Table 8.2. The range in TP, PI and PPD adopted for the model in the classification process.

Class	Pixel averaging square	TP	PI	PPD°
Residential	9*9	±0.23	±1.6	±60
	15*15	±0.23	±1	±43
Commercial	9*9	±11	±4	±25
	15*15	±5	±2.8	±16

8.5 Classification Process and Some Results

Two large sites in Sydney were selected for classification. One was around the Kingsford/Kensington suburbs, and the other around Bondi Junction (see Appendix E for a location map). The reason for choosing these two sites is that the orientation angles for subsets of the area are reasonably homogeneous

enabling an angle to be measured. Kingsford/Kensington has two different orientation angles, whereas Bondi Junction has only one. The selected areas contain a mixture of commercial, residential and park land.

Unfortunately no sites were available for smaller look angles (on the Northern side of Sydney harbour), this is mainly due to lack of orientation uniformity in areas covering a mixture of commercial, residential and park land. As mentioned in the previous section, the orientation angle is currently entered manually, although present research is examining automated techniques of edge detection and extraction. This is the reason for uniformity of orientation layout in the selected classification sites.

One of the limitations with the classification is that it only is equipped to analyse residential, commercial, and park lands. No consideration is given for industrial, or institutional land uses. Hence, industrial land use was not included in the classification area, however institutions were included as they were difficult to omit, and out of interest.

Over the two sites, two types of classifications were performed, one using the 9*9 and one using the 15*15 pixel averaging square. For both the pixel averaging square sizes, three different classifications were performed by varying the parameter specifications. The first classification required the TP, PI and PPD for an averaged AirSAR pixel, to be within the model's range of either the residential or commercial class, for it to be considered (ie., TP+PI+PPD). The second involved the TP and PPD to be within the range (ie., ((TP or (TP+PI)) and PPD). The final category was based on total power alone, (ie., TP or (TP+PI) or (TP+PI+PPD)). For future reference, these three types of classifications will be referred to as types (a), (b) and (c) respectively.

Therefore a type (a) classification requires the AirSAR pixel to be similar to the model's residential or commercial TP, PI and PPD for it to be classified as either residential or commercial respectively. Hence, this is the most rigorous test of the model. A type (b) classification requires the AirSAR pixel to have a

similar TP and PPD to the model, irrespective of the PI. A type (c) classification requires the AirSAR pixel to have only a similar TP to the model, with the results being independent of both the PPD and PI.

Note that the PI was not considered an important factor in the classification process, hence the second classification specifications (type (b)) were independent of it. The reason for this is due to the extensive overlap in its range between the residential and commercial class, hence its inability to distinguish between land uses.

Since the commercial TP range was large and could potentially overlap with the residential TP, the order of the classification process was important. Hence the TP of the pixel was compared with the model's residential class first before comparison with commercial. The whole classification process is demonstrated through a flow chart, shown in Figure 8.1.

The classification results are summarised in Table 8.3. The percentage of areas classified as a particular land use, or left unclassified, are given. The total number of pixels for the Kensington area is 75338 and for Bondi, 30552, so the classification area is quite extensive. The classified images are shown in full in Appendix I, however an example is given in Figure 8.2. Photographs are included to demonstrate the ground truth. They are shown in full in Appendix I, however and example is given in Figure 8.3.

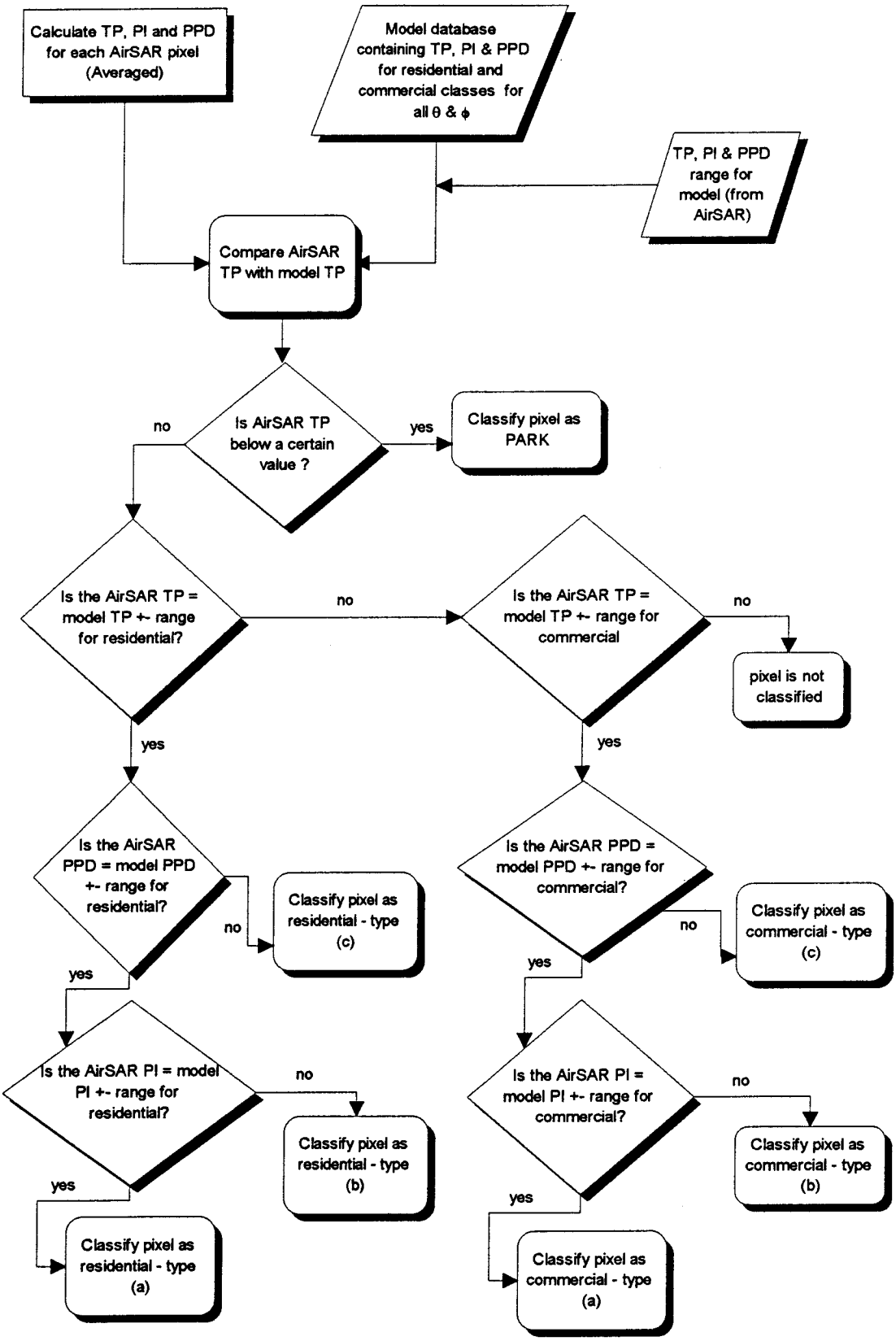

Figure 8.1. The classification process adopted for determining the land use of an AirSAR pixel using the model database. (a), (b) and (c) represent the type of classification according to parameter specification.

As Table 8.3 demonstrates, the percentage of park land in the classified image decreases when the size of the averaging square is increased from 9*9 to 15*15. The reason for this is the larger square being less sensitive to changes in land use, especially if one class has a much smaller land area. The results of this classification are discussed in Section 8.6.

The type (a) (ie., TP+PI+PPD) classification specifications produced poor results with up to 60% and more of the pixels left unclassified. However this percentage is substantially reduced when the PI is discarded in the second classification - type (b) (ie., (TP or (TP+PI)) and PPD). The 15*15 pixel square had a higher percentage of unclassified pixels compared to the 9*9 pixel square.

The final classification based on total power alone - type (c) (TP or TP+PI or TP+PI+PPD) had no pixels unclassified. This indicates that the range in total power for the residential and commercial classes were large enough to include all pixel values.

In future, when referring to the different classified images, the format will be, for example, 'kens9c', where 'kens' represents the area where the classification was performed (either Kensington or Bondi), the '9' represents the pixel averaging square size (ie., 9 or 15) and 'c' indicates the type of classification (ie., (a), (b), or (c)).

Table 8.3a. The percentages of each cover type classified from the two sites (Kensington and Bondi) and for two pixel averaging squares (9*9 and 15*15). Classification was type (a).

TP+PI+PPD	Kensington		Bondi	
Land Use	9*9 (%)	15*15 (%)	9*9 (%)	15*15 (%)
residential	12	3	0.7	0
commercial	2	0.4	8.5	0.3
park	20	15	17	13
non	66	81.6	73.8	86.7

Table 8.3b. The percentages of each cover type classified from the two sites (Kensington and Bondi) and for two pixel averaging squares (9*9 and 15*15). Classification was type (b).

(TP or TP+PI)+PPD	Kensington		Bondi	
Land Use	9*9 (%)	15*15 (%)	9*9 (%)	15*15 (%)
residential	43.5	41	45	48
commercial	5	3	9	6
park	20	15	17	13
non	31.5	41	29	33

Table 8.3c. The percentages of each cover type classified from the two sites (Kensington and Bondi) and for two pixel averaging squares (9*9 and 15*15). Classification was type (c).

TP	Kensington		Bondi	
Land Use	9*9 (%)	15*15 (%)	9*9 (%)	15*15 (%)
residential	68	73	71	76
commercial	12	12	12	11
park	20	15	17	13
non	0	0	0	0

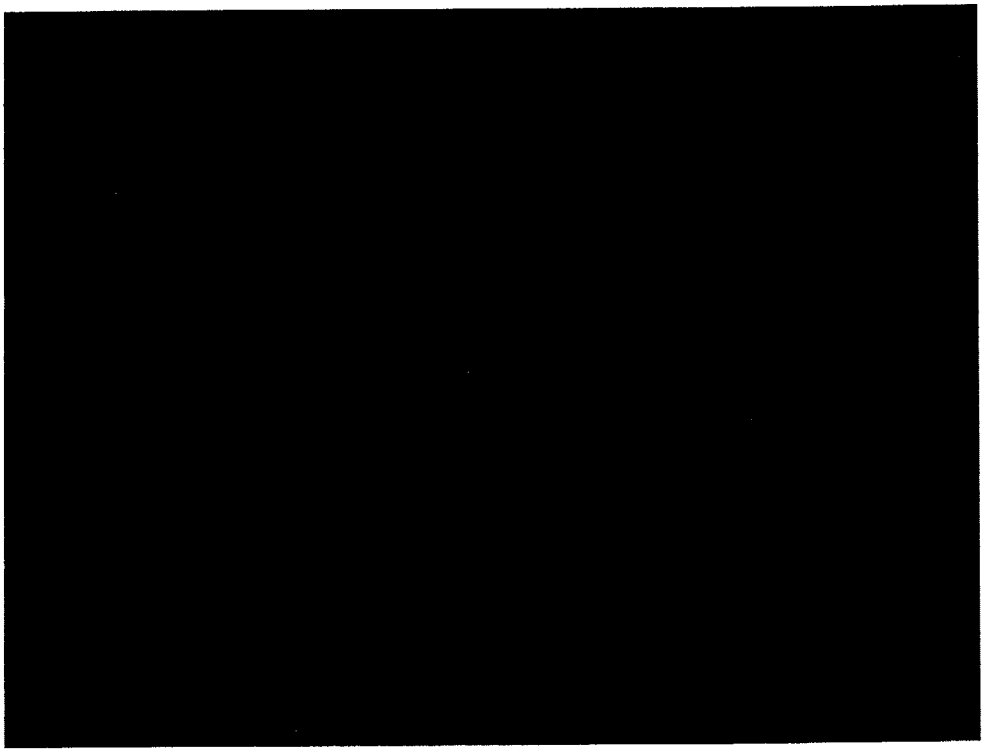

Figure 8.2. The classified image of Bondi9c. Red, blue and green represent the areas classified as residential, commercial and park land respectively. When compared with Figure 8.3 it shows how well the model has classified the area.

Figure 8.3. A copy of the photograph used to provide ground truth for the site over Bondi. Red, blue, and green represent residential, commercial and park land respectively. In addition, purple represents institutional and orange represents tower blocks.

8.6 Analysis and Accuracy of the Classification

In order to test the accuracy of the classifications, a comparison was made with some aerial photographs (1:25000) (which were confirmed by site visits) providing the ground truth. A 2mm grid, approximately 50m on the ground, was placed over both the photograph and classified image for a comparison to be made for each grid cell. The image and ground truth were digitised by hand with a number representing a particular land use. The numbers are shown in Table 8.4.

Table 8.4. The numbers used to represent each land use on both the classified image and photograph. Note that the Tower block represents large high-rise residential buildings.

Classified Image		Photograph	
Land Use	Number	Land use	Number
Residential	1	Residential	1
Commercial	2	Commercial	2
Park	4	Park	4
Unclassified	50	Tower blocks	10
		Institutional	20

Calculation of the difference between the classified image and ground truth for each pixel was performed numerically. Hence, where the classified image agreed with the ground truth, the cell value was 0. The other numbers represent errors of omission and commission. These accuracy (or difference) images are shown in full in Appendix I, however an example is shown in Figure 8.4. The difference numbers (ie., the difference between the classification and photograph) and what they represent, are shown in Table 8.5.

Note that no difference image was processed for bondi15a because there were only a few residential and commercial pixels classified as such, making them unidentifiable on the image. Kens15a is not shown either in the classified

Table 8.5. The difference number representing the omission/commission results when comparing the classified image with ground truth. Note the symbols in brackets will be used in future to represent the type of misclassification.

Difference Number	Description (future abbreviation)
0	Classification = photograph (C)
-1	Commercial classified as residential (CR)
-3	Park classified as residential (PR)
-9	Tower block classified as residential (TR)
-19	Institutional classified as residential (IR)
1	Residential classified as commercial (RC)
-2	park classified as commercial (PC)
-8	tower block classified as commercial (TC)
-18	institutional classified as commercial (IC)
3	residential classified as park (RP)
2	commercial classified as park (CP)
-6	tower block classified as park (TP)
-16	institutional classified as park (IP)
49	residential unclassified (RU)
48	commercial unclassified (CU)
46	park unclassified (PU)
40	tower block unclassified (TU)
30	institutional unclassified (IU)

images because, even though residential pixels were classified, they were not visible on the image due to their limited numbers. As the images show (Appendix I), there is a difference between the type (a), (b) and (c) classifications, when using a 9*9 and 15*15 pixel averaging square. This difference is especially visible when comparing images kens9c with kens15c or bondi9c with bondi15c. The 9*9 images produce smaller but more frequent 'patches' of commercial cover type mixed within the residential areas. The

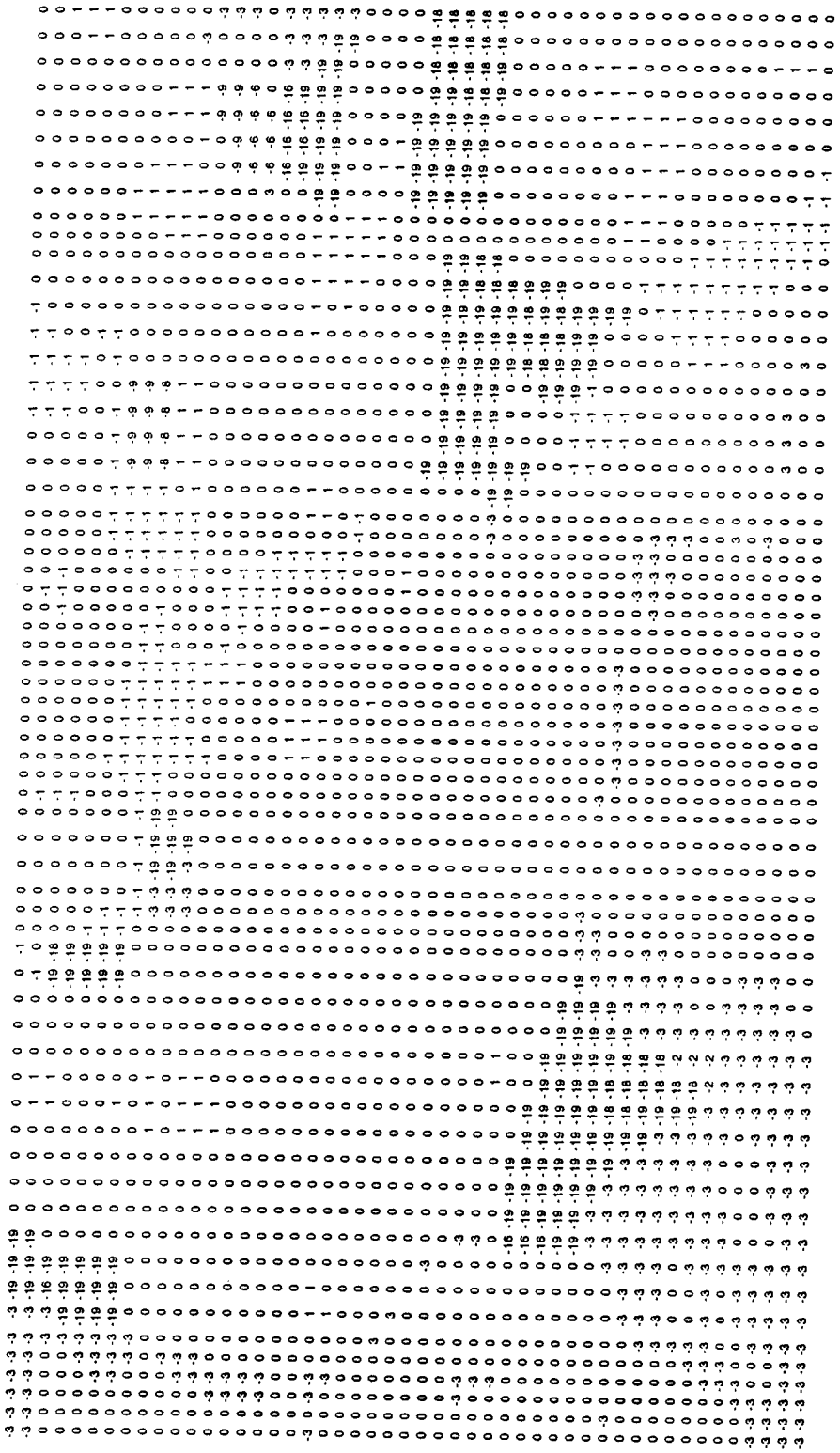

Figure 8.4. Difference image of Bondi9c. The image has been rotated 90° anti-clockwise from Figures 8.2 and 8.3. The numbers represent different omission/commission results as given in Table 8.5. Note how the high percentage of '0's indicates correct classification.

15*15 image has less 'patches' but they are larger. However, the disadvantage of the 15*15 image is that it is unable to identify small areas of commercial use due to the averaging effect with the surrounding residential area, reducing the total power.

The type of omission/commission errors were summed for each difference image (refer to Figure 8.4 and Appendix I) along with the number of correctly classified pixels. The results for the two separate study regions are shown in Appendix G. The results from the two images combined are presented in Table 8.6. All values are shown as percentages. (Refer to Appendix H for the omission/commission tables of the combined image, where units are given in pixel numbers). Note that the combined image of 15a was not included because both bondi15a and kens15a had a limited number of residential and commercial classifications. In future, the combined image will be referred to as '9a', '9b', etc.

Some of the omission/commission percentage values are small. However, they cannot be evaluated properly until the percentage of cover type for the whole area is given. This result, shown in Table 8.7, was determined from the photographs. The combined image consists of 105890 pixels, hence this area should be extensive enough to provide robust testing of the model.

As Table 8.6 shows, a 9*9 square produces a greater classification accuracy than a 15*15 square. This result was expected. As mentioned earlier, an averaging square of 15*15 pixels covers over 100*100m on the ground. Such an area will cause loss of some detail, especially on the border between cover types. However, the classification based on total power alone produces a similar number of correctly classified pixels for both the 9*9 and 15*15 square.

Table 8.6. The percentage of all the omission/commission results from the combined image (bondi and kens). Hence the values in the 'C' row indicate the accuracy of each image. Once again the '9' and '15' represents the size of the pixel averaging square, and the 'a', 'b', and 'c' indicate the type of classification.

Combined Images	9a	9b	9c	15b	15c
Description	%	%	%	%	%
C (classification = photograph)	26.8	54.1	66.3	48.9	64.8
CR (commercial classified as residential)	0.3	2.8	3.7	2.0	3.0
PR (park classified as residential)	0.7	2.1	7.0	2.5	10.0
TR (tower block classified as residential)	0.1	0.3	0.3	0.3	0.4
IR (institutional classified as residential)	1.7	7.8	12.1	6.2	12.8
RC (residential classified as commercial)	2.1	2.5	4.3	1.4	3.5
PC (park classified as commercial)	0	0.1	0.1	0	0.3
TC (tower block classified as commercial)	0	0	0	0.1	0.4
IC (institutional classified as commercial)	0.7	1.9	4.5	1.1	4.4
RP (residential classified as park)	0.5	0.5	0.5	0.1	0.1
CP (commercial classified as park)	0	0	0	0	0
TP (tower block classified as park)	0.1	0.1	0.1	0	0
IP (institutional classified as park)	1.1	1.1	1.1	0.3	0.3
RU (residential unclassified)	39.9	12.7	0	16.0	0
CU (commercial unclassified)	5.3	2.1	0	3.2	0
PU (park unclassified)	6.4	5.1	0	7.8	0
TU (tower block unclassified)	0.2	0	0	0.1	0
IU (institutional unclassified)	14.1	6.8	0	10.0	0

For the 9*9 pixel square results, the classification based on total power alone (type (c)) will obviously classify more pixels compared to the other two specifications (type (b) and (a)). The number of pixels correctly classified on the 9a image (TP+PI+PPD) are less than half of those for 9b (TP or TP+PI and PPD). Due to its better results, analysis will concentrate on the 9*9, rather than the 15*15 pixel averaging square.

Table 8.7. Percentage of ground truth coverage for each land use from the combined area.

Percentage of cover type for combined area	
Land Use	area coverage (%)
Residential	50
Commercial	7
Park	25
Tower block	0.5
Institutional	17.5

8.6.1 Analysis of Image 9a

Only 26.8% of the pixels on image 9a were correctly classified. Since 25% of the land area is park, and only 7.1% (ie., 6.4+0.7) of this was mis- or unclassified, 19.7% of the correctly classified pixels were park. Therefore only 7.1% of the correctly classified pixels were residential or commercial. Since residential and commercial made up 57% of the total land area, 12.5% (7.1/57*100) of these land uses were identified correctly. In relation to individual classes, the percentage of unclassified residential land use with respect to the total residential area was 79.8% (39.9/50*100). Similarly, 75.7% (5.3/7*100) of commercial land was unclassified. Hence slightly less commercial areas had the TP, PI and PPD parameters from the real data agreeing with the model, than residential.

8.6.2 Analysis of Image 9b

Image 9b has over 54% of its pixels classified correctly. However, it must be noted that a correct classification can only occur for residential, commercial and park land cover types. The reason for this is that the model was not designed to classify institutional land. Hence, any residential, commercial or park land classified as institutional is not necessarily an error, since any

institutional block could be a combination of these cover types as far as its physical structure is concerned. If the institutional cover types are examined, the results show that a greater percentage of those pixels are classified as residential (7.8%) compared to commercial (1.9%). However, this could be related to the fact that residential land use covers seven times more area than commercial for this case study.

Tower blocks, ie., tall residential buildings, were not considered in the model due to their small numbers. Any omission/commission classifications relating to this class are not necessarily errors. Half of the number of pixels on the photograph determined to be tower blocks were classified by the model to be residential, and the other half commercial. This mixture was expected because these residential unit blocks are tall like commercial buildings. However, they were made of brick, and generally had tiled roofs which would reduce the backscatter compared to real commercial buildings. Furthermore, their small land area coverage, once averaged with the 9*9 averaging square, will reduce the backscatter when surrounded by smaller residential buildings. Hence the tower blocks were classified as a combination of residential and commercial, which is not unrealistic.

If institutions, tower blocks and park cover types are ignored, then the percentage of pixels correctly classified can be estimated for residential and commercial classes only. The total percentage of residential and commercial pixels, either correctly classified, unclassified, or classified as the other, is 74%. The total number of pixels correctly classified is 54.1%, however this includes park land. Park land can be deducted from the total because 25% of the area is park, and 7.3% (2.1+0.1+5.1) of the total image was parkland incorrectly classified or unclassified. Hence approximately 17.7% (ie., 25-5.3) of the pixels correctly classified were park land leaving 36.4% for residential and commercial. Since 36.4% of the pixels were correctly classified as residential or commercial land use out of a possible 57% (50+7), the percentage of residential or commercial land use correctly classified is really

64% (36.4/57*100). Therefore, over half of the residential and commercial pixels which could have been classified, were correctly classified.

12.7% of residential land use for image 9b (TP+PPD), was unclassified. Since 50% of the total land area is residential, 25.4% (12.7/50*100) of AirSAR residential areas disagree with the PPD value given by the model. In relation to commercial land use, slightly more, 30% (2.1/7*100), commercial land was unclassified. Hence, the models ability to imitate residential and commercial land use appears to be of a similar standard relative to the PPD.

8.6.3 Analysis of Image 9c

Using a similar form of analysis to that of image 9b, the results show that 66.3% of residential, commercial, and park land use were correctly identified. No pixels were left unclassified due to the large range for the total power. Once again the institutional land use was classified as residential (12.1%), more than commercial (4.5%). Not only is this result indicative of the building sizes on institutional land, but it also could be related to the spacing between them, due to low backscatter between buildings reducing the average total power. Tower blocks were classified as residential and commercial in the ratio of 3:1. Hence some of the unclassified pixels of image 9b for the tower block land use area were classified as residential when using total power alone.

If park land is removed from the total number of positively identified pixels, then the percentage of correctly classified residential and commercial regions can be estimated as for the 9b image. The total percentage of mis-classified park land is 7.1%, the same as before. Hence, 17.9% of the correctly classified pixels are park land, leaving 48.4% (66-17.9) of residential and commercial areas. The total percentage of residential and commercial pixels is 57% (50+7). Hence, 85% (ie., 48.4/57*100) of the residential and commercial land use which could have been classified as either of the two, has been classified correctly based on total power alone.

The areas misclassified as either RC (residential classified as commercial) or CR (commercial classified as residential) (from Table 8.5) reveal a few trends in relation to their position. Some of the smaller commercial areas surrounded by residential buildings are not detected as commercial (ie., a CR error), partly because of their size, and partly because of the pixel averaging effects with residential buildings.

CR and RC errors are found to mostly occur in and around commercial areas. The classified image produces a 'patchy' result, therefore even though the image is detecting commercial land use in the general vicinity, there is some misalignment involved. Another reason for CR errors could be due to commercial areas going undetected when surrounded by other commercial buildings. This could be possible since some commercial buildings are too close together for double bounce effects to occur (such as large low-rise shopping complexes), so the radar is only exposed to the roof which is generally flat.

8.6.4 Comparison of Classification Results using a 9*9 and 15*15 Pixel Averaging Square

A brief comparison of the 9*9 images and 15*15 images reveal that the greatest difference between the two is that the 15*15 images classified fewer pixels correctly. On the type (b) (TP+PPD) images the number of pixels positively identified on the 9*9 image were 5% more than the corresponding 15*15 image. The TP classification (type (c)) produced similar results from both pixel averaging squares, with a difference of only 1.5% where the 9*9 image produced a slightly better outcome.

For images 9b and 15b (TP and PPD), other noticeable differences between the two were that more institutional areas on the 9*9 image were classified than on the 15*15 image, ie., 10.8% (7.8+1.9+1.1) and 3.9% (2.5+1.1+0.3) respectively. Furthermore, the 15*15 image had 16% of its residential area left

unclassified, while there was only 12.7% on the 9*9 image. Hence, the larger pixel averaging square was affecting the polarisation characteristics of the residential land use, for the worse. As mentioned before this could be due to the larger square overlapping further into other land uses.

The 9c and 15c images, classified according to total power alone, showed very similar results. All of the omission/commission results differed by no more than 3%. Therefore, the total power was not substantially affected by a change in the averaging square, unlike its polarisation properties.

8.6.5 General Classification Analysis

Further reasons for misclassification are not necessarily related to the model's output. Possible reasons for errors include:

(i) the image and photograph were not completely co-registered since this was performed manually - hence some omission/commission errors follow the border of a land use (as can be seen on the difference images in Appendix I);

(ii) a similar outcome is due to the averaging effects of the 9*9 or 15*15 square which may change the border of the land use on the image;

(iii) discrepancies in placing the 2mm grid over the image or photograph (only a small change in its placing influences the dominant land use in each square of the grid), and;

(iv) the randomness in deciding on the land use in a grid square when the coverage from two cover types is close to 50:50.

Small orientation angles are highly sensitive with respect to the backscatter, as has been demonstrated in earlier chapters. The orientation angles for the two classification areas were generalised to a certain extent. That is, the orientation angle was not measured for each block when they appeared to have a similar angle to their neighbouring blocks. This would result in some inaccuracies of the measured orientation angle, and hence could affect the comparison of the AirSAR with the model's results. This would in turn lead to a potential error in

the total power estimate. However, due to the present method of orientation determination being manual, such a technique was unavoidable.

It is worth noting at this point, that errors of omission or commission relating to park land are of no major concern. The potential for integrating radar data with optical information, which can easily distinguish between vegetation and built structures, is being realised. A substantial proportion of park land was classified as residential cover type. These misclassified regions occur where there are trees because the backscatter characteristics from trees are similar to residential buildings. Hence, out of the possible 25% park land, 8.4% (ie., 2.1/25*100) of it was misclassified as residential (as in the 9b image). This could be avoided with the use of visible/infrared remotely sensed data.

One possible reason for discrepancies between the model and AirSAR results with respect to polarisation information could be due to the averaging effects which are performed on the model block, ie., the buildings and their spacings are considered to be square. In the real world, buildings are generally rectangular in shape, and are spaced much closer together along the street than they are across (due to the rear open spaces). This changes the amount of double bounce occurring from building walls due to changes in radar shadow regions, and hence the polarisation characteristics. However, such an affect was unavoidable. Unless a technique can be designed to determine which streets the buildings are fronting, the averaging method performed in the model was necessary.

8.7 Summary

In summary, classification based on total power alone is more accurate than those performed using information about the total power and the PPD. The results demonstrated how the classification improved from 64% up to 85%, for the residential and commercial classes, when comparing type (b) (TP with PPD) and type (c) (TP alone) respectively. Both of these parameter

specifications are more accurate than a classification integrating the PI as a criterion. Whilst this is indicative of some of the faults in the model, it is also suggesting that all of the polarisation information is not vital to enable an urban classification to be performed. Concentrating on the total power may be sufficient for many urban radar processes.

As the results analysed in this chapter show there is merit in the use of the model. It is able to produce encouraging results, even with a simple classification technique, for such a complex problem. In reference to the discussion presented at the beginning of this chapter, the radar only detects what it 'sees'. The structure and layout of buildings are not always uniform for a particular land use. Some residential buildings may show characteristics of tall commercial buildings, while other small scale commercial buildings show little difference to their residential neighbours. This is a feature of urban areas that cannot be overcome. However, the radar's ability to separate tall, densely spaced buildings from the smaller scale structures is certainly apparent and will be discussed further in the next concluding chapter.

9. SUMMARY AND CONCLUSIONS

9.1 Introduction

Radar remote sensing has a significant role to play in the analysis of urban environments. The purpose of this thesis was to investigate some of this potential by developing a model able to predict the backscatter and polarisation characteristics of radar responses from a city. This was not an easy task because urban scenes are a complex mixture of different shapes, sizes, materials and spatial patterns, all influencing the radar return. However, the model developed here, has been able to demonstrate its ability to distinguish between residential and commercial classes with a reasonable degree of accuracy. Furthermore, it has revealed radar's great advantage of differentiating between different urban densities.

9.2 Summary of Thesis

This research began by demonstrating the urgent need for urban monitoring. The phenomenal rate of population growth, especially in cities of the developing world, is creating the need for efficient urban analysis. Such a need is not only for identifying where development is occurring, but also for population estimation.

Remote sensing has the ability to assist in urban analysis and monitoring. Optical remote sensing is more developed than radar, hence has more to offer as far as technology and familiarity is concerned. However, radar's ability, though only a relatively new concept, is also apparent, as was demonstrated through past and present research. In some developing countries that are constantly subject to rain and cloud cover, it may provide the only source of remotely sensed data available.

Radar remote sensing as a tool for urban monitoring was then addressed. Strong areas of interest appear to be in radar's ability for settlement detection, leading to its potential for population estimation. Further studies have demonstrated its benefits in urban classification. Radar can not only distinguish between urban and non-urban regions, but also between intra-urban classes (eg., residential, industrial) under the correct conditions. However, most studies to date have used visual interpretation methods which are time consuming and not based on a detailed theoretical analysis of the problem. Hence the need for a detailed understanding of the backscatter and scattering mechanisms, and an automated approach was revealed.

The advantages of combining radar with optical data for environmental monitoring were discussed. Most of the research agrees that information quality improves using the combined data set rather than the individual systems. Radar's unique ability to provide knowledge about the third dimension in the built environment were also investigated. However, such studies are relatively new and little research has been undertaken.

The aim of developing an urban model was to further investigate microwave radiation's interaction with the built environment, where the city of Sydney provided an example of varying urban characteristics.

Development of such a model requires an understanding of the scattering mechanisms most likely to occur in an urban area. However, it also requires many simplifications and assumptions to be made due to the complexities of a city. The important scattering processes adopted for the model were double bounce, single bounce, and volume scattering. The methods adopted for analysing these scattering mechanisms were the total backscatter, and polarisation characteristics.

The so called cardinal effect (dihedral corner reflection), perhaps the most influential phenomenon for urban monitoring with radar, was investigated both

from past research, and from an experiment performed as part of this thesis. The ability to predict such an affect eliminates much of the difficulties in urban monitoring (which the model is able to fulfil to a certain extent).

The simple scattering mechanisms adopted, were applied to the modelling of an urban building, and then expanded for estimation of the backscatter from a building block. This model concentrated on commercial and residential regions only. The primary reason for this was that residential and commercial areas are the dominant cover types in cities, hence it was much easier to find relevant test sites to provide ground truth for a variety of residential and commercial characteristics. Furthermore, these two classes provided a significant contrast in building shape, density, material, and other class parameters enabling different combinations of scattering mechanisms to be investigated.

Estimation of all relevant urban parameters was needed for such a model to be operational. This included the acknowledgment that buildings, especially tall commercial structures, have a high proportion of metal in them. Metals, being very strong radar scatterers, are found not only as cladding, or servicing facilities, but also to provide structural support for many buildings. Such factors required inclusion in the model for a more realistic result.

Once the model was fully developed and parameters defined, it was necessary to test how it performed in relation to a real urban environment. Fortunately, AirSAR data was available covering a significant extent of the eastern suburbs of Sydney. A model simulation was performed to compare the intensity and polarisation output from six test sites selected for their variation in look and orientation angles. A comparison was initially analysed for L-band, producing very encouraging results. The model appears to have detected the dominant scattering processes occurring from the two urban classes. However, as discussed in the relevant sections, some discrepancies were apparent between the model simulation and real urban backscattered data.

P- and C-bands did not perform as well as L-band, with the P-band simulation from the commercial land use giving a higher HH response than the AirSAR. Possible reasons for this have been addressed in the relevant sections. C-band gave the least reliable results. However, due to its short wavelength, difficulties arise in modelling its interaction with the urban environment. Hence, L-band was adopted to perform an urban classification to further test the model's applicability.

A simple parallelepiped classification approach was undertaken to investigate the model's potential as a classification tool. A data base was produced from model simulations to provide the residential and commercial backscatter and polarisation characteristics for all possible look and orientation angles. The AirSAR intensity and polarisation properties were compared with the model to decide whether the area should be classified as either residential or commercial class.

The classification results showed how well the model's Total Power, Polarisation Index, and Polarisation Phase Difference matched the AirSAR output. As the investigation demonstrated, the model's PI did not perform well, however, discrimination of the PI between residential and commercial classes from the real data was difficult. Apart from the PI, the model proved it can distinguish between residential and commercial land uses. Classification using the Total Power and PPD showed that the model could produce a 64% accuracy. However, its best result was from the Total Power alone, where 85% of the possible residential and commercial classes were correctly classified.

Although the classification results were not perfect, they were encouraging. This is especially so when the data averaging effects and the average modelled effects are considered, for example assuming the buildings and blocks to be square. The model does have the ability to detect different land uses in an urban environment with a reasonable level of accuracy. However, if such a concept is further refined and combined with other remote sensing systems, it may prove even more useful.

9.3 Recommendations

Remote sensing systems in the microwave region appear to have many unique advantages for monitoring the urban environment. One of its greatest benefits is the close correlation between the radar intensity and building bulk (ie., height and volume of buildings).

The potential of radar to determine bulk density appears to be much greater than its ability to distinguish between land use, due to the complexity of defining 'typical' land use characteristics. Some commercial areas show characteristics more similar to residential, and vice versa.

Implementation of an automated urban classification system using radar is not a simple task. Henderson and Wharton (1980) found that the visual interpretation provided more information than a density slice. However, manual interpretation is very time consuming, and hence inefficient.

In order to be able to monitor and analyse the urban environment, it is necessary to know the street orientation. **Edge detection** techniques, which are presently being developed (eg., Dong *et al.,* 1997c, Beauchenin *et al.,* 1996, Chabert *et al.,* 1996), need to be applied to urban areas to enable the determination of street directions. Such information would assist in modelling and eliminating the cardinal effect. It would change what is now a laborious manual task into a fast automated approach.

More accurate parameter estimations are needed for the **vegetation** found in urban regions. However, such an estimation would require local measurements to be obtained. This would be a very time consuming and difficult task, especially due to the variety of trees found in the built environment. As suggested by Richards (1990) measured values of forest parameters are needed for the different wavelengths and polarisations.

Multiple radar wavelengths may not be necessary for all urban applications, especially if optical data can be included to distinguish between vegetated and non-vegetated regions. There is not a great difference between urban polarisation responses for residential and commercial classes for C-, L- and P-band wavelengths (as Appendix F demonstrates).

Development of urban models needs to continue, especially using **multispectral data**. Although a number of researchers have already investigated combining radar with optical data for environmental monitoring, further work is required focusing on the urban scene, especially for delimiting urban boundaries and distinguishing between different urban classes. It has been suggested by Forster & Ticehurst (1994) that the optical data could be used to provide the planimetric density, while radar could be used as an indicator of the building bulk. Visible/infrared data is also able to provide a measure of vegetation in urban areas, and hence could easily detect park land.

The ease of interpretation of large flat open areas, such as airports, parks, parking lots and school yards, on radar images may prove helpful (Bryan, 1983). Although a visible/infrared system can determine differences in spectral responses for such land uses as a concrete parking lot and a grass athletic field, it cannot determine if these surfaces are smooth. Whereas radar cannot discriminate between the parking lot from a similarly smooth athletic field, but is able to discriminate a tree-covered park from a relatively smooth athletic field - both of which would have similar visible/infrared spectral responses due to their vegetative cover (Bryan, 1983).

Radar remote sensing information could enable population estimation algorithms to be formulated, especially when one can eliminate the uninhabited land uses. This could prove to be an extremely valuable tool, especially in the rapidly developing regions of the world.

9.4 Concluding Remarks

Urban analysis using remote sensing is a difficult task because cities consist not only of complex building shapes and sizes, but also contain various natural elements, such as trees, grass, water and soil (difficult monitoring tasks in themselves). However while research into the digital analysis of radar image parameters for urban studies is still limited, the current research has provided a significant step in moving towards a better understanding of radar's interaction with urban environments.

Once satellite data becomes available with a resolution as small as 1*1m (as predicted for the near future) it can be merged in Geographic Information Systems with radar image data. This would enable further investigation of the different urban scattering components with respect to radar. "More important, such data sets will provide the basis for the development of predictive models for population estimation and urban growth patterns" (Xia & Henderson, 1997, p100).

While radar as a remote sensing tool in the urban environment may not have the ability to operate as the sole provider of information, it can certainly contribute vital knowledge unobtainable from other data sources. Urban models need to be further developed to enable a greater understanding of radar's interaction in the built environment. Through such research, radar will be able to progress from its present investigative stages, into an operational technology for assisting urban monitoring.

REFERENCES

Agrawal,A.P. & Boerner,W.M., 1989. *Redevelopment of Kennaugh's Target Characteristic Polarisation State Theory using the Polarisation Transformation Ratio Formalism for the Coherent Case*. In IEEE Trans. on Geoscience and Remote Sensing, Vol.27, No.1, January, p.2-14.

Anderson,J.R., 1972. *Land Use Classification Schemes*. In Photogrammetric. Eng., Vol.37, p.379-382.

Australian Government Task Force to Investigate Modern Housing Techniques, 1974. Modern Housing Techniques, Australian Government Publishing Service, Canberra.

Balia,L.M. & Evans,A.H., 1995. FarmImage - Farmer's Imaging System, Version: 100c - April 1995. Computer software supported by the Centre of Remote Sensing and GIS, at the University of New South Wales, Sydney, Australia.

Baraldi,A. & Parmiggiani,F., 1995. *An Investigation of the Textural Characteristics Associated with Grey Level Cooccurrence Matrix Statistical Parameters*. In IEEE Trans. on Geoscience and Remote Sensing, Vol.33, No.2, March, p.293-304.

Barrett,E.C. & Curtis,L.F., 1992. Introduction to Environmental Remote Sensing, Chapman & Hall, London, 426pp.

Beaty,H.Wayne (Editor), 1990. Electrical Engineering Materials Reference Guide, McGraw-Hill Publishing Co. N.Y. USA.

Beauchemin,M., Thomson,K.P.B. & Edwards,G., 1996. *Edge Detection and Speckle Adaptive Filtering for SAR Images Based on a Second-Order*

Textural Measure. in Int. J. Remote Sensing, 1996, Vol.17, No.9, p.1751-1759.

Beckett,H.E. & Godfrey,J.A., 1974. Windows, Performance, Design and Installation, Crosby Lockwood Staples, London.

BHP steel, 1995. Structural Steel in Housing, 1st Edition, Span tables and Connection Details for Lintels, roof and floor beams, Pamphlet.

Bickel,D.L., Hensley,W.H. & Yocky,D.A., 1997. *The Effect of Scattering from Buildings on Interferometric SAR Measurements*, In Proceedings of International Geoscience and Remote Sensing Symposium (IGARSS'97), Singapore 1997, Vol.4 , p.1545-1547.

Bryan,M.L., 1983. *Urban Land Use Classification using Synthetic Aperture Radar*. Int. J. Remote Sensing, Vol.4, No.2, p.215-233.

Bryan,M.L., 1982. *Analysis of Two Seasat Synthetic Aperture Radar Images of and Urban Scene*. In Photogrammetric Eng. and Remote Sensing, Vol.48, No.3, March, p.393-398.

Bryan,M.L., 1979. *The Effect of Radar Azimuth Angle on Cultural Data*. In Photogrammetric Eng. and Remote Sensing, Vol.45, No.8, August, p.1097-1107.

Bryan,M.L., 1975. *Interpretation of an Urban Scene Using Multi-Channel Radar Imagery*. In Remote Sensing of Environ., Vol.4, p.49-66.

Bryan,M.L., 1974. *Extraction of Urban Land Cover Data from Multiplexed Synthetic Aperture Radar Imagery*. In 9th Int. Symposium of Remote Sensing of Environment, Ann Arbour, MI, p.271-288.

Burkhart,G.R., Bergen,Z. & Carande,R., 1996. *Elevation Correction and Building Extraction from Interferometric SAR Imagery*. In Proceedings of International Geoscience and Remote Sensing Symposium (IGARSS'96) Lincoln, U.S.A., 27-31 May 1996, Vol.1, p.659-661.

Carande,R., 1995. *Interferometric SAR 'Melts' Hurdles to Urban Mapping*, located at *http://www.vexcel.com/tech_feat/sept95.sarmelts.html* website.

Chabert,M., Tourneret,J-Y. & Mesnager,G., 1996. *Edge Detection in Speckled SAR Images using the Continuous Wavelet Transform*. In Proceedings of International Geoscience and Remote Sensing Symposium (IGARSS'96) Lincoln, U.S.A., 27-31 May 1996, Vol.3, p.1842-1844.

Chauhan,N.S., Lang,R.H., & Ranson,K.J., 1991. *Radar Modeling of a Boreal Forest*. In IEEE Trans. on Geoscience and Rem. Sens., Vol.29, No.4, July, p.627-638.

Chung,F.D.K., with Adams,C., 1991. Building construction Illustrated - 2nd Ed., Van Nostrand Reinhold, New York.

Clark,J., 1980. *Training Sites Statistics from Landsat and Seasat Satellite Imagery Registered to a Common Map Base*. ASP Fall Technical Papers, Niagara, New York, p.RS-1-F-1 to F-9.

Cloude,S.R. & Pottier,E., 1996. *A Review of Target Decomposition Theorems in Radar Polarimetry*. In IEEE Trans. On Geoscience and Rem. Sens., Vol. 34, No. 2, March, p.498-518.

Corr,D.G., Whitehouse,S.W., Mott,D.H. & Baldwin,J., 1996. *Automatic Change Detection in Spaceborne SAR Imagery*. In Algorithms for Synthetic Aperture radar Imagery III, Proceedings of SPIE Vol.2757, p.58-69.

Deguchi,C., Nakayama,Y., Sugio,S. & Yokota,H., 1995. *A Study on the Applicability of AMI-SAR Data to Land-Use Planning*. In Final Report of JERS-1/ERS-1 System Verification Program, by MITI & NASDA March 1995, Vol.2, p.485-492.

Dobson,M.C., Pierce,L.E. & Ulaby,F.T., 1996. *Knowledge-Based Land-Cover Classification using ERS-1/JERS-1 SAR Composites*. In IEEE Trans. on Geoscience and Remote Sensing, Vol.34, No.1, Jan, p.83-99.

Dobson,M.C., Ulaby,F.T., Brunfeldt,D.R. & Held,D.N., 1986. *External Calibration of SIR-B Imagery with Area-Extended and Point Targets*. In IEEE Trans. on Geoscience and Remote Sensing, Vol. GE-24, No. 4, July, p.453-461.

Dong,Y., Forster,B. & Ticehurst,C., 1997a. *Radar Backscatter Analysis for Urban Environments*. In Int. J. Remote Sensing, Vol.18, No.6, p.1351-1364.

Dong,Y., Forster,B. & Ticehurst,C., 1997b. *Optimal Decomposition of Radar Polarisation Signatures*. Submitted and accepted to IEEE Trans. on Geoscience and Rem. Sensing (to appear in the next edition).

Dong,Y., Forster,B. & Milne,A.K., 1997c. *Segmentation of Radar Imagery using Gaussian Markov Random Field Models and Wavelet Transform Techniques*. In Proceedings of International Geoscience and Remote Sensing Symposium (IGARSS'97), Singapore 1997, Vol.4 , p.2054-2056.

Dong,Y., Forster,B. & Ticehurst,C., 1996, *Radar Target Simulations for Urban Monitoring*, in Proceedings of 8th Australasian Remote Sensing Conference, Canberra, Australia 25-29 March 1996, p.128-132.

Dong,Y., 1995a. *Studies of Corner Reflector Structures in Urban areas*, A technical report, School of Geomatic Engineering, UNSW.

Dong,Y., 1995b. A Long Wavelength Radar Backscatter Model for Forests, PhD Thesis, Australian Defence Force Academy, University of New South Wales, Australia.

Dong,Y., Richards,J.A. & Cashman,J., 1995. *A Model of Volume Attenuation and Backscattering by Foliage at L- and P- bands*. In Int.J. Remote Sensing, Vol.16, No.7, p.1231-1247.

Dubois,P.C., Van Zyl,J.J. & Engman,T., 1995. *Measuring Soil Moisture with Imaging Radars*. In IEEE Trans. on Geoscience and Remote Sensing, Vol.33., No.4, July, p.915-926.

Dubois,P.C. & Norikane,L., 1987. Data Volume Reduction for Imaging Radar Polarimetry. In Proceedings of IGARSS '87 Symposium, Ann Arbour, May,1987, p.691-696.

Elachi,C., 1988. Spaceborne Radar Remote Sensing: Applications and Techniques, IEEE Press, New York.

Evans,D.L., Farr,T.G., Van Zyl,J.J. & Zebker,H.A., 1988. *Radar Polarimetry: Analysis Tools and Applications*. In IEEE Trans. On Geoscience And Remote Sensing, Vol.26, No.6, November, p.774-789.

Falcone,J.D., 1978. Principles and Practices of Residential Construction, Prentice-Hall, INC., Englewood Cliffs, New Jersey, USA.

Ferrazzoli,P. & Guerriero,L., 1995. *Radar Sensitivity to tree Geometry and Woody Volume: A Model Analysis*. In IEEE Trans. of Geoscience and Remote Sensing, Vol.33, No.2, March, p.360-371.

Forster,B.C., Ticehurst,C. & Dong,Y., 1996. *Measures of Urban Morphology from Optical and Radar Sensors*. In Proceedings of the 8th Australasian Remote Sensing Conference, Canberra, Australia 25-29 March 1996, p.33-40.

Forster,B.C., & Ticehurst,C., 1994. *Urban Morphology Measures from Optical and Radar Remotely Sensed Data - Some Preliminary Results*. In Proceedings of International Symposium on Resource and Environment Monitoring, ISPRS Commission VII, Rio de Janeiro, Brazil, 11 September 1994, p.291-296.

Forster,B.C., 1996. Introduction to Remote Sensing Data Processing and Analysis, The School of Geomatic Engineering, University of New South Wales, Sydney.

Forster,B., 1994. SURV9600 Principle of Remote Sensing course notes 1994, School of Geomatic Engineering, University of New South Wales, Sydney, Australia.

Forster,B.C., 1985. *An Examination of some Problems and Solutions in Monitoring Urban Areas from Satellite Platforms*. In Int. J. Remote Sensing, Vol. 6, No.1, p.139-151.

Freeman,A. & Durden,S., 1992. *A Three-component Scattering Model to Describe Polarimetric SAR data*. In Proceedings of SPIE Radar Polarimetry Conference, San Diego, July 23-24 1992, Vol.1748, p.213-224.

Fung,A.K. & Ulaby,F.T., 1983. *Matter-Energy Interaction in the Microwave Region*. In Manual of Remote Sensing, 2nd Edition, Vol.1. D.S.Simonett and F.T.Ulaby, (Eds), Falls Church, Virginia: American Society of Photogrammetry, p.115-164.

Griffiths,D.J., 1989. Introduction to Electrodynamics - 2nd Edition, Prentice-Hall International, Inc. New Jersey, USA.

Haack,B.N., 1988. *Shuttle Imaging Radar Analysis in Arid Environments.* In Technical Papers of American Society of Photogrammetry and Remote Sensing Annual Convention, St. Louis, MO, Vol.4, p.171-180.

Haack,B.N., 1984a. *L- and X-Band Like- and Cross-Polarised Synthetic Aperture Radar for Investigation of Urban Environments.* In Photogrammetric Eng. and Remote Sensing, Vol.50, No.3, March 1984, p.331-340.

Haack,B.N., 1984b. *Multisensor Data Analysis of Urban Environments.* In Photogrammetric Eng. and Remote Sensing, Vol.50, No.10, October, 1984, p.1471-1477.

Hara,Y., Atkins,R.G., Yueh,S.H., Shin,R.T. & Kong,J.A., 1994. *Application of Neural Networks to Radar Image Classification.* In IEEE Trans. on Geoscience and Remote Sensing, Vol.32, No.1 January, p.100-109.

Hardaway,G., Gustafson,G.C. & Lichy,D., 1982. *Cardinal Effect on Seasat Images of Urban Areas.* In Photogrammetric Eng. and Remote Sensing, Vol.48, No.3, March, p.399-404.

Harris,R., 1985. *SIR-A Imagery of Tunisia and its Potential for Population Estimation.* In Int. J. Remote Sensing, Vol.6, No.7, p.975-978.

Harvey,B.R., 1994. SURV1111 Introduction to Computing - Class notes 1994, School of Geomatic Engineering, University of New South Wales, Sydney Australia.

Harvey,B.R., 1991. Practical Least Squares and Statistics for Surveyors, The School of Surveying, University of New South Wales, Sydney Australia, 232pp.

Henderson,F.M. & Xia,Z-G., 1997. *SAR Applications in Human Settlement Detection, Population Estimation and Urban Land Use Pattern Analysis: A Status Report.* In IEEE Trans. on Geoscience and Remote Sensing, Vol.35, No.1, January, p.79-85.

Henderson,F.M. & Herrig,K., 1996. *Wavelength, Polarisation, and Incident Angle as Variables in Settlement Detection with Satellite SAR Imagery.* In Proceedings of XVIII ISPRS Congress, Vienna, Austria, 9-19 July 1996, Vol XXXI, Part B7, Commission VII, p.287-290.

Henderson,F.M., 1995. *An Analysis of Settlement Characterisation in Central Europe using SIR-B Radar Imagery.* In Remote Sensing of Environment, Vol.54, No.1, p.61-70.

Henderson,F.M. & Mogilski,K.A., 1987. *Urban Land Use Separability as a Function of Radar Polarisation.* In Int J. Remote Sensing, Vol.8, No.3, p.441-448.

Henderson,F.M., 1985. *Confusion Errors among Urban Land-Cover Types on SAR Imagery.* In Int.J.Remote Sensing, Vol.6, No.10, p.1607-1622.

Henderson,F.M., 1982. *An Evaluation of Seasat SAR Imagery for Urban Analysis.* In Remote Sensing of Environment, Vol.12, p.439-461.

Henderson,F.M. & Wharton,S.W., 1980. *Seasat SAR Identification of Dry Climate Urban Land Cover.* In Int. J. Remote Sensing, Vol.1, No.3, p.293-304.

Henderson,F.M. & Anuta,M.A., 1980. *Effects of Radar System Parameters, Population, and Environmental Modulation on Settlement Visibility*. In Int. J. Remote Sensing, Vol.1, No.2, p.137-151.

Hoekman,D.H., 1990. Radar Remote Sensing Data for Applications in Forestry, PhD thesis; Wageningen Agricultural University.

Hoekstra,P. & Delany,A., 1974. *Dielectric Properties of Soil at UHF and Microwave Frequencies*. In J. Geophysical Res., Vol.79, p.1699-1708.

Horton,F.E., 1974. *Remote Sensing Techniques and Urban Data Acquisition: Selected Examples*. In Remote Sensing: Techniques for Environmental Analysis, J.E.Estes & L.W.Senger (Ed), Hamilton Publishing Company, Santa Barbara, California.

Hubbert,J., Chandrasekar,V. & Bringi,V.N., 1992. *Radar and Optical Polarimetry: a Comparative Study*. In SPIE Vol.1748 Radar Polarimetry (1992), p.31-46.

Hussin,Y.A., 1994. *Effect of Polarisation on Radar Return from Urban Features using L-band Aircraft Radar Data*. Presented at the First International Airborne Remote Sensing Conference, Strasbourg, France, 11-15 Sept, 1994, Vol.2, p.13-21.

Imhoff,M.L., 1995. *A Theoretical Analysis of the Effect of Forest Structure on Synthetic Aperture Radar Backscatter and the Remote Sensing of Biomass*. In IEEE Trans. on Geoscience and Remote Sensing, Vol.33, No.2, March, p.341-352.

JPL., 1995. AirSAR Integrated Processor Documentation: Data Formats, version 0.01, California: Jet Propulsion Laboratory.

Kawamura,M., Jayamanna,S. & Tsujiko,Y., 1996. *Relation between Social and Environmental Conditions in Colombo, Sri Lanka and the Urban Index estimated by Satellite Remote Sensing Data.* In Proceedings of XVIII ISPRS Congress, Vienna, Austria, 9-19 July 1996, Vol XXXI, Part B7, Commission VII, p.321-326.

Kell,R.E. & Ross,R.A., 1970. Radar Cross Section of Targets, In Radar Handbook, Skolnik,M,I, (ed), McGraw-Hill, New York, 1509pp.

Kolawole,M.O., 1992. *On the Relationships between Attenuation and Volume Scattering Coefficients, and Vegetation Canopy Characteristics.* In Proceedings of 6th Australasian Rem. Sens Conference, Nov 1992, Wellington NZ, No.2, p.217-226.

Kolawole,M.O., 1991. *A Sparse Canopy Forest Backscatter Model.* In Proceedings IEEE, Int. Geoscience R.S. Symposium I, Helsinki, Finland, 1991 p.5-9.

Kraus,J.D., 1984. Electromagnetics, McGraw-Hill Book Company, New York, 775pp.

Kressler,F. & Steinnocher,K., 1996. *Change Detection in Urban Areas using Satellite Images and Spectral Mixture Analysis.* In Proceedings of XVIII ISPRS Congress, Vienna, Austria, 9-19 July 1996, Vol XXXI, Part B7, Commission VII, p.379-383.

LaPrade,G.L. & Leonardo,E.S., 1969. *Elevations from Radar Imagery.* In Photogrammetric Eng., Vol.35, No.4, April, p.366-371.

Lewis,A.J., MacDonald,H.C. & Simonett,D.S., 1969. *Detection of Linear Cultural Features with Multipolarised Radar Imagery.* In Proceedings of 6th

International Symposium on Remote Sensing of Env. Ann Arbour MI, p.879-893.

Lim,B.P., Rao,K.R., Tharmaratnam,K. & Mattar,A.M., 1979. Environmental Factors in the Design of Buildings Fenestration. Applied Science Publishers Ltd, London.

Lindgren,D.T., 1974. *Urban Application of Remote Sensing.* In Remote Sensing: Techniques for Environmental Analysis. J.E.Estes & L.W.Senger (Ed), Hamilton Publishing Company, Santa Barbara, California.

Lo,C.P., 1986. *Settlement, Population and Land Use Analysis of the North China Plain using Shuttle Imaging Radar-A Data.* In Professional Geographer, Vol.38, No.2, p.141-149.

Lo,C.P., 1984. *Chinese Settlement Pattern Analysis using Shuttle Imaging Radar-A data.* In Int. J. Remote Sensing, Vol.5, No.6, p.959-967.

McDonald,K.C. & Ulaby,F.T., 1993. *Radiative Transfer Modelling of Discontinuous Tree Canopies at Microwave Frequencies.* In Int. J. Remote Sensing, Vol.14, No.11, p.2097-2128.

MacGregor,J.G., 1988. Reinforced Concrete - Mechanics and Design. Prentice Hall, New Jersey.

Mackey,G.F.G., 1964. Modern Building Practice in Australia. Gregory's Guides and Maps Pty Ltd, Sydney.

Mann,P.A., 1989. Illustrated Residential and Commercial Construction. Prentice Hall, INC., Englewood Cliffs, New Jersey, USA.

Martin-Kaye,P.H.A., 1981. *Regional Interpretation of Radar Imagery.* In Int. Archives Photogramm., Int. Society Photogramm. 14th Congress, July, Presented papers, Hamburg W.Germany, 23,Pt.B, Comm.7.,623, p.624-633.

Mehta,J.B., 1978. High-Rise Buildings. Published by Author (Jashwant.B. Mehta), Bombay.

Moore,E.G., 1968. Side-Looking Radar in Urban Research: A Case Study, Research Report 40, Northwestern University, Department of Geography, Evanston I11.

Nasr,J.M. & Vidal-Madjar,D., 1991. *Image Simulation of Geometric Targets for Spaceborne Synthetic Aperture Radar.* In IEEE Trans. on Geoscience and Remote Sensing, Vol.29, No.6, November, p.986-996.

NATSPEC & Master Builders Australia, 1994. The National Housing Specification. NATSPEC Pty Ltd (Milsons Pt, Sydney) & Master Builders Australia Inc. (Turner, ACT).

Nunally,N.R., 1969. *Integrated Landscape Analysis with Radar Imagery.* In Remote Sensing of Environment, Vol.1, No.1, p.1-6.

Paudyal,D.R., Eiumnoh,A. & Aschbacher,J., 1995. *Textural Information in SAR Images for Land-Cover Applications.* In Proceedings of International Geoscience and Remote Sensing Conference (IGARSS'95), Firenze, Italy, 10-14 July 1995, p.1020-1022.

Pierce,L.E., Ulaby,F.T., Sarabandi,K. & Dobson,M.C., 1994. *Knowledge-Based Classification of Polarimetric SAR Images.* In IEEE Trans. on Geoscience and Remote Sensing, Vol.32, No.5., September, p.1081-1086.

Raney,R.K., Luscombe,A.P., Langham,E.J. & Ahmed,S., 1991. *Radarsat*, Individual paper, reprinted in Proceedings of the IEEE, Vol.79, No.6, June.

Richards,J.A., Milne,A.K. & Forster,B.C., 1994. SURV9609: Microwave Remote Sensing - Course Notes, School of Geomatic Engineering, University of New South Wales, Sydney, Australia.

Richards,J.A., 1990. *Radar Backscatter Modelling of Forests: a Review of Current Trends*. In Int. J. Remote Sensing, Vol.11, No.7, p.1299-1312.

Richards,J.A., Sun,G. & Simonett,D.S., 1987. *L-Band Radar Backscatter Modeling of Forest Stands*. In IEEE Trans. on Geoscience and Remote Sensing, Vol.GE-25, No.4, July, p.487-498.

Ruck,G.T., Barrick,D.E., Stuart,W.D. & Krichbaum,C.K., 1970. Radar Cross Section Handbook, Vol.1, Plenum Press, New York.

Ryan,B., 1990. The Good Building Guide. Doubleday, Moorebank NSW.

Schumann,R., 1996. *ERS Applications to Forestry, Agriculture and Soil Moisture*. Individual paper distributed at the 8th Australasian Remote Sensing Conference, Canberra.

Seifert,F.M., Kietzmann,H. & Zink,M., 1996. *Multifrequency and Polarimetric Analysis of Forests with SIR-C/X-SAR Data*. In Proceedings of International Geoscience and Remote Sensing Symposium (IGARSS'96) Lincoln, U.S.A., 27-31 May 1996, Vol.2, p.1086-1088.

Shaeffer,R.E., 1992. Reinforced Concrete - Preliminary Design for Architects and Builders. McGraw-Hill, Inc, New York.

Sieber,A.J., 1985. *Statistical Analysis of SAR Images*. In Int. J. Remote Sensing, Vol.6, No.9, p.1555-1572.

Sierra,J.E.E., 1994. Building Measurement. The open training education Network, Redfern.

Sun,G. & Ranson,K.J., 1995. *A Three-Dimensional Radar Backscatter Model of Forest Canopies*. In IEEE Trans. on Geoscience and Remote Sensing, Vol.33,No.2,March, p.372-382.

Sun,G., Simonett,D.S. & Strahler,A.H., 1991. *A Radar Backscatter Model for Discontinuous Coniferous Forests*. In IEEE Trans. on Geoscience and Remote Sensing, Vol.29, No.4, July, p.639-650.

Tajbakhsh,S., Kim,M-J., Berenyi,H.M. & Burge,R.E., 1995. *Simulated Images of Urban Areas Using an Extended GTD Ray Tracing Model of the Synthetic Aperture Radar*. In Proceedings of SPIE, Synthetic Aperture Radar and Passive Microwave Sensing Conference, Vol.2584, p.80-88.

Taket,N.D., Howarth,S.M. & Burge,R.E., 1991. *A Model for the Imaging of Urban Areas by Synthetic Aperture Radar*. In IEEE Trans. on Geoscience and Remote Sensing, Vol.29, No.3, May, p.432-443.

Toll,D.L., 1985. *Analysis of Digital LANDSAT MSS and SEASAT SAR Data for use in Discriminating Land Cover at the Urban Fringe of Denver, Colorado*. In Int. J. Remote Sensing, Vol.6, No.7, p.1209-1229.

Ulaby,F.T. & C.Elachi,C., (Eds) 1990. Radar Polarimetry for Geoscience Applications. Artech House Inc., MA.

Ulaby,F.T., Sarabandi,K., McDonald,K., Whitt,M. & Dobson,M.C., 1990. *Michigan Microwave Canopy Scattering Model.* In Int. J. of Remote Sensing, 1990, vol.11, No7, p.1223-1253.

Ulaby,F.T., Held,D., Dobson,M.C., McDonald,K.C. & Senior,T.B.A., 1987. *Relating Polarisation Phase Difference of SAR Signals to Scene Properties.* In IEEE Trans. on Geoscience and Remote Sensing, Vol.GE-25, No.1, January, p.83-92.

Ulaby,F.T., Moore,R.K. & Fung,A.K., 1981. Microwave Remote Sensing: Active and Passive, Vol.1,2, & 3 Addison-Wesley Publishing Company, Massachusetts 2162pp.

Van de Hulst,H.C., 1957. Light Scattering by Small Particles, John Wiley and Sons Inc., New York.

Van Zyl,J.J., 1989. *Unsupervised Classification of Scattering Behaviour Using Radar Polarimetry.* In IEEE Trans. on Geoscience and Remote Sensing, Vol.27, No.1, January, p.36-45.

Van Zyl,J.J., Zebker,H.A. & Elachi,C., 1987. *Imaging Radar Polarisation Signatures: Theory and Observation.* In Radio Science, Vol. 22, No. 4, July-August, p.529-543.

Wang,Y. & Davis,F.W., 1996. *Radar Backscatter Components from Ponderosa Pine Forests.* In International Geoscience and Remote Sensing Symposium (IGARSS'96), Lincoln, U.S.A, 27-31 May 1996, Vol. 2, p.1077-1079.

Wang,Y., Day,J. & Sun,G., 1993. *Santa Barbara Microwave Backscattering Model for Woodlands.* In Int. J. of Remote Sensing, 1993, Vol.14, No.8, p.1477-1493.

Wang,J.R. & Mo,T., 1990. *The Polarisation Phase Difference of Orchard Trees*. In Int J. of Remote Sensing, 1990, Vol.11, No.7, p.1255-1265.

Weast,R.C., (Editor) 1986. Handbook of Chemistry and Physics - 67th Edition (1986-1987) CRC Press, Inc. Boca Raton, Florida.

Weydahl,D.J., Becquey,X. & Tollefsen,T., 1995. *Combining ERS-1 SAR with Optical Satellite Data over Urban Areas*. In Proceedings of International Geoscience and Remote Sensing Conference (IGARSS'95), Firenze, Italy, 10-14 July 1995, p.2161-2163.

Xia,Z-G. & Henderson,F.M., 1997. *Understanding the Relationships between Radar Response Patterns and the Bio- and Geophysical Parameters of Urban Areas*. In IEEE Trans. on Geoscience and Remote Sensing, Vol.35, No.1, January, p.93-101.

Xia,Z-G., 1996. *Applications of Multi-Frequency, Multi-Polarisation and Multi-Incident Angle SAR Systems in Urban Land Use and Land Cover Mapping*. In Proceedings of International Geoscience and Remote Sensing Symposium (IGARSS'96), Lincoln, U.S.A, 27-31 May 1996, Vol.4, p.2310-2314.

Zebker,H.Z. & Van Zyl,J.J., 1991. *Imaging Radar Polarimetry: A Review*. In Proceedings of the IEEE, Vol.79, No.11, Nov, p.1583-1606.

Zebker,H.A., Van Zyl,J.J. & Held,D.N., 1987. *Imaging Radar Polarimetry from Wave Synthesis*. In International J. Geophysical Research, Vol. 92, No. B1, 1987, p.683-701.

Appendix A: Radar Terminology

This is a brief description of some common terminology used when discussing radar remote sensing, as used in this research.

Look Angle:	the angle in the plane of incidence, between the vertical, and the direction of radiation.
Incident Angle:	the angle which the radar wave contacts the imaged surface. Normal to the surface is an incidence angle of 0°. This is equal to the Look Angle when the surface is horizontal.
Look Direction:	the direction which the radar wave is transmitted.
Polarisation:	generally described as horizontal or vertical. A horizontally transmitted and horizontally received wave is represented as HH, similarly a vertical transmitted and received wave is represented as VV. These are termed co-polarised. Cross-polarisation is HV or VH, ie., horizontally transmitted, vertically received or vertically transmitted and horizontally received, respectively.
Wavelength:	The common radar remote sensing wavelengths are K-band (1.1-1.67cm), X-band (2.4-3.75cm), C-band (3.75-7.5cm), L-band (15-30cm), and P-band (30-100cm).

Appendix B: Relative Dielectric Constant of Materials relevant for Urban Environments

A variety of references were available to assist in estimating the dielectric constant from urban materials. From Griffiths (1989) it can be seen that glass has a real dielectric constant component ε_r of 4-7 and water has an ε_r of 80.4. Asphalt is given an ε_r of 2.7 (Weast, 1986). Beaty (1990) gives the real dielectric constant for ceramics to have an average range from ε_r around 6 up to 7.6. Dong (1995b) investigated the dielectric constant of soils. The dielectric constant varies with moisture and location for soil under eucalypts, but the values range from around 9.1+2.1i up to 11+3.5i, from two different calculation methods.

For soils and water, Ulaby *et al.* (1981) show that the dielectric constant does vary for different wavelengths but it is usually not a large amount, eg., when the wavelength is around C-band, ε_r is ~3.2 for dry soils (such as sand, silt, and clay) (Hoekstra & Delany, 1974) and ~77 for water (Richards *et al.,* 1994), but for around P-band ε_r has only increased to ~3.5 (Hoekstra & Delany, 1974) and ~79 respectively (Richards *et al.,* 1994). When soils become moist, the dielectric constant will increase quite considerably. As Ulaby *et al.* (1981) demonstrates, the dielectric constant will increase from around 3+0i with a volumetric moisture content of 0, up to ~10+2i when the moisture content is increased to 0.2(g/cm^3). These values enable a general range for the dielectric constants to be estimated. In the model, the dielectric constants are held constant for different wavelengths.

Appendix C: Discussion of Metals in a Residential Building

Metals play an integral role in the construction of a residential building. Hot and cold water pipes can be either internal (between the inner and outer walls) or external (for older style buildings). These pipes generally run parallel with the building wall edges. Gas piping in residential buildings can be made from iron or steel. The roof gutter for rainwater drainage runs along the building roof edge and down the downpipe (usually 100*50mm size) (Ryan, 1990) which runs down the exterior of the building. The downpipe must be fixed to brickwork, usually with galvanised steel straps screwed to the brickwork every 1.8m (Sierra, 1994).

Many modern residential buildings have aluminium framed windows. The power box, which can be situated on the exterior of the building, is also made of metal. The building cladding, being of reasonably low dielectric, allows the radar to penetrate further into the building and interact with metal in the wall.

Beneath the exterior cladding, metal can be found for the purposes of connecting building materials together. Some of this hardware includes nails, screws, anchor bolts, hangers, and straps. They can be made from steel, copper, zinc, brass, or aluminium (Falcone, 1978). Steel can be used as floor bearers, joists, roof strutting, beams, lintels, piling and other applications (BHP Steel, 1995).

The framing members can be timber, steel, aluminium, reinforced concrete, or some combination of these (Australian Government Task Force to Investigate Modern Housing Techniques, 1974), unless the building is double brick. However, "structural steel is playing an increasingly important role in traditional and medium density housing" (BHP Steel, 1995, p2). For apartments, reinforced concrete is used to strengthen floors. The metal reinforcement should have a minimum overlap of 225mm for general mesh or 500mm for trench mesh, and reinforcing bars should be spaced about 500mm apart (NATSPEC & Master Builders Australia, 1994).

Lintels, situated above openings in the walls, such as windows, can be made of timber or galvanised steel (Ryan, 1990). Flashing, to prevent fluid leakage inside the building, is often made of aluminium (Chung & Adams, 1991). The bracing of a residential building wall can be made of timber, but it is more common to use a strip of metal, or a sheet (such as chipboard) (Ryan, 1990).

Nails are used to connect all the building studs and bracing together. The exterior wall studs are usually spaced 40 to 61cm apart (Chung & Adams, 1991). The nails used for timber frames are often 100mm long, and there should be two nails at each end of the noggings between the studs, and a nail attaching the wall frame to the floor slab between each stud (Ryan, 1990). Metal ties, connecting the inner and outer walls are spaced about 61cm apart, and anchor bolts, connecting the wall to the foundations, are also about 61cm apart. Anchor bolts are at least 38cm in length (Falcone, 1987). For brickwork, metal wall ties should be spaced a maximum of about 2-2.5 bricks apart horizontally.

Some metals found in residential buildings (including some of those just discussed), particularly in and around the ceiling, will contribute to single bounce of the radar wave. The building gutters are made of metal acting as a strong scatterer. Roof tiles (of average size 450*300mm) are wired to the battens, with copper, which are nailed to the rafters for a timber framed building (Sierra, 1994). For terracotta tiles, each alternate tile is tied down. Concrete tiles are "holed to receive galvanised flat head nails, every third course being nailed to the battens" (Mackey, 1964, p90). Tiled roofs must have flashing placed in the junctions of roof coverings with walls. Roof trusses may be constructed from timber, steel, aluminium or a combination of timber and metal. The joints between the members are fixed by bolts, straps, rivets and welding (Mackey, 1964).

Hence, metals form a reasonably large component of residential buildings, and may contribute to the backscatter through both double and single bounce scattering.

Appendix D: Metals found in Commercial Buildings

In a commercial building, metal is required to fulfil a number of roles. A commercial building frame is generally made from reinforced concrete or steel. For reinforced concrete frames the percentage of metal required for reinforcement increases as the number of storeys in a building increase. If the steel exceeds 5-6% in reinforced concrete, it is more economical to have steel columns (Mehta, 1978). The average amount of reinforcement (ie., metal) used in concrete is roughly 2% by volume (MacGregor, 1988), but the percentage of metal depends on the buildings structural element. Most concrete columns are reinforced with 2-6% of metal (Shaeffer, 1992). Even though reinforced concrete contains up to 6% metal, the effect can give a strong radar response, like a pure metal conductor, where the spacing between the rods is small compared to the wavelength. This phenomenon is due to resonant elements which are metallic, or have a high dielectric constant, whose lengths and spacing are integer multiples of $\lambda/2$ (where λ is the wavelength). "Such objects have a reradiation pattern the same as that for an antenna of the same dimensions" (Ulaby *et al.,* 1981, p841).

The spacing of metal reinforcement is a function of the load to be placed on it. Metal bars in a concrete slab (for a building wall) should be no further than 18 in. (46cm) apart (Shaeffer, 1992), a reinforced column should have a metal rod spacing no more than 6 in. (15.24cm) apart for typical square, or rectangular columns (Shaeffer, 1992). Therefore, where the spacing between the metal is less than 23cm the response from reinforced concrete can be quite significant.

A number of buildings in the CBD of Sydney have reinforced concrete as their support, eg., The Sydney Hilton, AMP building, Hyde Park Square, and the MLC building (Mehta, 1978). The Sydney Hilton consists of reinforced concrete, composite steel and concrete, and prestressed concrete slabs (Mehta, 1978). The reinforced concrete columns of the AMP building have "hard grade 38mm square bar reinforcement" (Mehta, 1978), with the columns being 1.9*0.6m for the full building height. Its precast floor planks rest on

reinforced beams. The Hyde Park Square building is a composite steel and concrete frame with rectangular hollow steel sections for the perimeter columns. The flooring is a concrete slab "acting integrally with galvanised steel decking" (Mehta, 1978, p99). "A 140mm steel channel section trims the perimeter between the main beams" (Mehta, 1978, p100). The MLC Centre is a reinforced concrete tower, and is situated over two railway tunnels about 2.4m below the foundation level (Mehta, 1978).

Some metal is situated on the exterior of a commercial building. Aluminium frames are reasonably common. Some buildings have metal as part of the structural support placed externally for aesthetic purposes, while others have walls partially clad in aluminium. It is not uncommon for buildings to have metal shades covering the windows.

Although glass has a reasonably low dielectric constant (ε_r=5 to 10), some buildings in the CBD have tinted windows. Glass can be tinted to form heat-absorbing glass, heat reflecting glass, photo-chromatic glass, and clear glass treated with heat reflecting polyester films (Lim *et al.,* 1979). All glass types contain some form of metal.

Heat-absorbing glass has metal oxides added to the glass during production (Lim *et al.,* 1979). Heat reflecting glass has a very thin metallic film applied to the glass (Beckett & Godfrey, 1974), the amount of coating depending on whether it is single or double glazed glass (Lim *et al.,* 1979). Photo-chromatic glass contains silver (from silver halide crystals) (Lim *et al.,* 1979). The glass treated with heat reflecting polyester film has a polyester-coated reflected film applied to glass with an aluminium layer. The density of the aluminium coating depends on the solar control requirements (Lim *et al.,* 1979). These tinting techniques are visible in the city, especially in the large new buildings.

Therefore it is apparent that there is a the large proportion of metal in commercial buildings.

Appendix E: Location of Test Sites

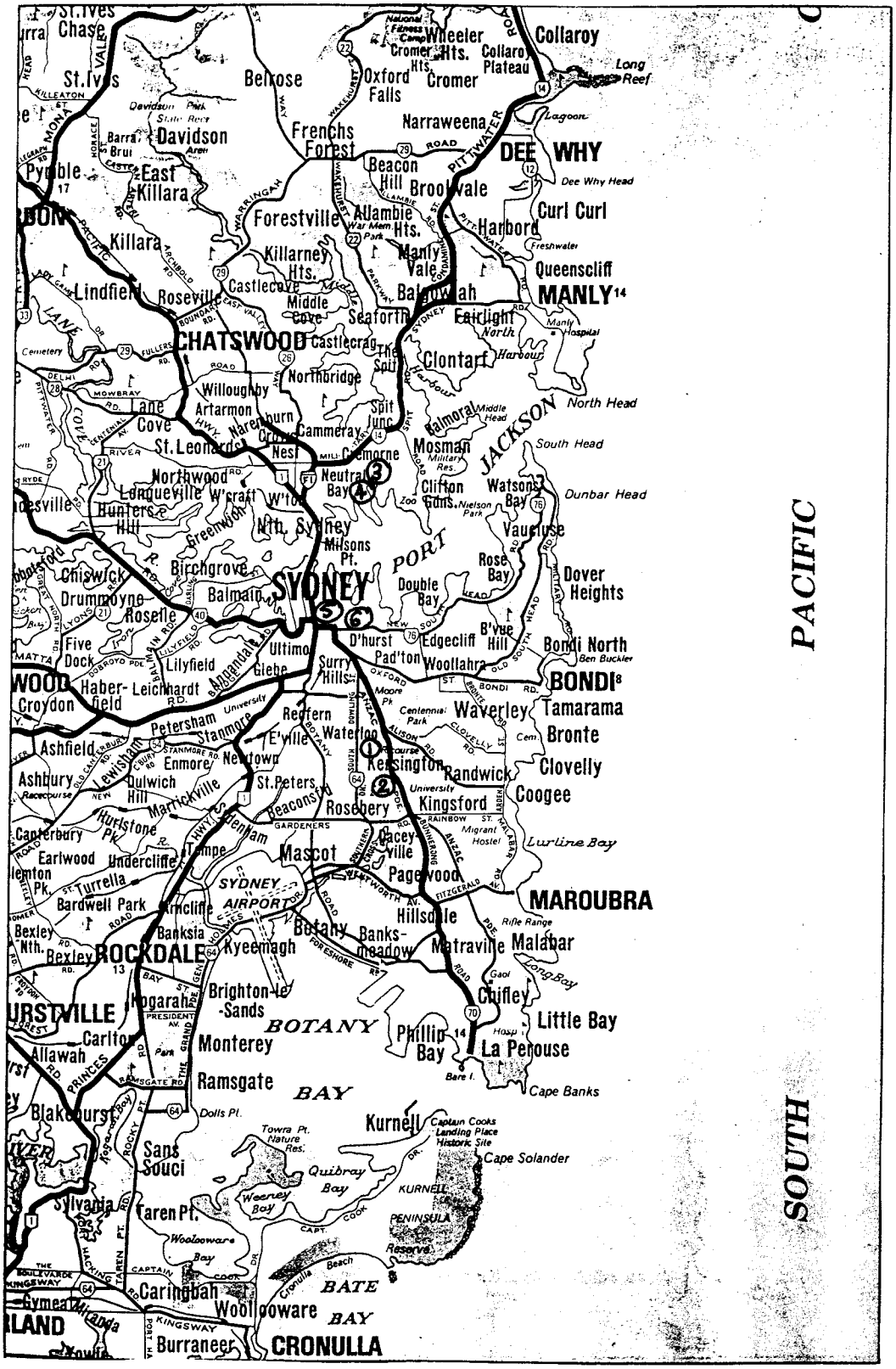

Figure E.1. The approximate location of the test sites (represented by their numbers - in red), from the AirSAR data, situated throughout Sydney, Australia. (Map from *Gregory's Sydney Street Directory*, 53rd Ed, 1988)

Appendix F: AirSAR Polarisation Signatures for C-, L- and P-band, for a Variety of Sydney Sites

There is not a large difference between the real polarisation signatures for C, L and P-band. As these polarisation signatures demonstrate here, for a large number of residential and commercial sites, there are no large discrepancies between the signatures for different wavelengths. Such results imply that multiple radar wavelengths may not provide significantly more information than single wavelength data. However, such a study was done only for residential and commercial land use, it may be different for other urban classes. Furthermore, wavelengths other than C-, L- and P-band, given here, may provide different information in an urban environment. It is these areas yet to be explored.

Once again the different sites were selected over Sydney. Their approximate location is given by their suburb name, and they are labelled as residential (res) or commercial (com). There are some polarisation signatures of the same suburb but different local site. Their exact location is of no concern since the primary purpose of these diagrams is to illustrate the similarities between signatures for different wavelengths of the same area.

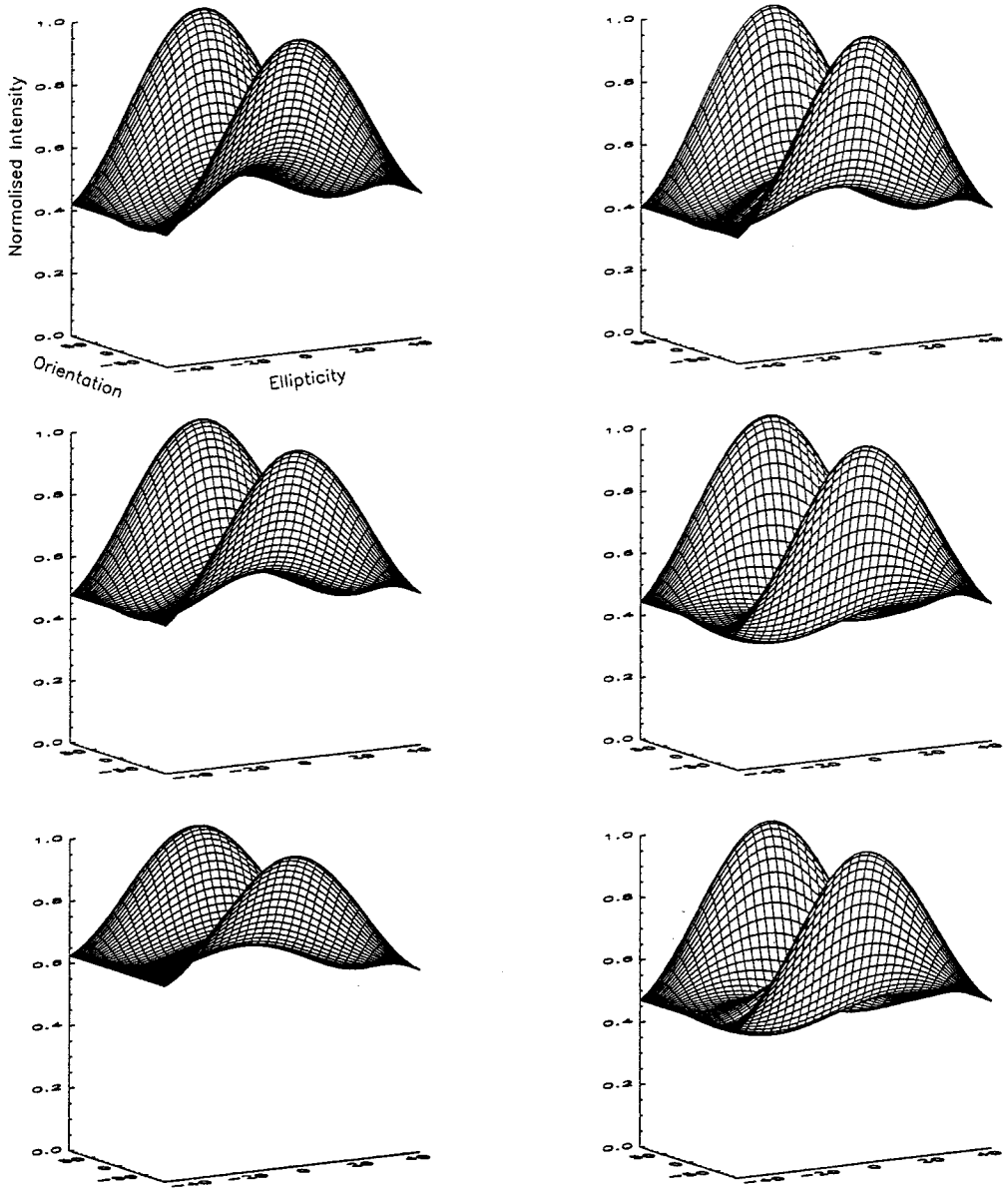

Figure F.1. Comparison of Normalised Polarisation Signatures from AirSAR data for C-, L- and P-band. The left column is for Kensington (res), and the right column is for Kingsford (res). The top, middle and bottom rows are for C-, L- and P-band respectively.

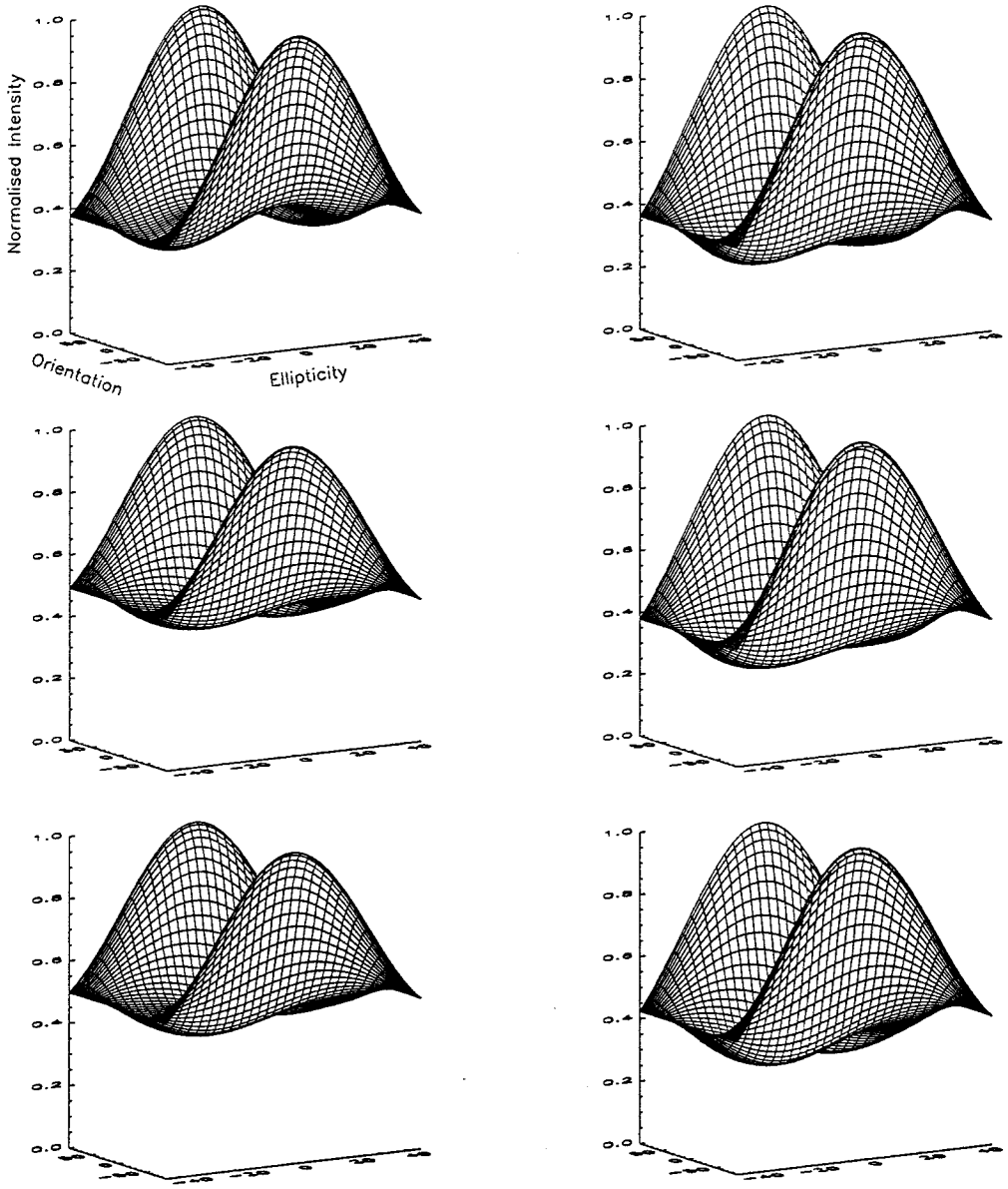

Figure F.2. Comparison of Normalised Polarisation Signatures from AirSAR data for C-, L- and P-band. The left column is for Kingsford (res), and the right column is for Kingsford (res). The top, middle and bottom rows are for C-, L- and P-band respectively.

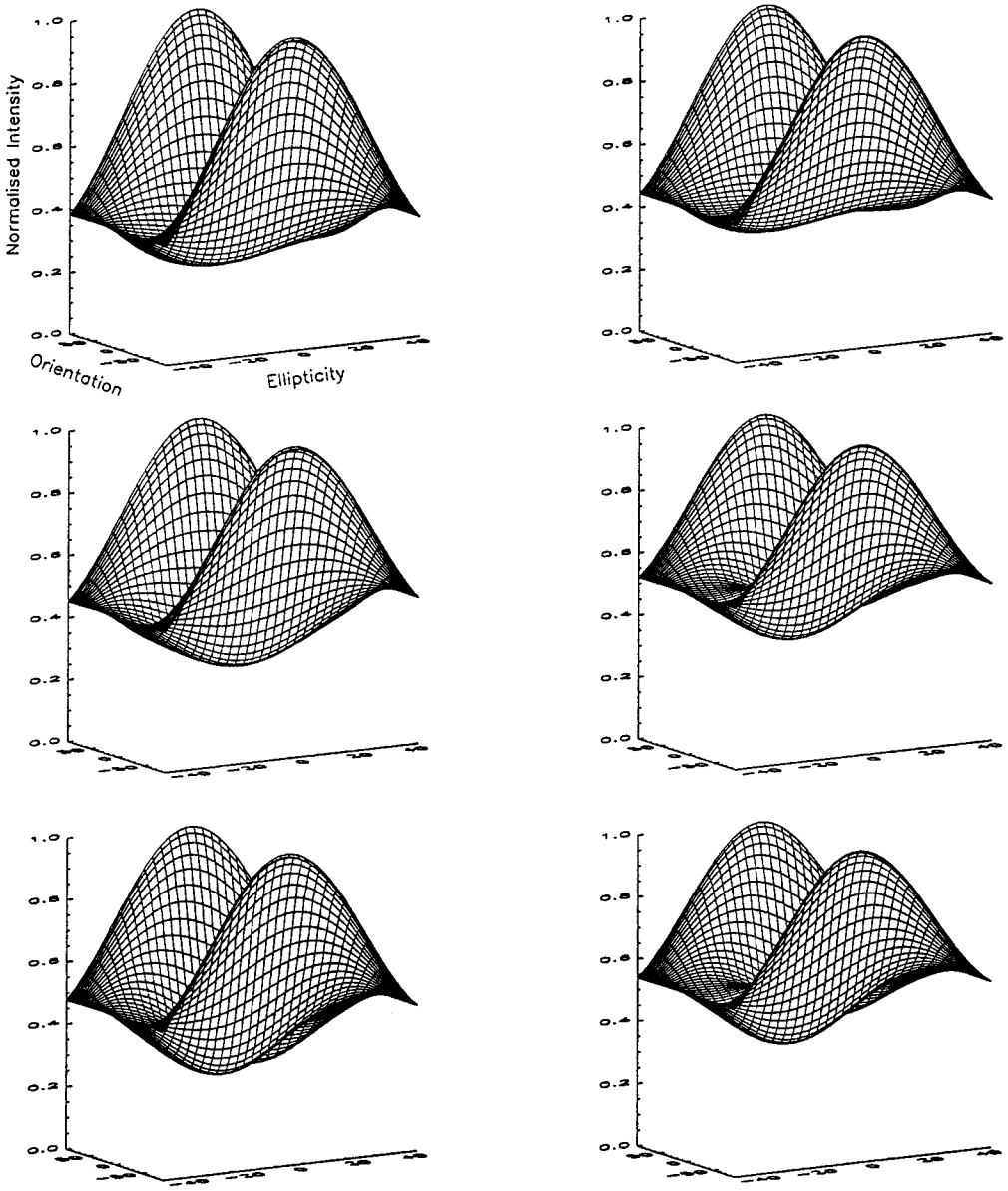

Figure F.3. Comparison of Normalised Polarisation Signatures from AirSAR data for C-, L- and P-band. The left column is for Centennial Park (res), and the right column is for Coogee (res). The top, middle and bottom rows are for C-, L- and P-band respectively.

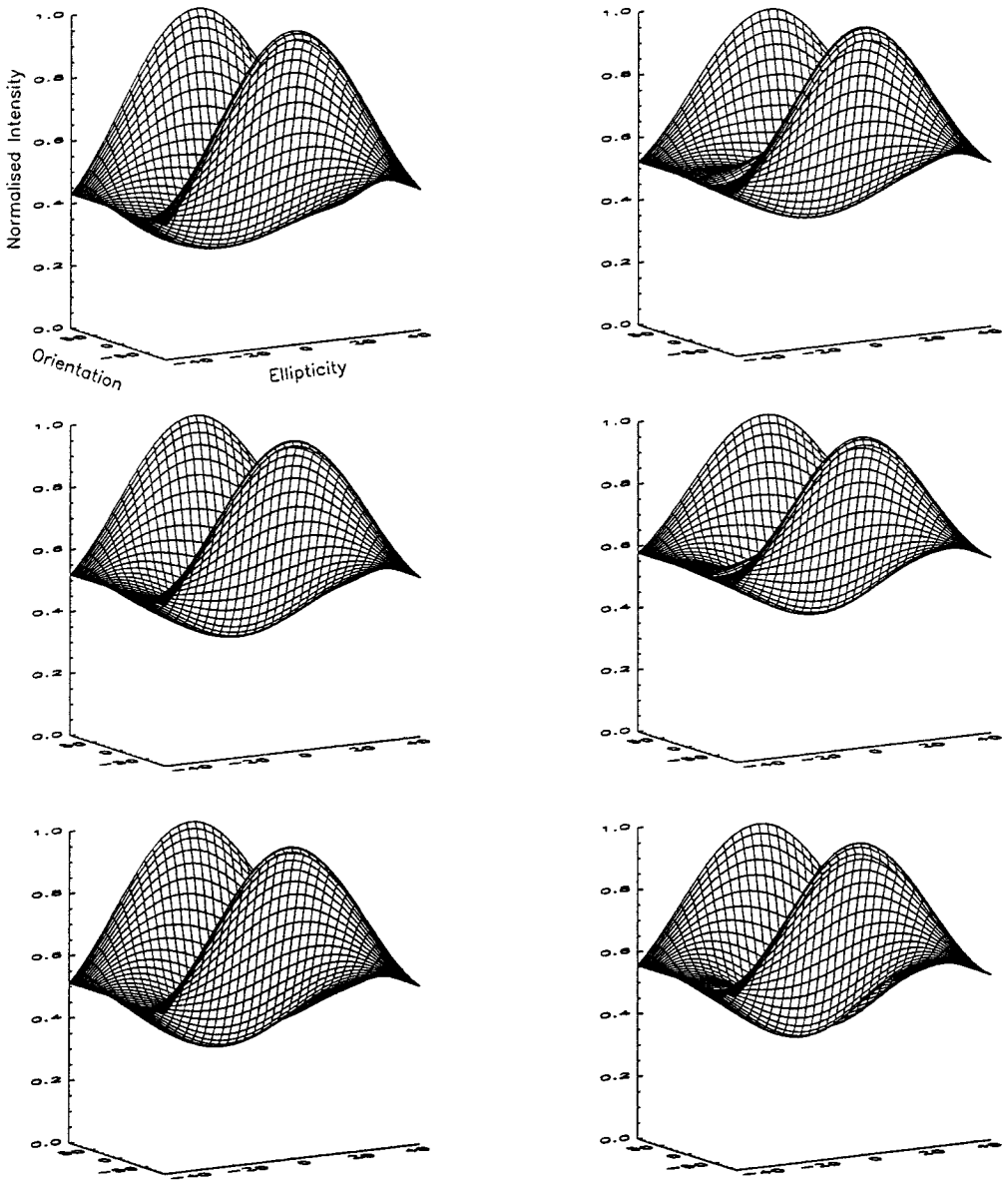

Figure F.4. Comparison of Normalised Polarisation Signatures from AirSAR data for C-, L- and P-band. The left column is for Queens Park (res), and the right column is for Bondi Junction (res). The top, middle and bottom rows are for C-, L- and P-band respectively.

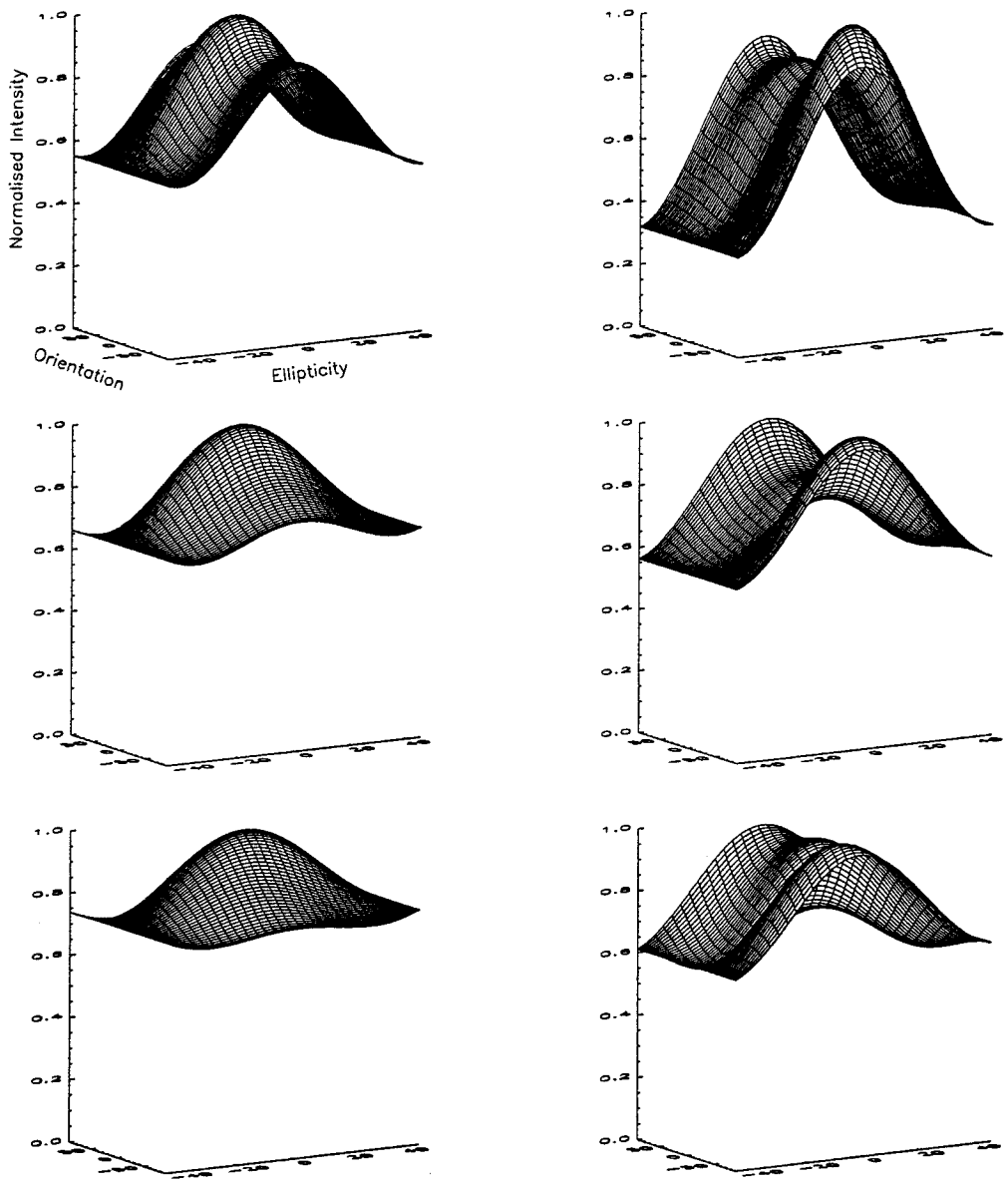

Figure F.5. Comparison of Normalised Polarisation Signatures from AirSAR data for C-, L- and P-band. The left column is for Paddington (res), and the right column is for Cremorne (res). The top, middle and bottom rows are for C-, L- and P-band respectively. It is worth noting that the Paddington site is showing an unusual polarisation response in relation to its location on the AirSAR image. (The site has a look angle of 54° and an orientation angle around 45°). Possible reasons for this different response compared to other residential sites, could be that Paddington contains a large proportion of rows of two storey terrace buildings, densely spaced.

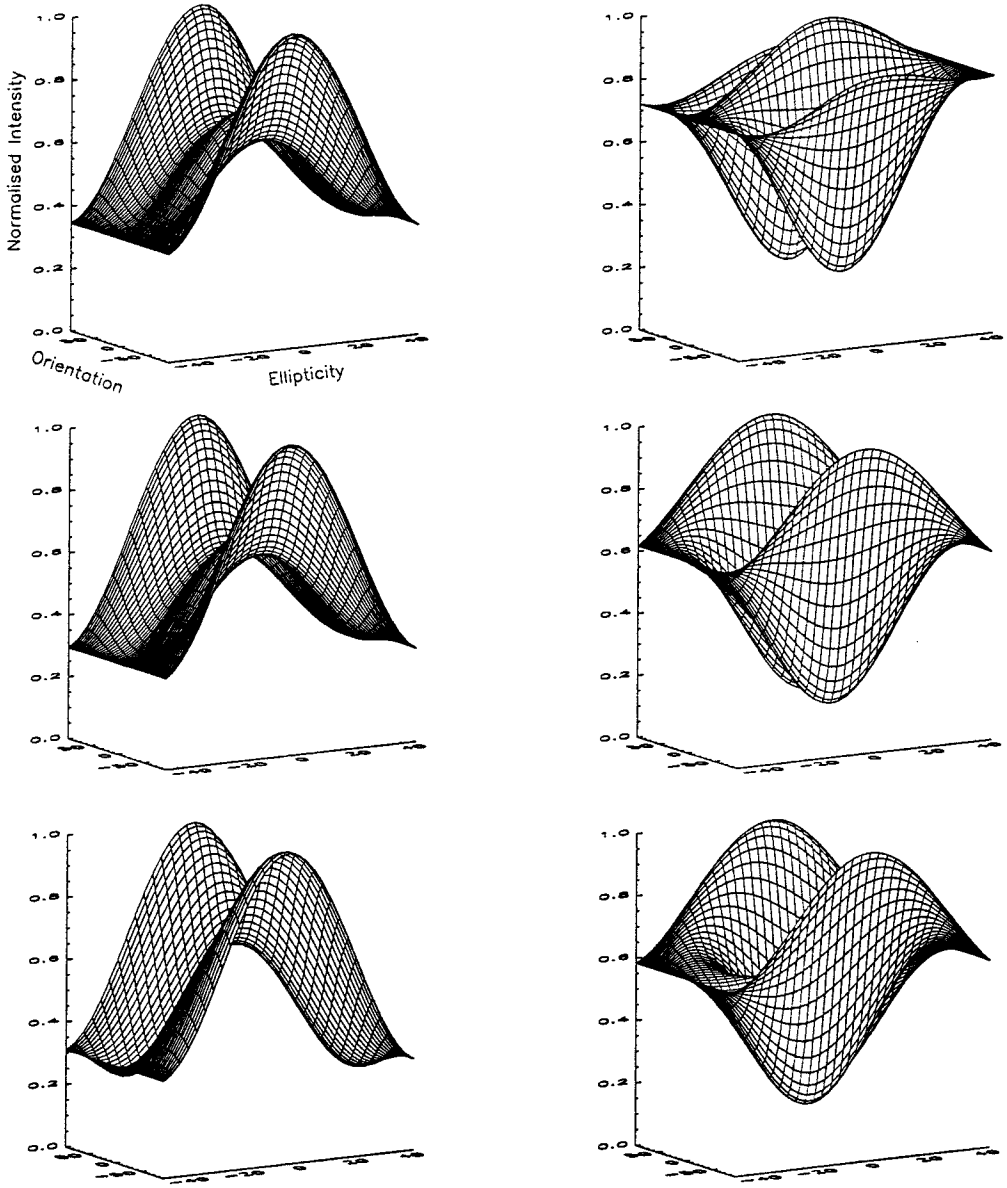

Figure F.6. Comparison of Normalised Polarisation Signatures from AirSAR data for C-, L- and P-band. The left column is for Neutral Bay (res), and the right column is for Sydney CBD (com). The top, middle and bottom rows are for C-, L- and P-band respectively.

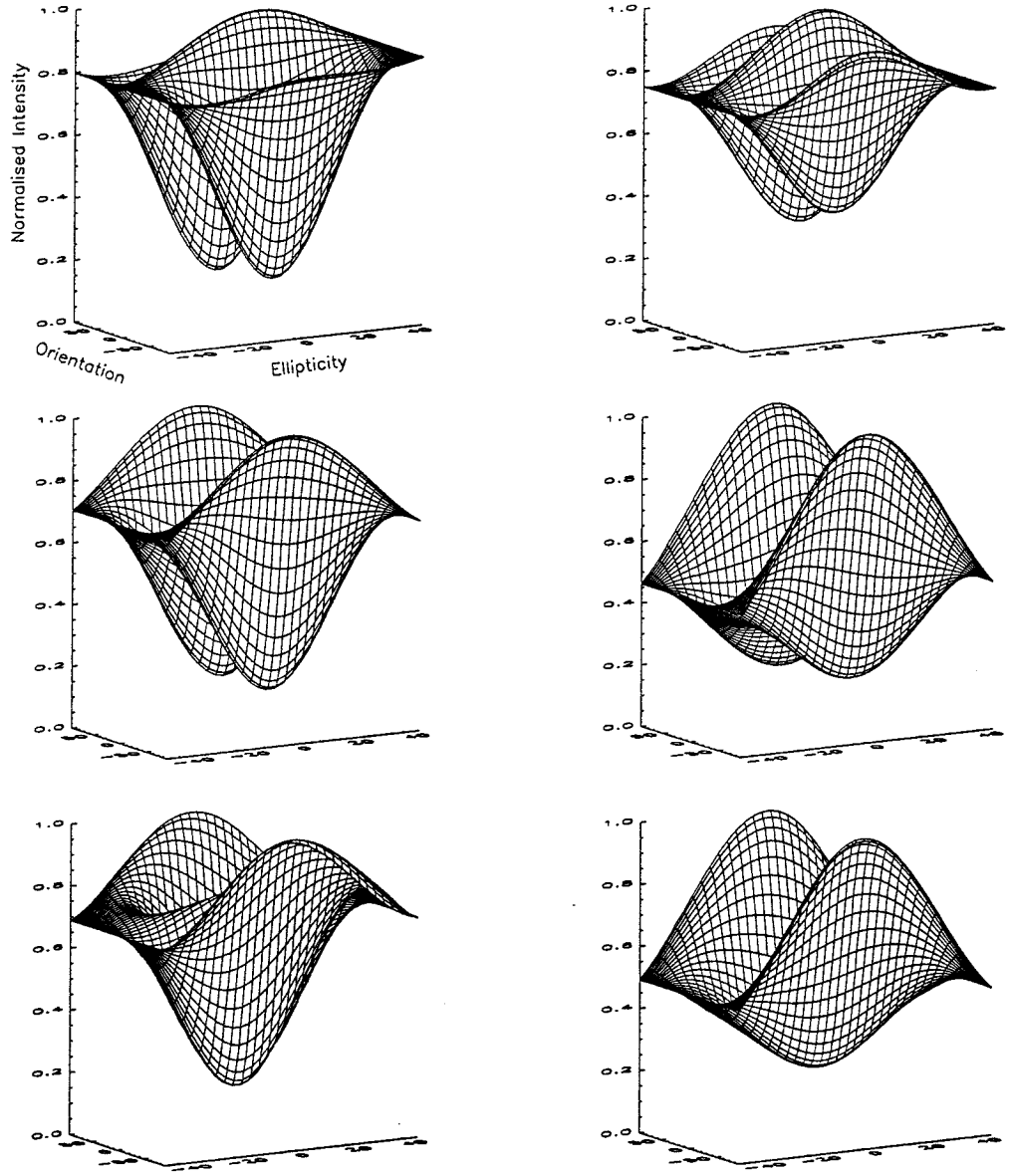

Figure F.7. Comparison of Normalised Polarisation Signatures from AirSAR data for C-, L- and P-band. The left column is for Sydney CBD (com), and the right column is for Sydney CBD (com). The top, middle and bottom rows are for C-, L- and P-band respectively.

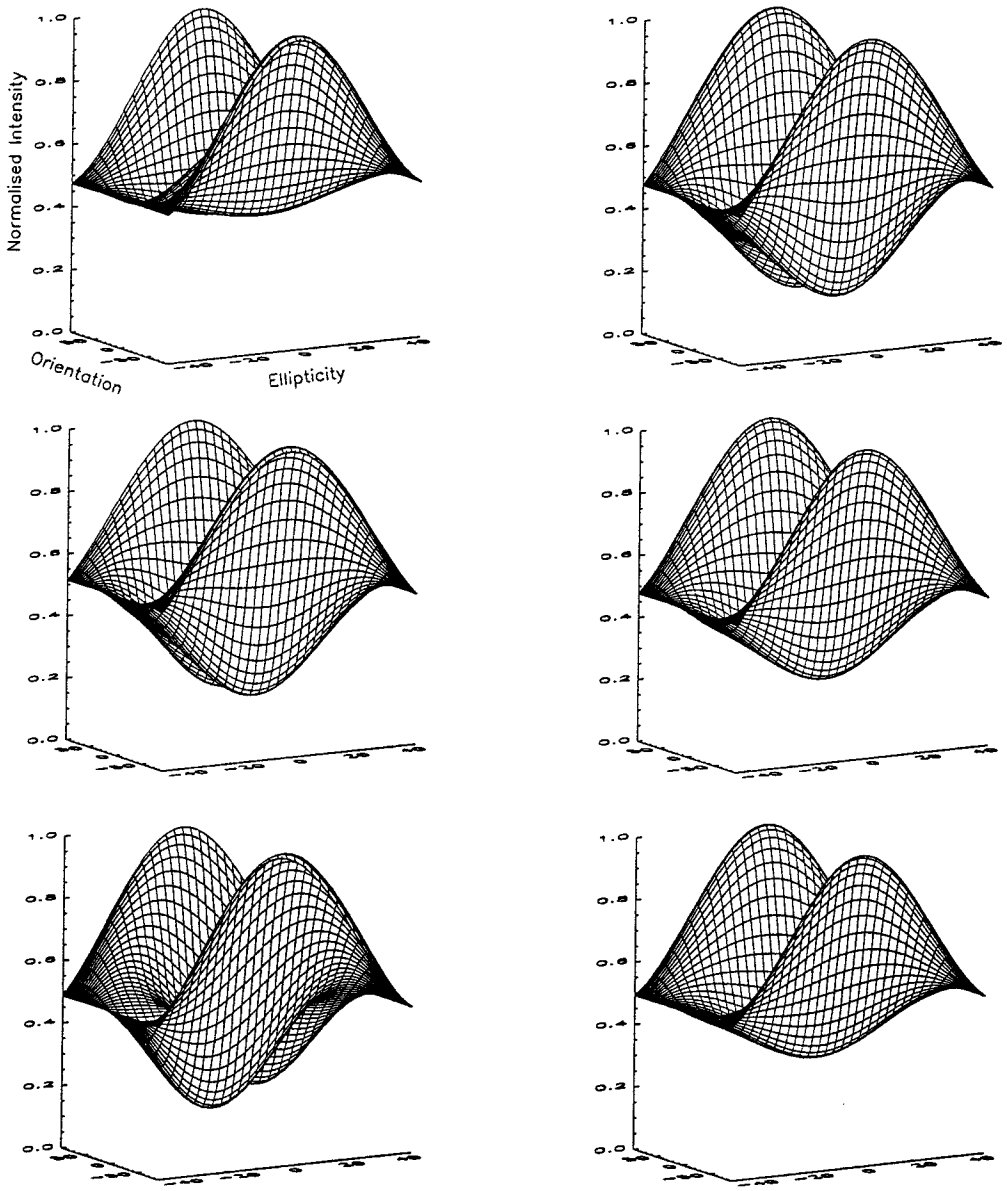

Figure F.8. Comparison of Normalised Polarisation Signatures from AirSAR data for C-, L- and P-band. The left column is for North Sydney (com), and the right column is for Bondi Junction (com). The top, middle and bottom rows are for C-, L- and P-band respectively.

Appendix G: Classification Results of Individual Kensington and Bondi Sites

Table G.1. The percentage of omission/commission results for the six types of classification performed for the Kensington test site. The omission/commission errors have been defined in Table 8.5. '9' and '15' represent the pixel averaging square, and 'a', 'b', and 'c' are the classification types (defined in Section 8.5).

Images	Kens 9a	Kens 9b	Kens 9c	Kens 15a	Kens 15b	Kens 15c
Description	%	%	%	%	%	%
C	29.3	52.1	63.1	17.8	45.3	62.1
CR	0.3	2.1	2.7	0	1.2	2.1
PR	1.1	2.8	6.3	0.3	3.3	8.8
TR	0.1	0.2	0.2	0.1	0.2	0.2
IR	2.4	10.1	15.1	1.0	7.5	15.9
RC	1.3	1.9	4.2	0.1	0.9	3.6
PC	0	0.1	0.2	0	0	0.4
TC	0	0	0	0	0	0.1
IC	0.7	2.5	6.0	0.4	1.6	6.2
RP	0.6	0.6	0.6	0.1	0.1	0.1
CP	0	0	0	0	0	0
TP	0.1	0.1	0.1	0	0	0
IP	1.5	1.5	1.5	0.4	0.4	0.4
RU	35.2	12.6	0	45.4	17.7	0
CU	4.0	1.3	0	4.6	2.7	0
PU	5.4	3.7	0	8.9	5.9	0
TU	0.1	0	0	0.2	0.1	0
IU	17.9	8.4	0	20.7	13.1	0

Table G.2 The percentage of omission/commission results for the six types of classification performed for the Bondi test site. The omission/commission errors have been defined in Table 8.5. '9' and '15' represent the pixel averaging square, and 'a', 'b', and 'c' are the classification types (defined in Section 8.5).

Images	Bondi 9a	Bondi 9b	Bondi 9c	Bondi 15b	Bondi 15c
Description	%	%	%	%	%
C	21.7	58.1	72.5	55.8	70.6
CR	0.2	4.3	5.8	3.6	5.0
PR	0.1	0.6	8.4	1.0	12.6
TR	0	0.5	0.5	0.5	0.5
IR	0.3	3.0	6.1	3.7	6.9
RC	3.6	3.8	4.4	2.5	3.3
PC	0	0	0.1	0	0
TC	0.1	0.1	0.1	0.3	0.3
IC	0.6	0.8	1.3	0.1	0.7
RP	0.2	0.3	0.3	0	0
CP	0	0	0	0	0
TP	0.2	0.2	0.2	0.1	0.1
IP	0.3	0.3	0.3	0	0
RU	49.3	12.9	0	12.5	0
CU	8.1	3.6	0	4.3	0
PU	8.5	8.0	0	11.7	0
TU	0.4	0	0	0	0
IU	6.4	3.5	0	3.9	0

Table G.3 Approximate percentage of cover types in the Kensington and Bondi test sites.

Cover Type	Bondi	Kens
Residential	53	48
Commercial	12	5
Park	26	24
Tower block	1	0.3
Institutional	8	23

Appendix H: Omission/Commission Tables for Combined Site

Table H.1. Errors of omission/commission for image 9a. Values are plotted in pixel numbers. The ground truth was provided by the photographs. Note that numbers are approximate due to the resolution of the grid used, and round-off errors. Abbreviations: Res (residential), Com (commercial), Unclass (unclassified), Twr Blk (tower block), and Instit (Institutional).

		Classified image				
	Image 9a	Res	Com	Park	Unclass	Total
Ground Truth	Res	7942	2224	529	42250	52945
	Com	318	1482	0	5612	7412
	Park	741	0	18954	6777	26472
	Twr Blk	106	0	106	212	424
	Instit	1800	741	1165	14930	18636
	Total	10907	4447	20754	69781	105889

Table H.2. Errors of omission/commission for image 9b. Values are plotted in pixel numbers. The ground truth was provided by the photographs. Note that numbers are approximate due to the resolution of the grid used, and round-off errors. Abbreviations: Res (residential), Com (commercial), Unclass (unclassified), Twr Blk (tower block), and Instit (Institutional).

		Classified Image				
	Image 9b	Res	Com	Park	Unclass	Total
Ground Truth	Res	36320	2647	529	13448	52944
	Com	2965	2224	0	2224	7413
	Park	2224	106	18742	5400	26472
	Twr Blk	318	0	106	0	424
	Instit	8259	2012	1165	7201	18637
	Total	50086	6989	20542	28273	105890

Table H.3. Errors of omission/commission for image 9c. Values are plotted in pixel numbers. The ground truth was provided by the photographs. Note that numbers are approximate due to the resolution of the grid used, and round-off errors. Abbreviations: Res (residential), Com (commercial), Unclass (unclassified), Twr Blk (tower block), and Instit (Institutional).

		Classified Image				
	Image 9c	Res	Com	Park	Unclass	Total
Ground Truth	Res	47862	4553	529	0	52944
	Com	3918	3494	0	0	7412
	Park	7412	106	18848	0	26366
	Twr Blk	318	0	106	0	424
	Instit	12813	4765	1165	0	18743
	Total	72323	12918	20648	0	105889

Table H.4. Errors of omission/commission for image 15b. Values are plotted in pixel numbers. The ground truth was provided by the photographs. Note that numbers are approximate due to the resolution of the grid used, and round-off errors. Abbreviations: Res (residential), Com (commercial), Unclass (unclassified), Twr Blk (tower block), and Instit (Institutional).

		Classified Image				
	Image 15b	Res	Com	Park	Unclass	Total
Ground Truth	Res	34414	1482	106	16942	52944
	Com	2118	1906	0	3388	7412
	Park	2647	0	15566	8259	26472
	Twr Blk	212	106	0	106	424
	Instit	6565	1165	318	10589	18637
	Total	45956	4659	15990	39284	105889

Table H.5. Errors of omission/commission for image 15c. Values are plotted in pixel numbers. The ground truth was provided by the photographs. Note that numbers are approximate due to the resolution of the grid used, and round-off errors. Abbreviations: Res (residential), Com (commercial), Unclass (unclassified), Twr Blk (tower block), and Instit (Institutional).

		Classified Image				
	Image 15c	Res	Com	Park	Unclass	Total
Ground Truth	Res	49027	3706	106	0	52839
	Com	3177	4130	0	0	7307
	Park	10589	318	15461	0	26368
	Twr Blk	424	424	0	0	848
	Instit	13554	4659	318	0	18531
	Total	76771	13237	15885	0	105893

Appendix I: Classification and Difference Images

Legend for all proceeding classifications:

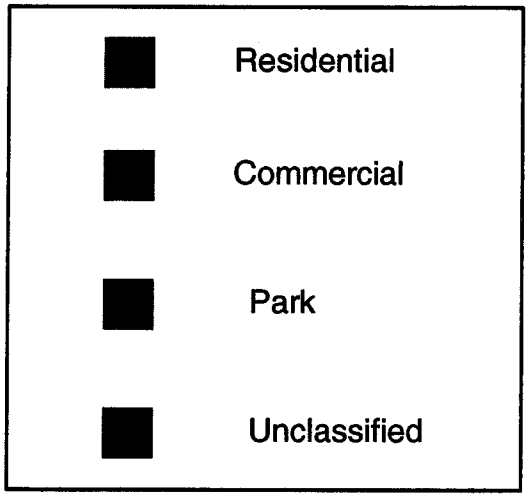

Refer to Section 8.5 for a further explanation of terminology.

Bondi classified images:

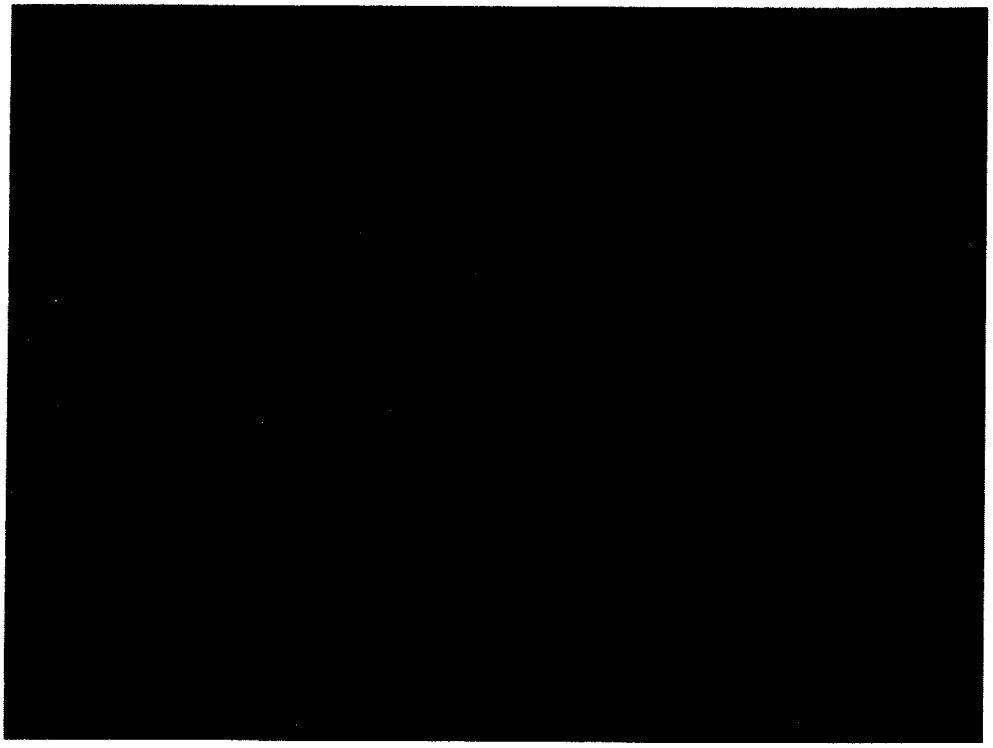

Figure I.1. Classified image of bondi9c (ie., using a 9*9 pixel averaging square, with total power as the classification criteria). Note that all pixels were classified. Refer to Figure I.11 for the ground truth.

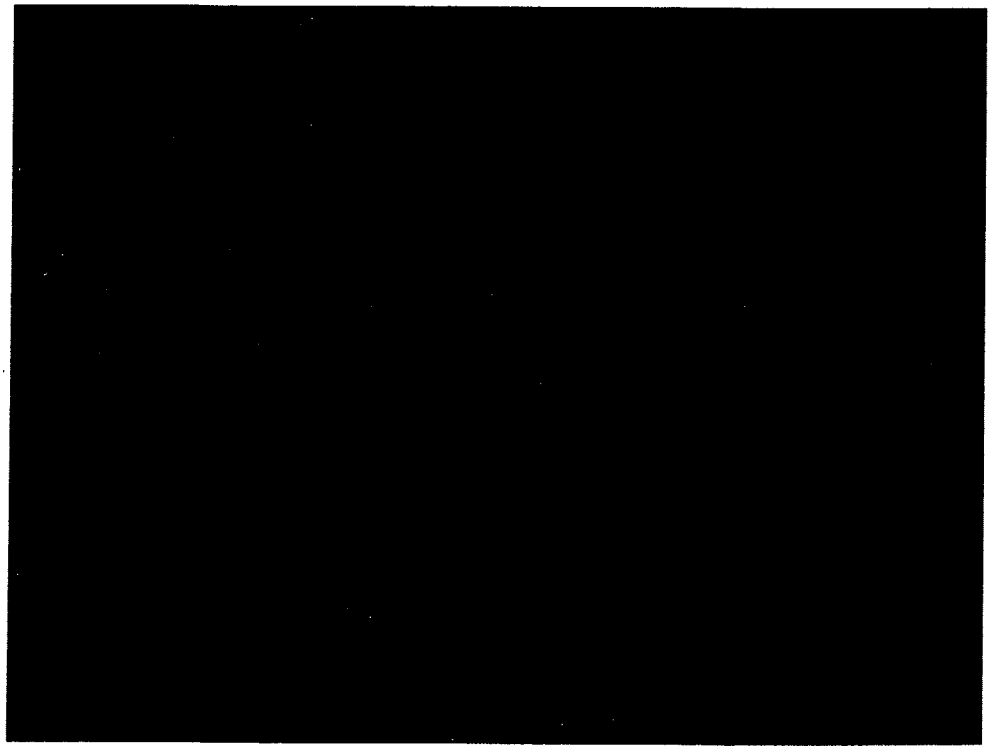

Figure I.2. Classified image of Bondi9b (ie., using total power and PPD as the classification criteria). Note the large unclassified region in the bottom left corner. This area is park land containing a reasonable portion of trees.

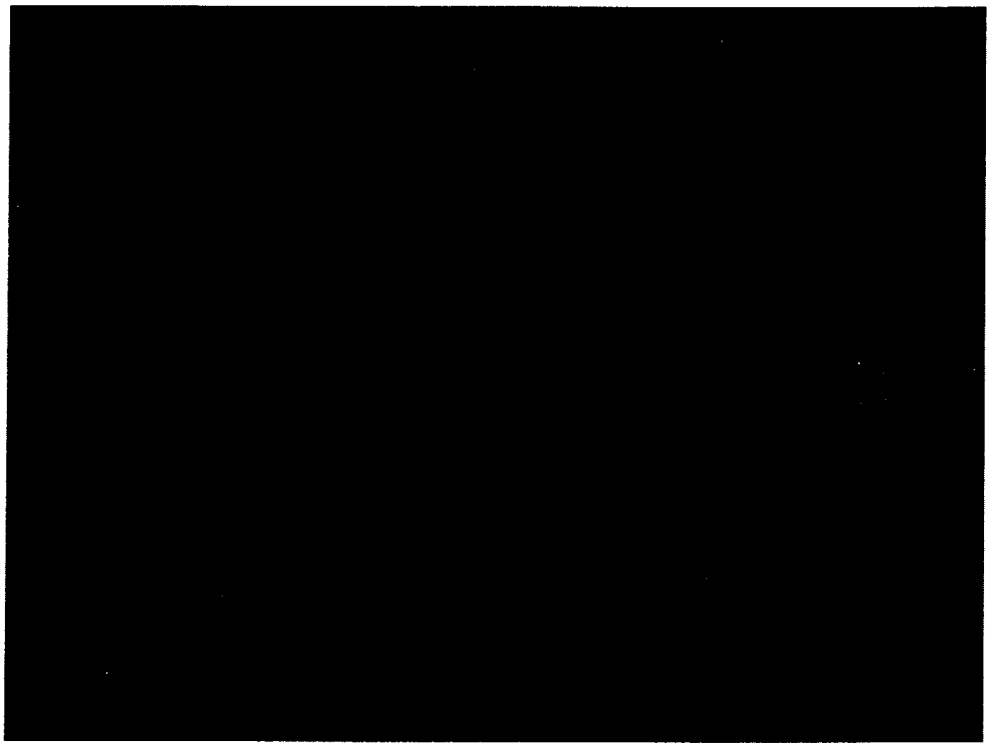

Figure I.3. Classified image of Bondi9a (ie., using total power, PPD and PI as the classification criteria). A large proportion of pixels were left unclassified.

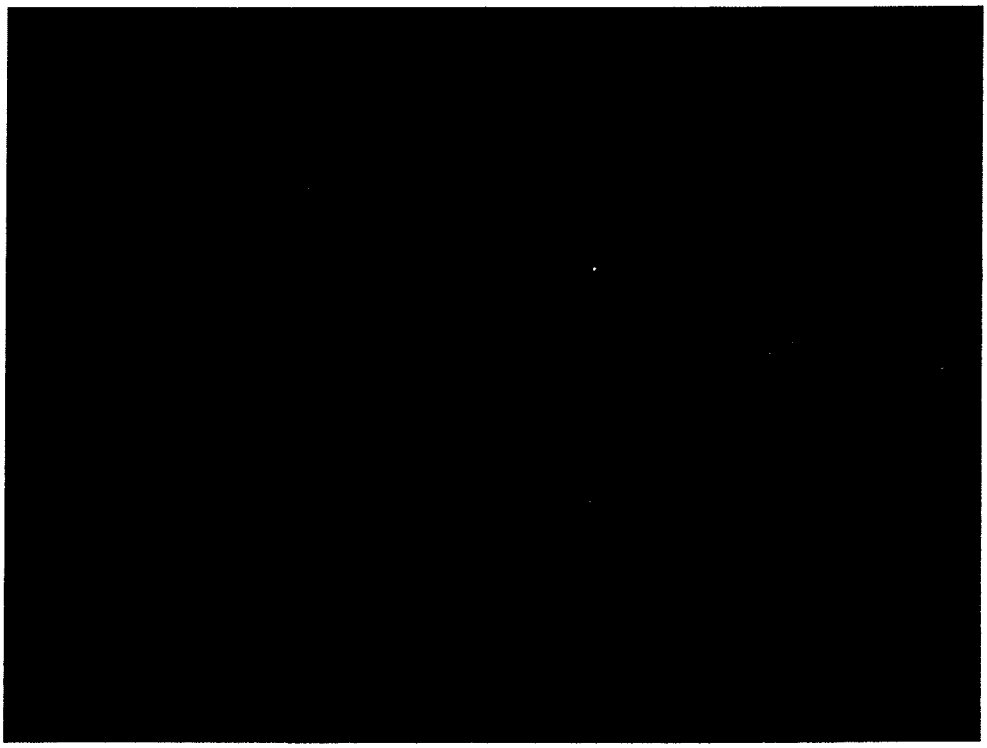

Figure I.4. Classified image of Bondi15c. All the pixels were classified. Note the large 'patches' on this image compared to Bondi9c.

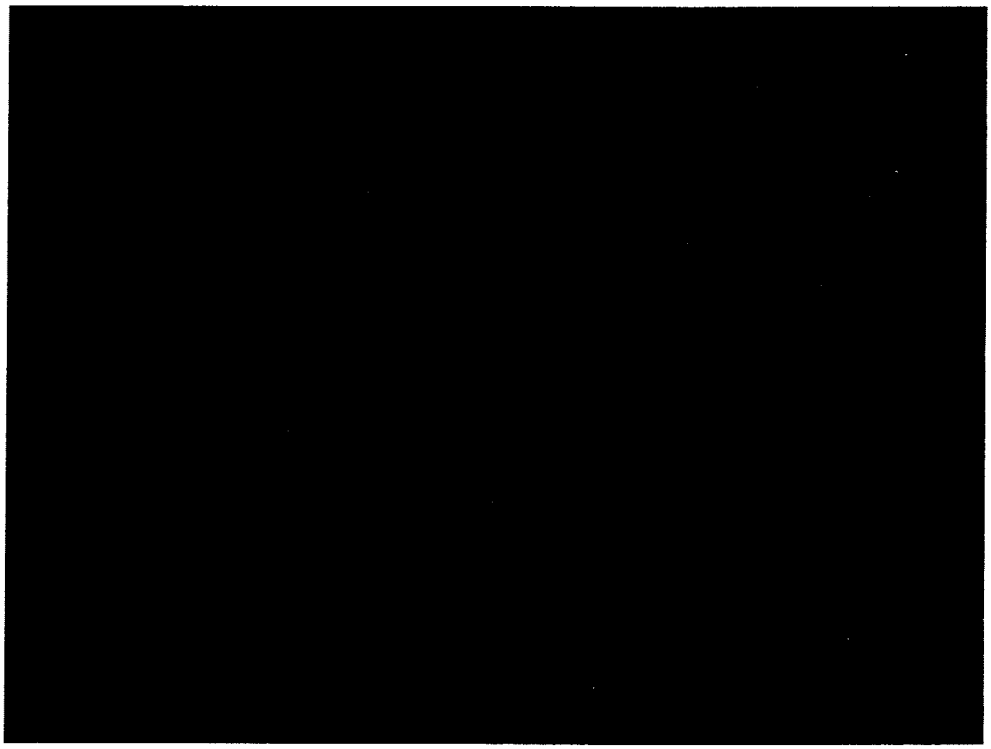

Figure I.5. Classified image of Bondi15b.

Note that the Bondi15a image was not included here. The few pixels, other than park, which were classified were unidentifiable on the image due to the resolution.

Kensington classified images:

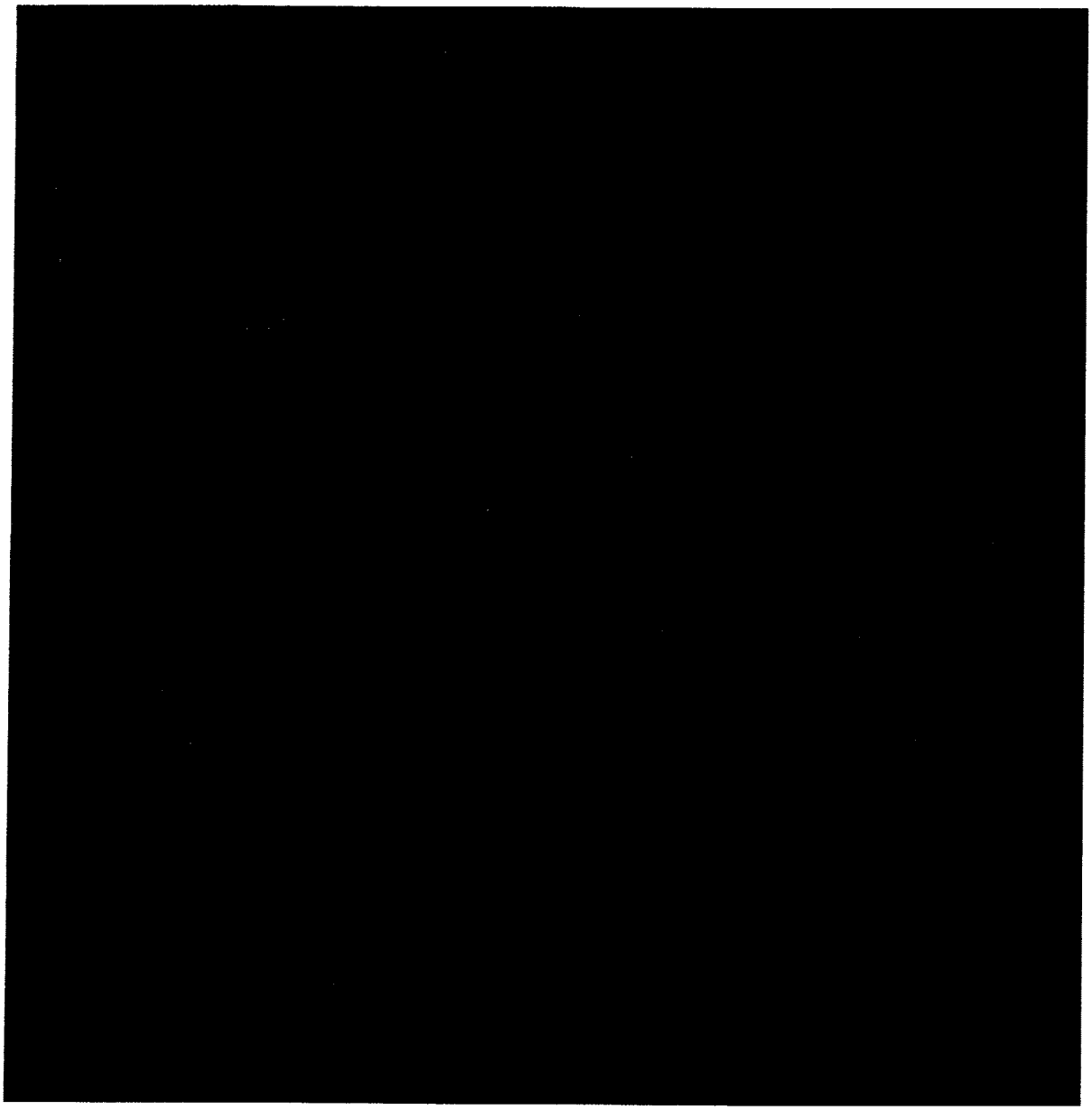

Figure I.6. Classified image of Kens9c. Note that all pixels were classified. The areas classified as commercial are indicative of building density. Refer to Figure I.12 for the ground truth.

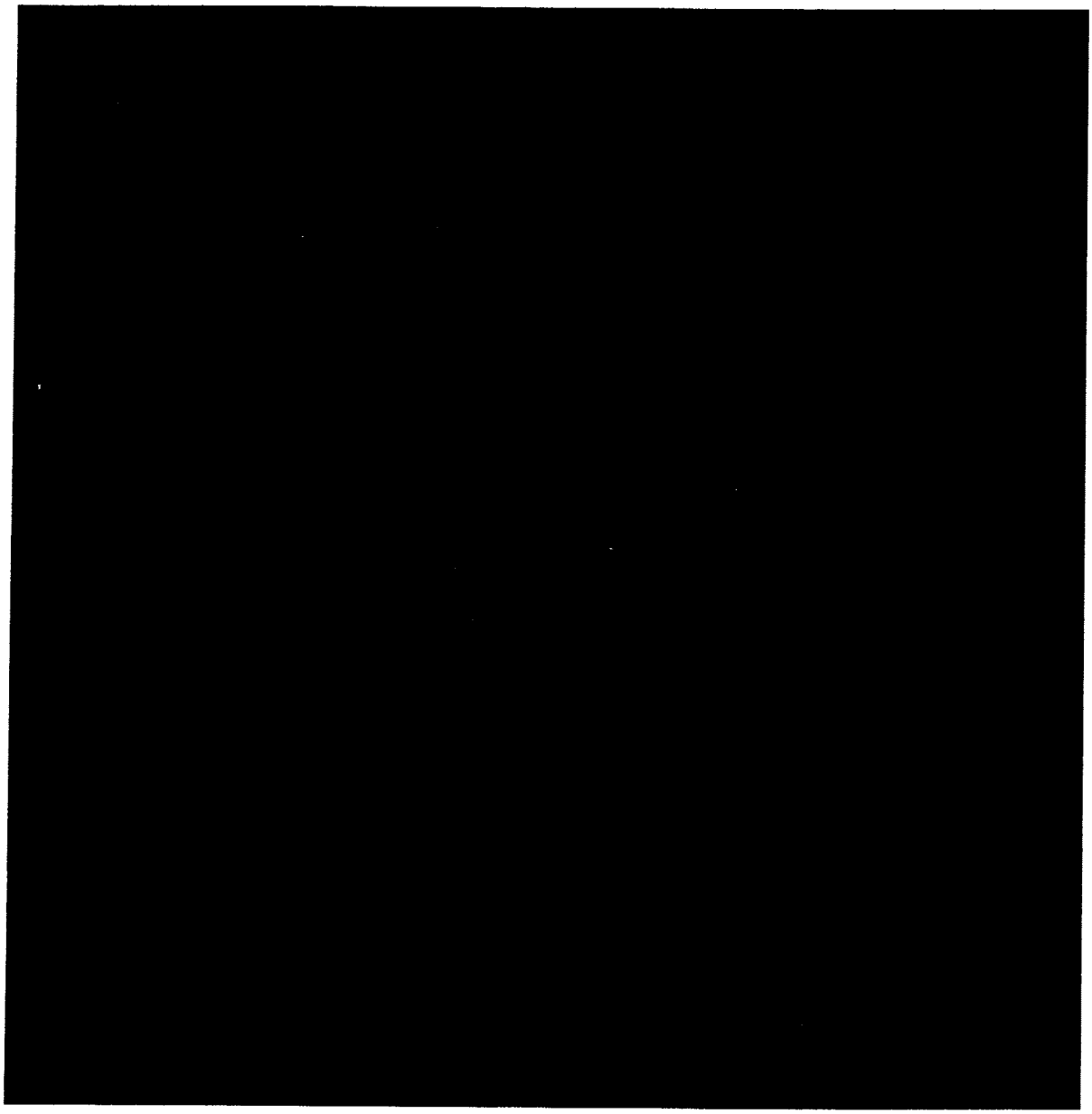

Figure I.7. Classified image of Kens9b.

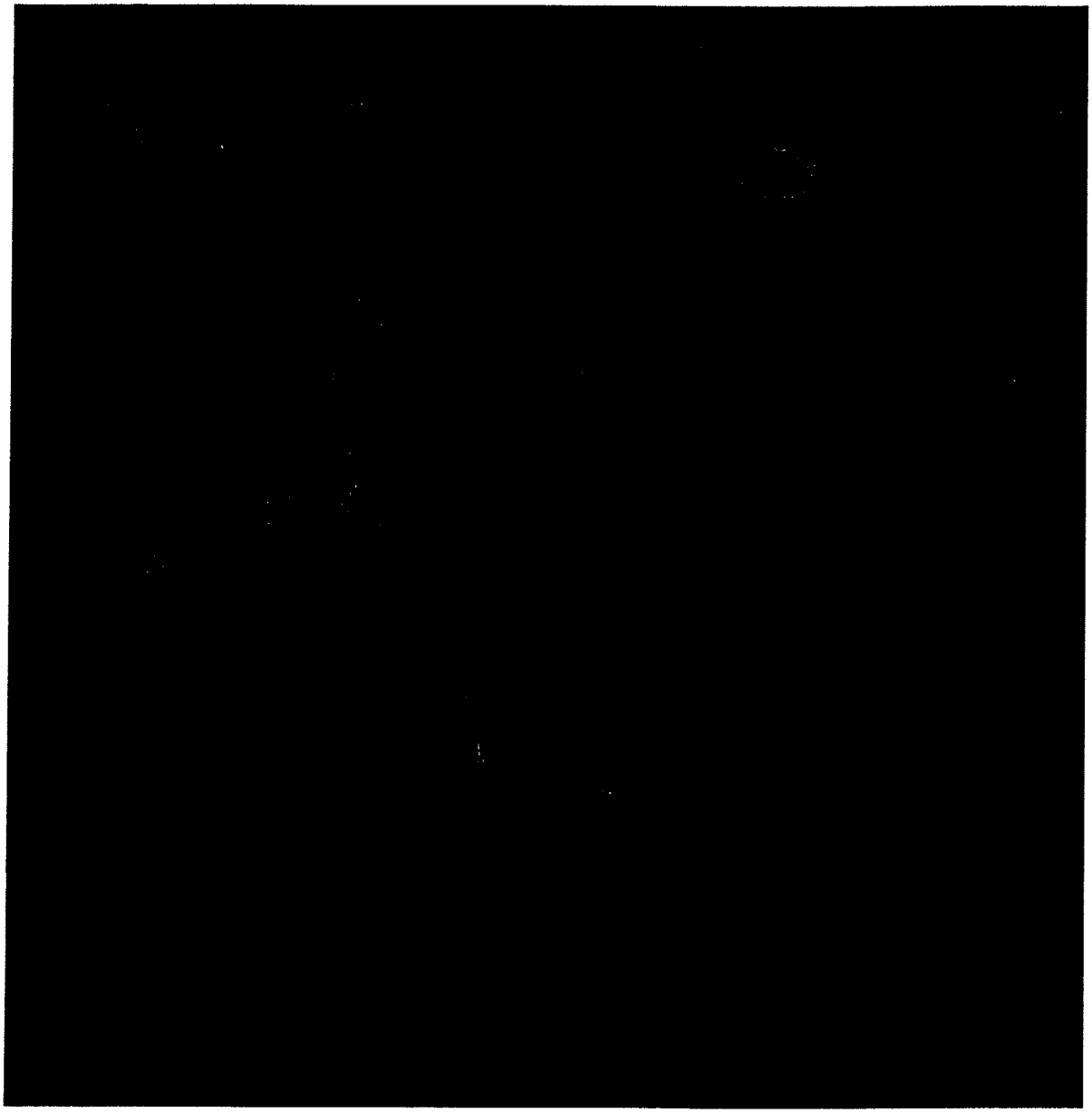

Figure I.8. Classified image of Kens9a. Large proportions of the pixels, particularly residential areas, were left unclassified.

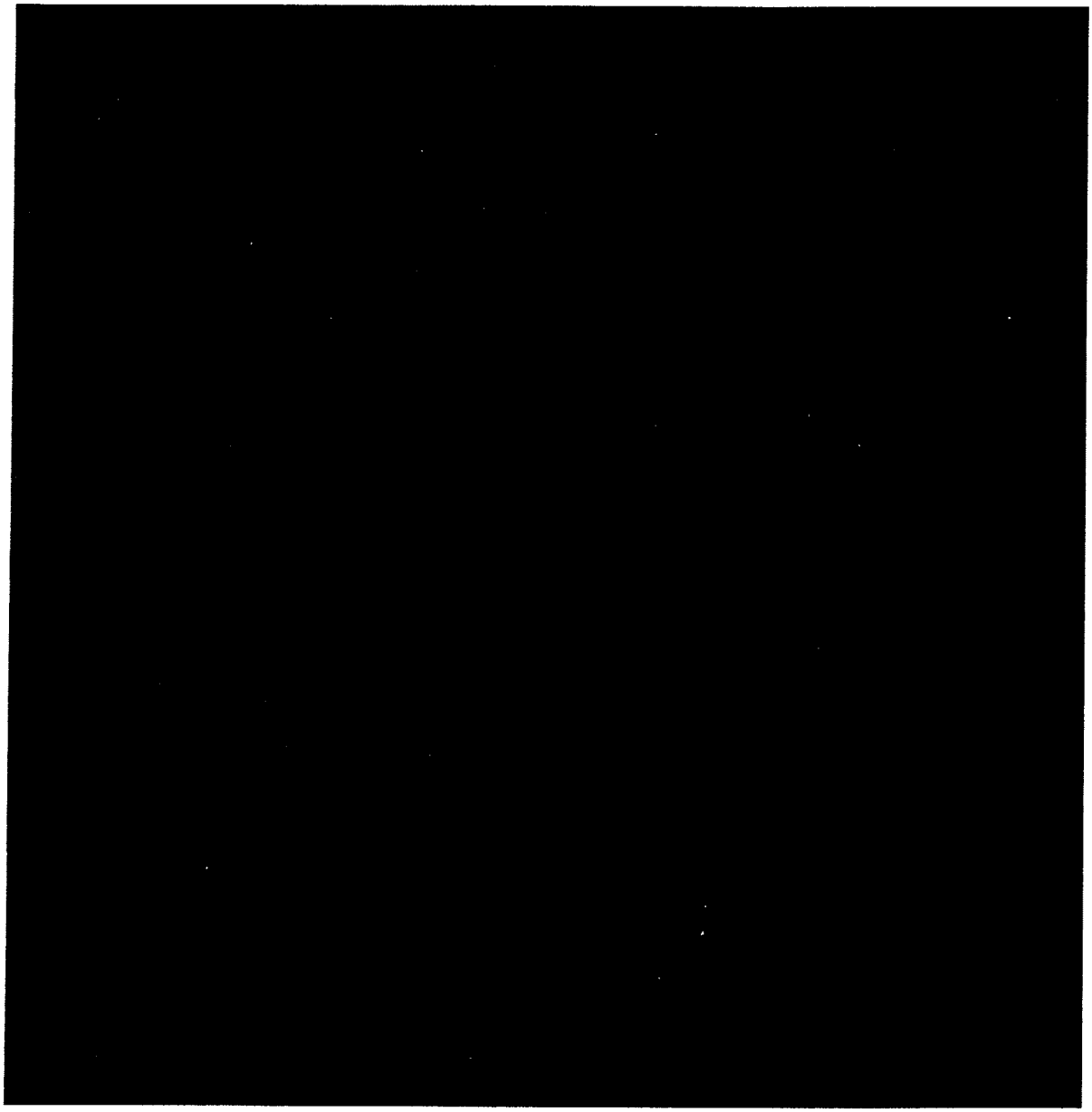

Figure I.9. Classified image of Kens15c. The 'patches' of commercial classes show a close relationship to the dense or tall buildings.

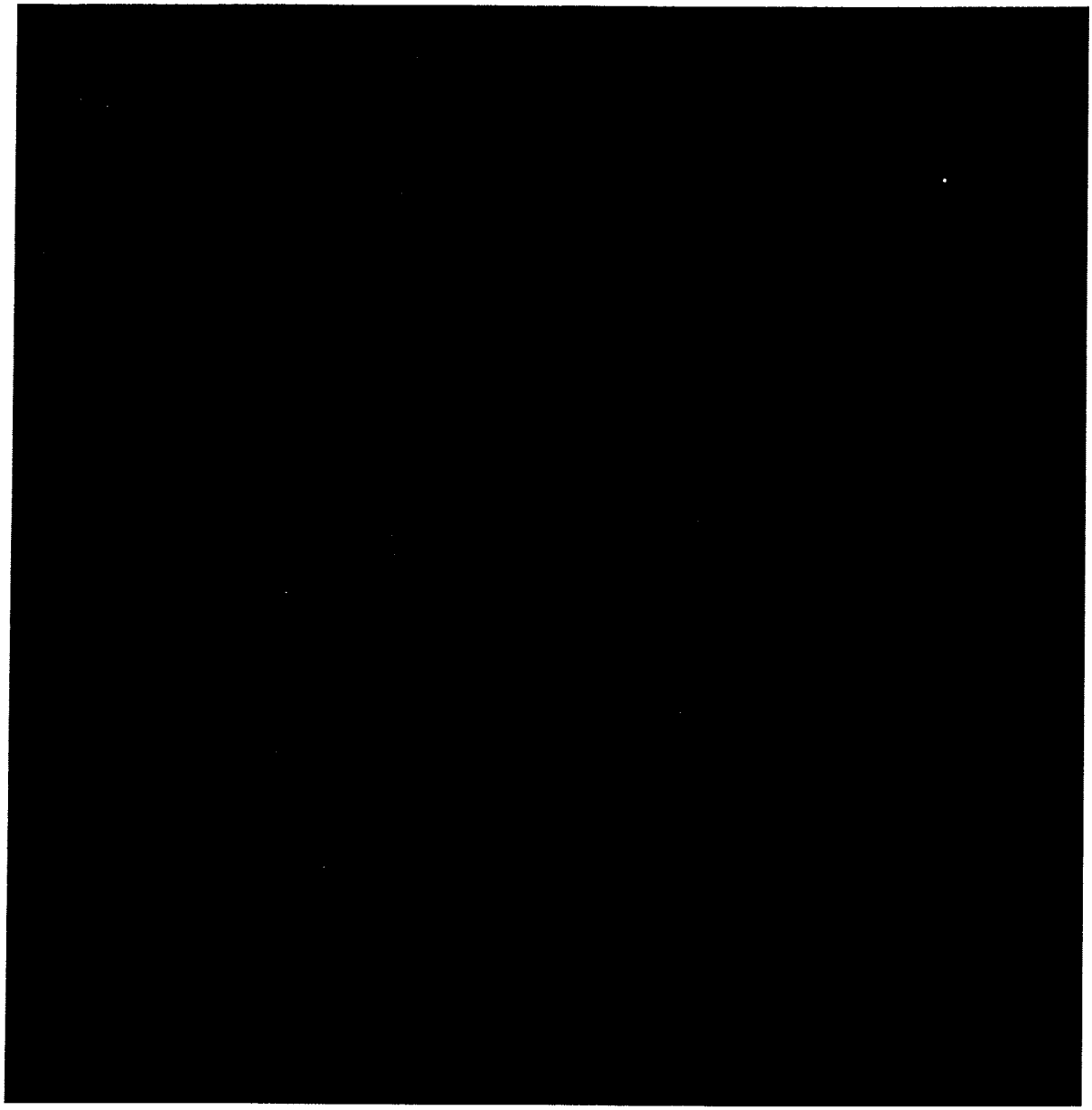

Figure I.10. Classified image of Kens15b.

Note that the Kens15a image was not included here. The few residential pixels which were classified were unidentifiable on the image due to the resolution. The commercial regions were very similar to those of Kens15b only slightly smaller.

Photographs providing ground truth:

Figure I.11. A photocopy of the aerial photograph covering the Bondi site, enlarged to the same scale as the classified imaged, used to provide ground truth. Although the copy is difficult to interpret, the colouring indicates the residential, commercial and parkland regions. The purple and orange colours (not in the legend at the beginning of this Appendix) represents institutional and tower block areas respectively.

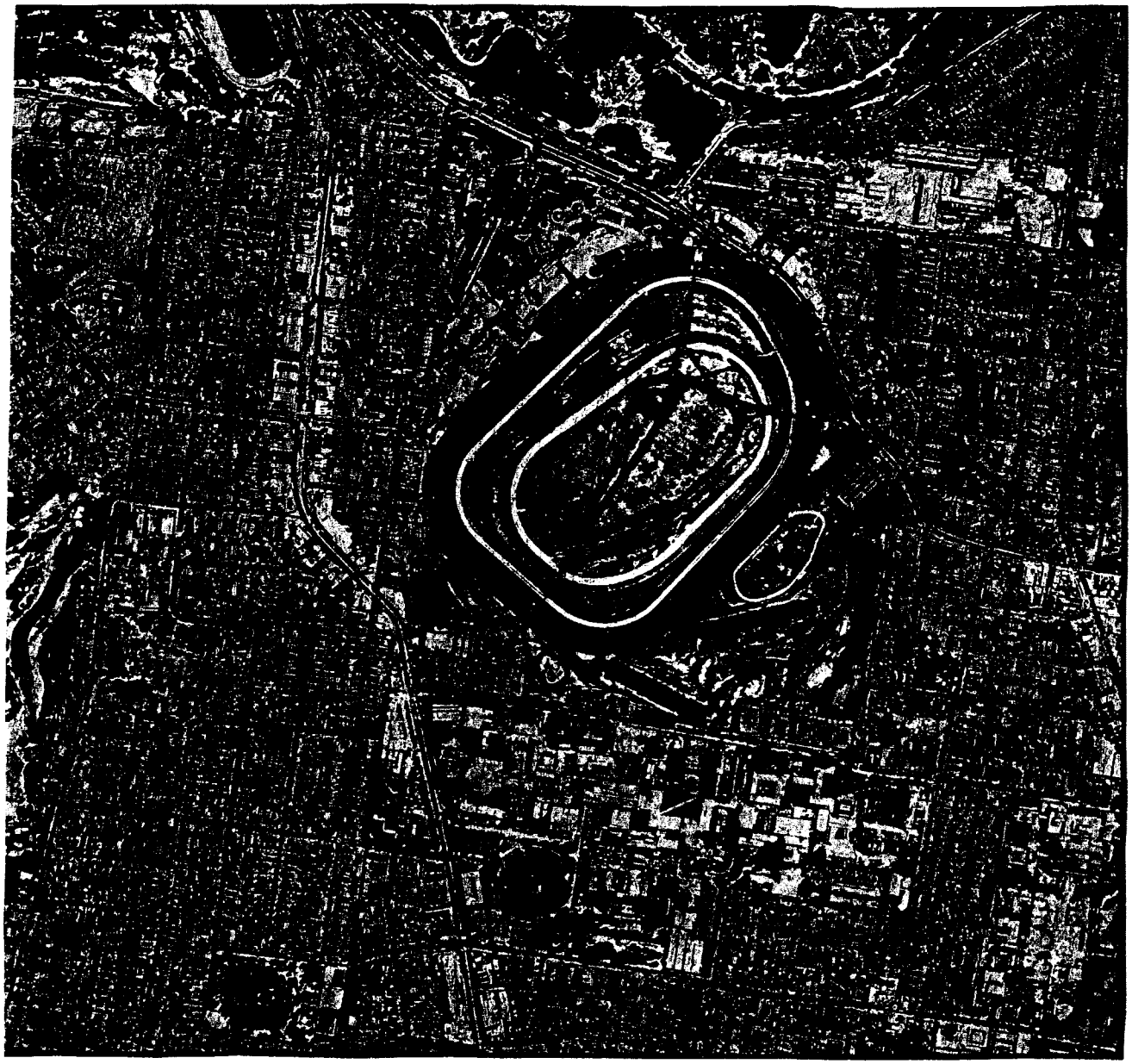

Figure I.12. A photocopy of the aerial photograph covering the Kensington site, enlarged to the same scale as the classified imaged, used to provide ground truth. Although the copy is difficult to interpret, the colouring indicates the residential, commercial and parkland regions. The purple and orange colours (not in the legend at the beginning of this Appendix) represents institutional and tower block areas respectively.

Difference Images:

The difference images illustrate the quality of each classification. These images are of the two test sites, Bondi and Kensington, where each difference number

is spatially positioned to indicate the successful and unsuccessful classification regions. The types of omission/commission results, and their respective difference numbers, are shown in Table I.1. (This table is very similar to Table 8.5). No difference image of Bondi15a exists due to the few correctly classified pixels being undetectable on the classification image.

Table I.1. The difference number representing the omission/commission results when comparing the classified image with ground truth.

Difference Number	Description
0	classification = photograph
-1	commercial classified as residential
-3	park classified as residential
-9	tower block classified as residential
-19	institutional classified as residential
1	residential classified as commercial
-2	park classified as commercial
-8	tower block classified as commercial
-18	institutional classified as commercial
3	residential classified as park
2	commercial classified as park
-6	tower block classified as park
-16	institutional classified as park
49	residential unclassified
48	commercial unclassified
46	park unclassified
40	tower block unclassified
30	institutional unclassified

It must be noted that all the difference images, ie., Figures I.18-I.22, are rotated 90° anti-clockwise from their respective classification images (Figures I.6-I.10). The reason for this was to maximise the numbers of the difference images, making them clearer to interpret.

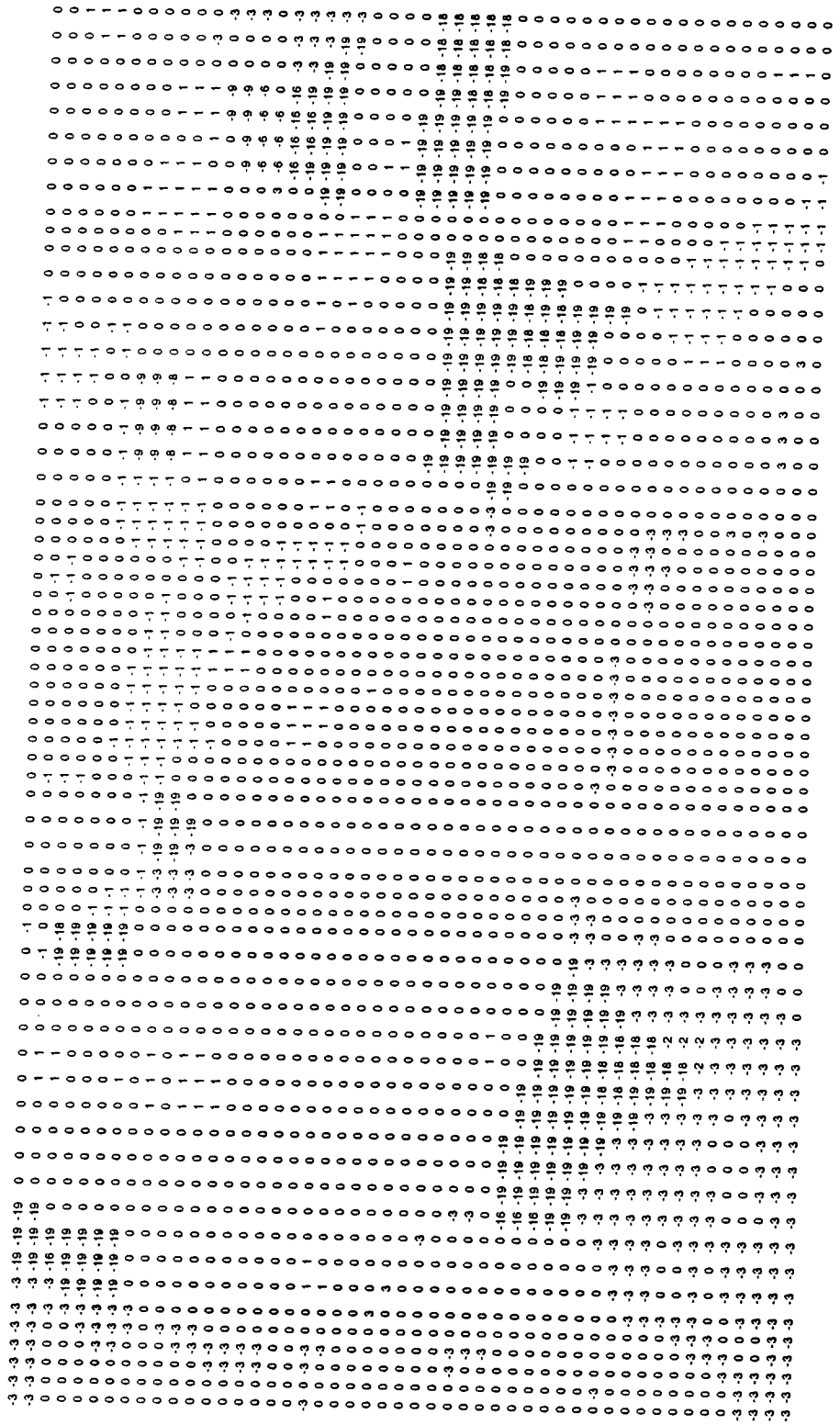

Figure I.13. Difference image of Bondi9c. The high proportion of '0's indicate correct classification. Furthermore '19' is not a classification error as it indicates where the institutional areas were classified as residential regions (since no institutional class exists for the model).

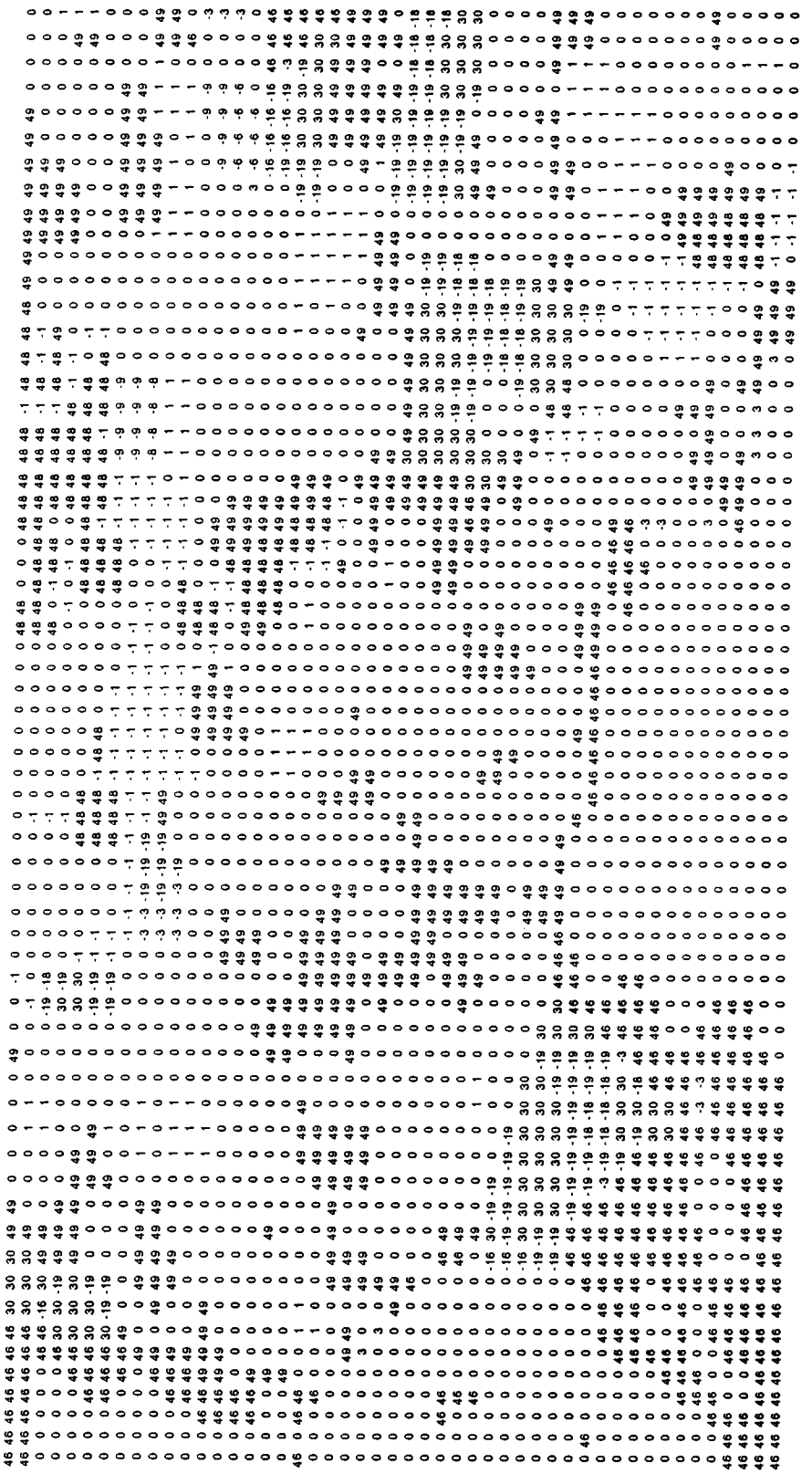

Figure I.14. Difference image of Bondi9b. The percentage of correctly classified areas are decreasing compared to Bondi9c, with more residential and commercial regions left unclassified (ie., '49' and '48' respectively).

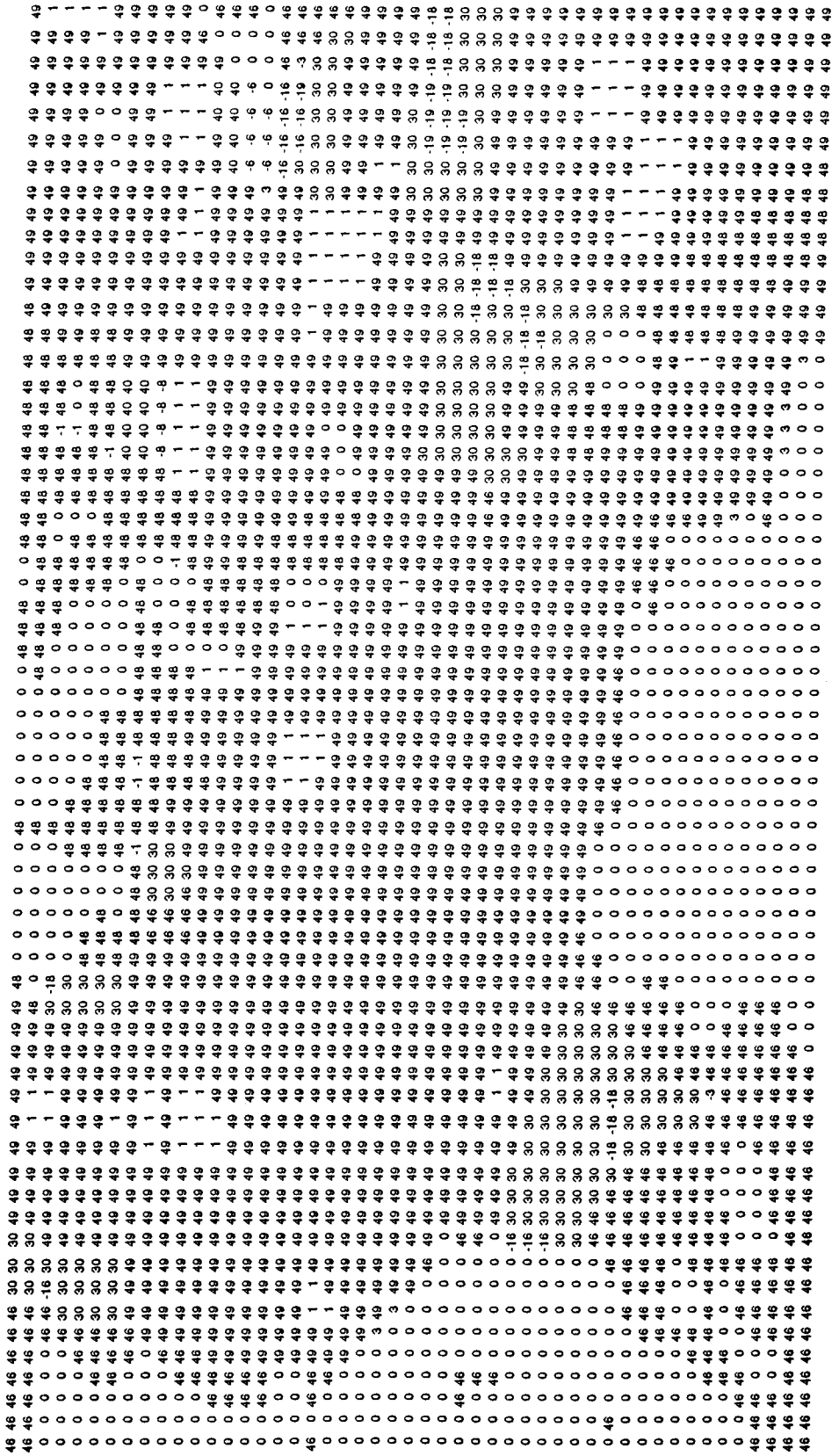

Figure I.15. Difference image of Bondi9a. There is a considerable proportion of unclassified residential and commercial areas.

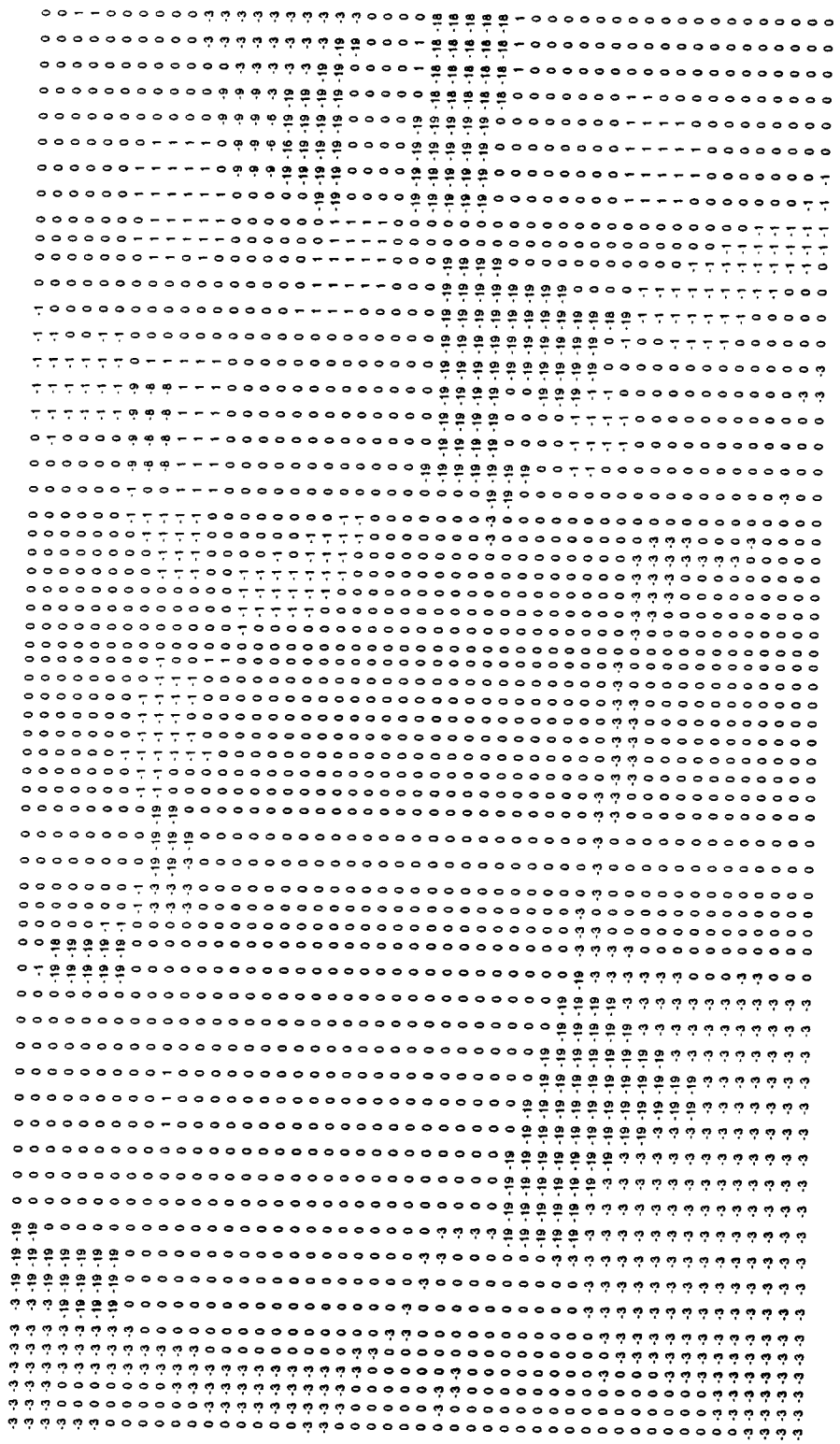

Figure I.16. Difference image of Bondi15c. The spatial patterns are quite similar to Bondi9c.

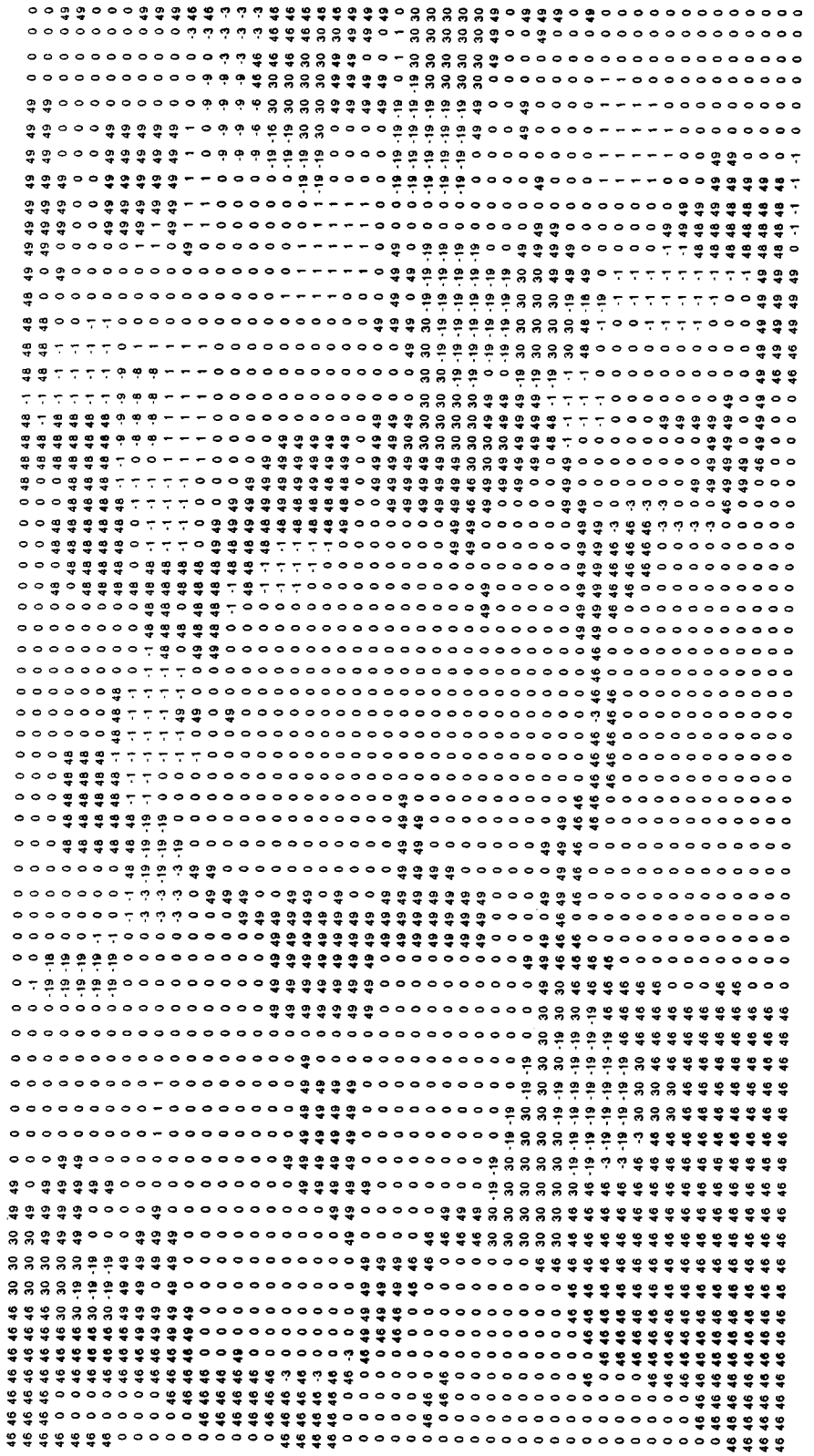

Figure I.17. Difference image of Bondi15b.

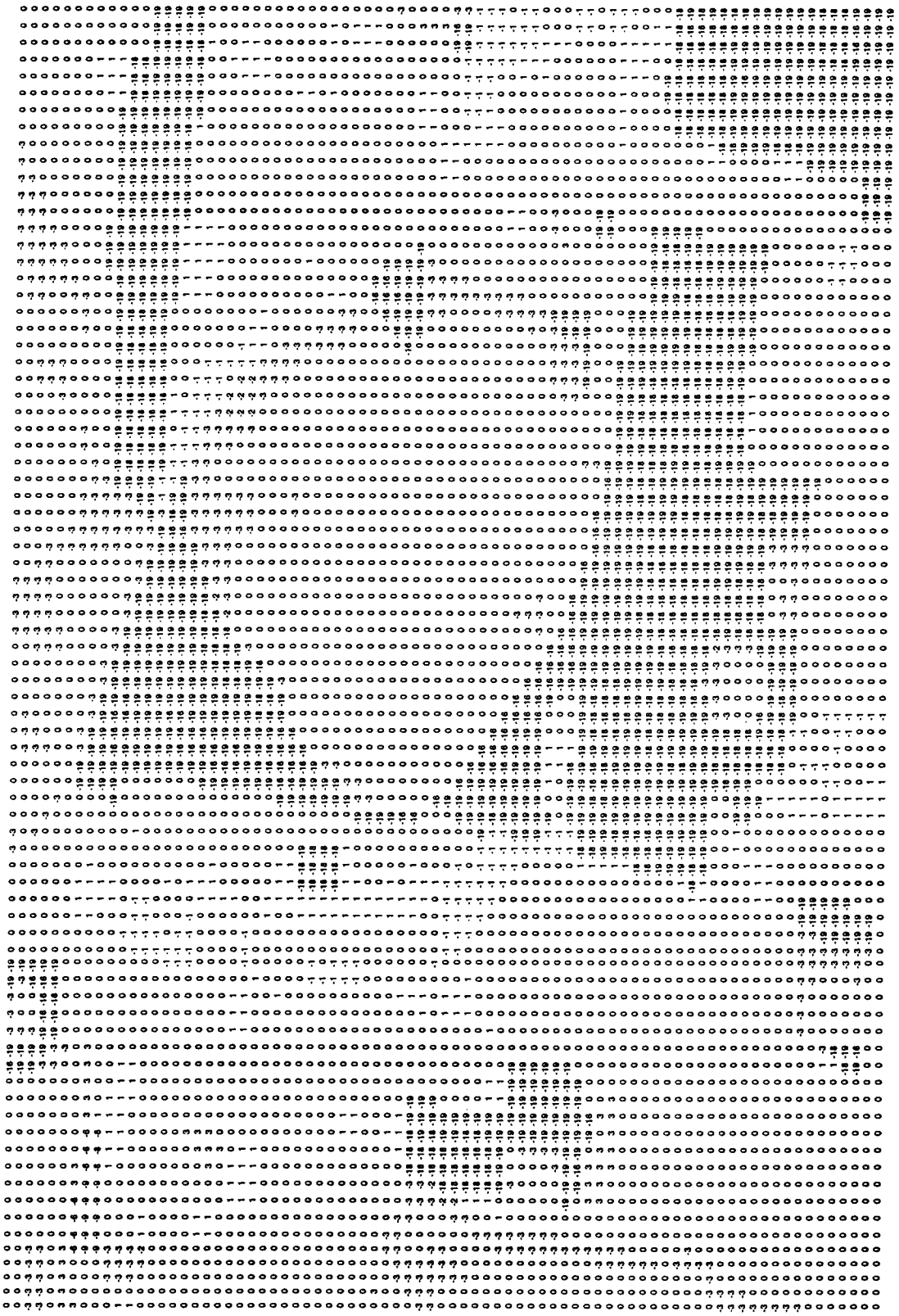

Figure I.18. Difference image of Kens9c. The high proportion of '0's indicate correct classification. Furthermore '18' and '19' are not classification errors as it indicates where the institutional areas were classified as commercial or residential regions respectively (since no institutional class exists for the model).

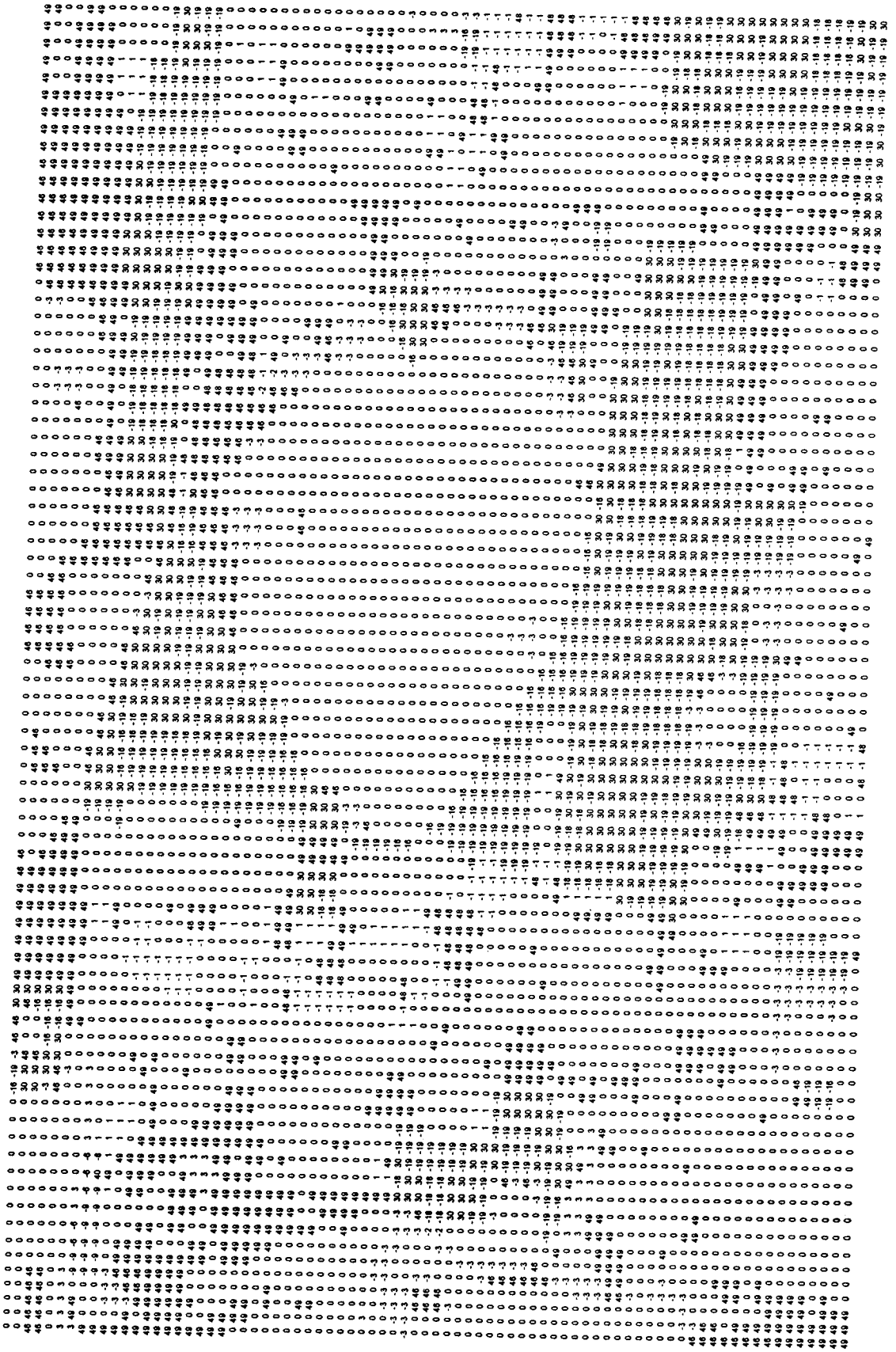

Figure I.19. Difference image of Kens9b. The percentage of correctly classified areas are decreasing compared to Kens9c.

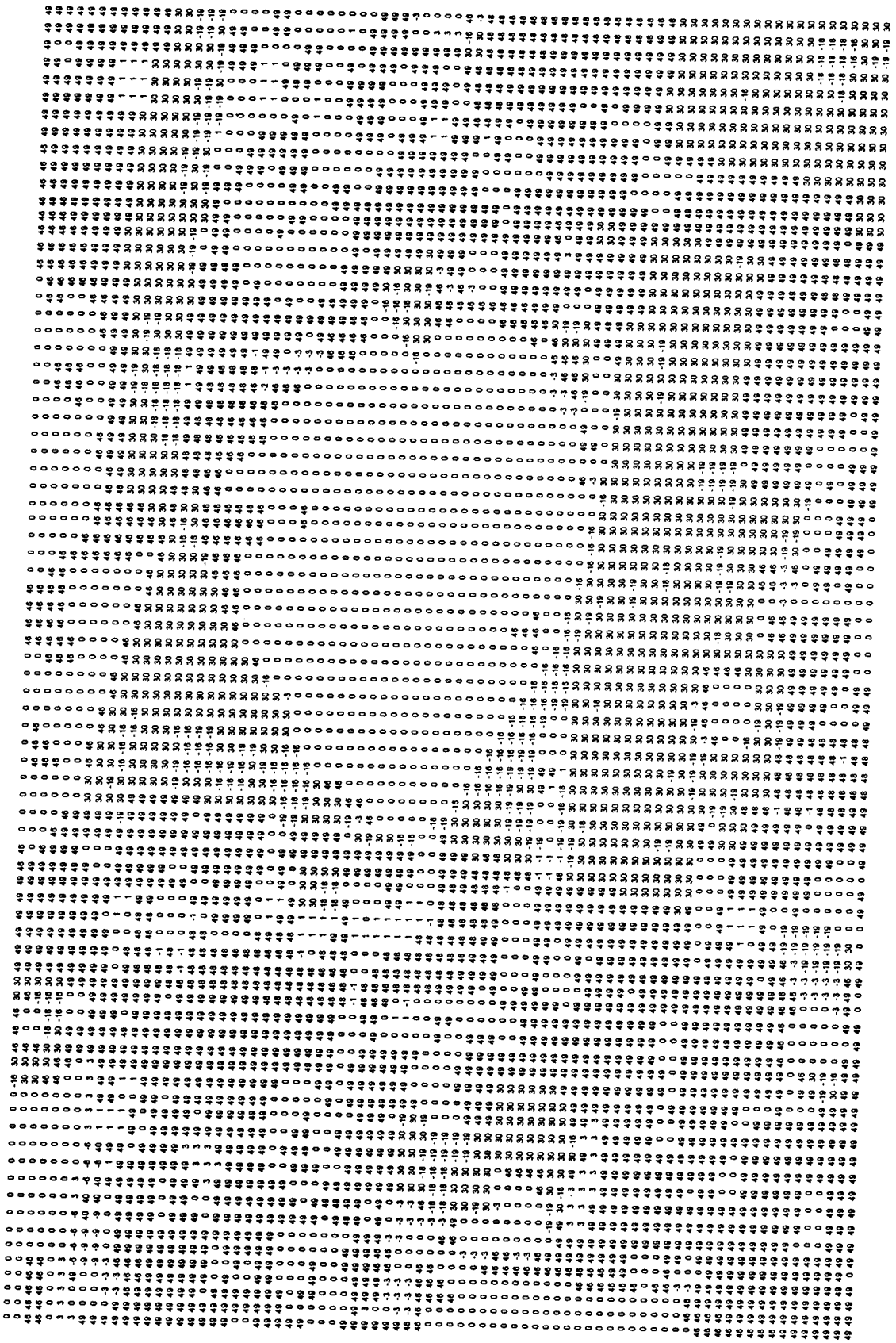

Figure I.20. Difference image of Kens9a. Apart for the large park land in the centre of the image (Randwick racecourse), many pixels are left unclassified.

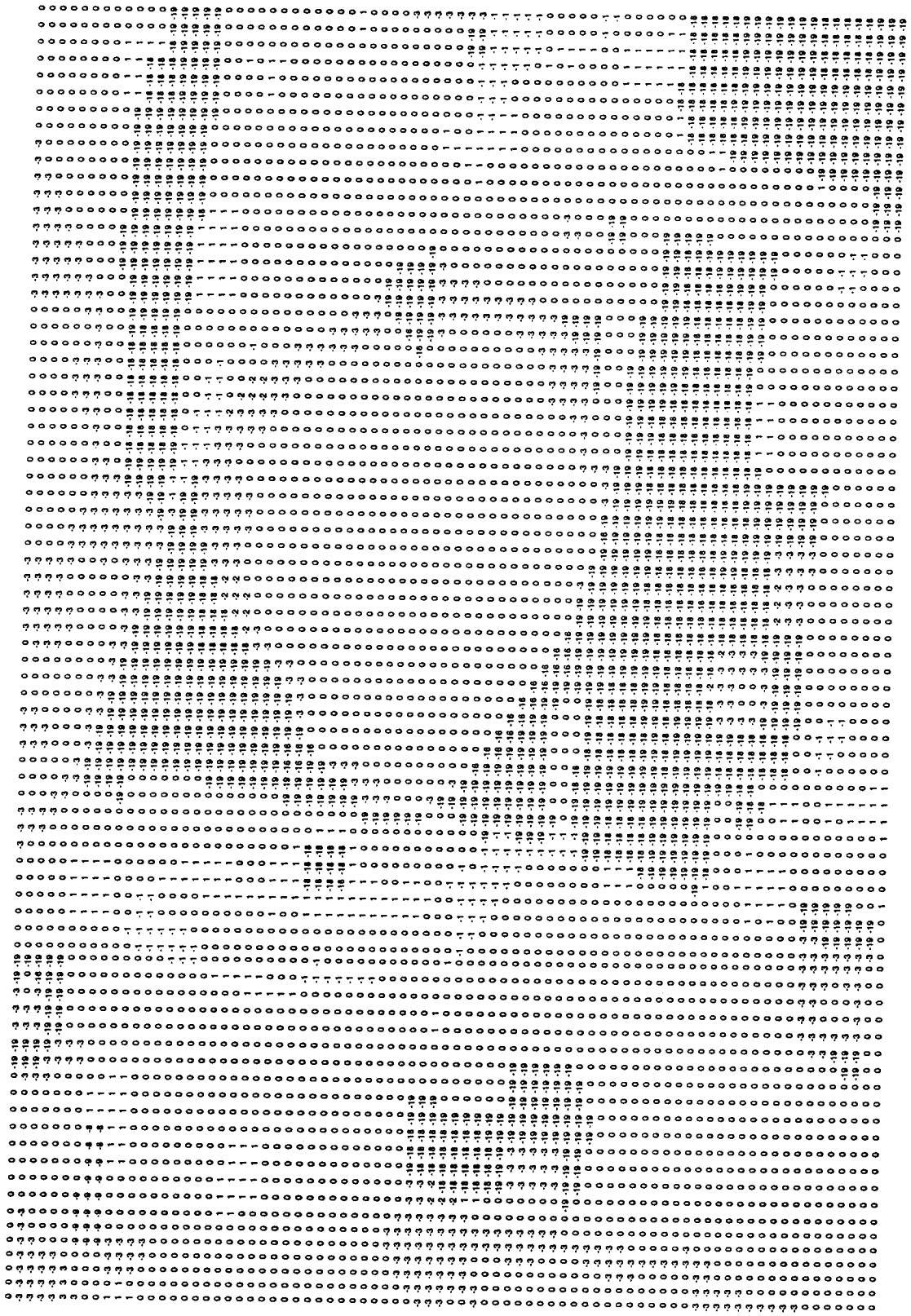

Figure I.21. Difference image of Kens15c. The spatial patterns are quite similar to Kens9c.

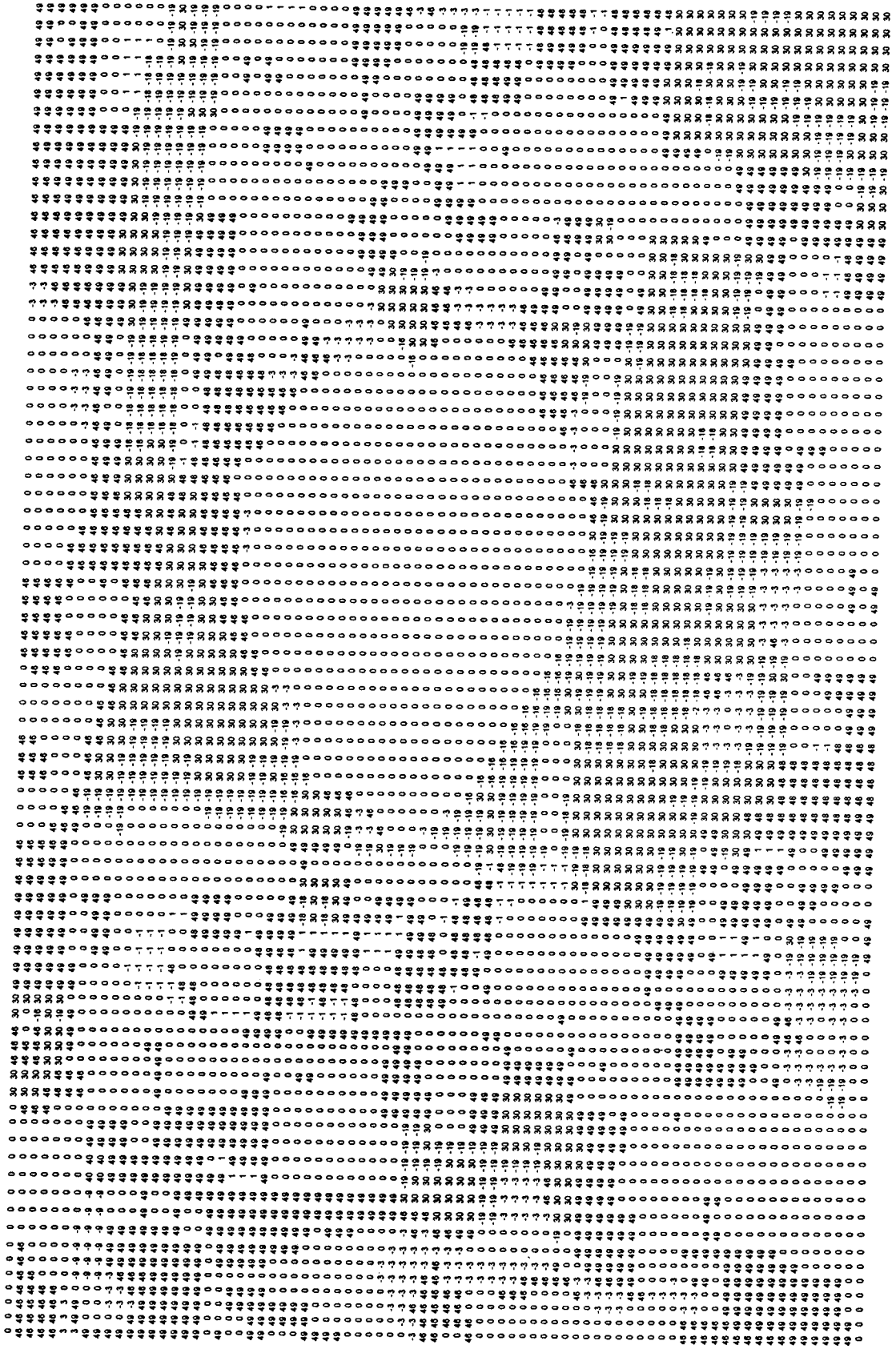

Figure I.22. Difference image of Kens15b.

Publications from

THE SCHOOL OF GEOMATIC ENGINEERING

(Formerly School of Surveying)

THE UNIVERSITY OF NEW SOUTH WALES

All prices include postage by surface mail. Air mail rates on application. (Effective March 1998)

To order, write to Publications Officer, School of Geomatic Engineering
The University of New South Wales, Sydney 2052, AUSTRALIA

NOTE: ALL ORDERS MUST BE PREPAID

UNISURV REPORTS - S SERIES

S8 - S20	Price (including postage) :		$10.00
S29 onwards	Price (including postage) :	Individuals	$25.00
		Institutions	$30.00

S8 A. Stolz, "Three-D Cartesian co-ordinates of part of the Australian geodetic network by the use of local astronomic vector systems", Unisurv Rep. S8, 182 pp, 1972.

S10 A.J. Robinson, "Study of zero error & ground swing of the model MRA101 tellurometer", Unisurv Rep. S10, 200 pp, 1973.

S12. G.J.F. Holden, "An evaluation of orthophotography in an integrated mapping system", Unisurv Rep. S12, 232 pp, 1974.

S14. Edward G. Anderson, "The Effect of Topography on Solutions of Stokes` Problem", Unisurv Rep. S14, 252 pp, 1976.

S16. K. Bretreger, "Earth Tide Effects on Geodetic Observations", Unisurv S16, 173 pp, 1978.

S17. C. Rizos, "The role of the gravity field in sea surface topography studies", Unisurv S17, 299 pp, 1980.

S18. B.C. Forster, "Some measures of urban residential quality from LANDSAT multi-spectral data", Unisurv S18, 223 pp, 1981.

S19. Richard Coleman, "A Geodetic Basis for recovering Ocean Dynamic Information from Satellite Altimetry", Unisurv S19,332 pp, 1981.

S20. Douglas R. Larden, "Monitoring the Earth's Rotation by Lunar Laser Ranging", Unisurv Report S20, 280 pp, 1982.

S29 Gary S Chisholm, "Integration of GPS into hydrographic survey operations", Unisurv S29, 190 pp, 1987.

S30. Gary Alan Jeffress, "An investigation of Doppler satellite positioning multi-station software", Unisurv S30, 118 pp, 1987.

S31. Jahja Soetandi, "A model for a cadastral land information system for Indonesia", Unisurv S31, 168 pp, 1988.

S33. R. D. Holloway, "The integration of GPS heights into the Australian Height Datum", Unisurv S33, 151 pp.,1988.

S34. Robin C. Mullin, "Data update in a Land Information Network", Unisurv S34, 168 pp. 1988.

S35. Bertrand Merminod, "The use of Kalman filters in GPS Navigation", Unisurv S35, 203 pp., 1989.

S36. Andrew R. Marshall, "Network design and optimisation in close range Photogrammetry", Unisurv S36, 249 pp., 1989.

S37. Wattana Jaroondhampinij, "A model of Computerised parcel-based Land Information System for the Department of Lands, Thailand," Unisurv S37, 281 pp., 1989.

S38. C. Rizos (Ed.), D.B. Grant, A. Stolz, B. Merminod, C.C. Mazur "Contributions to GPS Studies", Unisurv S38, 204 pp., 1990.

S39. C. Bosloper, "Multipath and GPS short periodic components of the time variation of the differential dispersive delay", Unisurv S39, 214 pp., 1990.

S40. John Michael Nolan, "Development of a Navigational System utilizing the Global Positioning System in a real time, differential mode", Unisurv S40, 163 pp., 1990.

S41. Roderick T. Macleod, "The resolution of Mean Sea Level anomalies along the NSW coastline using the Global Positioning System", 278 pp., 1990.

S42. Douglas A. Kinlyside, "Densification Surveys in New South Wales - coping with distortions", 209 pp., 1992.

S43. A. H. W. Kearsley (ed.), Z. Ahmad, B. R. Harvey and A. Kasenda, "Contributions to Geoid Evaluations and GPS Heighting", 209 pp., 1993.

S44. Paul Tregoning, "GPS Measurements in the Australian and Indonesian Regions (1989-1993)", 134 + xiii pp, 1996.

S45. Wan-Xuan Fu, "A study of GPS and other navigation systems for high precision navigation and attitude determinations", 332pp, 1996.

S46. Peter Morgan et al, "A zero order GPS network for the Australia region", 187 + xii pp, 1996.

S47. Yongru Huang, "A digital photogrammetry system for industrial monitoring", 145 + xiv pp, 1997.

S48. Kim Mobbs, "Tectonic interpretation of the Papua New Guinea Region from repeat satellite measurements", 256 + xc pp, 1997.

S49. Shaowei Han, "Carrier phase-based long-range GPS kinematic positioning", 185 + xi pp, 1997.

S50. Mustafa D Subari, "Low-cost GPS systems for intermediate surveying and mapping accuracy applications", 179 + xiii pp, 1997.

S51. Lao-Sheng Lin, "Real-time estimation of ionospheric delay using GPS measurements", 199 + xix pp, 1997.

S52. Merrin B Pearse, "A modern geodetic reference system for New Zealand", 324 +xviii pp, 1997.

S53. David B Lemon, "The nature and management of positional relationships within a local government Geographic Information System", 273 + xvi pp, 1997.

S54. Catherine Ticehurst, "Development of models for monitoring the urban environment using radar remote sensing", 282 + xix, 1998.

MONOGRAPHS

Prices include postage by surface mail

		Price
M1.	R.S. Mather, "The theory and geodetic use of some common projections", (2nd edition), 125 pp., 1978.	$15.00
M2.	R.S. Mather, "The analysis of the earth's gravity field", 172 pp., 1971.	$8.00
M3.	G.G. Bennett, "Tables for prediction of daylight stars", 24 pp.,1974.	$5.00
M4.	G.G. Bennett, J.G. Freislich & M. Maughan, "Star prediction tables for the fixing of position", 200 pp., 1974.	$8.00
M8.	A.H.W. Kearsley, "Geodetic Surveying", 96 pp, (revised) 1988.	$12.00
M11.	W.F. Caspary, "Concepts of Network and Deformation Analysis",183 pp., 1988.	$25.00
M12.	F.K. Brunner, "Atmospheric Effects on Geodetic Space Measurements", 110 pp., 1988.	$16.00
M13.	Bruce R. Harvey, "Practical Least Squares and Statistics for Surveyors", (2nd edition), 319 pp., 1994.	$30.00
M14.	Ewan G. Masters & John R. Pollard (Ed.), "Land Information Management", 269 pp., 1991. (Proceedings LIM Conference, July 1991).	$20.00
M15/1	Ewan G. Masters & John R. Pollard (Ed.), "Land Information Management - Geographic Information Systems - Advance Remote Sensing Vol 1" 295 pp., 1993 (Proceedings of LIM & GIS Conference, July 1993).	$30.00
M15/2	Ewan G. Masters & John R. Pollard (Ed.), "Land Information Management - Geographic Information Systems - Advance Remote Sensing Vol 2" 376 pp., 1993 (Proceedings of Advanced Remote Sensing Conference, July 1993).	$30.00
M16.	A. Stolz, "An Introduction to Geodesy", 112 pp., 1994.	$20.00
M17	Chris Rizos, "Principles and Practice of GPS Surveying", 565 pp., 1997.	$50.00